DEPARTMENT OF
ECOLOGY
State of Washington

WASHINGTON STATE UNIVERSITY

Applied Research and Extension for Second-Generation Organic Waste Processing: High Solids Anaerobic Digestion, Nutrient Recovery, and Pyrolysis

December 2013
Publication no. 14-07-010
Contract no. C1200132

Publication and Contact Information

This report is available on the Department of Ecology's website at https://fortress.wa.gov/ecy/publications/SummaryPages/1407010.html.

For more information contact:

Waste 2 Resources
P.O. Box 47600
Olympia, WA 98504-7600

Phone: 360-407-6900

Washington State Department of Ecology - www.ecy.wa.gov

- Headquarters, Olympia 360-407-6000
- Northwest Regional Office, Bellevue 425-649-7000
- Southwest Regional Office, Olympia 360-407-6300
- Central Regional Office, Yakima 509-575-2490
- Eastern Regional Office, Spokane 509-329-3400

If you need this document in a format for the visually impaired, call the Waste 2 Resources Program at 360-407-6900 Persons with hearing loss can call 711 for Washington Relay Service. Persons with a speech disability can call 877-833-6341.

Applied Research and Extension for Second-Generation Organic Waste Processing

High Solids Anaerobic Digestion, Nutrient Recovery, and Pyrolysis

by
Craig Frear, Quan-Bao Zhao, Baisuo Zhao, Jingwei Ma, Liang Yu, Mahesh Bule, Shulin Chen, Nicholas Kennedy, Manuel Garcia-Perez, Matthew Smith, Waled Suliman, Jereon de Graaf, Shi-Shen Liaw, Jesus Garcia-Nunez, Brennan Pecha, Georgine Yorgey, and Chad Kruger

Waste 2 Resources
Washington State Department of Ecology
Olympia, Washington

Table of Contents

List of Figures and Tables

Page

Figures

Tables

List of Abbreviations

AAS	Atomic Absorption Spectrometer
AD	Anaerobic Digestion
ADM1	Anaerobic Digestion Model No. 1
ADR	Advective-Diffusive Reactor
$AgNO_3$	Silver Nitrate
ASBR	Anaerobic Sequencing Batch Reactor
$BaCl_2$	Barium Chloride
BET	Brunauer, Emmet and Teller (surface area)
BOD	Biological Oxygen Demand
C:N ratio	Carbon to Nitrogen Ratio
$C_2H_4BrNaO_3S$	Sodium 2-bromoethanesulfonate
$CaCl_2$	Calcium Chloride
CAFO	Concentrated Animal Feeding Operation
CaOH	Calcium Hydroxide
CEC	Cation Exchange Capacity
CFD	Computational Fluid Dynamics
CH_4	Methane
CO_2	Carbon Dioxide
CO_3^{2-}	Carbonate
COD	Chemical Oxygen Demand
CSTR	Continuous Stirred Tank Reactor
DTG	Differential Thermogravimetric
EPA	Environmental Protection Agency
FC:VM ratio	Fixed Carbon to Volatile Matter Ratio
$FeCl_2$	Iron Chloride
FPU	Filter Paper Unit
FWHM	Full Width Half Maximum
GHG	Greenhouse Gas
HCl	Hydrogen Chloride
H_2CO_3	Carbonic Acid
H_2S	Hydrogen Sulfide
HSADRS	High Solids Anaerobic Digestion with Recycling Seeds
HCO_3^-	Bicarbonate
HRT	Hydraulic Retention Time
HSAD	High Solids Anaerobic Digestion
IC	Inorganic Carbon
ICP-MS	Inductively Coupled Plasma Mass Spectrometer
LCFA	Long Chain Fatty Acid
$MgSO_4$	Magnesium Sulfate
MSW	Municipal Solid Waste
N	Nitrogen
$NaHCO_3$	Sodium Bicarbonate

N_2O	Nitrous Oxide
NH_3	Ammonia
NOx	Mono-Nitrogen Oxides
N_p	Power Number
N_q	Flow Number
NR	Nutrient Recovery
NREL	National Renewable Energy Laboratory
OLR	Organic Loading Rate
OP	Ortho-Phosphorus
OTU	Operational Taxonomic Unit
P	Phosphorus
PCR	Polymerase Chain Reaction
PET	Polyethylene terephthalate
PO_4-P	Soluble Phosphate
Pr	Prandtl Number
Re	Reynolds Number
RNG	Renewable Natural Gas
SBP	Specific Biogas Production
SEM	Scanning Electron Microscopy
SG	Specific Gravity
SRT	Solid Retention Time
TAN	Total Ammonia Nitrogen
TGA	Thermogravimetric Analyzer
TKN	Total Kjeldahl Nitrogen
TN	Total Nitrogen
TOC	Total Organic Carbon
TP	Total Phosphorus
T-RFLP	Terminal Restriction Fragment Length Polymorphism
TS	Total Solids
TVS	Total Volatile Solids
UASB	Upflow Anaerobic Sludge Blanket
US	United States
USBR	Universal Sequence Batch Reactor
VFA	Volatile Fatty Acid
VOC	Volatile Organic Compounds
VS	Volatile Solids
VSLR	Volatile Solid Loading Rate
W2F	Waste 2 Fuels
WA	Washington State
WSDA	Washington State Department of Agriculture
WSU	Washington State University
WWTP	Wastewater Treatment Plant
XPS	X-ray Photoelectron Spectroscopy
$ZnCl_2$	Zinc Chloride

Acknowledgements

The authors would like to thank Cindy Alwine, Jonathan Lomber and Nicholas Kennedy for their help with analysis, laboratory procedures, and document preparation.

Executive Summary

Managing residual organic wastes from our cities, including green wastes, food scraps, and recalcitrant materials such as wood scraps and pallets, is one of the major sustainability challenges of our time. Recently, there has been a growing recognition that these "waste" materials that were once disposed of in landfills and wastewater treatment plants are in fact valuable raw materials. As such, they can support new local industries, generate renewable energy and yield other sustainable product lines.

Washington State citizens can take pride in the fact that we are re-routing a significant and growing proportion of green waste and food scraps to municipal and regional organics recycling facilities. The primary technology used at these facilities is aerobic composting, a proven "first generation" technology that has been commercially available for many years. Using composting technology, Washington, along with the rest of the West Coast, has led the United States in implementing food scrap diversion programs[1].

Food and green waste recycling and composting programs, though, have not been without serious challenges. Cities including Seattle, Toronto, Seoul, and Stockholm have all experienced odor, air quality and public health concerns from the increased flow of food and green waste diverted to regional composting facilities. In many cases, these materials are already decomposing prior to arrival to the compost facility due to storage and transportation timelines inherent in the collection process. Issues can be particularly apparent when large inflows of grass clippings add to facility burdens in the late spring and early summer, increasing potential for odors before the composting process has a chance to "catch up".

With these challenges in mind, it's becoming clear that new, "second-generation" technologies could be used to manage organic materials more sustainably while also producing renewable energy and value-added products. This is particularly true for food scraps and other materials that are energy rich and also problematic for current composting technology. By producing renewable energy and re-capturing carbon and nutrients that would otherwise be lost, organics recycling facilities will play a key role in solving future energy, climate, and sustainability challenges.

The Washington Department of Ecology's Waste 2 Resources program has thus strategically invested in Washington State University's Center for Sustaining Agriculture and Natural Resources to support research that will facilitate the commercialization of a suite of second-generation organics processing technologies that can be integrated with aerobic composting by our regional organics recycling industry. In this biennium, Waste 2 Resources funded research in three general areas:

- ***Anaerobic digestion*** may be combined with composting to treat both wet and dry material streams. They thus can treat complimentary material streams, and residual solids from anaerobic digestion are suitable for further processing via composting. Together, the combined action of the two technologies shows potential to improve overall emissions, odors and life cycle impacts. While some anaerobic digestion technologies (e.g. plug

flow) are well developed, others (e.g. high solids anaerobic digestion) are still in development. This report describes three projects that focus on (1) technical support, tech-transfer and applied problem-solving research for anaerobic digestion project developers in the state (2) modifications to plug flow technology that would allow for processing of food scrap liquids, and (3) an upgraded high solids anaerobic digestion pilot technology.

- ***Nutrient recovery*** technology, implemented in coordination with anaerobic digestion, will allow facilities to recapture and recycle nutrients. It will also allow facilities to more efficiently utilize and recycle water resources, significantly reducing fresh water inputs. Washington State University has previously commercialized nutrient recovery technology for livestock manure treated with anaerobic digestion. Building on this work, this report describes research focused on adapting that nutrient recovery technology to high solids anaerobic digestion of municipal organic wastes.

- ***Pyrolysis***, an emerging technology, has great promise for recovering energy and fuel from woody feedstock, as well as producing stable biochar for soils and pollutant capture. Woody feedstock would include construction and demolition wood debris, land clearing waste, pallets, and wood chips from mill operations. Pyrolytic treatment can produce a combination of either heat/char or fuel/char, depending upon the operational parameters used. Product generation can thus be tailored to meet the demands of emerging markets. Pyrolysis may also be suitable for integration with anaerobic digestion, in that pyrolysis produces a notable fraction of water soluble sugars and acids appropriate for subsequent anaerobic digestion. The char that is produced can serve as both a carbon sequestering media and a nutrient absorber, allowing for integration with, and enhancement of, nutrient recovery and export from a regional organics recycling facility. This report describes work focusing on integration of pyrolysis with other waste processing technologies and modification of biochar for nutrient recovery.

The applied research and extension projects described in this report were carefully selected to address specific barriers to commercial viability that exist with these emerging technologies, as well as to provide ongoing extension and technological support to the next generation organics industry in Washington State. Applied research projects were in the areas of:

- The application of developed nutrient recovery-anaerobic digestion systems to municipal organic wastes such as food scrap and grass waste,
- Understanding needs for integration of pyrolysis with anaerobic digestion and compost technologies,
- Treatment of food scrap to explore processing with existing commercialized anaerobic digestion technologies,
- Furthering steps to support a new high solids anaerobic digestion system developed at Washington State University by addressing green waste pretreatment and mixing issues important for technology scale-up, as well as pilot-scale design,
- Evaluating the suitability of integrating pyrolysis into existing composting recycling facilities, including identification of integration pathways, and design analysis for an Auger pyrolysis reactor for use in a composting facility, and

- Improving the ability of biochar as a nutrient recovery media, including producing engineered biochars with enhanced phosphate and ammonium recovery properties, and cost analysis of a biochar filtration unit to recover nutrients from a small dairy liquid waste stream.

As a body, this work increases the likelihood that the local organics recycling industry will be able to utilize second generation waste treatment technologies, and that the public will benefit from further improvements in environmental impact and reductions in nuisance and public health concerns associated with municipal food and green waste recycling programs.

References

[1] Yespen, R., 2009. U.S. residential food scrap collection and composting in *Biocycle* 50 (12) p. 35.

Applied Research and Extension for Second-Generation Organic Waste Processing: High Solids Anaerobic Digestion, Nutrient Recovery, and Pyrolysis

1.1—Next-generation organics conversion extension and outreach

Craig Frear

1.1.1—Abstract

To support commercialization of second-generation organics processing technologies, Washington State University (WSU) conducted an applied research and extension program aimed at "problem solving" for industry, and informing public and municipal agency personnel of the capability of the latest technologies. The program provided public and private industry with expertise pertaining to biomass, renewable energy, and sustainability with an emphasis on composting, anaerobic digestion (AD) and nutrient management and recycling. Speaking and extension events, were co-planned with the Washington State Department of Ecology Waste 2 Fuels (W2F) and the WSU Center for Sustaining Agriculture and Natural Resources emphasized core recycling and use concepts. In addition, WSU conducted numerous individual meetings with existing and new organics companies, and governmental, educational, and non-profit organizations. The following sections provide details on the outreach and extension accomplishments during the biennium.

1.1.2—Applied research and extension activities

Dr. Frear continued to lead project development, *Pro Forma* analysis and pre-engineering efforts for several projects in Washington State (WA) that integrate AD of organic waste and nutrient recovery (NR) with a specific aim at producing renewable natural gas (RNG) fuel. Specific projects include

- **The PacifiClean** project, which is aimed at integrating an AD and NR unit within a planned compost yard. A revised set of *Pro Forma* and engineering plans were presented last quarter to prospective investors and business developers.
- **Outlook POD**, a large dairy concentrated animal feeding operation (CAFO) project located in the Yakima Basin. This project is aimed at responding to area needs in nutrient management and new business models for AD development. Dr. Frear continued to work with project teams to develop the business plans of the project. As of June 2013 the project was entering the financing stage, with plans for construction in spring of 2014.

Much of the outreach work specific to the Yakima Basin project had also been in coordination with the United States (US) Environmental Protection Agency (EPA) Region 10, with WSU

providing instrumental support in educating/informing both EPA and concerned dairymen in on-going issues related to nitrate levels in the Basin (EPA, 2013b).

In addition to the proposed projects mentioned above, on-going demonstration of NR research through leveraged funding continued at Lynden and Enumclaw, WA, where two NR demonstration units were being operated alongside anaerobic digesters. WSU worked with industry partners and farmers on a weekly basis regarding attempts to refine and improve the technology. Dr. Frear was also assisting industrial partners in project development across the country.

Beyond work on specific products, WSU had continued to explore more sustainable ways to produce the desired co-products, and was working to improve the marketing and usability of developed products. Key tasks that had been implemented include:

- Working with industry and fertilizer distributors to grow mature markets for the developed products from NR (ammonium sulfate soil amendment and phosphorus-rich solids)
- Working with WSU Prosser scientists in improving knowledge about the effect these soil amendments had, at greenhouse scale, on yield and ecosystem services emissions such as greenhouse gases (GHG) and nitrates; and
- Coordinating with Washington State Department of Agriculture (WSDA) officials on licensing of fertilizer products and development of allowed storage and containment facilities for the soil amendments.

Lastly, WSU made numerous key presentations and met with valuable stakeholders throughout this biennium—all related to development of AD and NR. These presentations include the following:

- AICHE National Conference in Pittsburgh, PA
- USDA NIFA Meeting in Washington, DC
- WA Bioenergy Symposiums in Seattle, WA
- The PNW Fertilizer Association Annual Conference in Pasco, WA
- EPA Agstar National Conventions in Boise, ID, Syracuse, NY, and Indianapolis IN
- Biocycle National Conferences in Portland, OR and San Diego, CA
- California Dairy Summit in Modesto, CA
- Center for Dairy Innovation Markets Webinar
- ABO Algal National Conference in Denver, CO
- Oregon AD Summit in Portland, OR
- EPA AD Markets Summit in Washington, DC
- Qualco Farm Field Day in Monroe, WA
- WA Dairy Federation Meetings in Everett, WA
- US/China AD Symposium in Beijing, China

1.2—Application expansion of the developed NR/AD system to organic fraction of municipal solid waste

Craig Frear, Quan-Bao Zhao, and Cindy Alwine

1.2.1—Abstract

The NR system developed by researchers at WSU has been successfully used on anaerobically digested dairy manure at the commercial scale. However, to enhance the impact of this NR technology, it needs to be tested on organic waste and other non-agricultural feedstocks. A set of laboratory-scale experiments was conducted at WSU to test the recovery rates of nitrogen (N) and phosphorus (P) during the AD and NR of food scraps and green waste (e.g. grass clippings). The same aeration technique that was successful on dairy manure was applied to samples of anaerobically digested green waste, food scraps, a sample of mixed green waste and food scraps (30% green waste and 70% food scraps), and a sample collected from a wastewater treatment plant (WWTP). The highest NR was achieved from the combination of green waste and food scraps, with a total ammonia nitrogen (TAN) recovery approaching 80% after 12 hours of aeration and P recovery approaching 65% after 3 days of gravity settling. Compared to anaerobically digested dairy manure, all of the samples tested resulted in lower recovery efficiency for both N and P. This was presumably due to the unique alkalinity and form of P in dairy manure effluent. Nevertheless, the NR technology developed for dairy manure successfully treated food scrap and green grass clipping digestate. NR performed the best with a combined feedstock that closely resembled the materials that would be seen at composting facilities where this technology would most likely be applied.

1.2.2—Introduction

In 2010, the US EPA estimated that 250 million tons of trash was generated in the US (EPA, 2010). This “trash,” also referred to as municipal solid waste (MSW), comprised packaging, food scraps, grass clippings, sofas, computers, tires, refrigerators, and many other everyday items. Recognizing that landfill space is limited and that many of the items included in MSW could have value, municipalities and citizens have collaborated to divert some types of MSW. Currently, about 34.1% of total MSW is either recycled (batteries, newspapers, tires, glass containers, polyethylene terephthalate (PET) bottles and jars, and high density polyethylene (HDPE) bottles) or composted (paper/green waste/food scraps) (EPA, 2010).

Unfortunately, 54.2% of the total MSW is still discarded, while the remaining 11.7% is combusted for energy recovery (EPA, 2011b). One ongoing issue for landfills is the inclusion of biodegradable material. Organic waste, comprised mainly of paper, green waste and food scraps, contributes to a large portion of the total waste stream in the US. This trend is also evident in WA. Figure 1.2.1 illustrates the types of MSW generated in WA in 2009 with the largest category (27.2%) being composed of organics (Ecology, 2011).

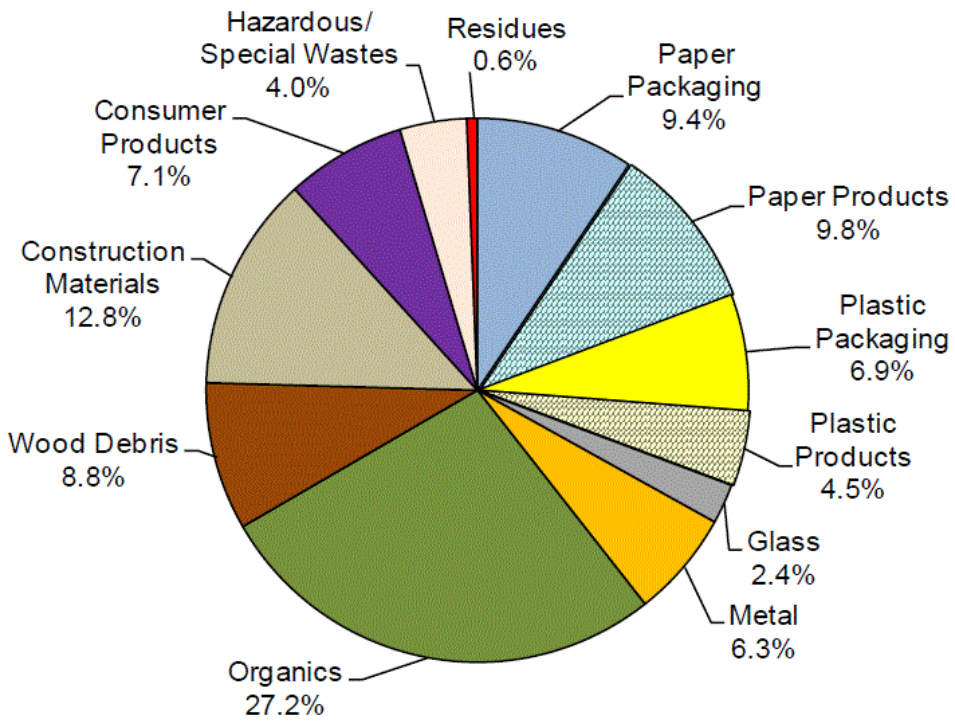

Figure 1.2.1: The composition of MSW in WA (Ecology, 2011)

Environmentalists and concerned citizens have increasingly focused on residual organics because they generate methane (CH_4), a potent GHG, when landfilled. One solution, used at many of the landfills in the US, is to capture the produced CH_4 and either flare to the atmosphere or burn it for energy production. However, CH_4 collection only begins *after* the landfill has been covered with an impermeable membrane. Thus, a significant amount of gas escapes into the atmosphere before the membrane has been applied (USCC, 2012). In WA, 1 million tons of food is landfilled annually. If 100% of this material was diverted and composted, it would reduce GHG emissions by 872,695 MT CO_2e, representing 1.8% of WA's target for GHG reduction by 2050 (EPA, 2011a). Furthermore, the state would also benefit economically. Many economic studies have shown that diverting the organic fraction of MSW via food scrap collection and recycling reduces costs by 20% relative to landfilling (Bloom, 2010).

Based on these environmental and economic benefits, a number of different strategies have been used to increase diversion of organics from landfills. In the US, composting has been the most common strategy (Kumar, 2011). Composting is a proven technique for converting organic solids into a biologically stable and valuable fertilizer. It is also operationally easy, compared to other techniques for stabilizing organic solids. However, composting can create environmental issues, particularly when putrescent materials such as food scraps are composted. Studies from Sweden (Sundberg, 2004), the US EPA (EPA, 2008), and the US Compost Council (Christiansen, 2009) demonstrated that the inclusion of partially decomposed food scraps can rapidly depress pH and alter compost pile biology. This in turn results in conditions that inhibit standard composting processes through a negative feedback loop (Ma et al., 2013c):

- The decomposition of putrescent material creates acids.

- These acids lower the pH of the compost pile, digester or container.
- A low pH environment provides conditions for a shift in the biology, and
- This biology shift results in more acids being produced.

This negative feedback can cause some areas of the compost pile to become anaerobic, slowing the aerobic progression required for rapid breakdown of organics. This results in the release of odor-causing volatile organic compounds (VOC) and ammonia (NH_3), an issue faced by many composting facilities when they incorporate food scraps into their feedstock.

One proven way to mitigate the environmental and odor issues that are associated with composting food scraps is via AD. In AD, organic wastes are consumed by anaerobic bacteria to produce biogas and a liquid effluent (Frear, 2009). Biogas can be combusted to produce energy in a combined heat and power unit or it can be upgraded to RNG or to meet natural gas pipeline standards (de Hullu et al., 2008). The liquid effluent can be used as a fertilizer. AD has been used commercially on many different waste streams including dairy, poultry, and swine manure, as well as medical and food processing wastes. The process provides numerous environmental benefits including odor reduction (Martin, 2004), volatile and pathogenic organics reduction in both the liquid and solid fractions of the effluent, and GHG emissions reduction (Frear, 2009).

One of the remaining environmental issues with AD is the fate of the nutrients, mainly N and P. During AD, N and P are not removed, only converted from their organic forms to inorganic forms. N and P are more prevalent in agricultural waste streams such as dairy manure or poultry waste, but early results have shown that the fate of P in municipal organics is similar to manures. Therefore, organic effluent with its high concentration of N and P has the potential to contribute to overloading of N and P if land applied (WA Ecology, 2011). Increases of N and P in the environment, in the form of ionic NH_3, nitrate, nitrite, and phosphate, are detrimental to aquatic systems (DeBusk, 2007; Rumburg et al., 2004). The release of N to the air in the form of NH_3 and mono-nitrogen oxides (NOx) can also contribute to acidification, while the release of nitrous oxide (N_2O) can contribute to the climate change since it is a potent GHG (298 times more potent than carbon dioxide (CO_2)) (Vitousek et al., 1997).

Various mechanical, chemical and biological NR processes used in the industrial and municipal wastewater industries have the potential to be adapted for organic waste. However, each of these approaches has drawbacks that may make them less appropriate for organic waste. These include difficulties dealing with the high concentrations of N and P or high solids content of organic waste, high input costs, or other operational issues (Frear & Dvorak, 2010; Reeves, 1972). Of the various existing techniques, air stripping has relatively low costs, and is not negatively affected by high concentrations of nutrients. The technique has been successfully utilized at wastewater treatment facilities. The technique has also been recently incorporated into an integrated N-(ammonium sulfate) and P-(phosphate) rich organic fertilizer recovery technology developed at WSU. The process has achieved high recovery rates of both N and P at pilot- and commercial-scales on dairy and poultry manure (Jiang et al., 2011; Zhao et al., 2012).

Figure 1.2.2 illustrates a simple schematic showing how the existing NR process could be applied to food scraps and green waste. Organic waste is introduced either with or without dairy manure, and effluent from the NR process will be used downstream to remove hydrogen sulfide (H_2S) from biogas for further upgrading to vehicle fuel (Kennedy, 2012). This downstream

process is outside the scope of this report, though an informative review by Ryckebosch et al. (2011) provides additional detail for interested readers. This study was designed to test the NR rates of N and P for organic wastes, and compare these to the rates previously achieved with dairy manure.

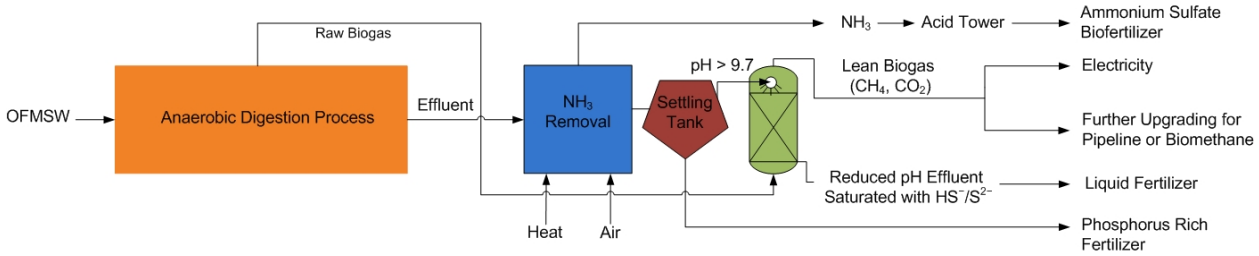

Figure 1.2.2: Simple schematic showing the AD and NR of organic waste, with the various products and co-products

1.2.3—Materials and methods

Green waste (grass clippings), food scraps, a combination of green waste + food scraps, and WWTP sludge were tested for volatile solids (VS) prior to AD. This was done to facilitate comparisons between the feedstocks. Each feedstock was tested in triplicate. Once the VS was measured each sample had a specific amount of VS placed within the test bottle and mixed with appropriate amount of inoculum and water to achieve the desired loading rate (see Table 1.2.1). The WWTP sludge, used as an inoculum in all treatments, was sampled from the Pullman WWTP, Pullman, WA. Green waste, food scraps and green waste + food scraps, with a total volume of 500 ml for each, were anaerobically digested for over 30 days in 1000 ml bottles. For the green waste + food scraps treatment, the mixture was 30% green waste and 70% food scraps. During AD, the bottles were placed in a temperature controlled incubator that was maintained at a mesophilic (moderate) temperature (37°C). Biogas production was monitored for 39 days.

After digestion was complete, the effluent of each experiment underwent aeration (air stripping) to determine the recovery rates of N and P. A 400 ml sample was taken from each reactor bottle and placed within a new 500 ml Pyrex bottle. Air was supplied to each bottle through an air stone at a flow rate of 400 ml/L for 12 hrs. The bottles were placed in a temperature controlled water bath that was maintained at 55°C. Figure 1.2.3 illustrates the experimental setup for the combined AD and NR process.

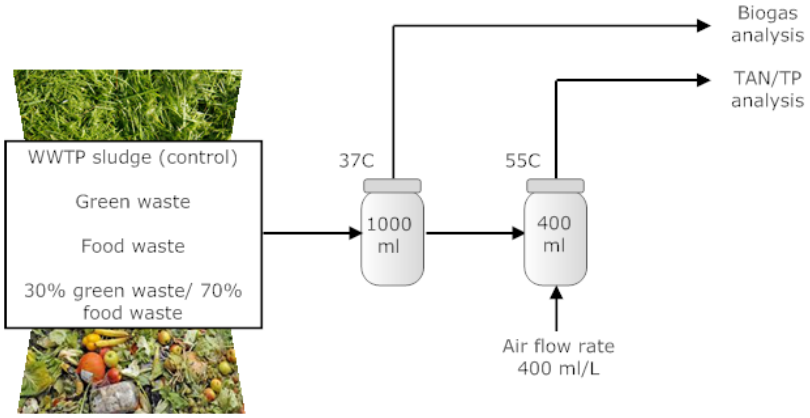

Figure 1.2.3: Schematic of the experimental setup and analyses that were conducted

Total ammonia nitrogen was analyzed using a Tecator 2300 Kjeltec Analyzer (Eden Prairie, MN, USA) (4500-NorgB; 4500NH3BC). Samples were taken periodically over a 12 hr aeration period to determine the change in TAN. After aeration, the mixed effluent was naturally settled for 1, 2 or 3 days. Thereafter, samples were taken from the middle height of the liquid and tested for total phosphorus (TP) using the Hach PhosVer® 3 ascorbic acid method. Online pH of the effluent was analyzed with an OM-CP-PH101 pH and temperature data logger connected to a PHE-4200 pH probe (Omega Engineering, Stamford, Connecticut, USA). Table 1.2.1 illustrates the sample sizes (g VS) used for these experiments.

Table 1.2.1: Sample sizes for comparison of biogas production, TAN, and TP

Sample	Green waste (yard waste, YW) (g VS)	Food scraps (FS) (g VS)	WWTP sludge (ml)	DI water (ml)
WWTP (triplicate)	0	0	210	290
YW	2.5	0	210	290
YW	2.5	0	210	290
YW	2.5	0	210	290
FS	0	2.5	210	290
FS	0	2.5	210	290
FS	0	2.5	210	290
YW+FS	0.75	1.75	210	290
YW+FS	0.75	1.75	210	290
YW+FS	0.75	1.75	210	290

1.2.4—Results and discussion

1.2.4.1—Biogas production

Biogas production of the different samples was monitored for over 30 days. Figure 1.2.4 shows the total biogas production that resulted from the AD of the various substrates. Each substrate had the same initial VS loading of 2.5 g. The final biogas production for WWTP (control), green

waste, green waste + food scraps and food scraps was 401±16, 1319±54, 2253±49 and 2583±32 ml, respectively. As indicated in the graph, the highest biogas production resulted from digestion of food scraps. This is to be expected since food scraps have been shown to have high biodegradability and CH_4 yield (Zhang et al., 2007a).

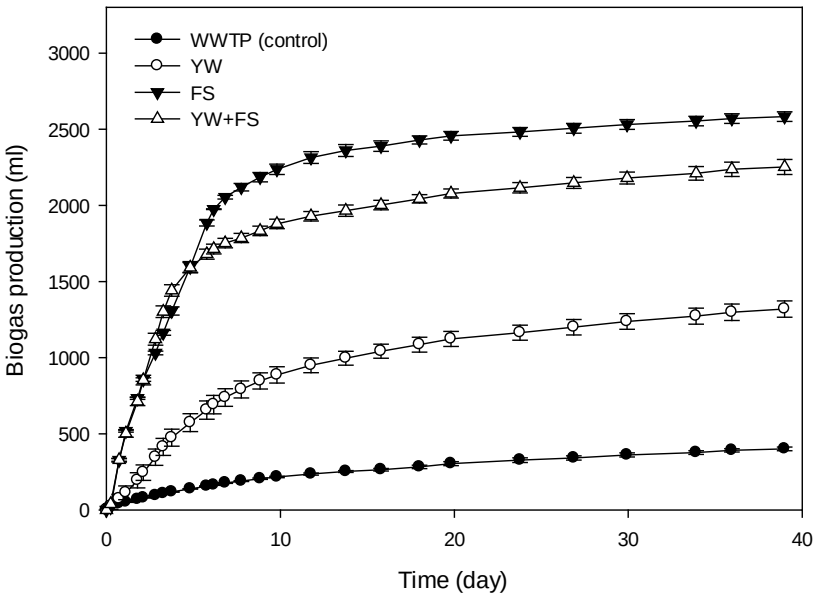

Figure 1.2.4: Biogas production of green waste (yard waste, YW), food scrap (FS), green waste + food scraps (YW+FS), and wastewater treatment plant (WWTP)

To compare biogas production in this study to those found in other studies, a specific biogas production (SBP) graph was prepared (see Figure 1.2.5). To calculate SBP, the biogas produced from WWTP control was subtracted for all three curves. With the same initial VS loading, the SBPs for green waste, green waste + food scraps and food scraps were 367±21, 741±20 and 873±12 ml biogas/g VS, respectively. Green waste had the lowest SBP, which indicated lower bioconvertible energy. For comparison, a healthy dairy manure digester typically has a specific CH_4 production of 230 ml CH_4/g VS or 383 ml biogas/g VS, which is close to the green waste sample in this study. In contrast, co-digestion of green waste + food scraps doubled biogas production compared to 100% green waste, providing positive evidence that co-digestion at composting facilities would result in higher biogas output. To check if there were any positive or negative interactions for biogas production between the green waste and food scraps in the combined green waste + food scraps sample, the anticipated SBP was calculated based on the SBP of green waste and food scraps alone. An anticipated SBP of 721 ml biogas/g VS was calculated. This result was very close to the experimental result of 741 ml biogas/g VS, indicating no additional positive or negative effect from co-digesting food scraps and green waste.

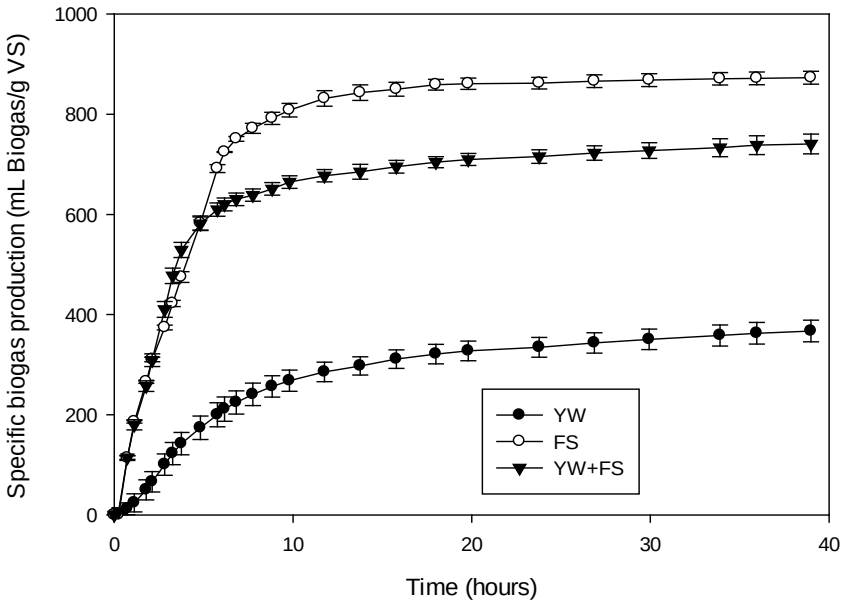

Figure 1.2.5: SBP of green waste (yard waste, YW), food scraps (FS) and green waste + food scraps (YW+FS)

Previous studies of co-digestion have not usually looked at combinations of green waste and food scraps that would be likely to be used at an urban anaerobic digester. Instead, most of these previous studies examined combinations of dairy manure and food scraps. One previous study conducted by researchers at WSU showed that the co-digestion of food scraps with dairy manure increased the VS by 48.7%, causing the CH_4 production to double (Frear et al., 2011). In this case, the food scrap-manure mixture had a better balance of macro-nutrients, alkalinity, preferred C:N:P ratios and pH, resulting in a better environment for AD (Frear et al., 2011). Other studies have shown that co-digestion of various agricultural wastes and organic waste increases the stability of methanogenesis and increases CH_4 yield (Carucci et al., 2005).

In this study, the green waste/food scrap combination doubled biogas production compared to the green waste only. This indicates that the main degradation took place on the highly degradable food scraps. Green waste had a higher biogas production than the control but was significantly lower than green waste + food scraps and food scrap samples. This could be attributed to the structure of grass clippings with its recalcitrant lignocellulosic material. However, it is important to note that even green waste significantly boosted biogas production compared with the control and thus should provide additional revenue from electrical generation or RNG compared to AD at a WWTP.

1.2.4.2—Effect of aeration on the effluent pH

Previous NR studies of anaerobically digested dairy manure (Frear et al., 2010) have shown that aerating the effluent allows for a rapid release of supersaturated CO_2 gas at an elevated temperature (55°C), which is important to the recovery of N and P. In this study, aeration experiments were performed on green waste, food scraps, and green waste + food scraps to determine the N and P recovery rates. Figure 1.2.5 shows the pH of the three different samples during aeration. All of the samples increased in pH over time due to the release of the supersaturated gases inside the samples.

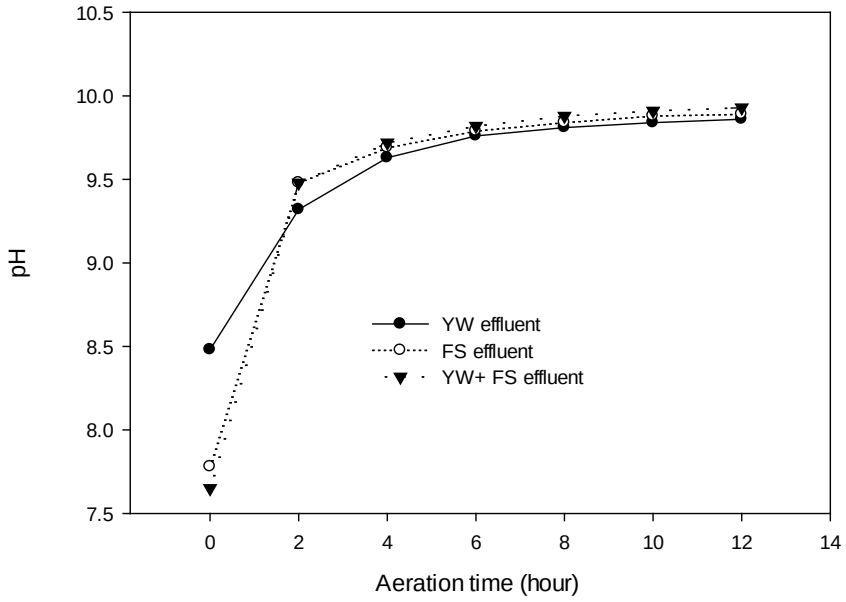

Figure 1.2.6: The effect aeration had on the pH of green waste (yard waste, YW), food scraps (FS), and green waste + food scraps (YW+FS) digestate at 55°C

The initial pH of the food scrap effluent and green waste + food scraps effluent were slightly lower than the green waste effluent. This could be due to the presence of an appreciable level of organic acids produced during hydrolysis/acidification of the green waste material prior to testing. After around 2 hours of aeration, the pH of all the samples was above 9. This indicates that aeration was able to eliminate a large portion of the supersaturated gases ($CO_{2\,(aq)}$, in equilibrium with carbonic acid (H_2CO_3), carbonate (HCO_3^-), bicarbonate (CO_3^{2-}), and some CH_4). After hour 5, pH was steady around 9.8, very similar to laboratory results from previous studies on dairy manure (Frear & Dvorak, 2010). This high pH combined with high temperature indicates preferred conditions for NR, as it should allow dissolved NH_3 to shift its equilibrium to gaseous free NH_3, enabling capture and removal as sulfate salt soil amendment when put in contact with sulfuric acid in a dedicated acid tower. In addition, since gases were knocked out during the aeration step, natural flocculation and settling of P-rich solids should more readily occur.

1.2.4.3—Nutrient recovery: nitrogen

During the aeration experiment, samples were collected and analyzed for TAN to determine how much recovery of N was achieved. Figure 1.2.7 illustrates the TAN removal efficiency on the three samples (green waste, food scrap, green waste + food scraps) as they were aerated. Figures 1.2.6 and 1.2.7 show a clear correlation between the pH and TAN removal efficiency. As the pH increased (see Figure 1.2.6), the TAN removal also increased. It has been shown that N recovery in the form of gaseous free NH_3^+ increases with increasing temperature and pH (Katehis et al., 1998). All three samples achieved over 70% TAN removal after 12 hrs of aeration. This is somewhat lower than the >90% removal efficiency that was achieved from the aeration of dairy manure effluent at 55°C (Frear et al., 2010). However, Figure 1.2.7 shows that a steady state had yet to occur after 12 hrs of aeration and that TAN removal rate was still increasing. This means that most likely higher removal efficiency would have been achieved if additional aeration time had been allowed.

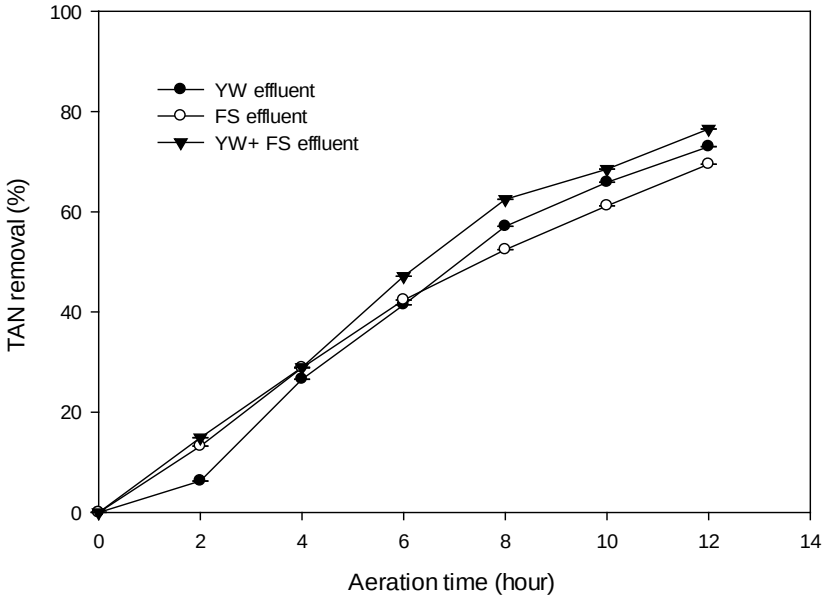

Figure 1.2.7: TAN removal during aeration of green waste (yard waste, YW), food scraps (FS), and green waste + food scraps (YW+FS) digestate at 55°C

The highest TAN removal (> 75%) was achieved with the green waste/food scrap mixture. This likely occurred because the highest pH was also achieved with the aeration of mixed wastes. The aeration experiments performed in this study provide evidence that achievable N recovery rates for organic waste may be slightly lower than recovery rates for dairy manure. There are indications that additional processing time and aeration rates might raise recovery rates for green waste and food scraps, though perhaps at additional expense.

1.2.4.4—Nutrient recovery: phosphorus

Once aeration was completed, P-solids were removed through gravity settling. Figure 1.2.8 illustrates the TP removal efficiency of the various samples over a 4 day gravity settling period. As Figure 1.2.8 (A) indicates, the percent removal of TP slowly increased over the 4 day gravity settling period with the highest removal efficiency occurring on day 3. Phosphorus rich solids for all four aerated samples settled more quickly, and with greater density, compared to effluent samples that had not undergone aeration (results not shown). These results indicate that aeration was effective at removing supersaturated gases present in each effluent sample.

Looking at the aerated effluent samples individually, the percent removal at day 3 was slightly higher than 50% on WWTP control effluent. The TP removal efficiency for green waste (Figure 1.2.8 (B)) was slightly lower than the control, which can be attributed to a lower concentration of P occurring within green waste. Figure 1.2.8 (C, D) shows that the TP removal efficiency increased significantly for food scraps and green waste + food scrap, with the highest removal efficiency resulting from the mixed waste effluent. The TP removal efficiency for the green waste + food scrap sample resulted in >60% removal of P from the effluent after only 1 day of gravity settling. Thereafter, the removal efficiency increased slightly and at day 3 was around 65%.

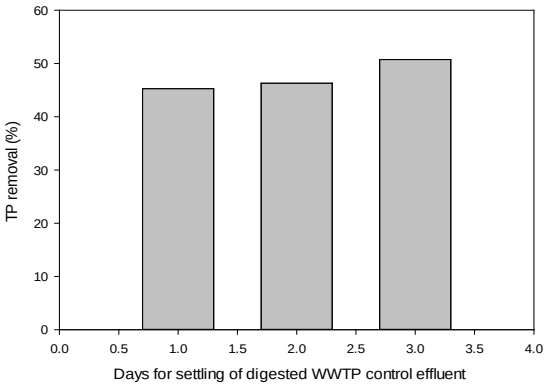

(A)

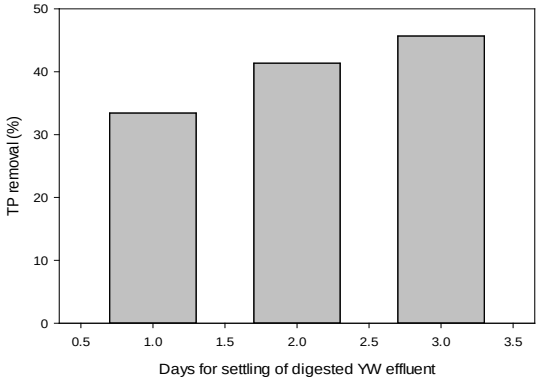

(B)

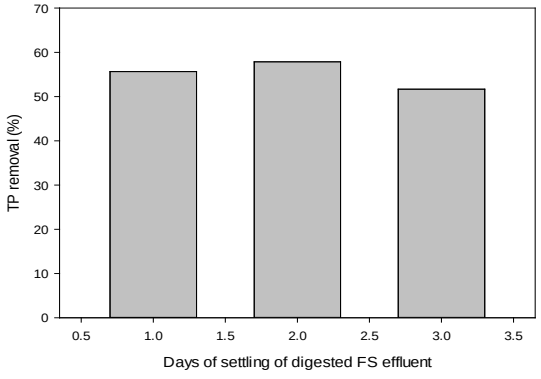

(C)

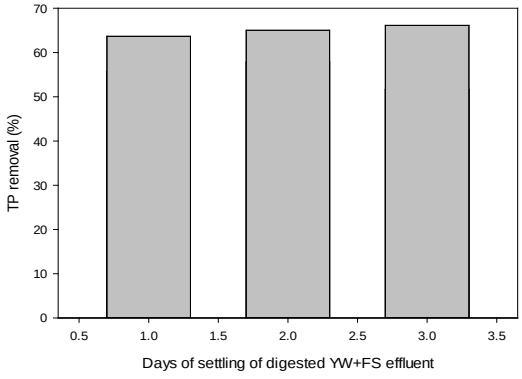

(D)

Figure 1.2.8: TP removal after aeration and settling for effluent samples of (A) wastewater treatment plant (WWTP), (B) green waste (yard waste, YW), (C) food scrap (FS), and (D) green waste + food scrap (YW+FS)

The TP removal efficiency of digested dairy manure effluent was slightly higher (> 80% TP removal) (Frear et al., 2010) when compared with each of the samples in these aeration experiments. This was presumably due to slight differences in P form with dairy manure. Dairy manure is known to have a high percentage of digested P as non-crystalline, colloidal magnesium/calcium phosphate solids. Within these tested green waste and food scrap substrates, perhaps a smaller percentage of P was in this settled solids form, presumably because of the lower concentration of calcium and magnesium present in the green waste and food scraps as compared to dairy manure. Further research would be needed to confirm this hypothesis.

Nonetheless, the tests carried out here provide evidence that the NR technology originally developed for removing P from dairy manure effluent can be applied on other waste streams. Aerating the effluent did increase the settling capacity of P-rich solids from green waste and food scrap effluent. The highest P settling efficiency, of about 65% in 3 days, occurred with a combination of green waste and food scraps.

1.2.5— Conclusions

Food scraps and green waste are generating significant odor emissions at composting facilities. AD is one possible solution, with a proven track record at digesting food scraps and a combination of wastes while reducing the odor emissions. Although N and P are not converted during the digestion process, these nutrients can be recovered from the effluent. This would reduce the threat of soil and water contamination and create another revenue source.

Aeration of the digestate from AD of green waste, food scraps, and combined green waste and food scrap resulted in significant stripping of N and P for every sample tested. The highest removal efficiencies occurred on the combination green waste/food scrap effluent. The results indicated that scale-up of this technology on non-manure waste streams is warranted.

If scale-up is successful, NR has the potential to resolve concerns related to NH_3 inhibition (a known concern during AD of green waste and food scraps) as well as reduce water usage. The water usage benefit arises from the fact that once the inhibitory NH_3 is removed, AD effluent could then be used as dilution water needed at the front end of the AD process.

1.3—Continued exploration of pyrolysis and torrefaction as unit operations integrated with AD

Shi-Shen Liaw, Craig Frear and Manuel Garcia-Perez

1.3.1—Abstract

There are reasons to think that pyrolysis and torrefaction (a low-temperature form of pyrolysis) might integrate well with AD, providing benefits to both. AD can potentially digest some or all of the smaller C_1–C_4 molecules produced from pyrolysis and torrefaction, byproducts that currently have no added value. From the AD perspective, these organic compounds should have synergistic impacts on biogas production when co-digested with dairy manure. And from a systems perspective, facilities that incorporated both technologies could accept a broader range

of feedstocks, increasing tipping fees. This task aimed to develop new knowledge and technologies to anaerobically digest C_1–C_4 molecules produced from pyrolysis and torrefaction of lignocellulosic waste.

To achieve this objective, researchers at WSU designed and built a fractional condenser to separate the C_1–C_4 molecules produced during the torrefaction and pyrolysis of lignocellulosic materials. Afterwards, they evaluated the suitability of the aqueous stream obtained for AD. First, model compounds of acetic acid, acetol, hydroxyacetaldehyde and phenols were co-digested with manure to determine how each intermediate affected biogas production. Acetic acid had the most significant impact with a peak biogas concentration of 400 ml being produced at a concentration of 1 mass % acetic acid after over 200 hours of digestion. Acetol generated a smaller increase, with maximum biogas production of over 200 ml of biogas at a concentration of about 0.25 mass % acetol. In contrast, hydroxyacetaldehyde and phenols depressed biogas production when co-digested with dairy manure. Biogas production peaked when these intermediates were at a concentration of 0.1 mass % and dropped dramatically at higher concentrations. This evidence that hydroxyacetaldehyde and phenols inhibit the AD process suggests that these intermediates should be removed before digesting C_1–C_4 molecules.

Building on these laboratory-scale results, a large-scale pyrolysis reactor was sampled for C_1–C_4 compounds. Sampled compounds were co-digested at various concentrations with dairy manure to determine the impacts on the AD process. The optimum concentration for biogas production was 0.5 mass % of C_1–C_4 compounds. At higher concentrations, inhibitors negatively impacted the anaerobic microbes and biogas production plummeted.

Lignocellulosic materials commonly considered as candidates for torrefaction were also sampled, torrefied and the resulting aqueous phase was anaerobically digested. Among the feedstocks tested, the aqueous phase from pea hay produced the most biogas, as well as the highest concentration of biogas, as long as inhibition did not occur. Finally, it was determined that biogas production increased linearly as the concentrations of the aqueous compounds were increased. As long as inhibition did not occur (for example, from the toxic compounds hydroxyacetaldehyde and phenol), the C_1–C_4 molecules were contributing to biogas formation. Together, these experiments lay a foundation for future work on the application of combined pyrolysis and AD.

1.3.2—Introduction

Pyrolysis and torrefaction are thermochemical processes that convert lignocellulosic wastes into a number of products, some of which can be used to generate energy. Suitable lignocellulosic materials include leaves, grass clippings, branches and twigs, crop residues, clean wood, pallets, and crates.

The products of pyrolysis and torrefaction include molecules with less than four carbon atoms (C_1–C_4) that are responsible for many undesirable properties of bio-oil (e.g. acidity, low thermal stability). They therefore currently represent a major commercialization hurdle for pyrolysis and torrefaction technologies. Finding innovative ways to separate and develop products from this fraction would make commercial-scale applications of pyrolysis more likely. The *overall goal* of this task was to build a foundation for anaerobically digesting C_1–C_4 molecules.

There are reasons to think that the torrefaction/pyrolysis processes might integrate well with AD. For example, AD can potentially digest some or all of the organic compounds produced during pyrolysis of lignocellulosic material. Furthermore, these organic compounds should boost overall biogas production when co-digested with manure. This would provide synergistic benefits to the AD. In addition, a facility with integrated pyrolysis/torrefaction and AD technologies could accept a wide range of feedstocks, improving waste management and increasing tipping fees.

Figure 1.3.1 illustrates the overall process. The torrefaction and pyrolysis processes produce bio-oil and aqueous phase rich organic compounds. The larger organic compounds (C_6) are separated from the smaller C_1–C_4 oxygenated organic compounds using fractional condensers, which are essentially scrubbers in series operating at two distinct temperatures. The heavier (C_{6-}) molecules that represent pyrolysis biofuel precursors are collected in the first condenser which typically operates around 80°C. Thereafter, formic acid, acetic acid, propionic acid, methanol, glycoaldehyde, and acetol are the main molecules recovered in the aqueous phase in the second condenser, which operates at around 25°C. The aqueous phase recovered in the second condenser comprises up to 50% by weight small organic molecules.

The main objective of this study was to understand how the chemical composition of aqueous phase (rich in C_1–C_4 molecules) from the pyrolysis and torrefaction of lignocellulosic materials affects the AD process when co-digested with manure. A secondary objective was to identify compounds that are toxic to the AD process, and determine the impacts on biogas production.

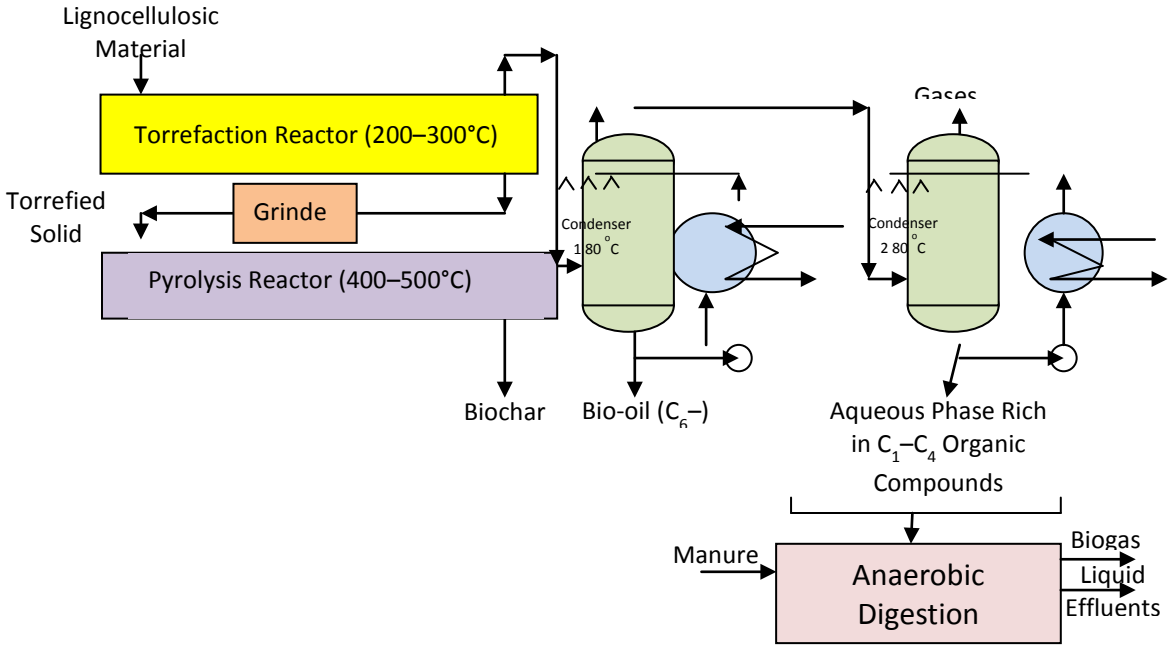

Figure 1.3.1: Stepwise pyrolysis concepts with a two-step condensation process for the recovery of C_1–C_4 oxygenated molecules

1.3.2.1. Background: torrefaction, pyrolysis, and their integration with anaerobic digestion

Torrefaction is an anaerobic thermal treatment in the relatively low temperature range of 225–300°C. The main aim of this technology is to produce a fuel with increased energy density by decomposing the reactive hemicellulose of lignocellulosic materials. A secondary benefit is that torrefaction induces large modifications in the structure of cellulose and lignin that dramatically decrease the required energy necessary for downstream grinding. During the torrefaction of lignocellulosic material, an important fraction of the feedstock is converted into an aqueous phase with up to 15% by weight of acetic acid.

Pyrolysis, on the other hand, is anaerobic thermal degradation at temperatures between 300 and 600°C. It produces biochar, bio-oil, gases and heat. Currently, there are two main business models to commercialize biomass pyrolysis technologies. The *first business model* is associated with the production of biochar and heat via slow pyrolysis. The *second business model* is the production of bio-oil and char via fast pyrolysis followed by downstream oil refining. Both technologies produce relatively large quantities of small molecules (C_1–C_4) (acetic acid, acetol, formic acid, hydroxyacetaldehyde) with limited marketability.

Because acetic acid is a known intermediate in the AD process, digestion of the aqueous (small molecule-containing) phases derived from the pyrolysis or torrefaction of lignocellulosic materials could be a viable approach that would generate value from this fraction and avoid pollution from these technologies. However, the behavior of these thermochemical products during AD is unknown. It is therefore necessary to test the effects these intermediates have on biogas production when co-digested with a widely used substrate in the AD industry such as dairy manure.

1.3.3—Materials and methods

1.3.3.1—Design of a two-step condensation system

A two-step condensation system coupled with an Auger Pyrolysis reactor was designed at WSU. Dried material is introduced into a hopper of a volumetric feeder (Barbender Technologies) and fed into the Auger reactor at a rate of about 1 kg/h. A carrier gas (N_2) was used to achieve a residence time of around 8 seconds for the vapors inside the pyrolysis reactor. The biomass was pushed through the hot zone of the reactor with a 1 hp variable speed motor, typically staying inside the reactor for about 1 min. A stainless-steel tube with a length of 58.5 cm and diameter of 10 cm was heated by a Linderberg/Blue M (model HFT55322A) furnace to the hot zone. Charred particles were collected and left to cool down in the char pot.

The design of the multi-step condensation system (see Figure 1.3.2) was completed early in 2012 and the construction was completed in May 2013 by Bill's Welding & Machine Shop (Pullman, WA) (Figure 1.3.3). The first condenser was a scrubber jacketed with hot water. The cooling liquid spray was formed by paraffinic oil immiscible in bio-oil. The second condenser was a vertical tube with cooling water coils. The third condensation step consisted of bubbling traps with water cooled by ice. The pressure inside the reactor was kept close to atmospheric pressure by applying suction at the final condenser. Once the new system was operating satisfactorily, preliminary tests were conducted with the condenser to study the effect of first condenser temperature (between 50 and 80°C) on the separation of C_1–C_4 molecules (collected in the second condenser).

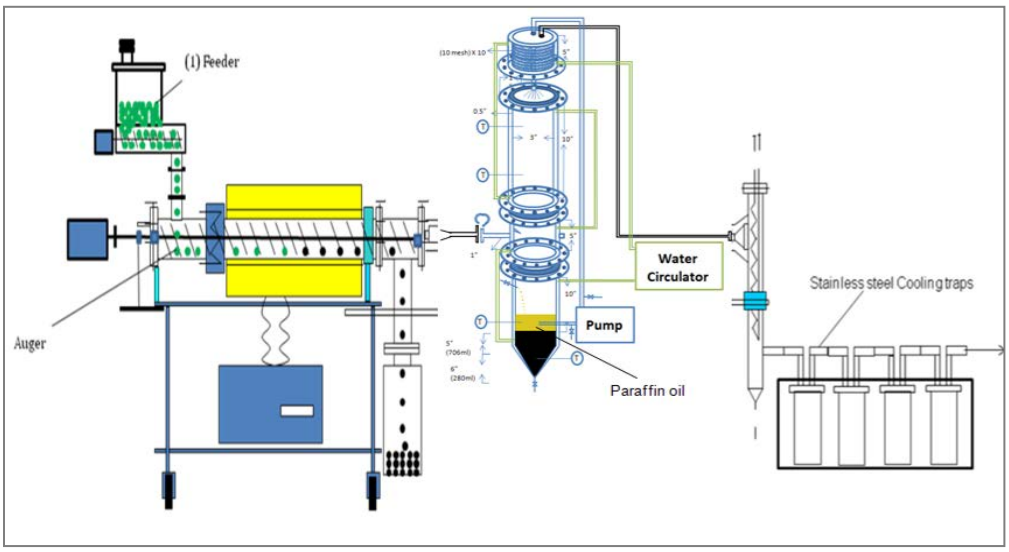

Figure 1.3.2: Scheme of the fractional condensation unit coupled with the pyrolysis reactor

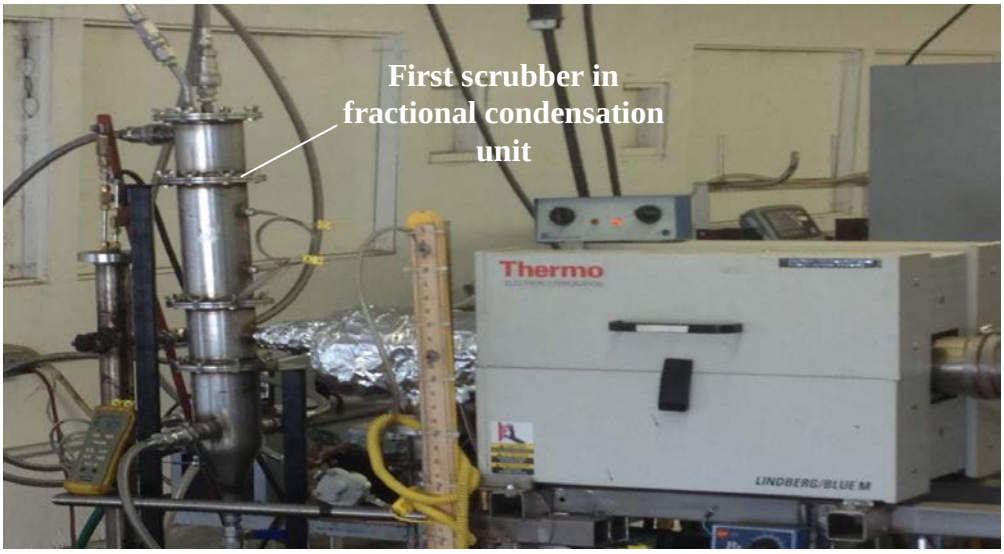

Figure 1.3.3: Picture of the fractional condensation unit

1.3.3.2—Anaerobic digestion of C_1–C_4 organic compounds

The biogas production experiments were performed using a dedicated 18-cell batch respirometer unit, outfitted with computer-controlled biogas and CH_4 flow meters (Challenger Systems, Fayettville, AK). The unit was operated at mesophilic conditions (37°C) using batch biomethane protocols. Each bottle was magnetically stirred at a speed of 185 rpm. Methane production was monitored using a respirometer (Challenge technology AER-200 respirometer, Springdale, AR, USA). Sodium hydroxide was used as scrubbing media to purify CH_4 by adsorbing CO_2 and H_2S, so that only CH_4 production was recorded. Triplicate analysis was carried out to ensure reproducibility of results.

1.3.3.3—Torrefaction of different feedstocks

The following feedstocks were torrefied in an Auger Torrefaction Reactor at 310°C: Arundo donax (giant cane), wheat straw, pea hay, sorghum biomass, and red fir wood chips. Product yields were recorded and the composition of the obtained aqueous phase was analyzed by Karl Fischer titration (Schott Instruments TitroLine Karl Fischer Volumetric Titrator) and GC/MS (Agilent, Column: HP-5MS, 30 m x 250 μm x 0.25 μm, 7890A Gas Chromatograph with a 5975C Mass Selective Detector).

1.3.4—Results and discussion

1.3.4.1—Anaerobic digestion of model compounds (acetic acid, acetol, hydroxyacetaldehyde and phenols)

Acetic acid, acetol, hydroxyacetaldehyde and 2-methoxyphenol were selected as model compounds to study possible inhibitory effects on the AD process. These choices were made based on the fact that lignin-related compounds (phenols and benzenes) are known to be toxic to methanogens. Although most of these compounds will be collected in the first condenser, a fraction of these compounds will also be present in the aqueous phases produced by pyrolysis and torrefaction. Thus, successful AD will require either that the AD process tolerate the concentrations of these compounds that exist in the aqueous phase, or that these compounds be screened out prior to AD.

The results of biogas production experiments shown in Figure 1.3.4 (A and B) suggest that the optimal concentrations of acetic acid and acetol were around 1~1.5 % by mass. In particular, the inclusion of acetol, up to a certain concentration, increased biogas production, providing evidence that anaerobic microbes can tolerate mild concentrations of this intermediate. However, the highest gas production (over 400 mL gas after 200 hours of digestion) occurred when acetic acid was used as an additive to dairy manure.

In contrast, hydroxyacetaldehyde (Figure 1.3.4; C) and phenolic compounds (Figure 1.3.4; D) were both quite toxic to the AD process. Based on these results, the content of phenols and hydroxyacetaldehyde in the aqueous phase should be reduced as much as possible before AD to ensure a more productive process.

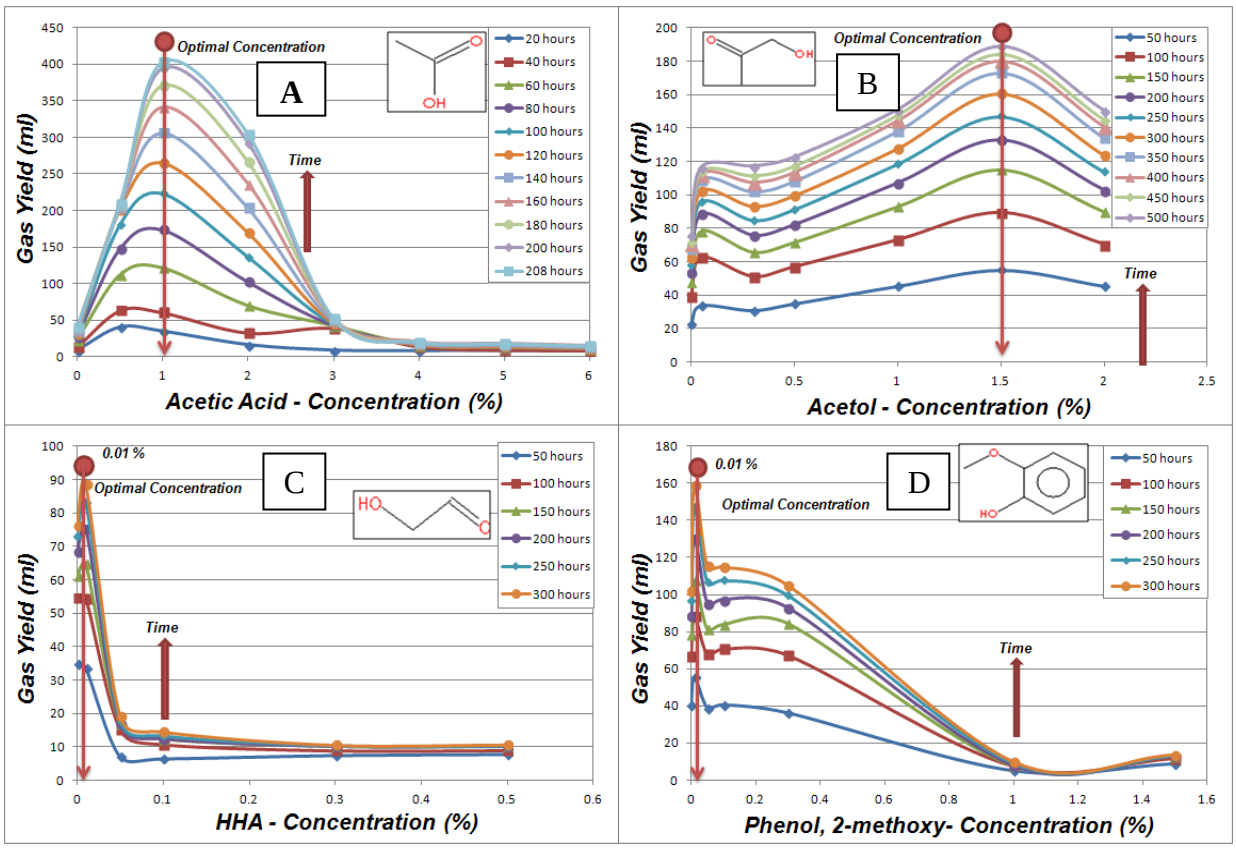

Figure 1.3.4: Gas yields as a function of concentration of selected model compounds at different residence times

1.3.4.2—Anaerobic digestion of C_1–C_4 compounds produced by Coates Engineering

In this experiment, the aqueous phase of pyrolysis rich in C_1–C_4 was collected in a large-scale two-step condensation system at Coates Engineering located in Utah, USA. This system was similar to the one designed for the authors' reactor. The chemical composition of the aqueous phase was determined by GC/MS and is shown in Table 1.3.1. The high content of acetic acid indicates a promising potential for CH_4 production. On the other hand, strong inhibitors including glycoaldehyde and mono-phenols were also present. This could inhibit microbial growth and negatively impact the AD process. Therefore, it is advised to separate or remove these intermediates, if possible, before feeding a digester with the organic compounds produced in the second condenser of a two-step condensation system.

Table 1.3.1: GC/MS quantification of volatile compounds present in the aqueous phase collected in the second step of a fractional condensation system

Compound	*Content (wt. %)*
Formic acid	1.09
Glycolaldehyde	0.27
Acetic Acid	5.62
Acetol	2.31
Propionic Acid	0.32
1-Hydroxy-2-butanone	1.17
Butanedial	0.14
Furfural (2-Furaldehyde)	0.16
Acetol acetate	0.41
Furan, tetrahydro-2,5-dimethoxy-	0.29
2(5H)-Furanone	0.22
Guaiacol (Phenol, 2-methoxy-)	0.01
2-Furanethanol, b-methoxy-(S)-	0.08
2-Butanone, 1-(acetyloxy)-	0.21
Phenol	0.01
O-Cresol	0.18
1,2-Benzenediol, 3-methoxy-	0.05
Phenol, 4-ethyl-2-methoxy-	0.01
Syringol	0.13
Eugenol	0.05
Vanillin	0.25
1,2,4-Trimethoxybenzene	0.03
5-tert-Butylpyrogallol	0.05
2-Propanone, 1-(4-hydroxy-3-methoxyphenyl)-	0.08
Levoglucosan	1.56
Phenol, 4-(ethoxymethyl)-2-methoxy-	0.25
Benzaldehyde, 4-hydroxy-3,5-dimethoxy-	0.20
Phenol, 2,6-dimethoxy-4-(2-propenyl)-	0.15
Acetosyringone	0.16
3,5-Dimethoxy-4-hydroxycinnamaldehyde	0.14

Gas production from AD of the full aqueous phase from Coates Engineering is shown in Figure 1.3.5. The results suggest that the optimal concentration of the aqueous phase rich in C_1–C_4 molecules was 0.5 mass %. At higher concentrations the production of gas was inhibited due to the presence of toxic compounds such as hydroxyl-acetaldehyde and phenol.

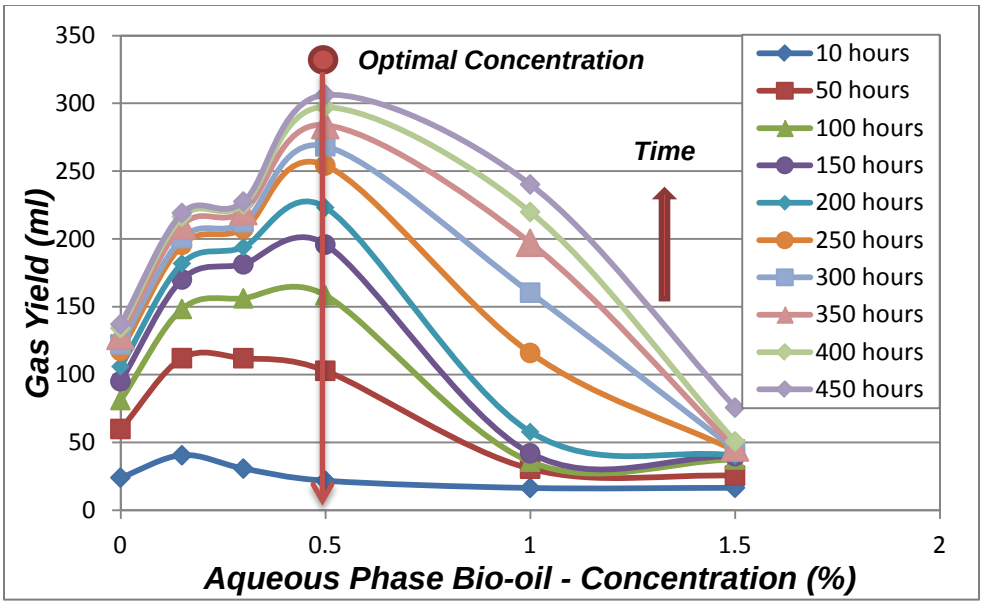

Figure 1.3.5: Production of biogas during AD as a function of the concentration of the aqueous phase obtained from Coates Engineering (studies with the respirometer)

At the optimal concentration of 0.5 mass %, the AD of aqueous phase bio-oil generated over 300 ml of biogas after 450 hrs of digestion. As the concentration increased above this level, biogas production began to fall precipitously. This indicates a threshold had been reached. Successful commercialization would likely require that aqueous phase dosing be kept well under this inhibitory threshold, to ensure that C_1–C_5 compounds do not overwhelm the digestion process. It also indicates the importance of further research aimed at minimizing the amount of inhibitory compounds in the aqueous phase.

1.3.4.3—Anaerobic digestion of condensed torrefaction liquids

A variety of feedstocks (corn stover, rye straw pellet, wheat straw, pea hay, sorghum biomass, Arundo donax, and red fir wood chips) were torrefied, and the composition of the liquid produced from the second condenser was analyzed (Table 1.3.2). The chemical composition varied dramatically, but all the aqueous phases studied had a very high content of acetic acid (between 6.6 and 17.7 wt. %). This would likely enhance biogas production when co-digested with dairy manure. Samples were then anaerobically digested in an 18-cell batch respirometer to study gas production. The results are shown in Figures 1.3.6–1.3.9.

Table 1.3.2: Content of selected compounds in the aqueous phase produced from the torrefaction of several lignocellulosic materials (wt. %)

	Corn Stover	Annual Rye Straw Pellet	Wheat Straw	Pea Hay	Sorghum Biomass	Arundo donax	Red Fir Wood Chips
Formic acid	0.20	0.80	0.71	0.55	0.59	0.24	2.09
Glycolaldehyde	0.58	0.97	1.33	0.22	0.88	0.70	0.74
Acetic Acid	6.58	7.93	8.35	8.77	9.66	17.65	14.24
Acetol	3.39	4.21	2.06	2.94	2.98	2.90	4.38
Propionic Acid	0.74	0.67	0.65	0.60	0.85	0.83	0.68
1-Hydroxy-2-butanone	2.39	2.57	2.10	2.22	2.80	3.58	1.69
Butanedial	0.12	0.17	0.28	0.10	0.14	0.08	0.49
Furfural (2-Furaldehyde)	0.11	0.19	0.21	0.09	0.15	0.17	0.78
Acetol acetate	0.84	1.05	0.82	1.06	1.01	1.64	0.99
Furan, tetrahydro-2,5-dimethoxy-	0.40	0.44	0.66	0.33	0.49	0.34	0.61
2(5H)-Furanone	0.01	0.01	0.02	0.01	0.01	0.02	0.03
Guaiacol (Phenol, 2-methoxy-)	0.24	0.37	0.34	0.01	0.40	0.36	0.39
2-Furanethanol, b-methoxy-(S)-	0.01	0.01	0.01	0.00	0.01	0.00	0.04
2-Butanone, 1-(acetyloxy)-	0.11	0.13	0.15	0.13	0.17	0.21	0.26
Phenol	0.43	0.41	0.35	0.33	0.44	0.46	0.33
O-Cresol	0.01	0.01	0.01	0.00	0.01	0.01	0.00
1,2-Benzenediol, 3-methoxy-	0.21	0.23	0.21	0.21	0.25	0.22	0.27
Phenol, 4-ethyl-2-methoxy-	0.03	0.08	0.07	0.03	0.08	0.07	0.10
Syringol	0.13	0.17	0.13	0.08	0.28	0.21	0.11
Eugenol	0.00	0.00	0.01	0.00	0.01	0.00	0.08
Vanillin	0.06	0.06	0.07	0.05	0.06	0.07	0.19
1,2,4-Trimethoxybenzene	0.21	0.23	0.22	0.22	0.23	0.22	0.30
5-tert-Butylpyrogallol	0.01	0.05	0.05	0.03	0.06	0.04	0.01
2-Propanone, 1-(4-hydroxy-3-methoxyphenyl)-	0.07	0.09	0.09	0.07	0.08	0.09	0.18
levoglucosan	0.21	0.21	0.23	0.21	0.22	0.24	0.38
Phenol, 4-(ethoxymethyl)-2-methoxy-	0.19	0.19	0.20	0.19	0.19	0.20	0.34
Benzaldehyde, 4-hydroxy-3,5-dimethoxy-	0.19	0.19	0.21	0.19	0.20	0.19	0.20
Phenol, 2,6-dimethoxy-4-(2-propenyl)-	0.19	0.21	0.20	0.20	0.21	0.21	0.20
Acetosyringone	0.19	0.20	0.21	0.19	0.20	0.20	0.42
Desaspidinol	0.19	0.21	0.21	0.20	0.22	0.20	0.23
3,5-Dimethoxy-4-hydroxycinnamaldehyde	0.00	0.00	0.00	0.00	0.00	0.20	0.20

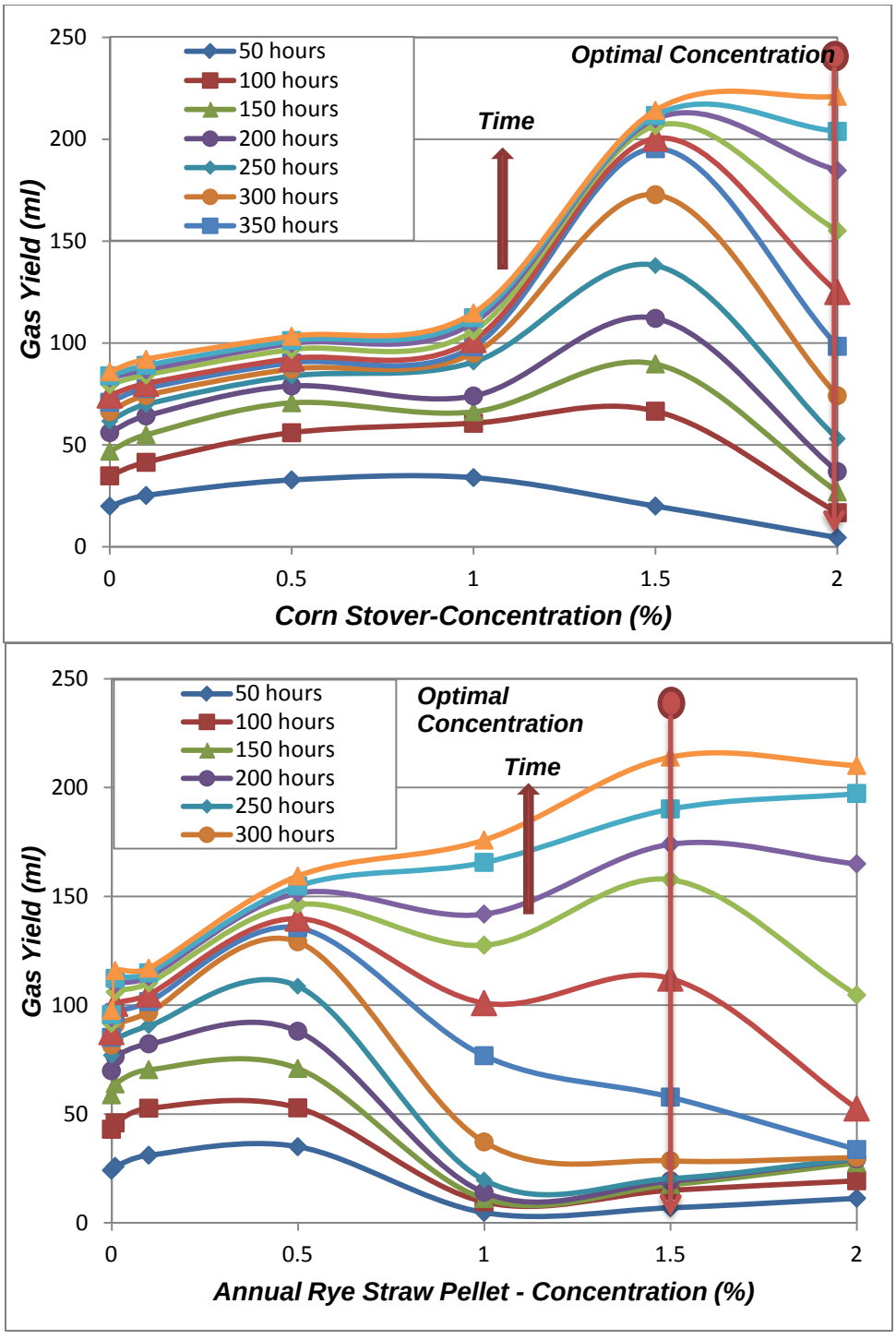

Figure 1.3.6: AD results of torrefaction aqueous phase derived from corn stover (*top*) and rye straw (*bottom*)

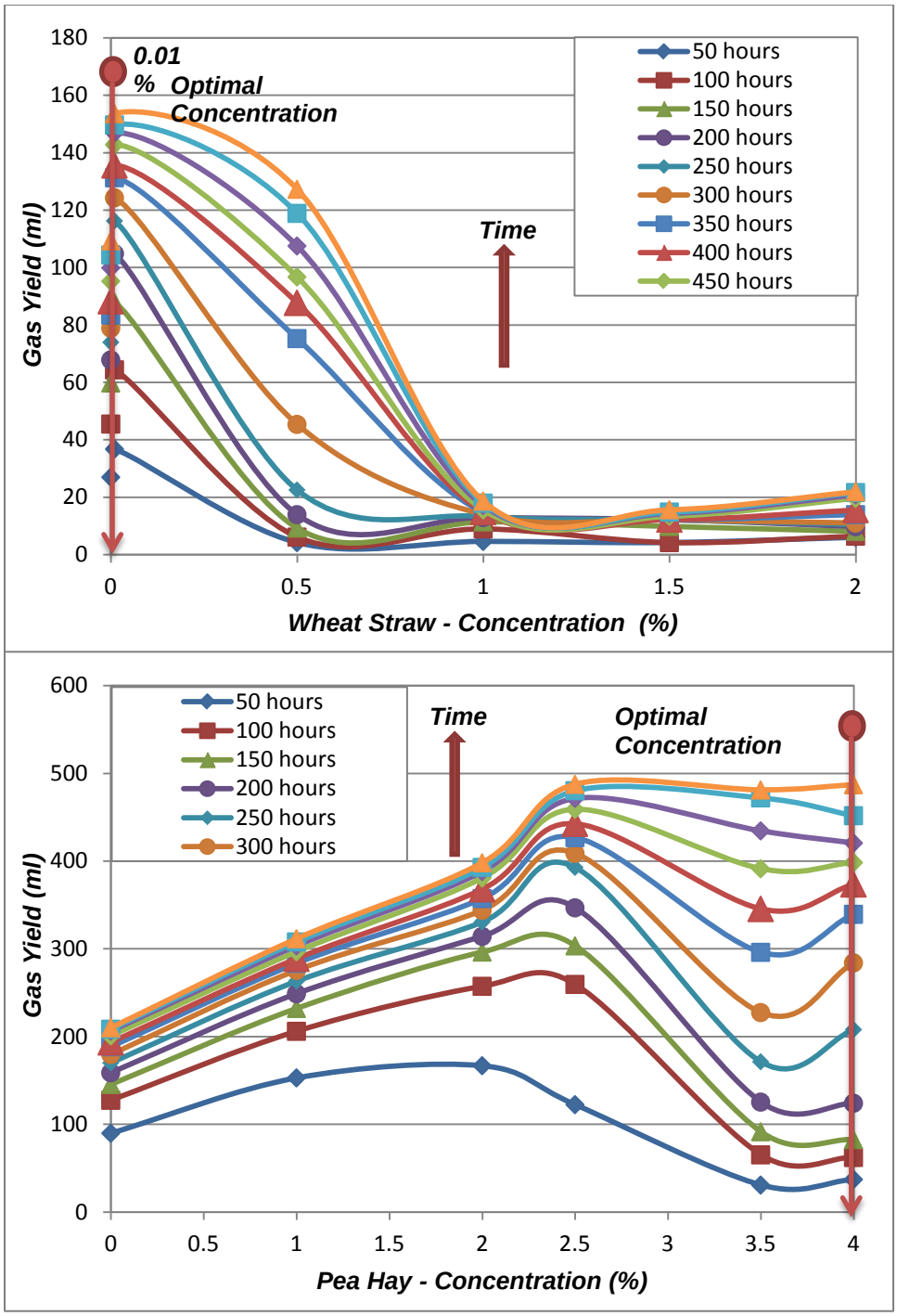

Figure 1.3.7: AD results of aqueous phase torrefaction products derived from wheat straw (*top*) and pea hay (*bottom*)

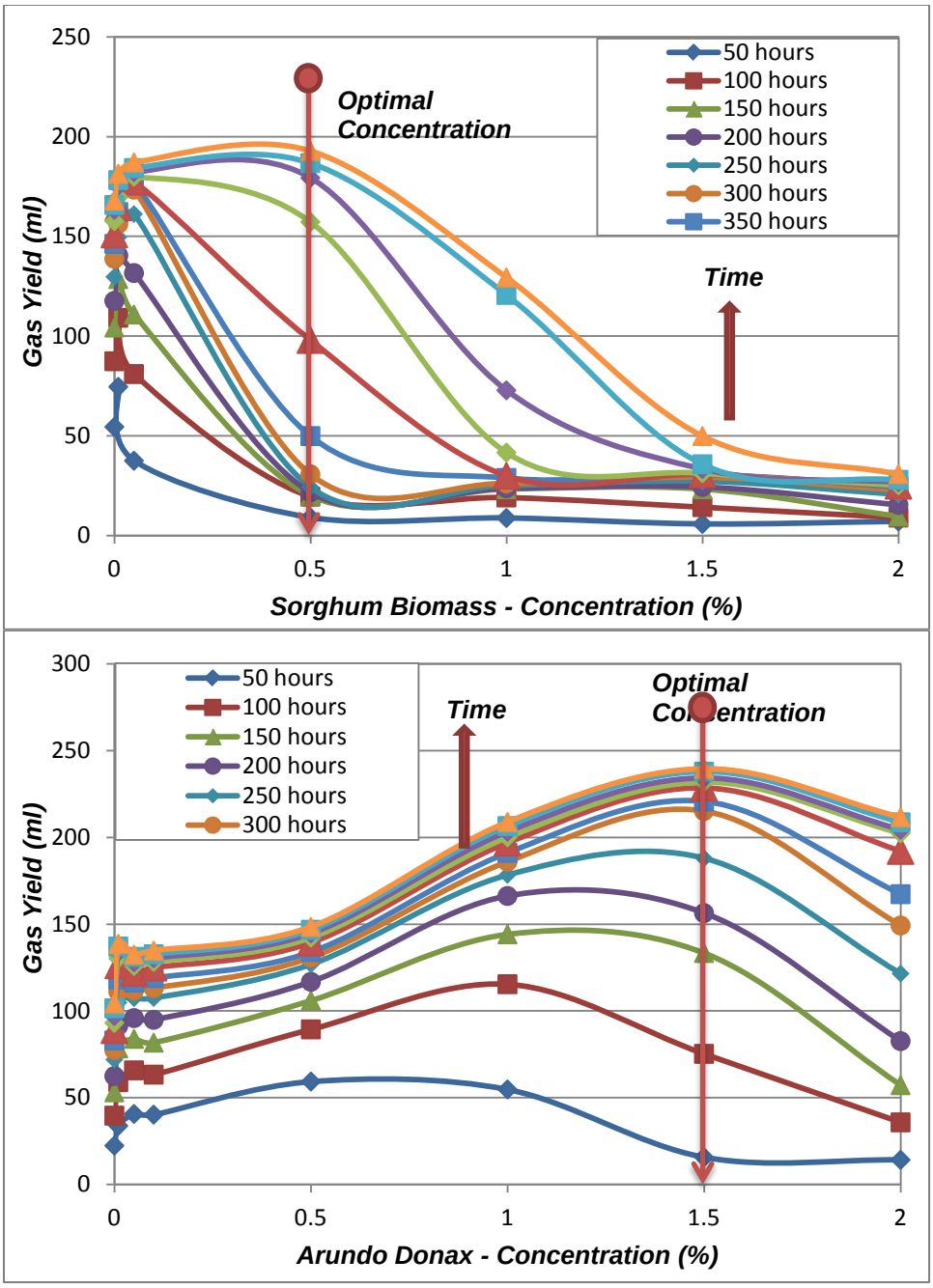

Figure 1.3.8: AD results of torrefaction aqueous phase products derived from sorghum and Arundo donax

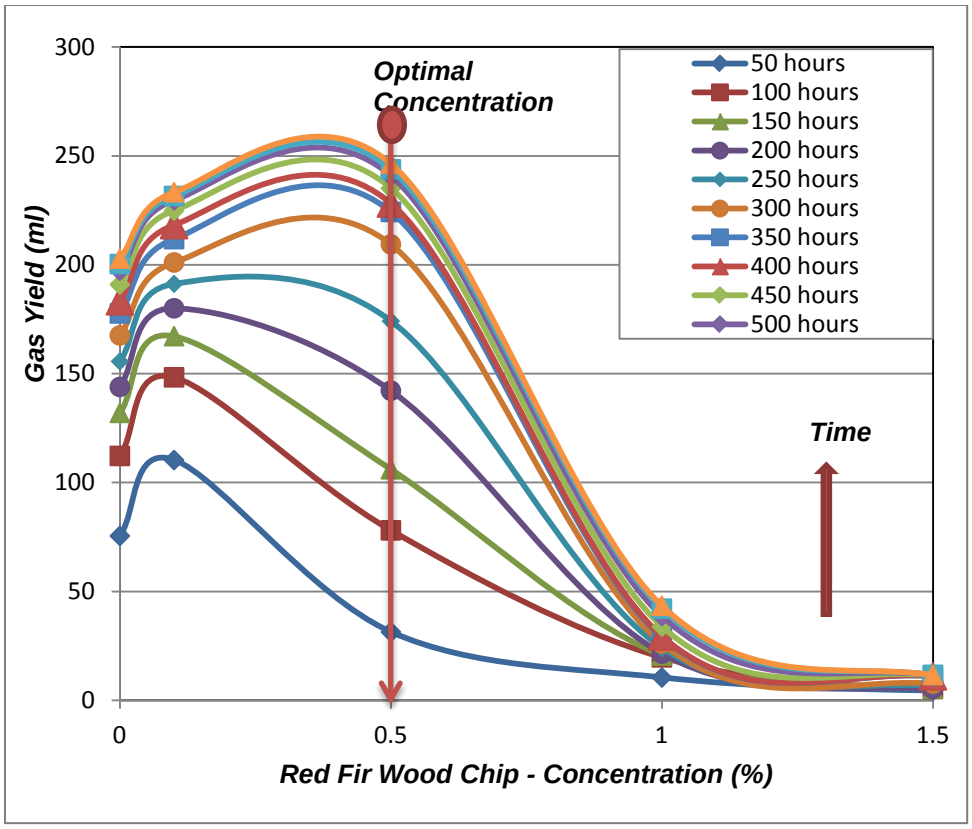

Figure 1.3.9: AD results of torrefaction liquid derived from red fir wood

The results indicated different optimum concentrations on a mass percent for each feedstock when it was torrefied and then co-digested with dairy manure. Among the feedstocks, the highest biogas production and highest biogas concentration was achieved when pea hay was co-digested with dairy manure. Biogas concentration increased as pea hay concentration increased up to 4% mass pea hay. At this concentration, almost 500 ml of gas was produced after 300 hrs of digestion. Further testing of pea hay should seek to determine why this specific type of lignocellulosic material was less inhibitory to the digestion process than other feedstocks.

1.3.4.4—Linear correlation between toxic compounds and biogas production

To better understand the impacts of toxic compounds on AD processes, the relationship between the concentration of toxic compounds (hydroaxyacetaldehyde and phenolics), and the optimal concentration for biogas production was investigated. Results indicated that as the concentration of toxic compounds (hydroxyacetaldehyde and phenol) within the aqueous phase increased, the biogas production decreased (Figure 1.3.10). This result is very important, as it suggests that in order to produce an aqueous phase from pyrolysis that has a high potential for AD it is necessary to control cellulose fragmentation reactions. These fragmentation reactions are responsible for the formation of hydroxyacetaldehyde, which inhibits the AD process. Furthermore, it is important to control lignin reactions and condensation conditions to reduce the content of mono-phenols in the aqueous phase. Figure 1.3.11 indicates that as the concentration of aqueous phase compounds increased during digestion, the biogas production also increased. This result confirms that as long as inhibition does not occur, the C_1–C_4 molecules are contributing to the formation of biogas.

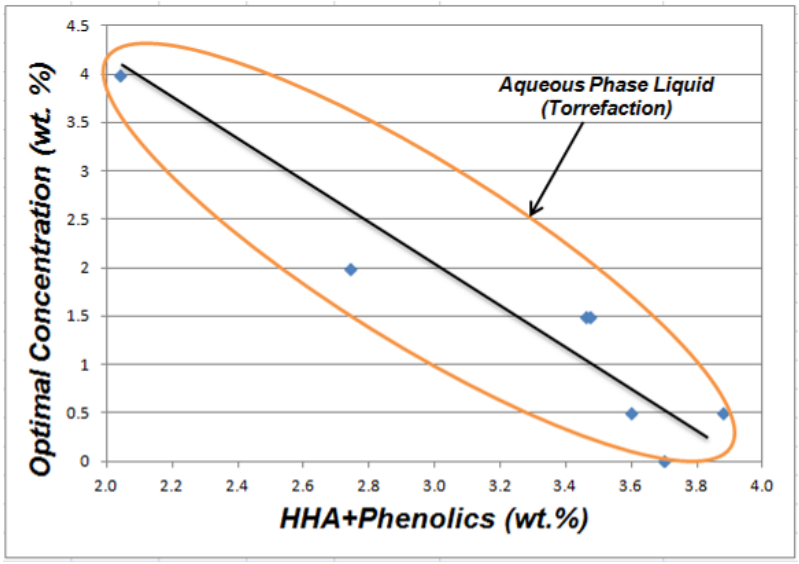

Figure 1.3.10: Correlation between the concentration of hydroaxyacetaldehyde and phenolics in the torrefaction liquid and the optimal concentration of torrefaction aqueous phase that can be digested

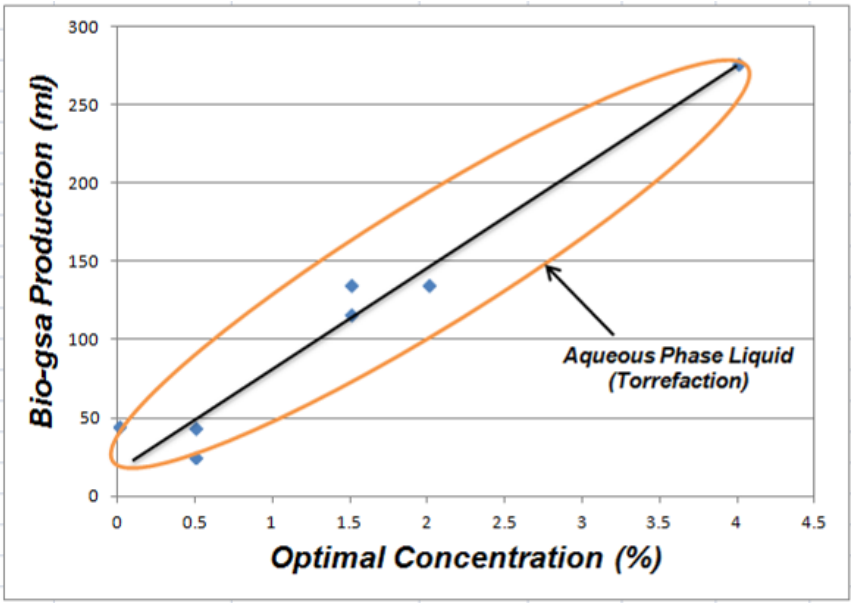

Figure 1.3.11: Correlation between the optimal concentration of torrefaction aqueous phase processed and the maximum biogas production

1.3.5—Conclusions

The main conclusions from this task are:

- Torrefaction and pyrolysis aqueous phases rich in C_1–C_4 molecules can be a source for CH_4 production via AD when co-digested with sludge.
- Hydroxyacetaldehyde and monophenols are the main inhibitors limiting higher concentrations of pyrolytic and torrefaction aqueous phase from being successfully digested.

In addition to these major conclusions, the negative linear correlation between the content of inhibitors and the optimal concentration of aqueous phase that could be digested confirms the key role these inhibitors play. Thus, future work should focus on minimizing the amount of these inhibitors in the aqueous phase. Toxins (hydroxyacetaldehyde and monophenols) present after the pyrolysis and torrefaction processes can likely be reduced through different pretreatment methods such as acid washing or sulfuric acid addition. Zhou et al. (2013) tested the effects of acid washing and sulfuric acid pretreatment prior to the pyrolysis of Douglas fir and hybrid Poplar wood showed that nitric acid wash and sulfuric addition resulted in lower levels of phenolic compounds such as hydroxyacetaldehyde. The results from the experiments performed in this study also suggest that future research should focus on optimizing the operational conditions for pyrolysis and torrefaction to reduce cellulose fragmentation that leads to the formation of hydroxyacetaldehyde.

1.4—Validate sequentially-dosed high volatile fatty acid leachate applied directly into plug-flow digester

Craig Frear, Quan-Bao Zhao, Cindy Alwine

1.4.1—Abstract

One fairly easy strategy for reducing composting odors associated with accepting food scraps is to squeeze liquids out of incoming food scraps and anaerobically digest them to produce biogas. This solution is based on the understanding that during composting with food scraps, odors are often caused by wet, putrescent material (e.g. food scraps) overloading the compost pile and creating anaerobic conditions. Thus, removing liquids from incoming wastes would allow for subsequent composting of solids with a reduced risk of odors and inhibition. Meanwhile, the liquid could be fed into a plug flow digester for co-digestion with other more recalcitrant feedstocks such as dairy manure. Plug flow digesters have been widely commercialized in the US, and thus would be relatively straightforward to install and operate.

To test this concept and provide some initial suggestions for optimization, a bench-scale plug flow reactor was designed, constructed, and used to digest dairy manure (a base, recalcitrant substrate) with acetic acid (a highly degradable substrate similar to the proposed food scrap liquids) dosed into later stages of the reactor. Varying concentrations of acetic acid were fed to the digester through ports at various locations along the bench scale reactor, over a 55 day digestion period. When levels of acetic acid were below a critical concentration threshold, additions of acid could be accomplished while maintaining overall operational stability of the

digester. Also, there were clear indications that volatile fatty acid (VFA) concentrations, as a measurement of total small chain acids, are an important rapid response indicator of digester instability, and thus could be used by digester managers as a tool to determine maximum thresholds for optimized loading and gas production. Not only acetic, but a range of VFA were present in undigested form in the effluent when the digester was fed a relatively high concentration of acetic acid (120 grams), thus overloading the digester and decreasing performance. Digester performance and stability also depended on neutral pH and alkalinity. These indicators showed a delayed response and thus would be of less use in managing digester stability.

1.4.2—Introduction

As food scrap composting has become more common, odor issues have become more frequent at compost yards. This increase is normally caused when highly degradable food scraps overload the compost pile and create anaerobic conditions. Based on this understanding, one solution that has been proposed is to squeeze liquids out of incoming food scraps. Solids could then be composted with a reduced risk of odors. The process would also reduce the risk that food scraps would inhibit the composting process. Meanwhile, the liquid could be fed into a plug flow anaerobic digester for co-digestion with other more recalcitrant feedstocks. The combination of feedstocks provides important synergies to the AD process. The more recalcitrant feedstock (e.g. dairy manure) can provide alkalinity that buffers the process from excessive pH swings, providing process stability. Meanwhile, highly degradable feedstocks generate significant amounts of CH_4, making the process more productive and profitable.

The possibility of integrating liquid from food scraps is of particular interest at co-digestion projects. AD is an appropriate waste management tool for a variety of different organic waste streams including animal waste, food scraps, green waste, and paper waste. In the US, the dairy industry has led AD adoption for animal waste streams. Co-digestion is used at the majority of these projects due to higher biogas production, greater stability for anaerobic microorganisms, more efficient use of equipment, and the cost-sharing that occurs when multiple waste streams are processed in a single facility (Alatriste-Mondragón et al., 2006). In urban or peri-urban areas, co-digestion could combine a variety of different substrates including food scraps and green waste with traditional AD substrates such as animal waste.

Two general types of digester configurations are used for AD projects. At the lower total solids (TS) concentrations, complete mixed reactors are usually preferred, while at higher TS concentrations a plug-flow reactor is preferred (Krich et al., 2005). When it comes to economics and simplicity, plug-flow reactors are generally the preferred choice since they have moderate capital and operational costs, though they do require that operations periodically be stopped so that cleaning can be carried out. In addition, new developments in plug flow technology are maintaining axial mixing throughout the plug flow, which allows it to operate at a variety of different solids concentrations, while maintaining the plug flow that allows for sequential entry of material. Complete mixed reactors or continuous stirred tank reactors (CSTR) are more complex systems since they incorporate some type of mixer, significantly increasing both capital and operational costs (ECOregon, 2009). In addition, they do not allow for sequential entry of material, unlike plug flow systems.

Industries that want to liquefy food scraps and then co-digest it at existing local digesters would like to be able to deliver liquefied waste with a low (but varying) TS and high organic loading rate (OLR). One potential candidate digester is the plug flow digester developed by DVO Inc. This digester operates at a wider range of TS than traditional plug flow digesters. It also has a relatively low energy requirement and hydraulic retention time (HRT), both of which may be preferred in this case.

Two general strategies have been proposed for co-digesting liquefied food scraps. One strategy is to mix the highly biodegradable food scraps with other more recalcitrant waste streams prior to feeding waste to a digester. An alternate strategy is to "dose" the high organic strength feedstock throughout a plug flow digester. This second strategy takes advantage of the fact that food scrap liquid is readily digested. Thus, it can be injected later in the digester process, but still achieve complete digestion. As long as dosing rates are not too high, and complete digestion is achieved, this would increase overall digester capacity and efficiency.

To explore this option, researchers at WSU and engineers at DVO Inc. designed a bench-scale plug flow digester and co-digested dairy manure (a base, recalcitrant substrate) with quickly decomposing acetic acid (similar to the proposed food scrap liquids). The acetic acid was dosed into the reactor at different stages of the digestion process to determine if the digester could achieve comparable performance to the control (manure only).

WSU researchers also conducted dosing studies of higher concentration acetic acid and biological oxygen demand (BOD) to determine the maximum OLR that the system could tolerate before failing. The microbial processes involved in AD are extremely complex and are sensitive to feedstock changes. When a digester is overloaded with high concentration wastes, the microbes become unable to decompose feedstock and the digestion process fails. Evaluating the maximum OLR was thus an important objective. VFA was used as one indicator that maximum OLR had been exceeded, as increased VFA in the digester effluent indicates incomplete digestion. It has been shown to be an early indicator of digester failure and is frequently used to monitor the stability of the digestion process (Dong et al., 2011; Labatut & Gooch, 2012). In addition, pH was monitored, as pH drops can also indicate digester "souring" and instability.

1.4.3—Materials and methods

The plug-flow reactor illustrated in Figure 1.4.1 was operated continuously for 59 days. Dairy manure was obtained from the WSU Dairy Knott Center and stored at 4°C prior to being fed into the plug-flow reactor. The bench-scale plug-flow reactor was constructed out of acrylic plastic that was 72" x 4.5" x 6". The reactor has several ports installed at the top of the digester for loading substrate. The main feed port was located to left of Figure 1.4.1 (P0), and six other ports were located at different positions along the digester for acetic acid and dairy manure dosing (P1−P6). The effluent exited through the port at the far right (Effl.). Air recirculation ports were located at the bottom of the digester to promote axial mixing throughout the plug-flow digester. The main plug-flow section of the digester was set inside an outer acrylic section. Water could be housed between the outer section and the reactor, maintaining a steady temperature throughout. The digester had a working volume of 20 L, and was operated at a temperature of 35°C in a temperature-controlled room. The digester was initially inoculated with 10 L of

primary anaerobic sludge from a WWTP and 10 L of anaerobically digested dairy manure. Acetic acid was used to represent a high VFA substrate such as food scrap liquid or biosolids. Two different concentrations of Acetic acid were included, 30 g and 60 g. The biogas produced from the digester was collected from the top of the reactor and measured by water-replacement with a tipping bucket.

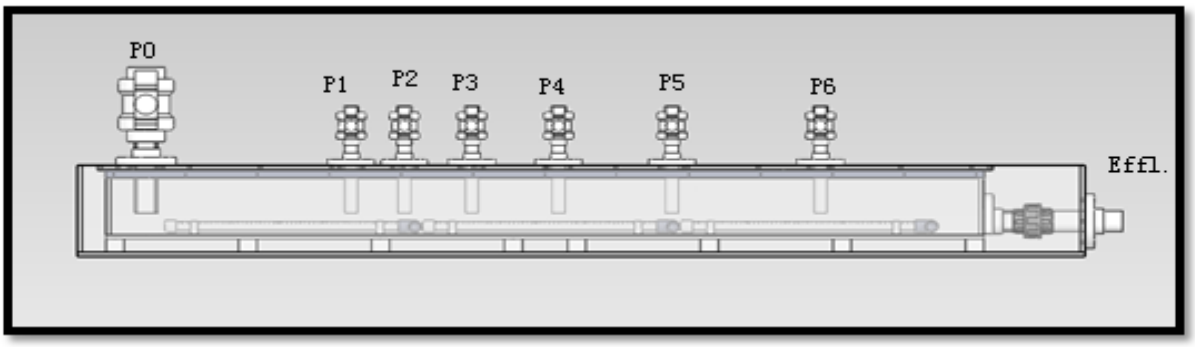

Figure 1.4.1: Schematic of the plug flow digester with different ports throughout the digester for dosing with high VFA and OLR substrate

Liquid samples were collected in 50 ml vials throughout the digestion process. Biogas was collected and analyzed for CH_4, CO_2, H_2S, H_2 with a Varian gas chromatograph (GC) (Santa Clara, California, USA), which was equipped with a thermal conductivity probe using a method described in Wen et al. (2007). Alkalinity was analyzed using a Mettler Toledo T50A Automatic Titrater (Schwerzenbach, Switzerland) (2320B) (Ripley et al., 1986). The concentrations of VFA were determined by a GC (Shimadzu Corp., Japan, Model GC-2014) equipped with a flame ionization detector and a length 30 m × id 0.25 mm × film thickness 0.25 μm capillary column (HP-INNOWax, Agilent Technologies, Palo Alto, CA). The pH of the effluent was analyzed with an OM-CP-PH101 pH and temperature data logger connected to a PHE-4200 pH probe (Omega Engineering, Stamford, Connecticut, USA). The total chemical oxygen demand (COD) was determined according to standard methods (Eaton et al., 2005).

1.4.4—Results and discussion

1.4.4.1—Biogas production

Biogas production throughout the digestion period is shown in Figure 1.4.2. As can be seen in the graph, the AD period was divided into five distinct phases (1–5), each with a distinct feeding regime. Digestion phase 1 was inoculum only and had a steady biogas production of around 400 L for around 4 days. Once 1 L/d of dairy manure was fed to port P0 and phase 2 began, biogas production steadily increased.

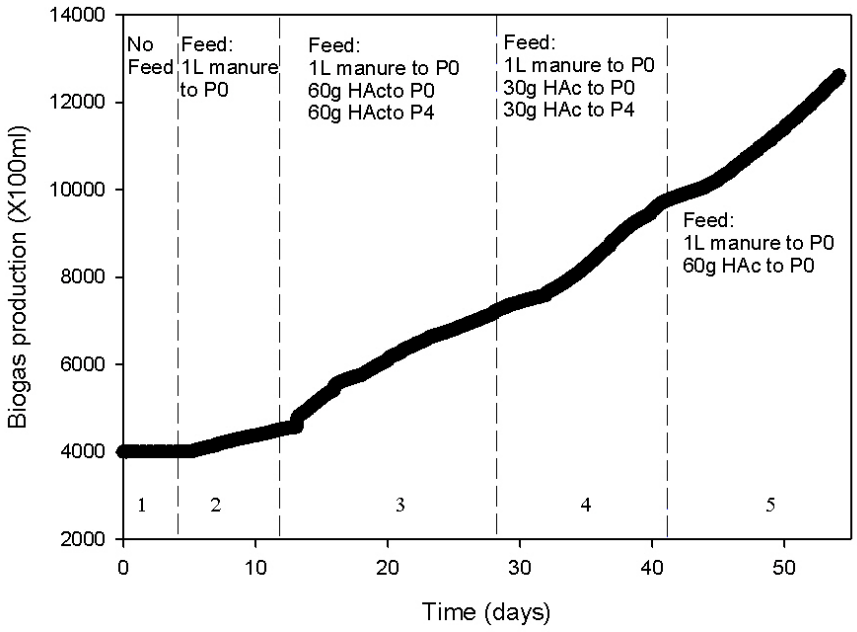

Figure 1.4.2: Biogas production during the experimental period. Five distinct operational phases were carried out, as follows: Phase 1: inoculum only. Phase 2: 1 L/day dairy manure fed at P0 (continuing through Phase 5). Phase 3: 60 g acetic acid added at P0 and P4. Phase 4: 30 g acetic acid at P0 and P4. Phase 5: 60 g acetic acid at P0

With the beginning of phase 3 on day 12, dosing of acetic acid was added. Initially, 60 g acetic acid was added at P0 and P4. Results indicated a significant increase in the biogas production resulting from the inclusion of acetic acid at P0 and P4. Cumulative biogas production during phase 3 increased from around 420 L to 750 L of biogas (a 79% increase).

During phase 4, the manure feed rate was maintained, while the concentration of acetic acid dosed to port P0 and P4 was decreased to 30 g. However, biogas production continued to climb to around 950 L, a 27% increase in cumulative biogas production over the course of phase 4.

After around 41 days of continuous digestion, the feed was changed once again, to 60 g of Acetic acid included with 1 L of manure to port P0. Once again the biogas production slowed initially but then increased significantly after day 45. Digestion was stopped after day 55. At this point, cumulative biogas production was above 1200 L (a 26% increase compared to phase 4).

The results indicated that the inclusion of acetic acid at different ports along the plug-flow reactor did not necessarily inhibit or overload the digester. As the manure-only feed from phase 2 moved along the plug flow it was combined with acetic acid, boosting the biogas production. This provides concrete evidence that dosing high VFA or highly decomposable liquid feedstocks along the plug flow digester can dramatically increase the biogas production while efficiently using the same digester volume. Biogas production began to taper off after phase 3. While the cumulative production continued to increase the rate of biogas production slowed, indicating the possibility that the digester was being overloaded with acetic acid. The digestion process might have failed if the high levels of acetic acid dosing had continued.

1.4.4.2—pH and alkalinity

The acidity of the effluent over the course of the digestion period is shown in Figure 1.4.3. The initial pH from the inoculum was around 7.3 (phase 1). After feeding with dairy manure (phase 2), the pH increased to around 7.5 from the alkalinity generated from the dairy manure. After dosing with 60 g of acetic acid to P0 and P4 began (phase 3), pH increased to 7.8 at first and then started to drop back down to around a pH of 7.5 indicating that the digester was performing satisfactorily and no inhibition was occurring. Late in phase 3, the pH dropped to its first low point of around 6.9 and then to its lowest point of pH 6.4. This indicates acetic acid overloading in phase 3. A total of 120 g acetic acid was added through ports P0 and P4. As the pH dropped below 6.9 on day 25, the total VFA concentration in the effluent had reached 7000 mg/L (see section 1.4.3). Thereafter, a lower dose of acetic acid (60 g acetic acid) was injected into the digester and the pH began to rise again, stabilizing at around 7.60 at the end of phase 4. In phase 5, the pH of the effluent increased gradually from 7.60 to 7.90.

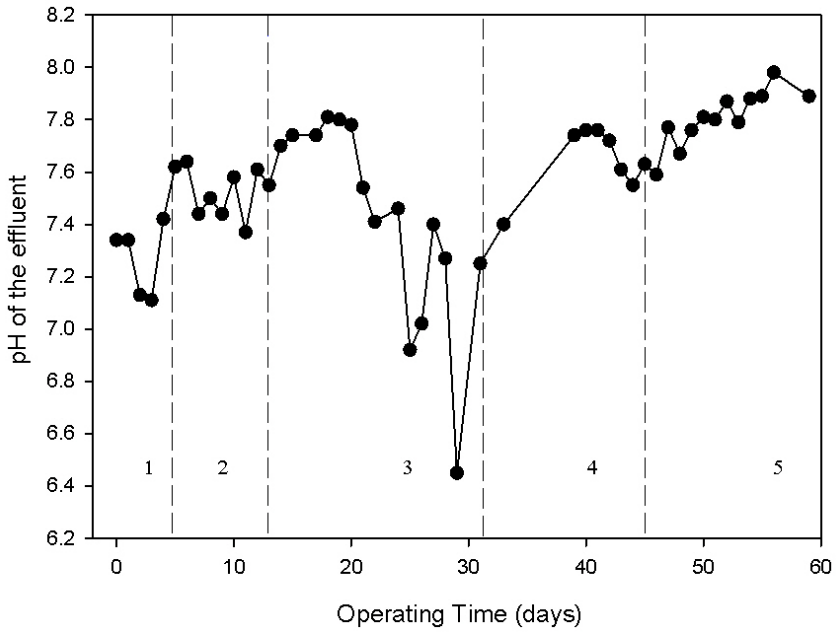

Figure 1.4.3: The change in effluent pH resulting from different dosing procedures

The alkalinity of the effluent (Figure 1.4.4) supports the interpretation provided for the pH results. The alkalinity in the effluent decreased to 7000 mg/L during the middle of phase 3 when acidity increased (driving pH down), and increased to 9350 mg/L during the recovery period at the end of phase 3 (corresponding rise in pH). However, due to the complex composition of the effluent, the alkalinity could vary dramatically even when the effluents had the same pH as shown in phase 3 and 5 in Fig 1.4.4. By the end of the experiment the alkalinity increased to its highest level of 13,000 mg/L. This may reflect the fact that the solids concentrations in the digester had increased in the later phases of the test. Maintaining solid suspension was difficult in such a small-scale digester.

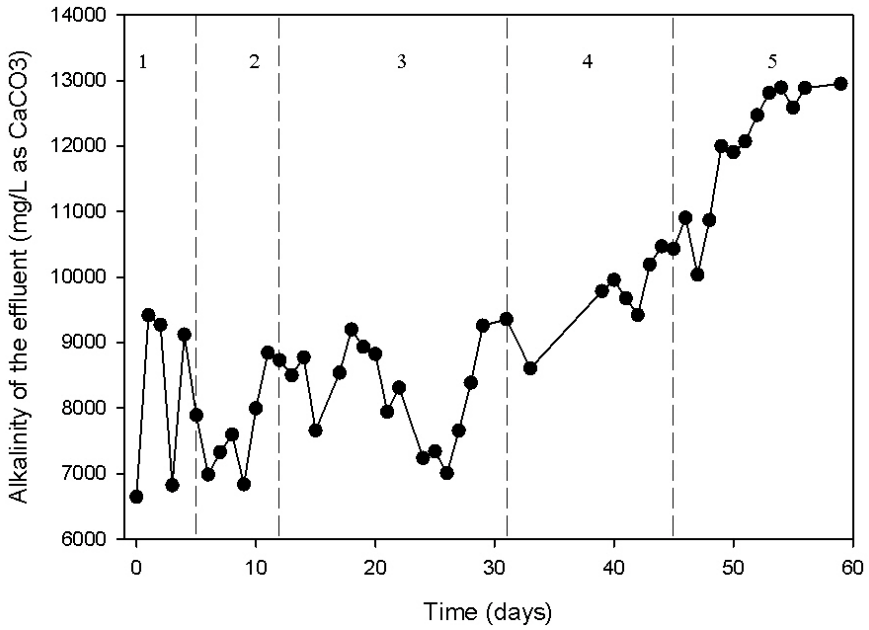

Figure 1.4.4: The change in effluent alkalinity resulting from different dosing procedures

1.4.4.3—Volatile fatty acids

The total VFA concentration in the effluent is shown in Figure 1.4.5. The VFA concentration in the digester was zero at the start-up of the digester (inoculum only). When 1 L/d of manure was fed into the digester, the VFA in the effluent suddenly increased to 2000 ppm. After six days it dropped to zero again, indicating that the digester had consumed all the VFA present in the 1 L dairy manure.

When acetic acid dosing began in phase 3, the total VFA started to accumulate once again after day 18, reaching its first peak of 7025 mg/L at day 25 and another peak 8534 mg/L at day 29. Also, C_3–C_5 fatty acids began to show up in the effluent (Fig 1.4.6), indicating poor digester performance. When comparing Fig 1.4.5 to Fig 1.4.2 and Fig 1.4.3, the authors noticed that a lag time occurred between the VFA accumulation, pH decrease, and the drop of biogas production rate. After decreasing the dosage of acetic acid from 60 g to 30 g to P0 and P4 in phase 4, the VFA dropped quickly to 200 mg/L, which indicated the digester had recovered from the inhibition. In phase 5, 60 g acetic acid dosing to port P0 resulted in no inhibition. The VFA in the effluent was around 100 to 300 mg/L by the end of phase 5. When the digester was operating well, only small amounts of acetic acid were present in the effluent and very small amounts of C_3–C_5 fatty acids were present, which is consistent with the literature (Ahring et al., 1995; Dong et al., 2011).

Together, these results indicate that dosing of 120 g of acetic acid into the plug flow digester at ports did have a negative impact on the digester performance. This indicates a maximum threshold that should be avoided when digesting high VFA substrates such as food scraps.

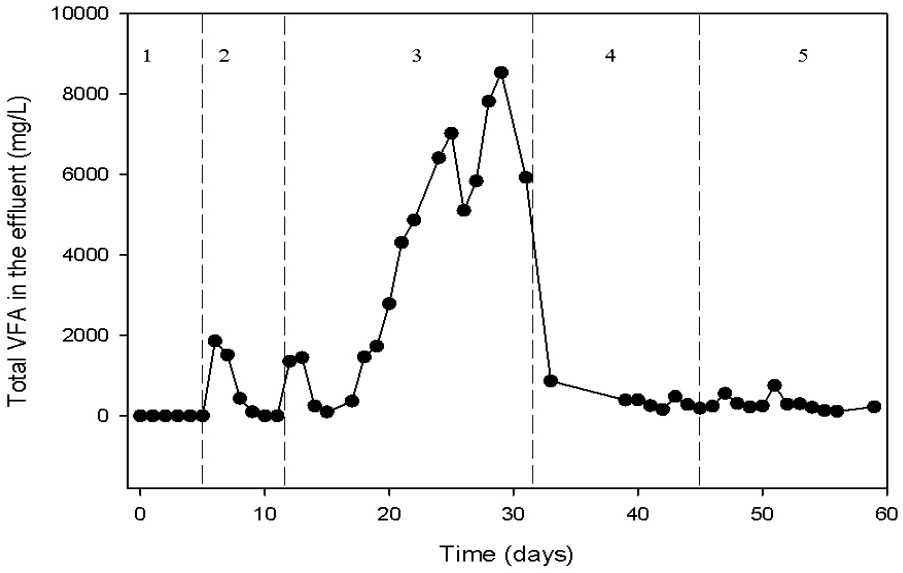

Figure 1.4.5: The change in effluent VFA resulting from different dosing procedures

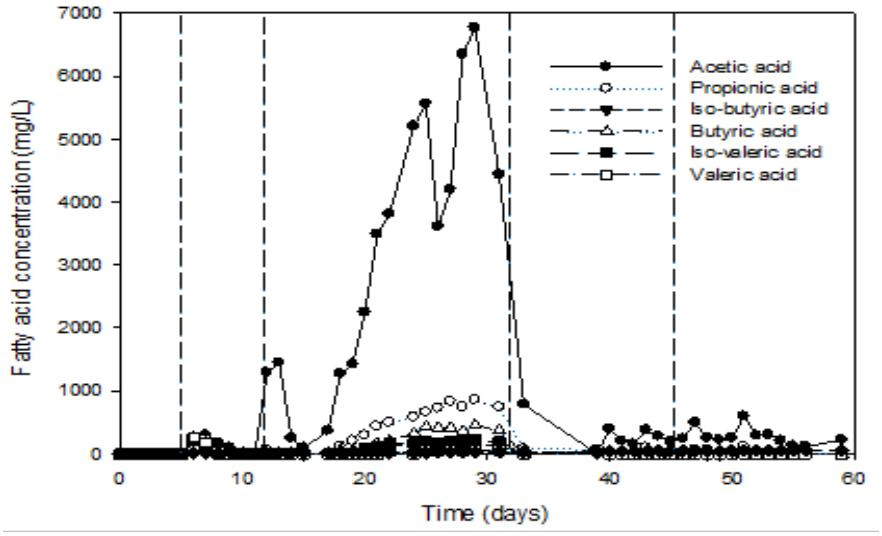

Figure 1.4.6: The changes of different types of VFA resulting from different dosing procedures

1.4.5—Conclusions

The strategy of multi-port feeding can reduce the initial shock at the beginning of a plug-flow digester. However, feeding the digester from different ports also increases the possibility of incomplete digestion of the organic matter due to the short retention time. At worst, this could result in a severe inhibition of the digester and high VFA content in effluent, which is not good for odor reduction. This strategy of multi-port feeding at two sites (the beginning and the middle) could generate two low pH zones from the feeding spots. When the organic loading is not high (in this study 30 g acetic acid), the buffer quickly neutralized the pH drop caused by the feedstock and the reactor was able to digest all the VFA. However, inhibition can occur if high amounts of acid are fed into the middle of the digester, which overwhelms the buffer system (in

this study 60 g acetic acid). In this case, the shorter HRT means that there is not enough time for full digestion to occur. When a high concentration of acetic acid was injected along the middle of the reactor (total of 120 g acetic acid at beginning and middle), the biogas production began to slow and VFA increased rapidly due to methanogen inhibition. It is important to note that the pH did not drop noticeably until VFA had accumulated to 7000 mg/L. At that point the pH dropped to around 6.4, indicating that the digester was beginning to fail. Alkalinity also performed poorly as an early indicator of digester failure, since it was not a sensitive indicator for VFA accumulation. When the reactor was inhibited, the low pH and high acetic concentration in the reactor created an environment for biologically forming C_3–C_5 fatty acids. One lesson learned from this study is that it is very important to control the organic loading that is fed into the digester to avoid VFA accumulation and negative impacts on the digestion process. In addition, results from the experiments indicated that VFA monitoring (more so than the pH or the alkalinity) is an important indicator to support adjustment of OLR, when multi-port dosing with highly degradable feedstocks is being used.

1.5—Proof of concept of next generation biofuel and bioproducts production from microalgae growth

Baisuo Zhao, Jingwei Ma, Shulin Chen, and Craig Frear

1.5.1—Abstract

Previous research conducted from 2007 to 2009 showed proof of concept for converting food and green waste to VFA through partial AD, as an alternative to completing the digestion to CH_4. The VFA could then be fed to algae so that they could convert the VFA to lipids, which in turn could be used to make drop-in liquid fuels. This biennium's experiments built on this previous foundation, aiming to optimize VFA production through control of HRT and perform a scale-up to a 5L reactor. After optimization of HRT at 12 days, the modest scale up achieved maximum total VFA concentration of 14.68±0.31 g/L after 20 days. On-going experiments are determining the impact the control of HRT has on the biological consortium carrying out the AD. This will hopefully lead the research team to new understanding about population control and microalgae species choice for optimal production of VFA, lipids and fuels.

1.5.2—Introduction

The oil recovered from microalgae biomass is considered a renewable source of biofuel and a practical technology for capturing CO_2 (Riebesell et al., 1993; Sialve et al., 2009). Microalgae may also represent one of the most sustainable and promising feedstocks to help meet global energy demands due to their high growth rate and productivity (Scott et al., 2010). Furthermore, some recognized microalgae species are able to thrive in extremely harsh environments such as seawater (salinity ~35 g/L), alkaline lakes (pH ≥ 8.5), non-potable industrial wastewater, and arid and barren land areas. Due to the harsh conditions where microalgae can grow, they would not directly compete with other uses for freshwater and arable land (McGinn et al., 2011; Wijffels & Barbosa, 2010). The concept of using microalgae biomass to produce biofuel was proposed by Golueke et al. (1954), and subsequently reviewed extensively by Oswald and Golueke (1960). In response to the oil crisis in the 1970s, numerous comprehensive efforts to develop biofuel

derived from microalgae were conducted between 1978 and 1996 (Sheehan et al., 1998). However, due to the high cost of algal oil compared to petroleum, research progress has been sporadic since 1996. Recently, highly motivated research on microalgae bioenergy has revived with the rising price of petroleum and recognition of its ultimate depletion (Harun et al., 2010; Wijffels & Barbosa, 2010).

Microalgae can be used to produce various biofuel and bioenergy products. They can be fermented into bioethanol (Bush & Hall, 2006; Ueda et al., 1996), or made into transesterified biodiesel (Chisti, 2007; Scott et al., 2010), photobiologically-produced biohydrogen (Ghirardi et al., 2000; Melis & Happe, 2001), or anaerobically generated CH_4 (Sialve et al., 2009; Uellendahl & Ahring, 2010). Amongst these energy products, producing CH_4 through AD of microalgae is a promising practical approach. This process is extremely useful for some species that are cultured in a photobioreactor or chemoorganotrophic bloom in an open polluted pond, which contain low lipid content. Because of their low lipid content, these species are not valuable for conversion to biodiesel (Sialve et al., 2009). The CH_4 yield from microalgae via AD has recently been reported to range from 0.09−0.45 L CH_4/g VS (De Schamphelaire & Verstraete, 2009; Lakaniemi et al., 2011; Mairet et al., 2011a; Mairet et al., 2011b; Mussgnug et al., 2010; Zamalloa et al., 2011). Such a wide range is unacceptable and is due to strongly species-dependent digestibility (Mussgnug et al., 2010).

The low carbon to nitrogen (C:N) ratio from algal biomass is another serious problem for AD. This ratio is an indication of the high protein content (39−71%) of algae biomass, which could produce high TAN during digestion and inhibit methanogenesis (Sialve et al., 2009). To avoid this issue, the co-digestion of microalgae biomass and a high carbon and low N substrate could diminish the NH_3 toxicity. It should also result in an increase in biogas production per unit volume of digester tank. For example, the CH_4 yield and productivity doubled when equal masses of wastewater sludge and *Spirulina* biomass were co-digested (Samson & Leduyt, 1982). Similarly, Yen and Brune (2007) added waste paper (50% w/w) to aquaculture algal sludge to adjust the C:N ratio to around 20−25:1 which, in turn, doubled the CH_4 production rate from 0.6 L/L liquid day to 1.2 L/L liquid day at 35°C with a HRT of 10 days.

Recently, another advanced biorefining technology, the MixAlco process within the ‘carboxylate platform’, was developed by Holtzapple and colleagues (Agler et al., 2011; Holtzapple et al., 1999; Holtzapple & Granda, 2009). In theory, the high concentrations of TAN from algal protein during the fermentation are easily acidified, producing high concentrations of carboxylic acids. Simultaneously, the high concentration of ammonium derived from algal TAN is able to neutralize the produced carboxylic acids, which can directly lead to a low supplement salt HCO_3^- buffer (Fu & Holtzapple, 2010b). The cow rumen contains more than 1000 bacterial operational taxonomic units (OTUs) associated with the biodegradation of lignocellulose (Hess et al., 2011). These bacteria provide rapid fermentation rates from the complex feedstock with high productivity of short-chain volatile carboxylic acids which includes acetic, propionic, and butyric acids (Weimer et al., 2009).

The goal of this work was to establish a mixed culture of cow rumen bacteria for the transformation of microalgae biomass to carboxylates using anaerobic sequencing batch reactor (ASBR) technology as a consolidated bioprocessing system. Figure 1.5.1 illustrates this

consolidated process to produce carboxylate with subsequent NR and downstream processing to biofuels.

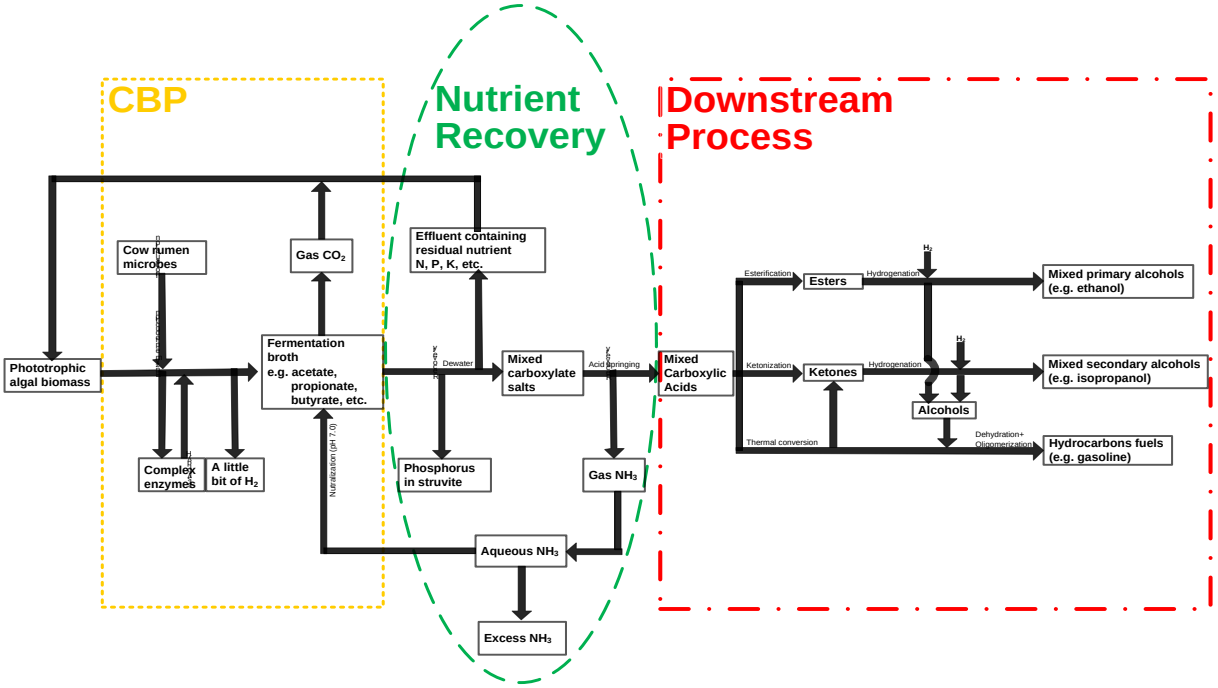

Figure 1.5.1: Overview of the consolidated bioprocessing from algal biomass to carboxylate salts

The specific bacterial consortium that carries out the transformations of the carboxylate platform is undefined. Therefore, during the experiments, the bacterial population dynamics and community were investigated by terminal restriction fragment length polymorphism (T-RFLP) technology. Understanding the microbial population and its community structure involved in the carboxylate platform will help us to (1) refine the design and operation of the bioreactor system, (2) facilitate the development of inoculum for large-scale implementation of this process, and (3) contribute to the developing body of knowledge regarding conversion and biofuel production from algal biomass.

1.5.3—Materials and methods

1.5.3.1—Feedstock and inoculum source

Scenedesmus dimorphus, a freshwater unicellular alga of class *Chlorophyceae*, was used in this study as the biomass feedstock for a series of fermentation experiments. The media for *S. dimorphus* cell culture was composed of 5 ml feed concentrate per gallon of filtered tap water. The feed concentrate was prepared as follows (w/v): 2.60% N, 1.20% phosphate, 2.40% soluble potash, 1.88% calcium, 0.78% magnesium, and 0.04% iron. The culture media was derived from the following: fish meal, composted seabird guano, kelp, rock phosphate, potassium carbonate, magnesium carbonate, calcium carbonate, calcium nitrate, magnesium nitrate, and iron EDTA. *S. dimorphus* were photoautotrophically cultured for 15 days at pH 6.0−8.4 at a temperature of 22−25°C in a closed pond. The algal biomass of *S. dimorphus* was harvested, dewatered, and dried using the HDD technology described by Algaeventure Systems (http://www.algaevs.com/). Thereafter, the microalgae biomass was desiccated at 105°C to a constant weight before

fermentation. Finally, the dried biomass was milled and passed through 1 mm screen in a Cyclone Analytic Grinder (USA). The seed inoculum of the mixed fiber and liquid from cow rumen used in the ASBR reactor was obtained from the farm of animal science at WSU in November 2010. The samples were immediately transferred in sterile N_2-full serum bottles, tightly sealed with butyl rubber stoppers, kept at room temperature during transportation, and then stored at 4ºC for later use. Aliquots of samples were added to inoculate the bioreactor vessels.

1.5.3.2—Bioreactor construction and performance monitoring

For the ASBR, 4 g dried algal biomass of *S. dimorphus* and 10% seed inoculum were inoculated in four serum bottles. The anaerobic cultures of the ASBR reactor were neutralized with aqueous (10% w/v) to a pH of between 6.95–7.05 before fermentation, flushed with O_2-free N_2 gas for 15 min to induce an anaerobic condition, and incubated at 39±1ºC and 200 rpm. After 95 h of reactor operation, 95, 50, 33.3, and 25 ml of the cultured medium for 4.2, 8, 12, and 16 days of HRT were replaced by equal volume of fresh medium containing 3.8, 2, 1.33, and 1 g algal biomass, respectively. The reactors were operated again for 95 h. From the second cycle, every operation was comprised of a decanting period (10 min), feeding period (20 min), neutralizing acids period (20 min), flushing period (10 min), and reacting period (varied by HRT). The initial volatile solid loading rate (VSLR) was decreased stepwise by increasing HRT from 4.2, 8, 12, and 16 days. The experimental design conditions for the different HRT in the ASBR system are shown in Table 1.5.1. Constant substrate consumption and carboxylic acids production (±5% variation) were considered as indicators for the steady state conditions.

Table 1.5.1: Operational parameters and characteristics of un-extracted algal biomass samples

ASBR fermentation	**A**	**B**	**C**	**D**
HRT (days)	4.2	8	12	16
VSLR (g VS fed/L liquid day)	7.51	3.96	2.65	1.98
Total carboxylic acid concentration (g/L liquid)	3.62±0.63	7.50±0.81	12.35±0.53	14.06±0.59
Product distribution				
Acetic acid (wt %)	54.85±7.96	49.16±9.88	44.90±3.33	36.28±3.50
Propionic acid (wt %)	15.48±2.76	15.23±1.83	14.56±1.52	12.21±1.69
Butyric acid (wt %)	19.23±1.41	22.04±1.94	21.48±0.75	21.48±2.17
Valeric acid (wt %)	10.43±1.35	13.57±0.82	13.88±1.49	17.12±3.29
Caproic acid (wt %)	0.00±0.00	0.00±0.00	4.18±2.91	6.72±1.39
Heptanoic acid (wt %)	0.00±0.00	0.00±0.00	0.00±0.00	6.58±0.68
Conversion (g VS digested/g VS fed)	0.208	0.381	0.526	0.598
Yield (g total acids/g VS fed)	0.115	0.237	0.388	0.443
Selectivity (g total acids/g VS digested)	0.552	0.621	0.738	0.742
Total carboxylic acid productivity (g total acids/L liquid day)	0.862	0.938	1.029	0.879
Acetic acid yield (g acetic acid/g VS fed)	0.063	0.116	0.174	0.161
CH_4 productivity (g CH_4/L liquid day)	0.0002	0.0009	0.0006	0.0010
TAN (mg/L)	522.2	551.7	584.7	626.7

The lab-scale ASBR bioreactor (New Brunswick Scientific Inc., Model Bioflo 110 Fermentor, NJ) was operated with 5 L working volume supplied with 3% seeds of 12 HRT (Figure 1.5.2) at 39±1ºC and 200 rpm. The reactor was perfectly sealed and the head unit included functional ports such as feed inlet and outlet, temperature probe and pH probe. Prior to start-up of the reactor, it was sparged with O_2-free N_2 gas for 25 min. During the fermentation, 30% aqueous was pumped automatically into the fermenter to maintain a pH within 7.0±0.1.

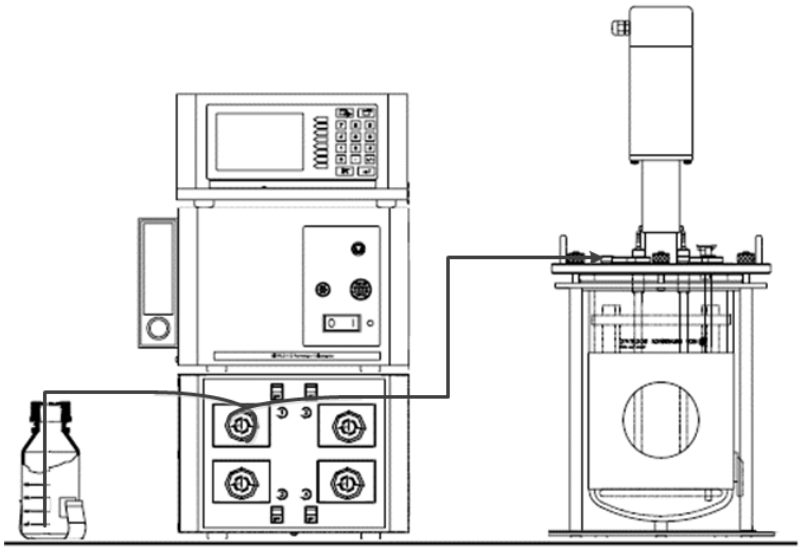

Figure 1.5.2: Schematic of the fermentation process with attached monitoring system

Methanogens were inhibited by a concentration of 25 mg iodoform/L which came from a concentrated solution (25 g iodoform/L ethanol) during the fermentation (Fu & Holtzapple, 2010a). The concentrated solution was stored in a sterile sealed N_2-full serum bottle encased in aluminum foil at 4ºC due to the sensitivity of iodoform to light and air. The iodoform was taken through the butyl rubber stopper with the 1 ml syringe, and added into the reactor every two days to prevent CH_4 production.

1.5.3.3—Analytical methods

Elemental analysis for carbon, H, O, N, and sulfur of *S. dimorphus* was performed according to standard methods (Pella, 1990) at the Stable Isotope Core Laboratory, WSU. The total cell lipid was determined after fatty acid methyl ester synthesis using capillary GC on a SP-2560, 100 m x 0.25 mm x 0.20 μm capillary column (Supelco), as described by O'Fallon et al. (2007). The TAN was determined by N-Macro Kjeldahl method. The total phosphate level was assessed using TS and VS in the initial substrates and fermentation residues, measured using the national renewable energy laboratory (NREL) standard laboratory analytical procedures (http://www.nrel.gov/biomass). The TS was dried to constant weight (±0.1%) at 105ºC and the ash was determined after the dry oxidation (±0.3 mg) at 550ºC.

Prior to measurement of the total carboxylic acids, the samples from the fermentation solutions were first centrifuged at 13000 rpm for 3 min. Subsequently, the supernatant liquids were mixed with an equal amount of internal standard solution (4-methyl-n-valeric acid, 1.162 g/L), acidified by formic acid (1% m/v) with the ratio of 1:4 (v/v), and then filtrated through Millipore 13 mm non-sterile membrane (0.20 μm; Fisher, PA, USA). The concentrations of carboxylic acids were analyzed using a Shimadzu GC outfitted with an AOC-5000 auto-sampler and FID detector operated at 300ºC (GC-2014; Sunnyvale, CA, USA) using a HP-INNOWax column of 30 cm length, 0.25 mm ID and 0.25 μm film. Start temperature was 70ºC, ramped at 15ºC per min to a hold temperature of 230ºC for three mins. Split/split-less injector temperature was 250ºC at a split ratio of 40/1 using helium carrier gas. Detector temperature was 300ºC.

To express all carboxylic acids on a common basis, the carboxylic acid concentrations were converted to acetic acid equivalents (α) (Fu & Holtzapple, 2010b) by the following equations:

$$\alpha \text{ (mol/L)} = \text{acetic (mol/L)} \quad (1.5.1)$$
$$+ 1.75 \times \text{propionic (mol/L)} \quad (1.5.2)$$
$$+ 2.5 \times \text{butyric (mol/L)} \quad (1.5.3)$$
$$+ 3.25 \times \text{valeric (mol/L)} \quad (1.5.4)$$
$$+ 4.0 \times \text{caproic (mol/L)} \quad (1.5.5)$$
$$+ 4.75 \times \text{heptanoic (mol/L)} \quad (1.5.6)$$

On mass basis, the acetic acid equivalent can be expressed as:

$$A_e \text{ (g/L)} = 60.5 \text{ (g/mol)} \times \alpha \text{ (mol/L)} \quad (1.5.7)$$

$$\text{VSLR} = \frac{\text{VS fed (g)}}{\text{liquid in reactor (L)} \times \text{time (day)}} \quad (1.5.8)$$

$$\%\ \text{Conversion} = \frac{\text{VS digested (g)}}{\text{VS Fed (g)}} \times 100 \quad (1.5.9)$$

$$\%\ \text{Yield} = \frac{\text{Total carboxylic acids produced (g)}}{\text{VS fed (g)}} \times 100 \quad (1.5.10)$$

$$\%\ \text{Selectivity} = \frac{\text{Total carboxylic acids produced (g)}}{\text{VS digested (g)}} \times 100 \quad (1.5.11)$$

$$\text{Total acid productivity} = \frac{\text{Total carboxylic acids produced (g)}}{\text{liquid in reactor (L)} \times \text{time (day)}} \quad (1.5.12)$$

1.5.3.4—Molecular analysis of bacterial communities

Genomic DNA from the microbial community was extracted from each 2 ml solid-liquid mixture sampled from the series of tests in the ASBR reactor using the Power Soil DNA Isolation Kit (MoBio Laboratories, CA). Genomic DNA purity was assessed and quantified by A_{280}/A_{260} ratio (Johnson & Soltis, 1994) using the NanoDrop Spectrophotometer ND-1000 (NanoDrop Technologies). The genomic DNA was used for T-RFLP analysis and clone library construction for phylogenetic analysis.

For T-RFLP analysis, bacterial 16S rRNA genes were amplified with a forward primer 8F and a universal reverse primer 1492r (Zhao et al., 2010). The 5' end of the 8F primer was labeled with the fluorescent tag 6-FAM (6-carboxyfluorescein). Polymerase chain reaction (PCR) was performed as follows in a 50µl reaction volume using GoTaq® Green Master Mix (Promega, USA): initial denaturation step at 95°C for 5 min, followed by 20 cycles of denaturation at 95°C for 60 sec, annealing at 55°C for 60 sec and primer extension at 72°C for 90 sec, with a final 5 min extension step at 72°C. Three replicate PCRs were run per sample, pooled after amplification, and purified using the QIAGEN PCR purification kit (Valencia, CA, USA). Subsequently, the PCR products were individually digested with *Hae* III (GG′AC, Takara Bio, USA) and *Rsa* I (GT′AC, Takara Bio, USA) for 8 h at 37°C to determine which digestion resulted in better detection of different types. It was found that *Hae* III was suitable in this study. Furthermore, separation of T-RFs was run on an ABI 3730xl DNA sequencer in GeneScan mode (GENEWIZ, Inc. USA) together with an internal size standard (GeneScan 500 LIZ; Applied Biosystems). T-RFs were analyzed using GeneMarker V 2.2 (SoftGenetics LLC., USA) including fragments with the lengths ranging from 50 to 500 bp, an initial peak detection

threshold of 50 relative fluorescent units, and a peak area with both > 500 and its relative abundance > 0.5%. Peaks of < 0.5 bases apart from each other were merged. The T-RFs profiles were normalized by calculating the relative abundance (percentage) of each fragment (each T-RF peak area divided by the total peak area of each sample). The T-RFs peaks were assigned through Phylogenetic Assignment Tool (PAT, https://secure.limnology.wisc.edu/trflp/) (Kent et al., 2003), using a modified database from Ribosomal Database Project (Cole et al., 2005) and our database from 16S rRNA gene clone library (still under construction) was generated by ISPaR tool of MiCA (http://mica.ibest.uidaho.edu) (Shyu et al., 2007).

1.5.3.5—Nucleotide sequence accession numbers

Bacterial sequences generated in this study have been deposited in the GenBank database under accession numbers X to Y. All submissions conform to the "minimum information standards" recommended by the genomic Standards Consortium (http://gensc.org/gc_wiki/index.php/Main_Page) (Yilmaz et al., 2011).

1.5.4—Results and discussion

1.5.4.1—Characteristics of *S. dimorphus* biomass

The biomass of *S. dimorphus* was harvested at approximately 0.5 g dry weight/L liquid with 0.791 g VS/g TS and 0.291 g ash/g TS, implying this strain can offer abundant metal elements for microbial nutrition during anaerobic processes. The significant organic nutrients were carbon (39.62%), hydrogen (5.66%), oxygen (28.66%), N (6.65%), and sulfur (1.25%), respectively. The crude protein is generally regarded to be 6.25 times total N, which indicates that the protein content of *S. dimorphus* was approximately 41.6%. This is consistent with the protein range of values (29–71%) given by Sialve et al. (2009). The total lipids were only 7.22% because it was grown phototrophically without any nutrient stress to induce lipid accumulation. Three prominent fatty acids were present including palmitic ($C_{16:0}$, 13.75 %), linoleic ($C_{18:2n6}$, 8.60 %), and linolenic ($C_{18:3n3}$, 7.63 %), respectively. Since the total lipid content in *S. dimorphus* were less than 40%, AD of *S. dimorphus* whole biomass to produce CH_4 might be a practical strategy for sustainable bioenergy recovery (Sialve et al., 2009). Generally, an optimum C:N ratio of 20–30:1 for the production of CH_4 is considered an optimum range, though there is still some disagreement on this ratio (Parkin & Owen, 1986; Yen & Brune, 2007). Unfortunately, the ratio of C:N in *S. dimorphus* (5.96/1) was too low to generate CH_4, it would result in high concentrations of both TAN and carboxylic acids, would inhibit the methanogenic activity and result in failure of the AD process (Parkin & Owen, 1986; Yen & Brune, 2007). Therefore, we proposed the current study of the anaerobic conversion of *S. dimorphus* biomass to carboxylates as a more attractive, effective and competitive strategy.

1.5.4.2—Carboxylic acids production in anaerobic sequencing batch reactor with different hydraulic retention times

Continuous carboxylic acids production was operated simultaneously in ASBR with 100 ml working volume at different HRT including 4.2 (A), 8 (B), 12 (C), and 16 (D) days. As HRT increased, the VSLR decreased to 7.51, 3.96, 2.65, 1.98 g VS fed/L liquid day, respectively. Four reactors were running for 80 days with *S. dimorphus* as a feedstock and a steady-state production of the total carboxylic acids was achieved during the phase of 60–80 days (data not shown). Table 1.5.1 summarizes the operating parameters and constant experimental results of four HRT fermentations. Data showed that the different HRT led to variation in the total carboxylic acid concentration, productivity, yield, conversion, selectivity, and even metabolite patterns. With 4-

day and 8-day HRT, low digestibility occurred although the VSLR was high. The main reason for this was that the algal cell wall was composed of a diverse array of fibril, matrix and crystalline polymers, which were not easily biodegradable by bacteria in this relatively short operational period. With 12-day and 16-day HRT, the digestibility was significantly enhanced, indicating that specific microbial consortiums selected under pressure of the chosen HRT have been established for the biodegradation. The maximum total carboxylic acid yield (0.879 g/L day), selectivity (0.742 g total acids/g VS digested) and conversion (0.598 g VS digested/g VS fed) occurred at 16-day HRT fermentation (VSLR = 1.98 g VS fed/L liquid day) with a total carboxylic acids concentration of 14.06±0.59 g/L liquid. Meanwhile, the highest productivity (1.029 g total acids/L liquid day) resulted from the 12-day HRT fermentation (see Figure 1.5.3) (VSLR = 2.65 g VS fed/L liquid day) with a concentration of 12.35±0.53 g/L liquid. Since industry generally finds productivity of total carboxylic acids most important, the optimum HRT was 12 days.

The profiles and proportions of individual acids from *S. dimorphus* biomass in the effluents were significantly different depending on HRT, and were also different from those of sugarcane bagasse and sewage sludge found by others (Fu & Holtzapple, 2010a; Fu & Holtzapple, 2011; Rughoonundun et al., 2010). As indicated in Table 1.5.1, as HRT increased, the patterns and concentrations of carboxylic acids in the fermentation effluent shifted from lower molecular weight acids (i.e. acetic acid and propionic acid) to higher molecular weight acids (i.e. valeric acid, caproic acid and heptanoic acid). For instance, the major carboxylic acids from *S. dimorphus* consisted of acetic acid (36.28–54.85 wt % of the total carboxylic acids), propionic acid (12.21–15.48 wt %), butyric acid (19.23–22.04 wt %) and valeric acid (10.43–17.12 wt %).

In order to effectively test and enhance total carboxylic acid productivity for a modest scale-up at the chosen HRT of 12 days, a 5 L working volume lab-scale ASBR bioreactor was conducted to mimic common industrial operation conditions. After 32 days' incubation, the performance metrics were quite stable and significantly greater at the 5 L working volume than at the 100 ml working volume. A maximum total carboxylic acid concentration of 14.68±0.31 g/L liquid was reached after 20 days (see Figure 1.5.3) and a yield of 0.462 g total acids/g VS fed was achieved, higher than that from the previous study. Total carboxylic acid productivity was 1.223 g total acids/L liquid day with a biomass conversion of 63.15% g VS digested/g VS fed and selectivity of 0.731 g total acids/g VS digested.

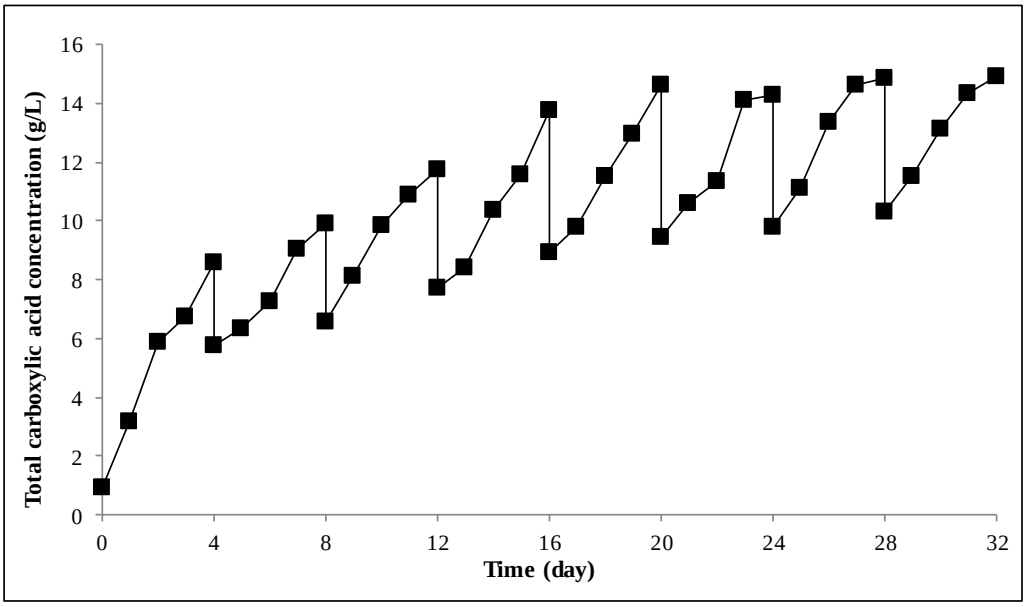

Figure 1.5.3: The total acid concentration for the lab-scale ASBR bioreactor at a 12-day HRT

During anaerobic fermentation, protein is degraded and the accumulated ammonium (the main N form) can be released into liquid phase (Zamalloa et al., 2011). The TAN of liquid effluent was on the average 1.165 g/L. This data indicates a lower concentration than the concentration that has been found from the cyanobacteria *Spirulina maxima* (up to 7.0 g/L) (Samson & LeDuyt, 1986) and higher than that found from the marine microalgae *Phaeodactylum tricornutum* (0.546 g/L) (Zamalloa et al., 2011). The high concentration of NH_3 from *S. dimorphus* also suggested the protein rich microalgae are unable to produce a high volume of biomethane as NH_3 has some toxic effects on methanogenesis. As Table 1.5.1 shows, the NH_3 can be recovered from the digestion effluent using sulfuric acid as an adsorbent through aeration at elevated temperature of 50°C (Data not shown). The concentration of soluble phosphates (PO_4-P) in the effluent from *S. dimorphus* was on average 0.267 g/L whereas the concentration of total phosphate was on average 1.898 g/L, indicating that almost 86% phosphates were still in the solid effluent.

These results indicate that it may be possible to recycle N and P from algal waste via the carboxylate platform. This is a promising strategy, as there is huge demand for both of these important nutrients for microalgae cultivation. This would also avoid the need to have to treat process byproducts to remove N and P, to avoid releasing excess N and P to the air or water.

1.5.4.3—T-RFLP analysis of bacterial community at different hydraulic retention times

Once the mixed cultures of rumen microorganisms were established, T-RFLP analysis was used to investigate the diversity and relative abundance of bacterial community at the different HRT. The T-RFLP profiles of bacterial fragments digested with Hae III are shown in Figure 1.5.4. The percentage of each T-RF in these profiles varied significantly depending on the HRT. This suggests that a dynamic shift in the bacterial community occurred in response to HRT.

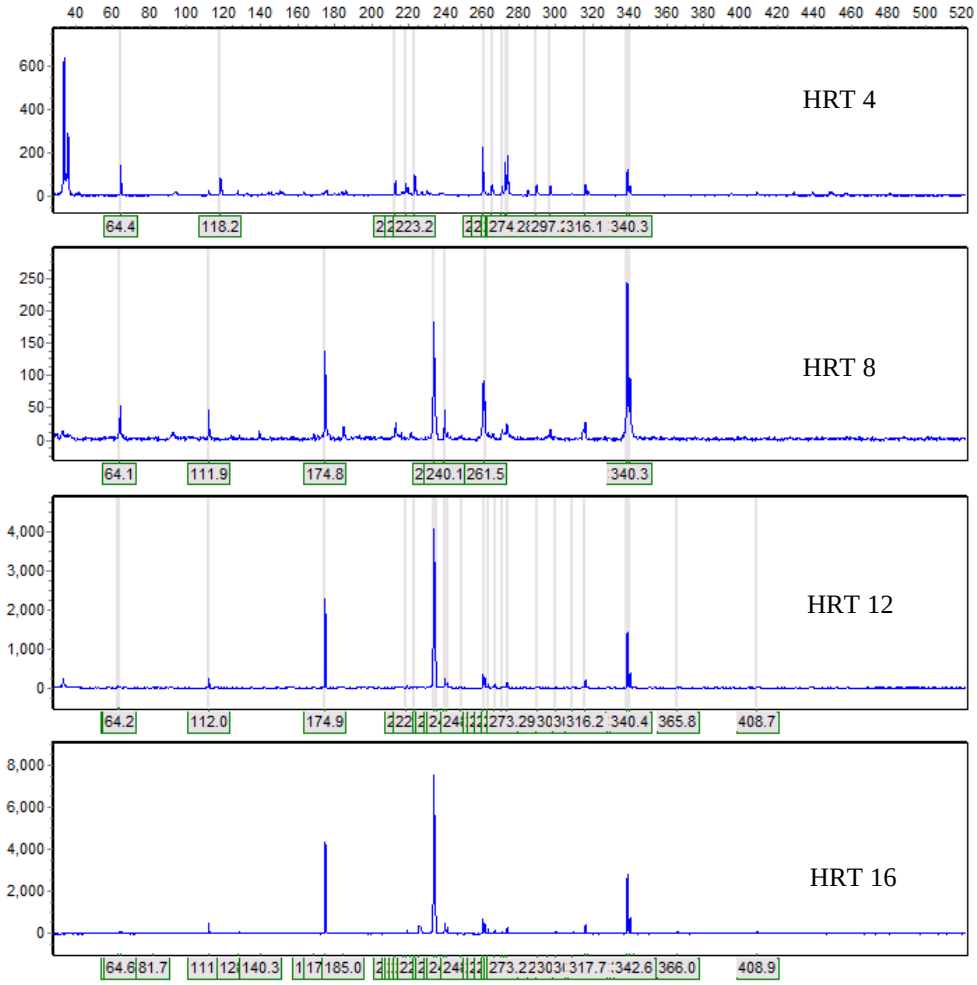

Figure 1.5.4: T-RFLP pattern of PCR-amplified nearly full-length bacterial 16S rRNA genes of different HRTs digested with the restriction enzyme Hae III

One major T-RF, 274, could be seen in the sample from HRT 4 days but not from HRT 8, 12, and 16 days Figure 1.5.4). There were also several major T-RF (of 112, 175, 339, and 340 bp) that were not dominant in the sample from HRT 4 days, but that were dominant in the samples from HRT 8, 12, and 16 days. Having a better understanding of the shifts in bacterial communities under different operational parameters, such as HRT, could allow researchers in the future to promote bacterial shifts to allow for greater production of biogas or other co-products.

1.5.5—Conclusions

S. dimorphus was investigated in this study for its ability to undergo AD. This microalgae was not suitable for the production of biomethane, due to its low C:N ratio of 5.96/1. Therefore, partial AD was used to produce carboxylate salts, which can be further processed downstream to carboxylic acid and ultimately biofuels such as ethanol, isopropanol, or gasoline. The experiments conducted in this project showed that the production of carboxylates was impacted by the HRT, with the highest productivity occurring at an HRT of 12 days. Thereafter, *S. dimorphus* was anaerobically digested in a 5 L working volume ASBR reactor at 12 days HRT to

showcase the production of carboxylate acids at a larger scale, closer to common industrial operational conditions. At this scale, a maximum total carboxylic acid concentration of 14.68±0.31 g/L liquid was achieved after 20 days, with steady state production occurring thereafter. The pathway to carboxylate salts provides another option for the AD of algal biomass residue, which may be more appropriate than the production of CH_4.

Further analysis with T-RFLP indicated shifts in the diversity and relative abundance of members of the bacterial community, in response to changes in HRT. Following up on these results, a clone library of the species present in the digester operated at 12 day HRT is being carried out. Results will provide more insight into the bacterial community that is dominating during the digestion process.

Pilot-project for High Solid AD

2.1— Obtain design parameters for green waste and biosolids from activated sludge for pilot testing and scale-up design

Liang Yu, Mahesh Bule, Shulin Chen

2.1.1—Abstract

Working in collaboration with the Washington Department of Ecology, WSU previously developed a new high solids anaerobic digester that continuously seeds the reactor with recycled effluent (high solids anaerobic digestion with recycling seeds (HSADRS)). For better integration into existing waste management strategies, this novel digester would most likely need to be able to accept green waste as well as food scraps. Unfortunately, green waste provides a challenge for AD due to its high fiber content and crystalline cellulose and lignin. Thus, an essential part of determining this novel digester's suitability for green wastes is determining whether pretreating green waste can make it more suited for AD. The authors tested the effect of various pretreatments had on grass waste and thereafter subjected these pretreated samples to AD to understand the effects of pretreatment on biogas production. Pretreatments of ground grass tested in this study included ozone, soaking aqueous ammonia (SA ammonia), ozone plus soaking aqueous ammonia (combination), and reduction of grass particle size. SA ammonia was the most effective pretreatment, enhancing the specific CH_4 yield of AD to 0.48 L CH_4/g VS, representing a 30% gain in CH_4 production over 10 days compared to untreated grass. Specific CH_4 yields of ground untreated grass, ozone, SA ammonia, combination, and reduced grass particle size were 0.4, 0.36, 0.48, 0.46, and 0.36 L CH_4/g VS, respectively.

2.1.2—Introduction

Previous research has indicated that the HSADRS system can achieve competitive efficiencies and productivities for digesting food scraps. However, proving that the system can competitively handle green waste would greatly enhance the system's potential for reaching commercial viability in urban settings, and its contribution to waste management efforts.

Grass clippings contain greater amounts of crystalline cellulose, hemicellulose, and lignin than food scraps. These crystalline structural materials are insoluble, and thus resistant to degradation. Layers of lignin linked to cellulose and hemicellulose also prevent enzymatic hydrolysis (aka hydrolysis) (Agbor et al., 2011; Frigon et al., 2012), a critical and rate-limiting step in the AD of lignocellulosic substrate. Hydrolysis (the first stage of decomposition in AD) converts cellulose into the simple sugar glucose, and is a critical and rate-limiting step in the AD of grass clippings and all lignocellulose feedstocks. Pretreatment is generally used to make these difficult feedstocks more digestible, allowing AD to be effectively carried out. Pretreatment processes are broadly classified under three categories including (1) mechanical/physical, (2) chemical and physico-chemical, and (3) biological. The literature reports that pretreatment can increase biogas production by 28.6–225.6% compared to digestion of untreated lignocellulosic wastes (Chandra

et al., 2012; He et al., 2009). Pretreatment can have one or more of the following impacts on substrates (Carlsson et al., 2012):

- Particle size reductions
- Solubilization
- Enhancement of biodegradability
- Formation of refractory compounds or
- Loss of organic material

For grass waste, the capacity to hydrolyze green grass determines the range of loading and operational capacities of the digester. Pretreatment strategies include altering or removing the biochemical barriers to digestion, such as the lignin seal, cellulose crystallinity, and degree of polymerization. It also includes treatments aimed at enhancing the attachment of cellulase enzymes to the surface of the grass. These enzymes enable a range of bacterial species to decompose cellulose. Enhancing the solubility of hemicellulose also makes cellulose decomposition easier for enzymes and microbes. Thus, the biodegradation and solubilization of crystalline cellulose and hemicellulose, as well as lignin, could lead to more efficient hydrolysis and ultimately improved biogas production.

Researchers at WSU applied four pretreatment methods to grass waste prior to AD. These methods included ozone pretreatment, SA ammonia, combination (ozone and SA ammonia), and grass particle size reduction. Ozone was aimed primarily at reducing the lignin barrier, while SA ammonia was aimed at increasing the cellulose digestibility. Opportunistically, post treatment NH_3 can be recycled from the AD process and reused.

2.1.3—Materials and methods

2.1.3.1— Characteristics of grass waste, inoculum, and feedstock

The grass waste, inoculum, and feedstock were analyzed for a variety of different characteristics which included TS, total volatile solids (TVS), ash, total COD, carbohydrate, protein, fat and total nitrogen (TN), and TP according to standard methods.

2.1.3.2—Feedstock and inoculums

Poa pratensis L. (Kentucky bluegrass) grass waste was mowed from the yard of a suburban home in Pullman, WA. The grass is a perennial native to North America, Europe, Asia, and Northern Africa. After mowing, the grass was dried in an oven for 24 hrs at 60°C, and ground to a particle size < 1 mm in a mill. Samples were then sieved through a 32–42 mesh Tyler Standard Screen Scale. Dry grass particle density was 136 kg/m^3. Except for reduced size particle treatments, experiments were conducted with grass waste particles of 0.354–0.5 mm.

Anaerobic sludge containing a microbial community of hydrolyzing, acid producing, acetate producing and CH_4^+ producing microbes was sampled from a digester located at the Pullman Wastewater Treatment Facility, WA. The sludge had a concentration of 17.1 g TS/L (11.7 g VS /L) and pH of 7.5. Active sludge was used to inoculate the grass waste, generating the feedstock used in the subsequent experiments, at a ratio of 1.0 g VS waste/g VS inoculum.

2.1.3.3— Ozone pretreatment procedure and pretreatment techniques

Ozone pretreatment was carried out on ground/sieved grass particles with a goal of achieving the maximum possible ozonolysis effect on lignin structure. Ozone was produced by a L11–L24

Ozone Generator (Pacific Ozone, California USA). Prior to treatment, 3 g of grass waste particles were adjusted to a moisture level of 90% w/w and placed into an enclosed stainless steel reactor. The ozonation reaction was performed under 5.3% w/w ozone concentration at a flow rate of 2 L/min for 10 mins (Bule et al., 2013), for a total ozone dose of 0.79 g O_3/g TS.

2.1.3.4—Soaking aqueous ammonia pretreatment procedure

SA ammonia pretreatment was used to degrade the crystalline structure of cellulose. This pretreatment was carried out using 28–30% (w/w) ammonium hydroxide solution (JTB-9721-03 ammonium hydroxide 28–30%) with a solid to liquid ratio of 2:10 at 50°C for 24 hrs with no agitation in 1000 ml screw cap Pyrex solution bottles (Gao et al., 2012). Afterwards, grass was washed twice thoroughly with distilled water to reach a neutral pH. The resulting cake was dried at 50°C.

2.1.3.5—Combined ozone and soaking aqueous ammonia pretreatment procedure

The combination treatment included both ozone and SA ammonia treatments. The combination treatment also aimed to overcome the relatively long (24 hr) time required for the SA ammonia treatment by combining ozone for 10 min and SA ammonia for 6 hrs. Ozone treatment was carried out as described in section 2.1.3.3, while SA ammonia treatment was carried out as described in section 2.1.3.4.

2.1.3.6—Reduced grass particle size

Research by others has suggested that grinding and milling more effectively reduce the particle size and cellulose crystallinity compared to chipping. This is probably as result of the shear forces generated during milling (Agbor et al., 2011). For this treatment, milled grass waste particles were sieved through a 42 mesh Tyler Standard Screen Scale to obtain grass waste particles with a size less than 0.354 mm.

2.1.3.7—Biomass composition, acid soluble and insoluble lignin analysis

For compositional analyses, grass samples were dried at 105°C in a hot air oven for 24 h. Carbohydrate content was determined according to the NREL standard laboratory analytical procedure for determination of structural carbohydrates in biomass (Sluiter et al., 2008). For two-stage acid hydrolysis, 0.3 g of sample was used. After initial hydrolysis at 37°C with 3 mL of 72% (w/w) sulfuric acid, the samples were diluted with distilled water to a total volume of 84 mL and autoclaved for 1 h in pressure tubes. Sugars in the aqueous phase were determined using ion chromatography (Dionex ICS-3000 with Dionex Pac PA20 column and CarboPac PA20 guard column). The samples were run for 60 min, and the column was flushed between runs with 100% 200 mM NaOH followed by de-ionized water. Sugar concentration was calculated by comparison to a standard sugar sample. All measurements were taken in triplicate. Acid soluble and insoluble lignin content was calculated according to NREL's Laboratory Analytical Procedure (Sluiter et al., 2008; Sluiter et al., 2005).

2.1.3.8—Enzymatic hydrolysis

Enzymatic hydrolysis of control and pretreated lawn grass was performed at 1% (w/v) solid loading in 0.05 M sodium citrate buffer (pH 4.8) containing 100 µl 2% sodium azide with 30 filter paper unit (FPU)/g of cellulase (Novozymes NS 50013) and 30 CBU/g of β-glycosidase (Novozymes NS 50010). The enzymatic reaction was performed at 50°C in an orbital incubator shaker (Gyromax 747) for 72 h. After 72 h of incubation, total released sugars were measured using DIONEX-IC.

2.1.3.9—Batch anaerobic digestion

Triplicate batch AD assays were performed for untreated ground grass and each of the experimental pretreatments. The batch experiments were conducted in 250 ml glass serum bottles with a liquid volume of 120 mL, and at 37±1°C in a thermostatic room. For determination of VFA accumulation, 10 mM Sodium 2-bromoethanesulfonate ($C_2H_4BrNaO_3S$, Sigma-Aldrich Corporation, USA) was used to inhibit methanogenic bacteria (Chidthaisong & Conrad, 2000). Biomethane production was evaluated with a biochemical methane potential assay (Ma et al., 2013a), and measured with a respirometer (Challenge technology AER-200 respirometer, Springdale, AR). Sodium hydroxide was used to absorb CO_2 and H_2S, so that only CH_4 production was measured.

2.1.3.10—Volatile fatty acid analysis

The concentrations of VFA, including acetate, propionate, butyrate, i-butyrate, valerate, and caporate in the effluent were determined daily by a GC (Shimadzu Corp., Japan, Model GC-2014) equipped with a flame ionization detector and a 30 m × 0.25 mm inner diameter × 0.25 μm film thickness capillary column (HP-INNOWax, Agilent Technologies, Palo Alto, CA). The liquor samples were first centrifuged at 12,000 rpm for 5 min, and were then acidified with formic acid, filtered through a 0.22 mm membrane, and measured for free acids. The temperatures of the injector and detector were 250 and 300°C, respectively. The initial temperature of oven was 70°C for 3 min. This was followed by an increase of 15°C/min to a final temperature of 230°C for 3 min. The carrier gas was N with a flow rate of 0.93 mL/min.

2.1.3.11—Additional analyses

The total COD, soluble COD, TP, total ortho-phosphorus (OP), TS and VS were determined according to standard methods (Eaton et al., 2005). The pH was measured daily using a Fisher Scientific AB15 pH meter. Total organic carbon (TOC) and inorganic carbon (IC) were analyzed using a SHIMADZU TOC-5000. Gas composition was analyzed using a Varian CP-3800 GC. Total Kjeldahl nitrogen (TKN) was measured using a 2300 Kjeltec Analyzer Unit (Tecator, Perstorp Analytical).

2.1.4—Results and discussion

2.1.4.1—Characteristics of grass waste, inoculum, and feedstock

Table 2.1.1 shows the determined characteristics of grass waste, inoculum, and feedstock used in these experiments.

Table 2.1.1: Characteristics of grass waste, inoculum, and feedstock

Parameters	Unit	Value
Grass waste particles		
TS	% (w/w)	96.3
TVS	% (w/w)	68.1
Ash	% (w/w)	28.1
Inoculum (active sludge)		
TS	% (w/w)	1.54
TVS	% (w/w)	1.18
Ash	% (w/w)	0.36
Feedstock (grass waste plus active sludge)		
TS	% (w/w)	2.5
TVS	% (w/w)	1.7
Ash	% (w/w)	0.81
Total COD	g/L	22.2
Carbohydrate	g/L	7.9
Protein	g/L	5.6
Fat	g/L	-
TN	g/L	0.8
TP	g/L	0.3

2.1.4.2—Effect of different pretreatments on grass waste composition

Table 2.1.2 shows the effect of the different pretreatments on composition of grass waste samples. The composition of reduced particle size was not determined, as additional grinding was assumed not to alter the composition of the waste. The sugar concentration of grass waste particles decreased only slightly after ozone pretreatment (30.55±0.46 to 28.58±0.20) in line with others' findings by Sun and Chen (2002). Ben-Ghedalia & Miron (1981) and Binder et al. (1980) found that ozone selectively degrades lignin and does not attack sugars. They reported loss of cellulose after ozone pretreatment to be below 5% when working at low pH values. Meanwhile, the acid soluble lignin content of grass waste increased from 3.73% to 4.18% after ozone pretreatment, while the insoluble lignin content decreased from 16.66 % to 14.21%. Together, these changes in acid soluble and insoluble lignin content indicate fragmentation of the lignin polymer. Ash decreased only slightly with ozone pretreatment, to 26.43%.

In contrast, overall sugar content of SA ammonia and combination pretreated grass increased to 46.55±0.05 and 46.73±0.54, respectively (Table 2.1.2). This amounts to roughly a 50% increase in total sugars after treatment, indicating successful pretreatment. The change could be due to removal of ash, extractives and conversion of insoluble lignin into soluble lignin. Both SA ammonia and combination pretreatments decreased both acid insoluble and acid soluble lignin content, with combination pretreatment most effectively lowering acid insoluble lignin content to 11.13%. Generally, the decreases in acid insoluble lignin are positive indications for pretreatment, while decreases in acid soluble lignin are not beneficial. SA ammonia and combination pretreatment also decreased the ash value, from 27.15% to 13% and 11.29% respectively. This decrease in ash is beneficial for downstream treatment, as it generally leads to easier digestion and handling and lower costs for equipment maintenance.

Table 2.1.2: Compositional analysis of untreated and pretreated grass

Components	Control grass (% w/w)	Ozone treated grass (% w/w)	SA ammonia treated grass (% w/w)	Combination treated grass (% w/w)
Sugars				
Arabinose	2.90 ± 0.08	1.90 ± 0.01	3.70 ± 0.01	4.35 ± 0.36
Galactose	1.23 ± 0.02	0.89 ± 0.01	1.28 ± 0.01	0.83 ± 0.02
Glucose	16.91 ± 1.07	16.14 ± 0.11	30.85 ± 0.02	30.96 ± 0.13
Xylose	9.52 ± 0.50	9.65 ± 0.06	10.73 ± 0.04	10.59 ± 0.04
Total	30.55 ± 0.46	28.58 ± 0.20	46.55 ± 0.05	46.73 ± 0.54
Lignin				
Acid insoluble	16.66 ± 0.57	14.21 ± 0.13	13.41 ± 0.86	11.13 ± 1.01
Acid soluble	3.73 ± 0.09	4.81 ± 0.72	1.89 ± 0.34	2.51 ± 0.47
Extractives				
Ethanol	5.83 ± 0.21	ND	ND	ND
Water	4.18 ± 0.39	ND	ND	ND
Total proteins	1.52 ± 0.002	ND	ND	ND
Ash	27.15 ± 1.27	26.43 ± 0.74	13.00 ±0.38	11.29 ±0.51

ND: Not determined

2.1.4.3—Effect of grass pretreatment on sugar recovery

Recoverable sugars are an important indicator of the system's ability to produce VFAs, and subsequently CH_4. Table 2.1.3 reports on sugar recovery from grass samples with and without pretreatment. As expected, cellulolytic enzymes were unable to hydrolyze sugars from untreated grass samples. Ozone pretreatment improved sugar recovery up to 48.50%. This yield is comparable to previous reports on similar substrates; for example, a longer 2.5 hr ozone pretreatment of wheat straw resulted in 88.6% sugar recovery (Garcia-Cubero et al., 2009). The relatively long 24 hr SA ammonia pretreatment resulted in 86.71% sugar recovery. The combination pretreatment resulted in 89.63% sugar recovery, similar to the SA ammonia treatment despite the shorter treatment time (10 mins of ozone followed by 6 hrs of SA ammonia treatment in the combination pretreatment).

Table 2.1.3: Sugar recovery of lawn grass sample after different pretreatments

Sample	**Sugar recovery**
Untreated grass	0.0 ± 0.00
Ozone treated grass	48.50 ± 2.17
SA ammonia treated grass	86.71 ± 0.20
Combination treated grass	89.63 ± 2.09

2.1.4.4—Effect of grass pretreatment on volatile fatty acid production

During AD, VFA is formed during hydrolysis and then rapidly converted to CH_4 by methanogenic bacteria. In these experiments, with methanogenesis blocked by $C_2H_4BrNaO_3S$, VFA accumulation indicates that acidogenesis and acetogenesis occurred. Figure 2.1.1 (A) shows the effect of grass waste pretreatment on the total VFA concentration, with a sharp

increase of over the first several days, but little production after that point. The highest production was observed from the SA ammonia and combination pretreatments. Statistically, there was no significant difference ($P > 0.05$) between the SA ammonia and combination pretreatments. The production from the SA ammonia pretreatment was 53% higher than the control grass waste over 10 days and 41% higher over 30 days. Thus, the effect of SA ammonia pretreatment on production decreased with greater time in the digester. The VFA production for ozone pretreatment was also enhanced compared to the control grass, by 28%.

In contrast, reducing grass waste particle size did not improve VFA production in this study, as confirmed by a one-way ANOVA test ($P > 0.05$). Other researchers have also found that further reduction of biomass particle size below 40 mesh (0.400 mm) had little effect on the rates and yields of biomass hydrolysis (Chang et al., 1997).

The effect of grass waste pretreatment on specific VFA's (propionic and acetic acid) concentration is shown in Figure 2.1.1 (B) and (C), respectively. Results show generally the same pattern as for total, with the bulk of production occurring over the first several days. Marchaim and Krause (1993) have suggested that the propionic acid to acetic acid ratio can be used as an indicator of digester imbalance, with propionic acid to acetic acid ratio greater than 1.4:1 indicating impending digester failure (Xie et al., 2011). In this study, the propionic acid to acetic acid ratio was less than 1.0 for all treatments, suggesting a well-balanced digester.

Ozone increased propionic acid production by roughly 100%, while SA ammonia and combination pretreatment increased propionic acid production by about 200% compared to untreated grass. In contrast, acetic acid production was not greatly affected by the ozone, SA ammonia or combination pretreatment. Propionic acid, which is currently produced predominantly by petrochemical methods (Liang et al. 2012) is a very important chemical widely used in the production of cellulose plastics, herbicides, perfumes, food, and feed preservative (Dishisha et al., 2012). Our results indicate that the possibility of producing propionic acid through SA ammonia and combination pretreatment may merit further investigation.

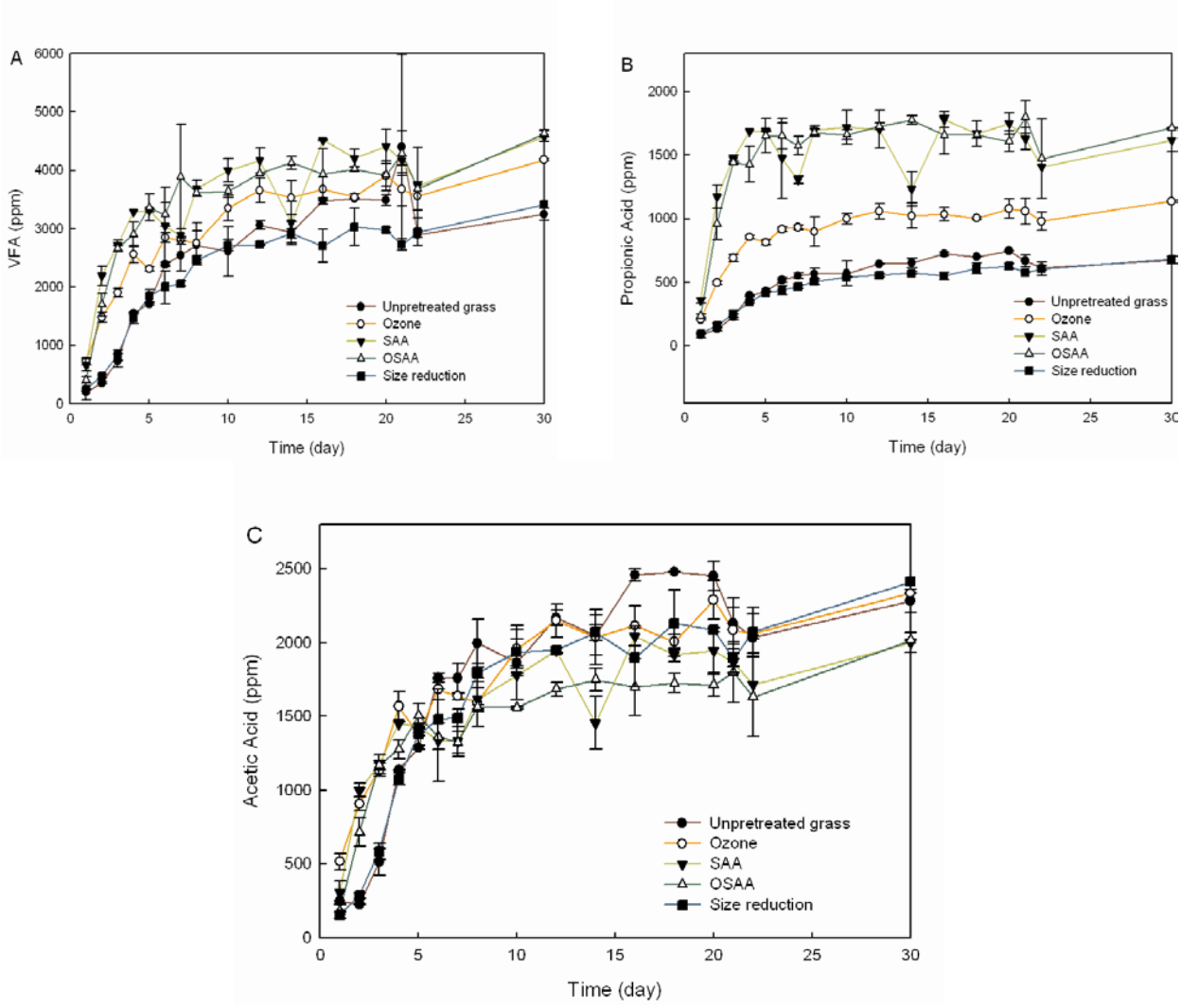

Figure 2.1.1: Changes in (A) total VFA, (B) propionic acid, and (C) acetic acid with time for different pretreatments

2.1.4.5—Effect of grass pretreatment on methane production

Figure 2.1.2 shows cumulative CH_4 production for the control and each pretreatment during the 30-day batch AD study. For all treatments, greater than 99% of CH_4 was produced in the first 10 days of digestion. Several factors indicated that AD was occurring stably: the grass wastes had low VS (1.73%), pH was maintained at about 7.5, and samples taken every two days confirmed that VFA was not accumulating.

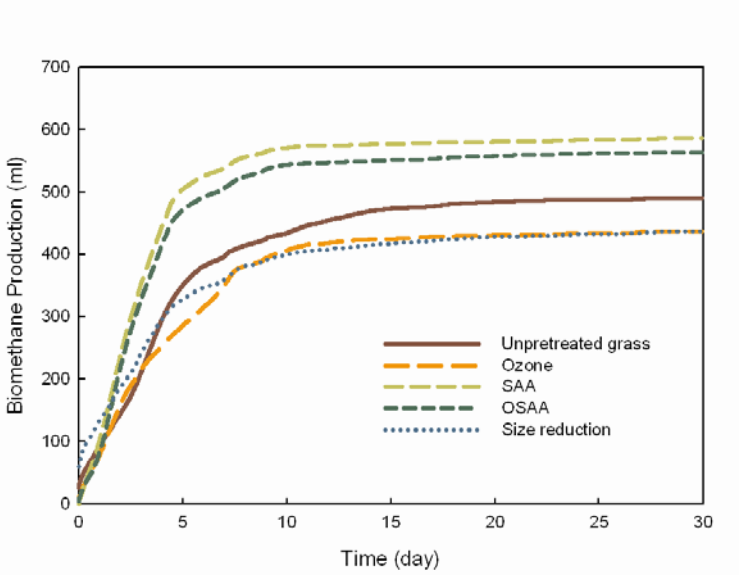

Figure 2.1.2: Cumulative CH_4 production of untreated and pretreated lawn grass during 30-day batch AD

As shown in Figure 2.1.2, the highest CH_4 production was obtained by SA ammonia pretreatment of grass waste and the highest specific CH_4 yield was 0.48 L CH_4/g VS. This was about 31% more than the specific CH_4 yield of untreated grass over 10 days (0.4 L CH_4/g VS). The specific CH_4 yields of ozone, combination and size reduction were 0.36, 0.46, and 0.36 L CH_4/g VS over 30 days, respectively. With additional time, the control grass sample continued to generate small amounts of CH_4, so that the difference in specific CH_4 yield between SA ammonia and untreated grass fell to 19% over the full 30 days.

The ozone pretreatment decreased CH_4 productivity compared to no treatment, despite the fact that sugar recovery (Table 2.1.3) and VFA production (Figure 2.1.1) had improved. One possible explanation for these seemingly contradictory results is that ozone was overdosed. The ozone dose used in this study, 0.79 g O_3/g TS, was much higher than the maximum limit that others have suggested of 0.15 g O_3/g TS for use prior to AD (Bougrier et al., 2006). While Bougrier et al. (2006) suggested several explanations for this limit, the one most supported by the results in this study is that ozone treatment at high levels prompted the formation of compounds that may inhibit methanogenic bacteria. Thus, while sugars and VFA formed appropriately, VFA could not be converted to CH_4.

Although SA ammonia and combination treatments both increased CH_4 production compared to the control, there are some indications that the ozone treatment in combination caused a small amount of inhibition of methanogenic bacteria. Though not statistically significant, the combination pretreatment resulted in slightly higher VFA production, and yet had slightly lower CH_4 production than the SA ammonia pretreatment. The CH_4 production from SA ammonia pretreatment was 5% higher than that from combination pretreatment over 10 days and 4% higher over 30 days.

Smaller grass particles actually lowered CH_4 productivity. Methane production for smaller particles was less than the control by 7% and 12% over 10 and 30 days, respectively. One reason for this is that the smaller reduced-size grass had higher ash content (33.66% dry) compared to 27.15% (dry) in the control grass. This result also likely reflects the fact that there was no positive impact of reduced particle size on VFA accumulation (Figure 2.1.1).

2.1.4.6—Comparison of volatile fatty acid products before and after pretreatment

To further explore the digestion process and the impacts of SA ammonia pretreatment, concentrations of various fatty acids were compared for the SA ammonia and untreated grass waste at 2 days and 30 days (Figure 2.1.3 (A) and (B)). Highly significant increases in VFA were observed in SA ammonia pretreated grass waste after 2 days. The differences decreased with time. By day 30, the acetic acid concentration of untreated grass waste was higher than that of SA ammonia pretreatment. This is significant because fatty acids can be converted to CH_4, and may also be produced as a final byproduct of the AD as a value-added product. Figure 2.1.3 (B) also indicates that the types of lower molecular weight fatty acids were produced early during digestion and higher molecular weight acids were produced with more time in the digester. It can be inferred that a short fermentation time would be better when SA ammonia pretreatment is being used for CH_4 production. In contrast, if the process is operating over a longer period of time, especially using SA ammonia pretreatment, value-added products could be targeted instead of, or in addition to, CH_4 production.

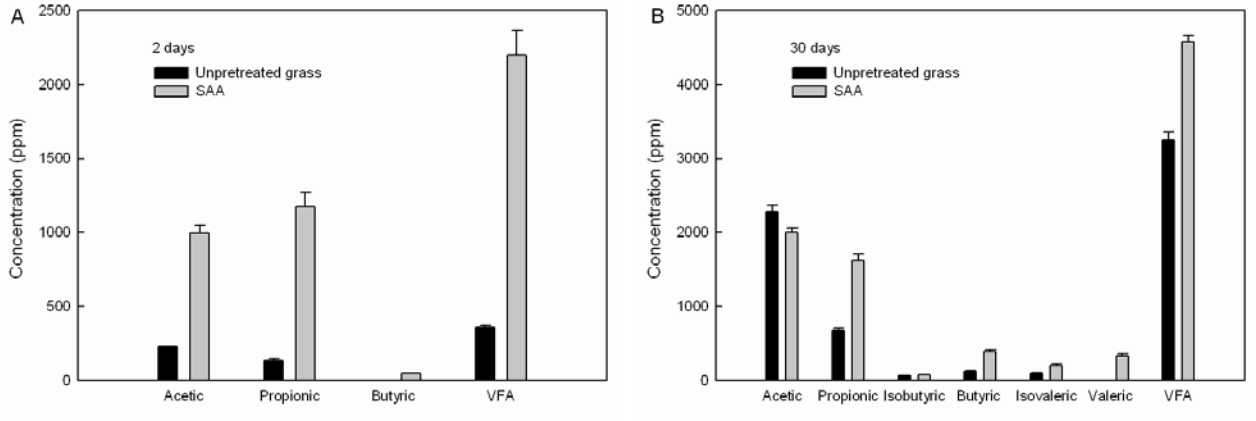

Figure 2.1.3: Comparison of VFA production with SA ammonia pretreatment and without pretreatment at (A) 2 days and (B) 30 days; there was no isobutyric, isovaleric, or valeric acid at 2 days

2.1.4.7—Comparison of volatile fatty acid production of grass waste to volatile fatty acid production of wheat straw

Wheat straw is a lignocellulosic feedstock frequently used to study the production of renewable fuels and chemicals. Thus, to facilitate comparison of our results with the available literature, we compared the VFA production from this grass clipping study to wheat straw with the same pretreatments. Wheat straw pretreatments were completed as part of separate studies (Bule et al., 2013; Gao et al., 2012). Figure 2.1.4 shows VFA production for grass waste and wheat straw at 10 days (A) and 30 days (B). At 10 days, pretreatment resulted in more

significant increases in the fatty acid concentration from grass waste than from wheat straw. The differences in fatty acid production between pretreated grass waste and wheat straw decreased by 30 days. This is likely due to a higher lignin content in the wheat straw compared to grass waste. The high lignin content blocks the sugar release (and thus also fatty acid production, which relies on sugar release) at the beginning. As time proceeds, the lignin matrix can be gradually broken by anaerobic microorganisms releasing more sugar from wheat straw.

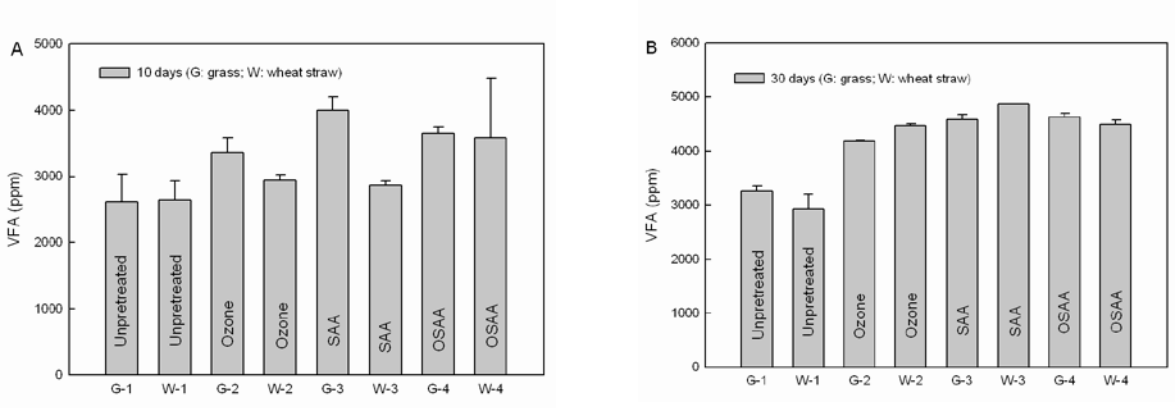

Figure 2.1.4: VFA production for untreated and pretreated grass and wheat straw at (A) 10 days and (B) 30 days

2.1.4.8—Comparison of total solids and volatile solids reductions in volatile fatty acid and methane production

The pretreated wastes were then digested in bench-scale reactors to determine the effects TS/VS had on VFA and CH_4 production. Figure 2.1.5 shows TS (A) and VS (B) concentrations at 30 days for grass waste digested. In some cases methanogenesis (the final step of AD) was inhibited (G), while in others it was not inhibited (G'). When methanogenesis is inhibited, the system is being operated to produce VFAs. When methanogenesis is not inhibited, VFAs are converted rapidly to CH_4. The results show that more TS and VS reduction occurred during CH_4 production than when CH_4 production was inhibited using $C_2H_4BrNaO_3S$. For all treatments including the control (untreated) grass, more TS and VS reduction occurred when CH_4 was produced.

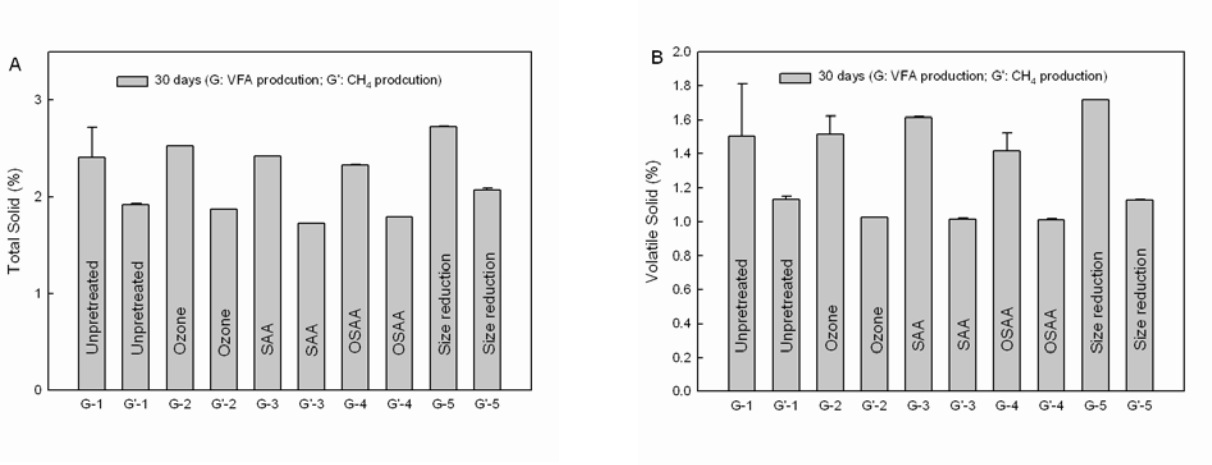

Figure 2.1.5: Comparison of (A) TS and (B) VS reductions in VFA and CH_4 production

2.1.4.9—Effect of increasing volatile solids on volatile fatty acid production in untreated grass

To further investigate the impact of varying VS concentration on VFA production, untreated grass waste was digested for 30 days at various VS concentrations, with 10 mM $C_2H_4BrNaO_3S$ to inhibit methanogenic bacteria. Figure 2.1.6 shows the total fatty acids (A), and specific acetic acid (B) and propionic acid (C) at different VS concentrations at 10 and 30 days. At 10 days, a steep increase in VFA production occurred as VS increased from 2.82 to 3.40. At 30 days, the increase in VFA production was linear with increased VS. Thus, early in the digestion process, there is a critical value for VS over which VFA production can be significantly increased. Comparing VFA production found here in Figure 2.1.6 (A) to the VFA production in Figure 2.1.1 (A), higher VFA production from SA ammonia pretreatment is equivalent to the productivity resulting from a 30% increase in VS.

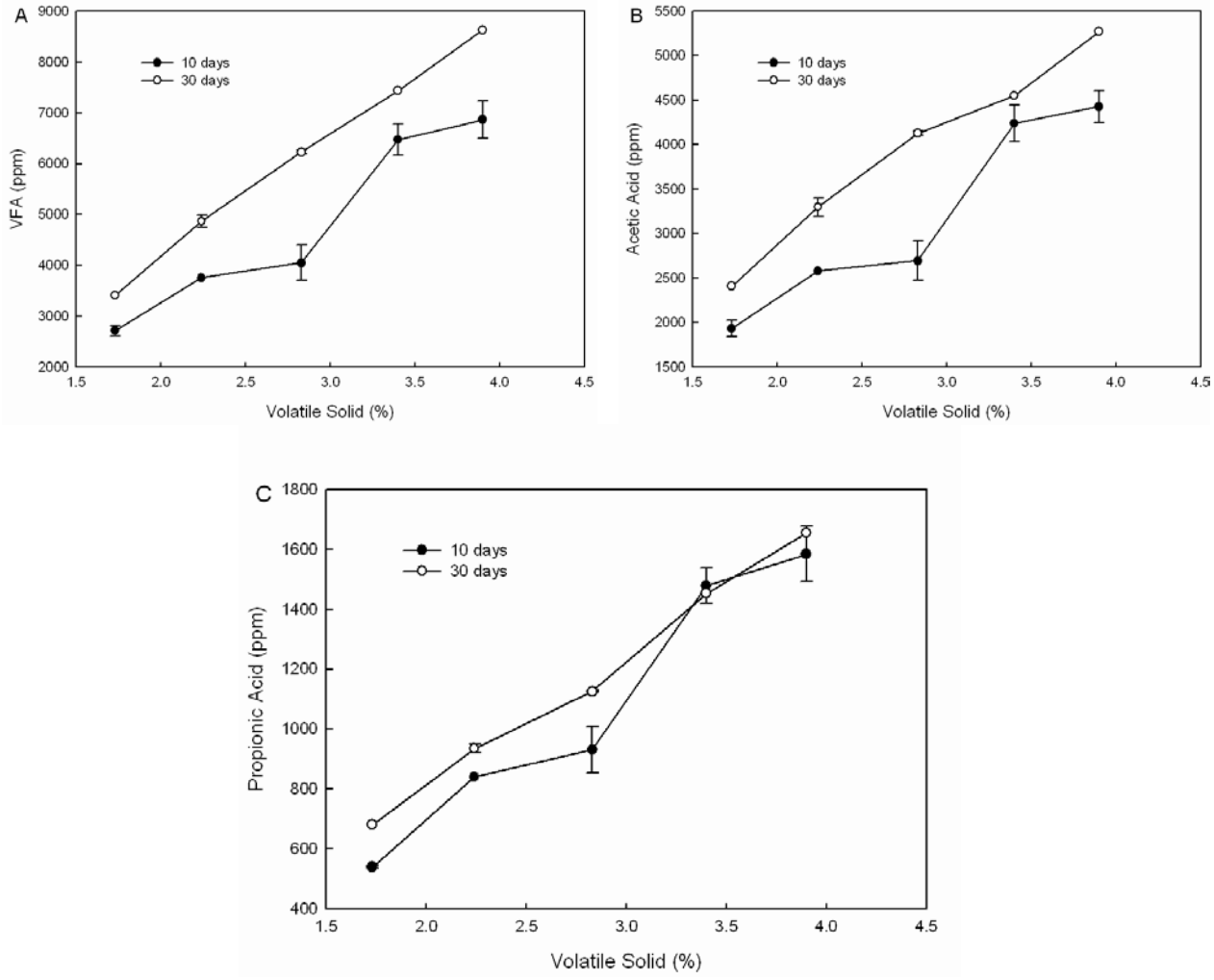

Figure 2.1.6: Effect of VS on (A) total VFA, (B) acetic acid and (C) propionic acid production

2.1.4.10—Effect of increasing total solids and volatile solids on methane production in untreated grass

Following up on the study of VFA production from untreated grass (described in Section 2.1.4.9), CH_4 production was studied in untreated grass of various TS and VS content in bench-scale batch tests. Methane production increased sharply over the first 10 days, and then leveled off (Figure 2.1.7), with higher rates of CH_4 production from grass waste with higher concentrations of TS and VS. Corresponding to the VFA production results shown in Figure 2.1.6, a steep increase of CH_4 production was found as VS increased from 2.82 to 3.40. These results support the previous conclusion that there is a critical TS (and VS) value for VFA and CH_4 production.

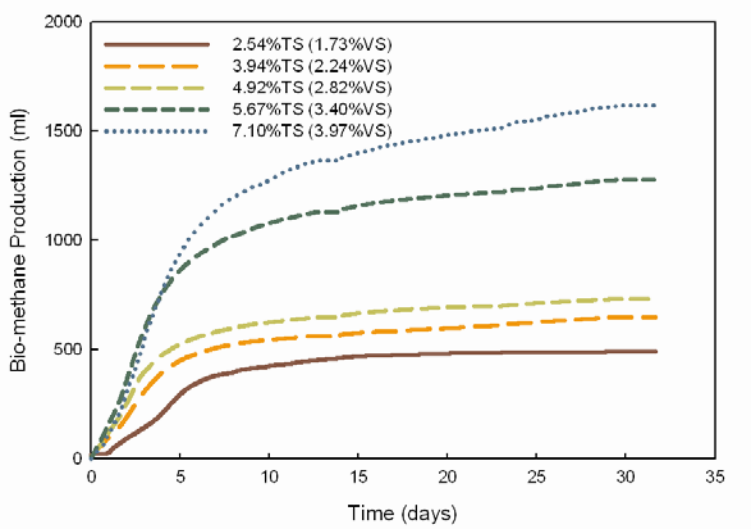

Figure 2.1.7: Effect of TS/VS on CH_4 production

This study also indicates that green waste acted very differently than food scraps during the bench-scale digestion. Unlike food scraps, green waste could produce CH_4 stably in one stage at higher TS, while food scraps normally required multiple digestion steps to successfully produce CH_4. However, as can be seen in Table 2.2.1, different feedstocks have varying physical properties. In the case of food scraps, the properties of high protein and fats make it easily degradable. Unfortunately, its application for AD is limited by its TS concentration since even at relatively low TS of 1% the pH of the system drops below 6 and the digester fails. However, green waste digestion is capable of maintaining a stable pH of around 7 at a much higher TS (7.10%, see Figure 2.1.7) with no failure in AD; thus, green waste is a suitable feedstock for high solids anaerobic digestion (HSAD).

The specific yields of CH_4 from green waste digestion decreased with an increase of TS and VS. The specific CH_4 yields of green waste with 2.54 %TS, 3.94 %TS, 4.92 %TS, 5.67 %TS and 7.10 %TS were 402.5, 261.8, 194.3, 250.6, and 249.6 ml CH_4/g VS, respectively. This suggests that there is a trade-off that needs to be considered when increasing CH_4 productivity by increasing TS and VS or by using pretreatment.

2.1.5—Conclusions

Batch AD assays were carried out for ground grass, and pretreatments including ozone, SA ammonia, combination, and reduction of grass particle size. SA ammonia was the most effective pretreatment, enhancing the specific CH_4 yield of AD to 0.48 L CH_4/g VS, representing a 31% higher CH_4 production over 10 days compared to grass that was not pretreated (0.40 L CH_4/g VS). There were indications that the pretreatments that included ozone (ozone and combination) inhibited CH_4 production, despite very positive impacts on VFA production. From this study, the authors suggest SA ammonia is the best pretreatment tested. In addition to its performance, this pretreatment could integrate with other technologies developed at WSU including NR since the NH_3^+ can be recycled and used in the NR process for the production of soil amendments. Another positive attribute is that the SA ammonia proccess does not require any special handling, making it easier to integrate than the combination pretreatment process. However, a further technoeconomical analysis will be required to develop this integrated pretreatment process.

2.2—Computational fluid dynamics and kinetics

Liang Yu, Shulin Chen

2.2.1—Abstract

A combination of computational fluid dynamics (CFD) and kinetics modeling was used to model mixing within a HSAD tank digester. This newly developed model represents a scaled-up HSAD that will be broadly applicable to a range of scale-up efforts, including the new HSADRS developed by researchers at WSU. To support scale-up efforts, the model is available to be used in collaboration with specific commercial partners, using their proposed specifications.

In this project, the model was developed and validated using experimental data. To illustrate potential uses, the model was then used to explore issues related to the flow characteristics of manure at a range of TS, mixed using an A-310 impeller. Two different TS concentrations were investigated, as TS concentration of waste is an important parameter in AD. TS can change the fluid dynamics in the digester, and subsequently influence the pH, temperature uniformity and effectiveness of the microorganisms in the decomposition process.

In the modeled system, adequate flow velocity and good overall CH_4^+ production were predicted for low TS concentrations (TS < 5%). In contrast, flow velocities were low throughout the slurry with higher TS concentration (TS = 10%), and CH_4^+ production likewise was low. Discharge flow numbers (N_q) indicated typical, if not slightly high, pumping capacity of the impeller at TS < 5%. (Modeled N_q stabilized at 0.76 with consistent downward flow, compared to experimental data were in the range of 0.55–0.73 under turbulent conditions.) However, the predicted fluid dynamics in the digester with 10% TS indicated that upward flow dominated at low Reynolds (Re) numbers. With increases in the Re, the impeller pumping direction was gradually switched to downward. This presented further indication of non-ideal mixing at TS = 10%.

When the impact of change in TS on power number (N_p) and N_q was explored across a range of TS from 2% to 12%, the response of N_p to TS was nearly linear, at least in this range, indicating that higher power input was required to agitate digesters with higher solids. Meanwhile, a nearly exponential decay was observed in the relationship between N_q and TS, indicating that the pumping capacity of impeller A-310 was impaired by higher TS.

Shear stress and shear rates were also predicted, to explore potential negative impacts of mixing on methanogenic microbes. The calculated results suggest a small increase in shear stress and shear rate with increasing Re up to a threshold of 10000 in < 5% TS slurry and 100 in 10% TS slurry. As Re increased beyond these two thresholds, there was a sharp increase in shear stress and shear rate. In addition, the maximum impeller wall shear stress and shear rate of the 10% TS digester were much higher than that of the < 5% TS digester due to the high viscosity. This points to concerns for the digester with 10% TS, though it is possible that enzymes and bacteria could live within lower shear zones away from the impeller. If this occurred, operation might successfully continue despite the higher shear stress and shear rate.

2.2.2—Introduction

AD is a complex system of biochemical and physical processes (Appels et al., 2008). Due to the complexity of the process, it has traditionally been treated as a black box system, with optimization based on experience or trial and error. As AD optimization experiments are expensive and time consuming, modeling can provide a useful tool for understanding and optimizing the AD process. Reliable models are particularly useful for revealing non-linear behaviors and quantifying performance under alternative operational setups, both of which are important for optimizing the economic and technical performance of full-scale plants (Lidholm & Ossiansson, 2008; Tomei et al., 2009). Most previous research in this area has focused on process kinetics, which is based on an understanding of the biochemistry and microbiology of the AD process (Angelidaki et al., 1999; Batstone et al., 2006b; Lubken et al., 2010; Pavlostathis & Giraldogomez, 1991; Saravanan & Sreekrishnan, 2006; Tomei et al., 2009). Process kinetics quantitatively describes waste utilization rates, along with the operational and environmental factors affecting these rates. The first dynamic mathematical model was described by Andrews (1968) and considered only the acetoclastic methanogenic process step, thus assuming that hydrolysis and acidification were not rate-limiting (Andrews, 1968; Lubken et al., 2010). Following this, the acetoclastic methanogenesis is assumed by many authors as the rate-limiting step, and the process is described in most studies by Monod kinetics instead of Haldane kinetics using both the dissociated and undissociated acetic acid as substrate (Lubken et al., 2010). Many newer models incorporate hydrolysis as a second rate-limiting step, especially for lignocellulosic biomass (Hobson, 1987; Noike et al., 1985).

The models described so far do not fully account for the complex composition of natural feedstocks. Instead, the particulate substrate is either assumed to be synthetic (generally glucose), or is considered to be homogenous. The necessity of a more realistic and generally applicable model was recognized by Angelidaki et al. (1999), who developed a comprehensive model that incorporated co-digestion and was calibrated and validated for different wastes. To consolidate the variety of different mathematical models describing the AD process, the IWA Task Group on Mathematical Modeling of AD Processes was founded in 1997. The result of the group's work was the Anaerobic Digestion Model No. 1 (ADM1), which referred to

Angelidaki's work and represents the first generalized model of AD (Batstone et al., 2006b; Montiel-Escobar et al., 2012).

With the advances in computer performance over the last decades, many researchers have turned to CFD, which numerically simulates fluid motion (Paul et al., 2004). These models have not previously incorporated process kinetics, but are useful to predict flow fields and improve mixing performance in anaerobic digesters (Karama et al., 1999; Wood et al., 1995). In the past decade, CFD has been used to simulate the flow behavior of wastewater treatment units including wastewater ponds (Shilton et al., 2008), lagoons (Pougatch et al., 2007) and tanks (Terashima et al., 2009). These approaches most often use the single phase Euler approach to describe the flow behavior in digesters, and the finite volume numerical method to solve their problems (Yu, 2012).

CFD modeling studies can be less expensive than direct experiments, and are particularly helpful when it is difficult to experimentally detect the mixing parameters. Several recent examples of CFD application to AD in tanks illustrate how modeling results can be helpful during scale-up. Wu and Chen (2008) took slurry circulation into account to obtain flow fields in lab-scale, scale-up, and pilot-scale anaerobic digesters and concluded that power input per unit digester volume increases logarithmically for the scale-up digesters. Hoffmann et al. (2008) simulated mechanical mixing only in a low solid digester (TS < 5%) treating animal manure. Yu et al. (2011) extended the simulation to a high solid digester (TS > 10%) treating animal manure. In each of these examples, CFD and kinetics were used as a design tool for modifying anaerobic digesters and processes to optimize operating conditions for specific feedstocks.

In this study, AD kinetics were incorporated into a CFD model to better understand the effect of mixing on biomethane production, and to provide support for design, optimization and scale-up of HSAD systems (including future efforts to scale up the HSADRS system). Since flow field and power consumption are greatly affected by substrates' rheological properties (its ability to deform and flow), a mathematical model with non-Newtonian fluid theory was created to describe mixing. The difficulty of making a combined (kinetics and CFD) model necessitated that more simple kinetics modeling be used in place of the more complex kinetics used in ADM1, with the result that this model is best used to describe flow, and supplemented with ADM1-based modeling for information on mass transfer and biochemical reactions (see section 2.3).

In addition to the practical applications of this model for supporting scale-up efforts for the HSADRS system and other HSAD systems, this work by creating a combined CFD and kinetics model sets the stage for future efforts to incorporate more elaborate kinetics modeling, working towards one integrated model that can be used to describe flow, mass transfer, and biochemical reactions.

2.2.3—Materials and methods

2.2.3.1—System

Figure 2.2.1 is a 3D illustration of the modeled reactor, mixed with an A-310 impeller. The impeller is located at the bottom of the reactor where it can provide mixing throughout the reactor. The A-310 impeller consists of three blades connected to a shaft. Table 2.2.1 indicates

the characteristics of the model and A-301 impeller. The reactor diameter and height were 152 and 370 mm, respectively.

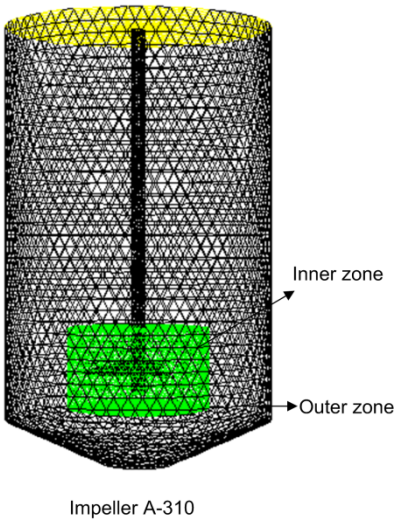

Figure 2.2.1: Geometric representation of the digester and A-310 impeller

Table 2.2.1: Measurements of the modeled tank and A-310 impeller

Reactor diameter (mm)	152
Reactor height (mm)	370
Liquid height (mm)	194
Cone height (mm)	26
Cone angle (deg)	25
Impeller diameter (mm)	62

2.2.3.2—Computational fluid dynamics mixing model

Mechanical mixing of anaerobic digesters is most often accomplished with rotational impellers. For modeling purposes, this requires that the model be divided into multiple fluid cell zones, with interface boundaries between zones. The inner zone includes the impellers, which generate the motion of fluid in digesters. The outer zone contains no moving parts, and is passively driven by the impeller. Zones, which contain moving components, are solved with moving reference frame equations, whereas the stationary zones are solved using stationary frame equations. A steady-state modeling method called the Multiple Reference Frame (MRF) (Luo et al., 1994) was developed to solve this class of problem.

The high level of TS in liquid manure and waste slurries has a significant impact on the fluid properties, and significantly alter the flow characteristics in anaerobic digesters. Turbulent flow is suppressed by high viscosity, and laminar flow prevails in HSAD systems. The turbulence model is applicable when TS < 12.1%; when TS > 12.1%, the laminar flow is relevant.

The CFD governing equations are provided in the FLUENT documentation (NA, 2006). The continuity equations are defined as:

$$\nabla\left(\rho\vec{v}\right)=0 \qquad 2.2.1$$

where ρ is the density of liquid manure, and v is fluid velocity in tensor form.

The momentum equations are expressed as:

$$\nabla\left(\rho\vec{v}\vec{v}\right)=-\nabla p+\nabla\left(\bar{\bar{\tau}}\right)+\rho\vec{g}+\vec{F} \qquad 2.2.2$$

where p is static pressure, $\overline{\overline{\tau}}$ is stress tensor (described below), ρg is gravitational force and F is Coriolis and centripetal force.

The stress tensor, $\overline{\overline{\tau}}$, is expressed by:

$$\overline{\overline{\tau}} = \mu\left[\left(\nabla\vec{v} + \nabla\vec{v}^{\mathrm{T}}\right) - \frac{2}{3}\nabla\cdot\vec{v}I\right] \quad 2.2.3$$

where μ is molecular viscosity.

The turbulence models take the form of the Standard κ-ε Model as follows:

$$\frac{\partial}{\partial t}(\rho\kappa) + \frac{\partial}{\partial x_i}(\rho\kappa u_i) = \frac{\partial}{\partial x_j}\left[\left(\mu + \frac{\mu_t}{\sigma_\kappa}\right)\frac{\partial\kappa}{\partial x_j}\right] + G_\kappa + G_b - \rho\varepsilon \quad 2.2.4$$

And

$$\frac{\partial}{\partial t}(\rho\varepsilon) + \frac{\partial}{\partial x_i}(\rho\varepsilon u_i) = \frac{\partial}{\partial x_j}\left[\left(\mu + \frac{\mu_t}{\sigma_\varepsilon}\right)\frac{\partial\varepsilon}{\partial x_j}\right] + C_{1\varepsilon}\frac{\varepsilon}{\kappa}\left(G_\kappa + C_{3\varepsilon}G_b\right) - C_{2\varepsilon}\rho\frac{\varepsilon^2}{\kappa} \quad 2.2.5$$

In these equations, G_κ represents the generation of turbulent kinetic energy due to the mean velocity gradient, G_b the generation of turbulent kinetic energy due to buoyancy, $C_{1\varepsilon}$, $C_{2\varepsilon}$, and $C_{3\varepsilon}$ the constants; and σ_κ and σ_ε are turbulent Prandtl (Pr) numbers for κ and ε, respectively.

The eddy or turbulent viscosity μ_t is computed by combining κ and ε as follows:

$$\mu_t = \rho C_\mu \frac{\kappa^2}{\varepsilon} \quad 2.2.6$$

where C_μ is constant. The model constants: $C_{1\varepsilon}$, $C_{2\varepsilon}$, $C_{3\varepsilon}$, σ_κ and σ_ε have the following empirical values: $C_{1\varepsilon}$=1.44, $C_{2\varepsilon}$=1.92, C_μ=0.09, σ_κ=1.0 and σ_ε=1.3

Liquid manure is described by the following non-Newtonian Fluid Model:

$$\tau_{ij} = \eta\left(\frac{\partial u_i}{\partial x_j} + \frac{\partial u_j}{\partial x_i}\right) \quad 2.2.7$$

where η is non-Newtonian viscosity, which is only considered to be a function of the shear rate, γ.

The viscosity in the non-Newtonian power law is expressed as:

$$\eta = K\gamma^{n-1}e^{T_0/T} \quad 2.2.8$$

where K is the consistency coefficient (Pa s^n), γ is the shear rate (s^{-1}), n is the power-law index that determines the class of fluid (i.e., n < 1 for pseudo-plastics, n = 1 for Newtonian fluid, and n>1 for dilatant fluid), T_0 is the reference temperature (K), and T is the slurry temperature (K).

Achkari-Begdouri and Goodrich (1992) concluded manure in the range of 2.5–12.1% TS at temperatures between 20 and 60°C, forms and flows like a pseudo-plastic. Meanwhile, the results of El-Mashad et al. (2005) indicated that manure (10% TS) behaves as a real plastic

material when sheared at different rates (2.38–238 s^{-1}). Landry et al. (2004) provided experimental data for the rheological properties of solids up to 20% TS.

Conventionally, the Re is defined in Newtonian fluid, with the following agitation formula:

$$\mathrm{Re} = \frac{\rho N D^2}{\mu} \quad 2.2.9$$

where N is rotational speed (rps) and D is impeller diameter (m).

Due to the rheological behavior of manure and waste, Wu and Chen (Wu & Chen, 2008) introduced a Re number for non-Newtonian fluid which was derived from pipe flow (Metzner & Reed, 1955).

$$\mathrm{Re}_g = \frac{\rho U_\infty^{2-n} D^n}{K\left(0.75 + \frac{0.25}{n}\right)^n 8^{n-1}} \quad 2.2.10$$

where U_∞ is the average velocity of the fluid (m/s) and D the pipe inside diameter (m).

In this study, the flow characteristics are caused by agitators, and therefore the Re can be relevantly described as the equation (Metzner & Otto, 1957):

$$\mathrm{Re} = \left(\frac{D^2 N^{2-n} \rho}{K}\right)\left[8\left(\frac{n}{6n+2}\right)^n\right] \quad 2.2.11$$

Impeller power can be directly obtained from impeller torque, and the N_p is defined as the following equations (Wu & Pullum, 2000):

$$P = 2\pi N M \quad 2.2.12$$

$$N_p = \frac{P}{\rho N^3 D^5} \quad 2.2.13$$

where P is impeller power (w), M is impeller torque (n·m) and N_p is power number.

To calculate the flow rate produced by the impeller, a surface needs to be created for the discharge region. For an axial flow impeller, this surface is circular. By integrating the total outflow through this surface, the flow rate and subsequently the N_q can be obtained by the following equations (Patwardhan, 2001; Paul et al., 2004):

$$Q = \int v_z dA \quad 2.2.14$$

$$N_q = \frac{Q}{N D^3} \quad 2.2.15$$

where Q is flow rate (m^3/s), A is surface cell area (m), and N_q is flow number.

2.2.4—Kinetics model

Chemically reacting flows are those in which the chemical composition, properties, and temperature change as the result of a simple or complex chain of reactions in the fluid. Depending on the implementation, reacting flows can require the solution of multiple conservation equations for species, some of which describe reactants, and others of which describe products. To balance the mass transfer from one species to another, reaction rates are

used in each species conservation equation, and have as factors the molecular weights, concentrations, and stoichiometries for that species in all reactions.

The process of AD occurs in four key biological and chemical stages: hydrolysis, acidogenesis, acetogenesis, and methanogenesis. In most cases, biomass is made up of large organic polymers. For the bacteria in digesters to access the energy potential of the material, these chains must first be broken down into their smaller constituent parts. These constituent parts, or monomers, such as sugars, are readily available to other bacteria. To incorporate the kinetics model into CFD model, the biochemical kinetics of AD process was therefore simplified to:

Hydrolysis: $C_6H_{10}O_4$ (organic waste) + $2H_2O \rightarrow C_6H_{12}O_6$ (glucose) + H_2 R-2.2.1
Acidogenesis: $C_6H_{12}O_6 \rightarrow 2C_2H_5OH$ (ethanol) + $2\ CO_2$ R-2.2.2
Acetogenesis: $2C_2H_5OH + CO_2 \rightarrow 2CH_3COOH$ (acetic acid) + $2CH_4$ R-2.2.3
Methanogenesis: $CH_3COOH \rightarrow CH_4 + CO_2$ R-2.2.4
Methanogenesis: $CO_2 + 4H_2 \rightarrow CH_4 + 2H_2O$ R-2.2.5

The conservation equations for chemical species including biochemical reactions took the following form:

$$\frac{\partial}{\partial t}(\rho Y_i) + \nabla(\rho Y_i u_i) = -\nabla \cdot J_i + R_i \qquad 2.2.16$$

where Y_i is the mass fraction of each species including $C_6H_{10}O_4$, H_2O, $C_6H_{12}O_6$, H_2, C_2H_5OH, CH_4, and CO_2. J_i is the diffusion flux of species I, which arises due to concentration gradients. R_i is the net rate of production of species I by biochemical reactions (R-2.2.1–R-2.2.5):

$$J_i = -\left(\rho D_{i,m} + \frac{\mu_t}{Sc_t}\right)\nabla Y_i \qquad 2.2.17$$

where $D_{i,m}$ is the diffusion coefficient for species *I* in the mixture. Sc_t is the turbulent Schmidt number and set as 0.7.

A turbulence-biochemistry interaction model was used to understand the mixing effect on biomethane production. In this study, pH was assumed to be maintained at 7. Therefore, the negative mixing effect for acidification was negligible.

$$R_i = v_{i,r} M_{w,i} A \rho \frac{\varepsilon}{k} \min_R \left(\frac{Y_R}{v_{R,r} M_{w,R}}\right) \qquad 2.2.18$$

where Y_R is the mass fraction of a particular reactant. A is an empirical constant equal to 4.0. $v_{i,Y}$ is the stoichiometric coefficient for reactant *i* in reaction. $v_{R,Y}$ is the stoichiometric coefficient for products *i* in reaction. M_w is the molecular weight.

2.2.5—Results and discussion

2.2.5.1—Model validation

The model for mixing of Newtonian fluid was validated by comparing computed velocities for a tank mixed by an A-310 impeller with experimental data from Hoffmann et al. (2008). Figure 2.2.2 shows that the model's predictions matched well with experimental results. The small deviations between predicted and experimental data may be attributed to differences in the blade width and chord angle between the model and the actual structure of the A-310 impeller.

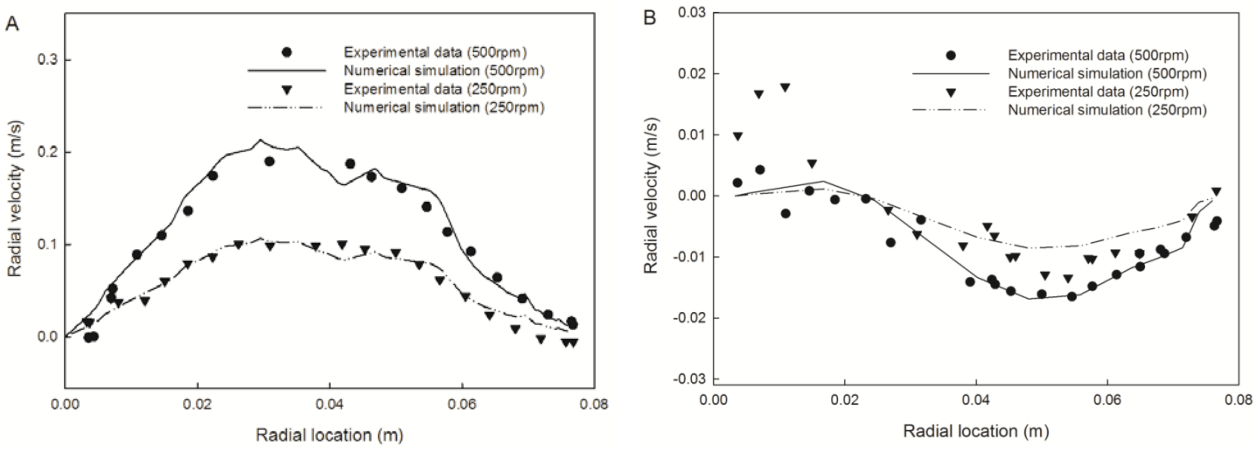

Figure 2.2.2: Comparisons of prediction and experimentation in radial average velocity (A) z = 5 cm (B) z = 13 cm (Hoffmann et al., 2008)

2.2.5.2—Modeled flow characteristics

Using the validated model, the modeled flow patterns during stirring with an A-310 impeller were compared for manure with < 5% TS and 10% TS content. These two different TS concentrations were investigated, as TS concentration of waste is an important parameter in AD. The fluid dynamics in the digester can be affected by the TS related to the slurry rheological behavior, which subsequently influences the pH, temperature uniformity and effectiveness of the microorganisms that carry out decomposition. The mixing intensity was set at 500 rpm to achieve medium agitation and give the digester a good ability to handle transient hydraulic and organic shock load (Hoffmann et al., 2008).

Figure 2.2.9 shows quantitative comparisons of flow patterns for < 5% TS and 10% TS manure. Significantly different flow fields were formed by agitation of the same impeller in these two slurries. The cross-section of the digester, with < 5% TS, showed that a large area of high velocity formed close to the impeller. Although fluid velocity decayed with increased distance from the impeller, most flow fields of the digester were over 0.03 m/s. Compared to the digester with < 5% TS, the digester with 10% TS had less efficient mixing. Significant velocity only occurred at or near the impeller, with most flow fields under 0.03 m/s (Figure 2.2.9). This indicates that high TS impeded the convection process of the A-310 impeller.

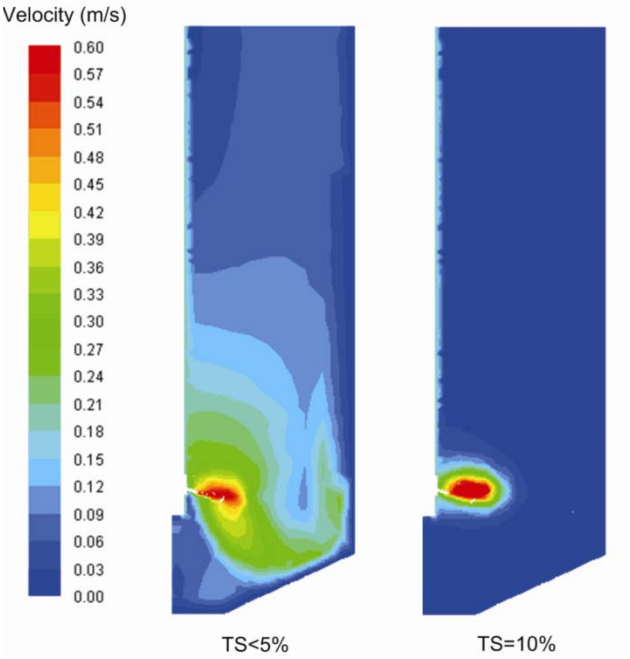

Figure 2.2.3: Comparison of velocity contour in TS < 5% and TS = 10%

N_p and N_q are important parameters for assessing the mixing performance of impellers (Chudacek, 2002). These parameters were computed for impeller A-310 in the digesters with < 5% and 10% TS. In a stirred tank mixing system, perhaps the most fundamental measurement one can make is that of the power draw of the system, as many scale-up rules depend heavily on the specific power input. The power draw of an impeller is characterized by its N_p. The CFD simulation can give this key prediction at low cost. Based on the value of the Re number, flows fall into either the laminar regime, with small Re numbers, or the turbulent regime, with high Re numbers. The transition between laminar and turbulent regimes occurs throughout a range of Re numbers rather than at a single value. In mixing tanks, the location of the transition usually depends on the N_p of the impeller.

The simulation results (Figure 2.2.4) show that the N_p decreased with increasing Re. A curve drop occurred in the N_p for the digester with < 5% TS as the Re increased while a more linear drop occurred in the digester with 10% TS. The different shapes indicate a different relationship between N_p and Re, in other words, between the power draw and flow pattern. For 5% TS, the power draw decreased more quickly with an increase of Re. For 10% TS, power draw decreased more slowly with an increase of Re. Once the Re in digester with < 5% TS was greater than 1000, the flow gradually changed to turbulent flow and the N_p stabilized. This prediction is in good agreement with many researchers' experimental results (Paul et al., 2004). This study predicts that the N_p will be 0.34 in the turbulent flow of a digester with < 5% TS, and 0.47 in the turbulent flow of a digester with 10% TS, indicating that more energy consumption takes place in digesters with higher solids concentration.

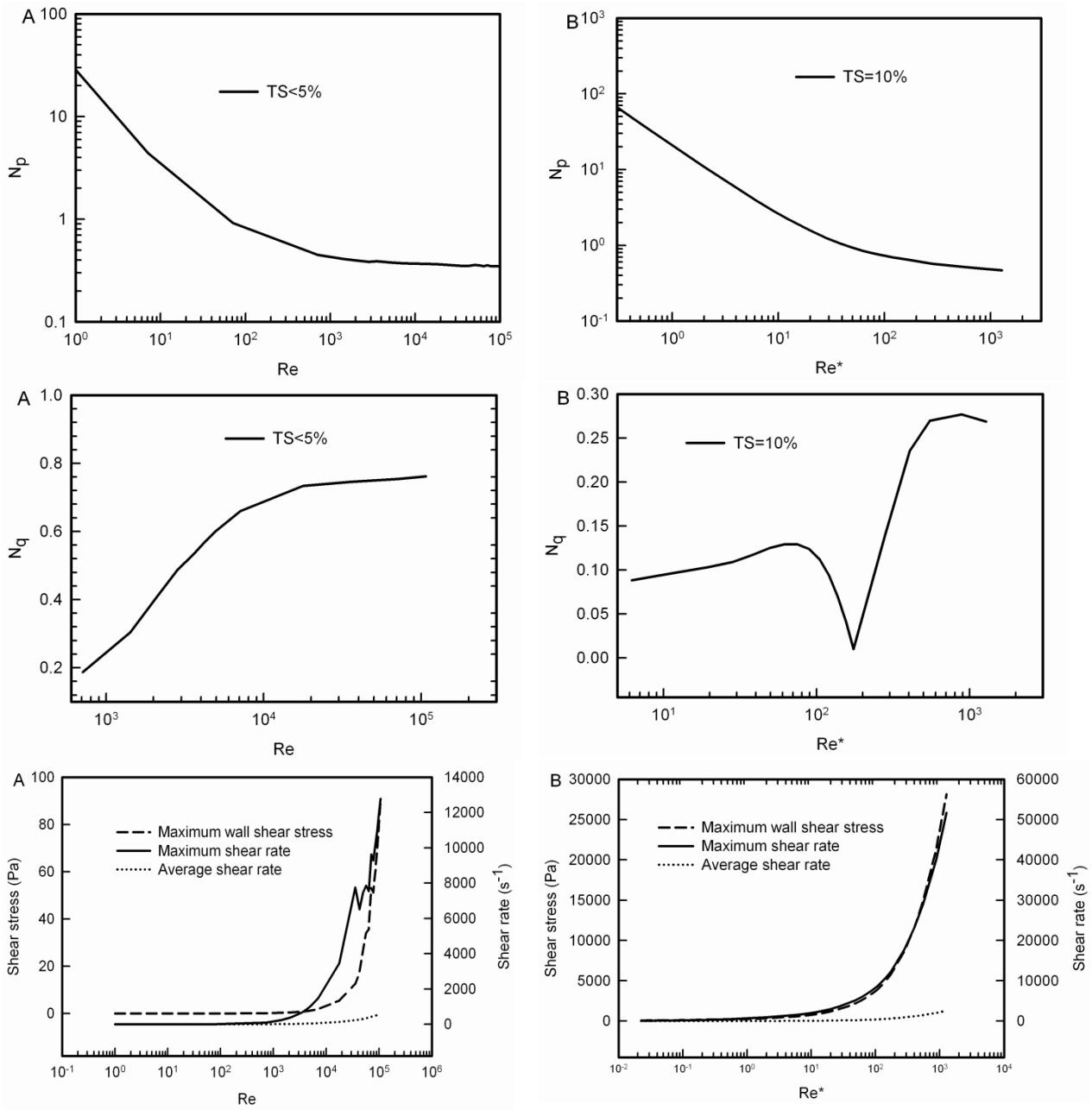

Figure 2.2.4: N_p and N_q, vs. impeller Re for (A) TS < 5% and (B) TS = 10%

The impeller discharge N_q indicates the pumping capacity of the impeller in a given geometry. Typically, the N_q increases as Re increases up to 10000, and becomes constant at higher Re (Paul et al., 2004). For the manure of < 5% TS, the modeled N_q was 0.76, while the experimental data were in the range of 0.55–0.73 under turbulent conditions for impeller A-310 (Paul et al., 2004). However, a different trend was observed for TS = 10%. When Re in the digester with 10% TS was less than 200, the N_q increased first, but then decreased sharply. Once the Re in the digester with 10% TS was over 200, the N_q increased quickly to approach a constant. This is because the impeller pumping direction was affected by the high viscosity of 10% TS fluid. The predicted fluid dynamics in the digester with 10% TS showed that the upward flow dominated at low Re.

With increases in Re, the impeller pumping direction was sharply switched downward. This flow behavior was different from that with < 5% TS in which downward flow always dominated.

2.2.5.3—Modeled impacts on shear forces

Shear rate is also important for assessing impeller performance (Chudacek, 2002). In addition to indirect impacts on microbes (e.g. through bringing microbes into contact with substances in the mixture), mixing can also directly impact the microbes in the digester. Microbial cells are susceptible to mechanical forces (Morales-Barrera & Cristiani-Urbina, 2006), which disrupt the cell membrane and can even kill some microorganisms. Continuous shear, in particular, negatively affects microbial flocs (Hoffmann et al., 2008).

Therefore, data on shear stress and shear rate across Re were modeled for impeller A-310 in the digesters with < 5% and with 10% TS (Figure 2.2.5). The maximum shear stress and shear rate on the impeller tip would be difficult to determine experimentally. The results showed a small increase in shear stress and shear rate with increasing Re up to a Re of 10000 in < 5% TS slurry and 100 in 10% TS slurry, with a sharp increase occurring as the Re increased beyond those points. In addition, the maximum impeller wall shear stress and shear rate of the 10% TS digester were much higher than that of the < 5% TS digester due to the high viscosity. This creates potential concerns for the digester with 10% TS that would need to be further investigated. If the enzymes and bacteria stayed near the impeller tip, modeling results indicate a large impact due to the shear rate. However, the average shear rate was reduced by an order of magnitude compared with the maximum shear rate, indicating a steep velocity gradient within this digester. It is possible that most of enzymes and bacteria might find a low shear zone away from the impeller to live, in which case operation might successfully continue.

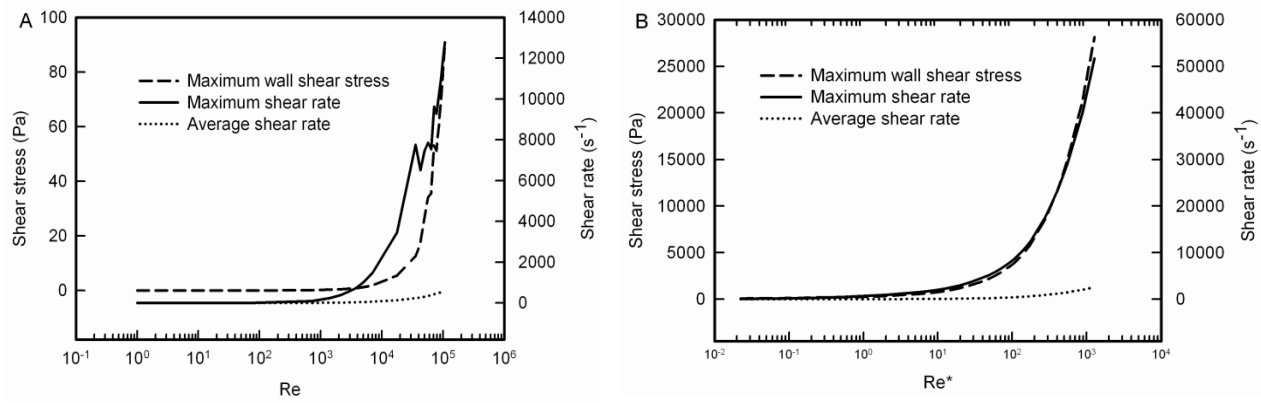

Figure 2.2.5: Maximum wall shear stress and shear rate and average shear rate vs. impeller Re for TS < 5% (A) and TS = 10% (B)

2.2.5.4—Effect of total solids on flow characteristics

To further understand the impact of TS on flow characteristics, the impact of TS on N_p and N_q were modeled across a range of TS from 2–12% (Figure 2.2.6). The response of N_p to TS was nearly linear, at least in this range, indicating that higher power input was required to agitate digesters with higher TS. A nearly exponential decay was observed in the relationship between N_q and TS, indicating that the pumping capacity of impeller A-310 was impaired by higher TS.

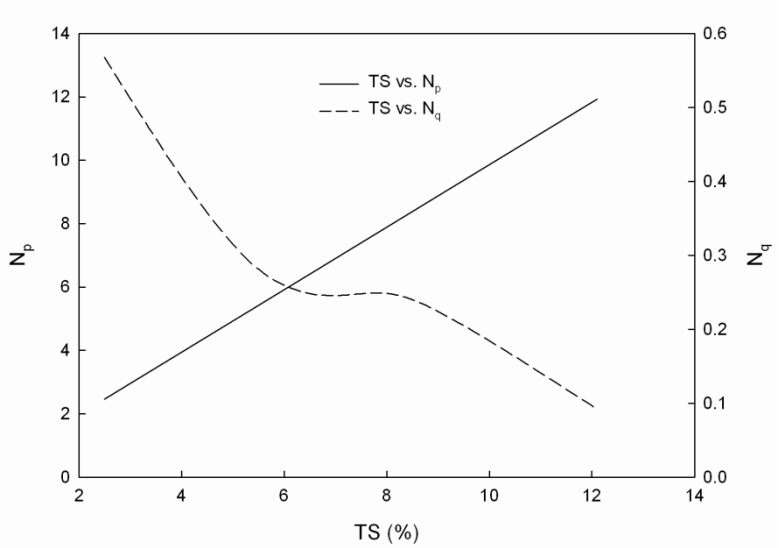

Figure 2.2.6: N_p and N_q change with TS

2.2.5.5—Change in methane production over time

In this study, the kinetics for AD was added into the CFD model, and pH was assumed to be constant at 7.0. Therefore, the trend of acidification due to intensive mixing can be ignored. The effect of mixing on concentration and distribution of CH_4 is shown visually in Figure 2.2.7. The local contour of CH_4 concentration does not match the velocity distribution shown in Figure 2.2.2, indicating that the highest CH_4 concentration did not occur in the region of the highest flow velocity. Instead, the region nearest to the highest flow velocity had the highest CH_4 production concentration. As time went by, the CH_4 concentration increased and gradually dispersed to the top area of the reactor.

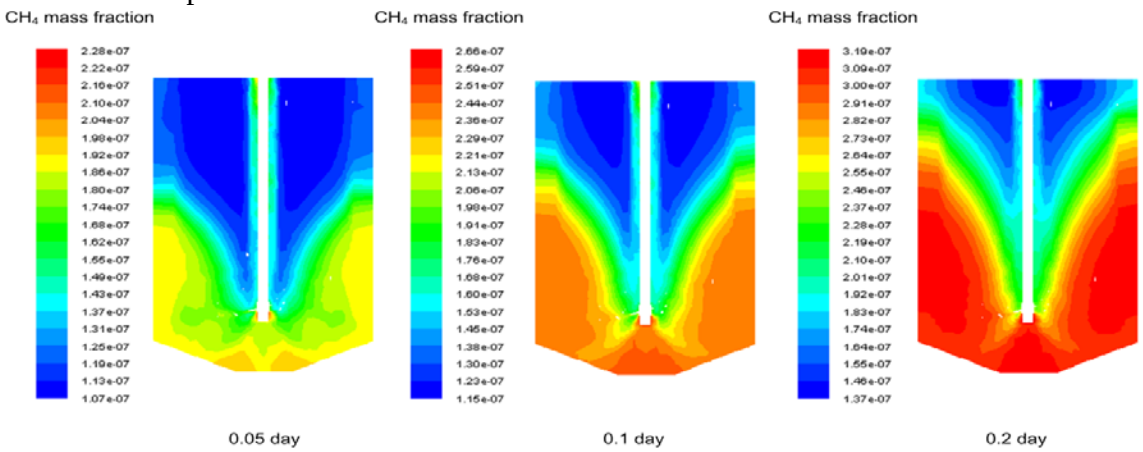

Figure 2.2.7: Contour of CH_4 mass fraction in the A-310 stirred tank with TS < 5%

Figure 2.2.8 shows the effect of mixing manure with < 5% and 10% TS on CH_4 production. As previously mentioned, significantly different flow fields were formed by agitation of the same impeller in these two slurries (Figure 2.2.6). The distribution of CH_4 concentration was also different. In the stirred tank with low TS (< 5%), higher CH_4 productivity was reached due to good mixing, with high CH_4 productivity especially near the wall and bottom. However, very

low CH_4 productivity was achieved in the stirred tank with high TS (= 10%), due to poor agitation and mixing

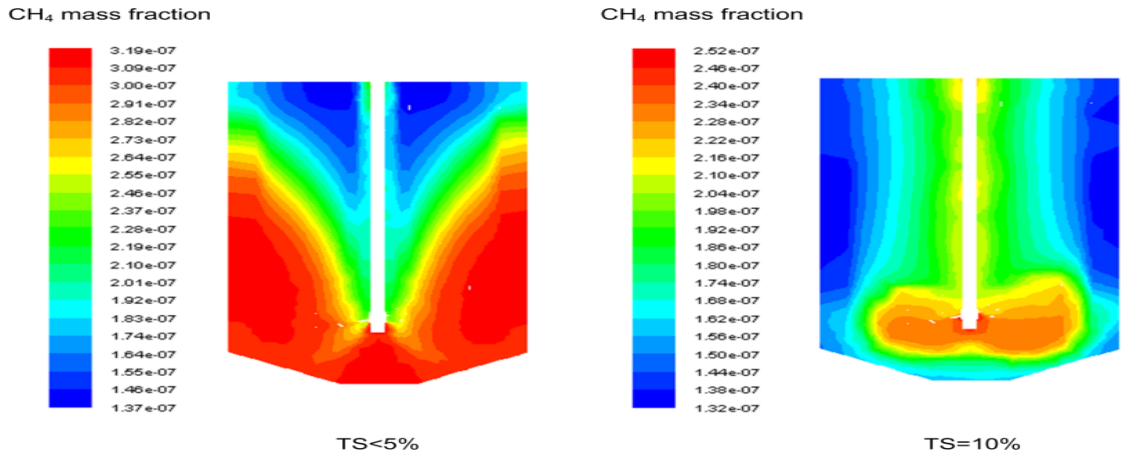

Figure 2.2.8: CH_4 mass fraction contour in TS < 5% and TS = 10%

2.2.6—Conclusions

The model developed in this study successfully incorporated AD kinetics into a CFD model to better understand the effect of mixing on CH_4 production, and provided support for assessing alternate system configurations and system optimization efforts. The model performed well compared to published experimental data, and represented a valuable resource that could support scale-up efforts of the HSAD systems, including WSU's HSADRS system. The difficulty of developing a combined (kinetics and CFD) model necessitated that more simple kinetics modeling be used, with the result that this model is best used to describe flow, and supplemented with more complex ADM1-based modeling for information on mass transfer and biochemical reactions (see section 2.3). However, this work sets the stage for future efforts to incorporate more elaborate kinetics modeling, working towards one integrated model that can be used to describe flow, mass transfer, and biochemical reactions.

To illustrate potential uses of the model, the model was used to explore issues related to the flow characteristics of manure at a range of TS, mixed using an A-310 impeller. In the modeled system, adequate flow velocity and good overall CH_4 production were predicted for low TS concentrations (TS < 5%). In contrast, flow velocities were low throughout the slurry with higher TS concentration (TS = 10%), and CH_4 production likewise was low. More energy was consumed by mixing in the digester with higher solids, with a N_p of 0.47 in the turbulent flow of a digester with 10% TS, compared to 0.34 in the turbulent flow of a digester with < 5% TS. Discharge N_q indicated typical, if slightly high, pumping capacity of the impeller at TS < 5% (modeled N_q stabilized at 0.76 with consistent downward flow, compared to experimental data were in the range of 0.55–0.73 under turbulent conditions). However, the predicted fluid dynamics in the digester with 10% TS indicated that upward flow dominated at low Re numbers. With increases in Re, the impeller pumping direction was gradually switched to downward. This presented further indication of non-ideal mixing at TS = 10%. When the impact of change in TS on N_p and N_q was explored across a range of TS from 2% to 12%, the response of N_p to TS was nearly linear, at least in this range, indicating that higher power input was required to agitate digesters with higher solids. Meanwhile, a nearly exponential decay was observed in the

relationship between N_q and TS, indicating that the pumping capacity of impeller A-310 was impaired by higher TS.

Shear stress and shear rates were also predicted, to explore potential negative impacts of mixing on methanogenic microbes. The calculated results suggest a small increase in shear stress and shear rate with increasing Re up to a Re of 10000 in < 5% TS slurry and 100 in 10% TS slurry, and a sharp increase as Re increased beyond those points. In addition, the maximum impeller wall shear stress and shear rate of the 10% TS digester were much higher than that of the < 5% TS digester due to the high viscosity. This points to concerns for the digester with 10% TS, though it is possible that enzymes and bacteria could live within lower shear zones away from the impeller. If this is the case, operation might successfully continue despite the higher shear stress and shear rate.

2.3—Overall reactor system modeling and pilot test design

Liang Yu, Shulin Chen

2.3.1—Abstract

A stand-alone process kinetics model was developed to describe WSU's proposed HSADRS system. The stand-alone kinetics model was based on the ADM1, one of the most complete and accurate models developed to date, was thus able to generate more complete information on mass transfer and biochemical reactions. This information complements the flow information generated from the combined CFD-kinetics modeling described in section 2.2.

The model consisted of a HSAD in the first stage followed by a universal sequence batch reactor (USBR) in the second stage. To test the accuracy of this model, researchers conducted laboratory experiments with a bench-scale HSAD and compared them to model predictions. A sensitivity analysis showed good agreement between the experimental data and the model, indicating the suitability of this model for real-world applications.

Thereafter, multiple parameters were explored to further illustrate the applicability of the model. One of the most interesting model predictions resulted when methanogens were recirculated from the USBR back to the HSAD. Without methanogen recirculation, the CH_4 content in the biogas was near zero in the first stage reactor due to a low HRT. When methanogen recirculation was turned on, the CH_4 production increased to nearly 60%, demonstrating how powerful modeling can be for avoiding inadequate design that leads to digestion failure.

To support scale-up efforts from lab-scale experiments to commercial-scale applications, the model was also used to investigate how the biogas production, acetic acid production and pH would be affected when the USBR height and cross-sectional area were altered. The model predicted that the CH_4 production in the HSAD was impacted the most when the cross-sectional area was increased. Similar comparisons of other possible design and operational parameters, conducted with future commercial partners, will be a cost-effective and efficient way to support future scale-up and optimization.

2.3.2—Introduction

As described in the previous section, AD modeling has been used effectively to help with scale-up efforts, and to determine the limiting factors to the AD process. One of the most commonly used models, ADM1, was a collaborative work of many international experts, and was developed to simulate the complex processes and interactions between anaerobic microorganisms during the AD process (Batstone et al., 2006a). This model has been used as a foundation for further model development and has improved understanding of the AD process. It has also proven to be an effective tool for reducing the time and costs associated with scaling up new technologies, as it reduces the need for an extended period of trial and error to compare design options and hone in on key operational parameters. To complement the detailed flow information generated from the combined CFD-kinetics modeling (described in Section 2.2), this project used a stand-alone process model based on ADM1 to describe WSU's proposed HSADRS system. This model was developed to generate comprehensive and accurate information on mass transfer and biochemical reactions.

As discussed in Section 2.2, the ADM1 model, developed by the IWA Task Group consolidates the variety of different mathematical models that described the AD process at that time, and represents the first generalized model of AD (Batstone et al., 2006b; Montiel-Escobar et al., 2012). The model has been applied to many types of AD, including two-stage digestion of various feedstocks including sewage sludge, traditional Chinese medicine wastewater, olive pulp, and grass silage (Blumensaat & Keller, 2005; Chen et al., 2009; Koutrouli et al., 2009; Thamsiriroj & Murphy, 2011). The ADM1 model has proved itself useful as a design tool for two-stage digestion, even for these complex feedstocks.

The AD system developed by researchers at WSU is illustrated in Figure 2.3.1. HSADRS is a two-stage digestion technology that combines a HSAD and upflow anaerobic sludge blanket (UASB) seed reactor together to treat food scraps with high TS content. Experimental observations indicated that the HSAD reactor naturally separated into two zones due to biogas floatation and low specific gravity (SG) of solid waste with respect to water. In the HSAD reactor, the solid waste was agitated and retained in the upper zone while soluble organics and liquid leachate, which didn't need agitation, were retained in the lower zone. Thus, for modeling purposes, the upper zone of the HSAD reactor was assumed to be a CSTR while the lower zone of the HSAD reactor was assumed to be an advective-diffusive reactor (ADR). Liquid effluent was cycled out of the two-stage HSAD system for bacterial seeding, VFA removal, and pH control. The UASB seed reactor was modeled as an ADR, because this allowed for more effective analysis of reactor cross-sectional area and height for reactor design.

To test the new two-stage model, the pH, VFA, and biogas production were modeled and then experimentally verified in two batch digesters including a HSAD reactor and a UASB reactor. The ability of the model to predict experimental results also indicates its usefulness as a tool to be used in future scale-up efforts and commercial testing.

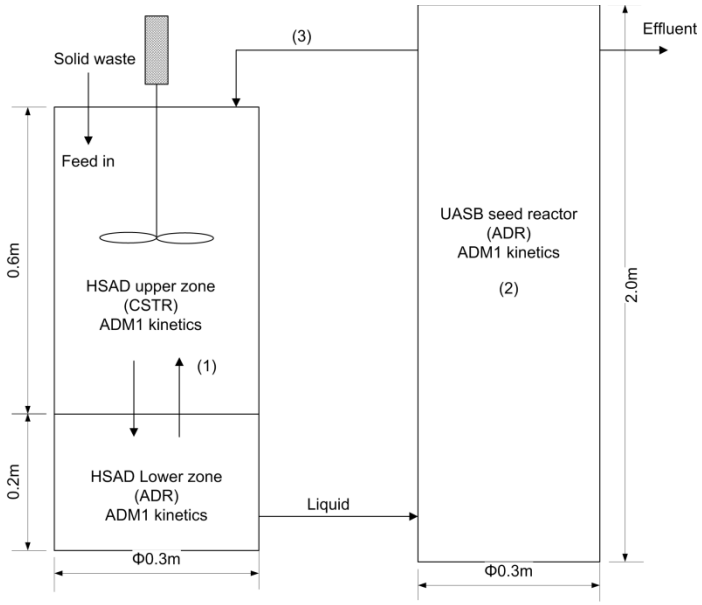

Figure 2.3.1: Model structure of the two-stage HSAD system consisting of a HSAD (CSTR+ADR) reactor (*left*) and a UASB (ADR) reactor (*right*)

2.3.3—Material and methods

2.3.3.1—System description

Figure 2.3.1 illustrates a schematic of the model that was developed, comprising a mesophilic (35°C) two-stage HSAD system with a recycling ports located at the bottom and top of each reactor. The HSAD reactor (located at the left in Figure 2.3.1) had a working volume of 0.057 m^3 with a tank diameter of 0.3 m and height of 0.8 m. The volume ratio of the upper and lower zones for the HSAD reactor was 3 to 1. The UASB reactor (located at the right in Figure 2.3.1) had a working volume of 0.14 m^3 with tank diameter of 0.3 m and height of 2.0 m. Solid and liquid retention as well as liquid recycling for both the HSAD and UASB reactor were modeled against varying solids retention, hydraulic retention, and recycle rates.

Based on experimental observations, the HSAD reactor was assumed to naturally separate into two zones, an upper zone (CSTR) and a lower zone (ADR). The solid substrates consisted of complex composite particulate and particulate carbohydrates, proteins and lipids (Batstone et al., 2002). Around 99% of the solid substrates were assumed to be suspended in the upper zone of the HSAD reactor. The liquid leachate from the UASB reactor and the hydrolytic solutes were recycled back to the HSAD reactor via a port at the top of the HSAD reactor. Thereafter, this effluent flowed into the lower zone until ultimately feeding back to the UASB reactor. Mechanical mixing with a shaft and vertical impeller blades was utilized in the upper zone of the HSAD reactor to enhance mass transfer of the solid waste. Soluble substrates within the lower zone of the HSAD reactor flowed without the need of mixing. This allowed for an environment favorable to methanogenic bacteria growth and biogas flotation (Vavilin & Angelidaki, 2005).

The two-stage HSAD system was operated in both batch and continuous mode. In batch mode, solid waste was fed into the HSAD reactor once all the effluent was recycled in the system. The batch process was operated at a solid retention time (SRT) of 9 days and a HRT of 1 day. In the continuous mode, solid waste was continuously fed into the HSAD reactor and effluent was in part discharged out of a port located at the top right of the USAB reactor. The continuous process was operated at a SRT of 30 days and a HRT of 1 day. After the SRT was achieved, the solid residuals were discharged out of the bottom of the HSAD reactor for composting (not shown in Figure 2.3.1). In the UASB seed reactor, bacterial biomass, which was depicted as being retained granules were assumed to be constant (Seghezzo et al., 1998), at an experimentally determined average of 15 kg COD/m^3. Based on additional experimental data, approximately 4.87% of acetic acid and hydrogen degrading organisms as well as all other degrading organisms were recycled to the HSAD reactor for seeding of bacteria, VFA removal and pH control. The UASB reactor was operated at a HRT of 1 day.

2.3.3.2—Experimental set-up

Food scraps, including plastic and paper packaging (about 2.7%), were obtained from a WSU cafeteria. The waste was mechanically cut into shreds producing a paste with TS of 30.6%. The characteristics of the waste are summarized in Table 2.3.1. Upon loading into the HSAD reactor, the TS were diluted to 15.4%, while maintaining a pH of 5.47. Bacteria inoculums and granular seeds were obtained from commercial starch water UASB reactor (Penford Foods, Richland, WA, USA). Prior to system evaluation, the HSAD and UASB systems were operated for 4 months to allow for system acclimation. The experimental data were sampled from the two-stage HSAD system after four months of seeding with the granule inoculum, which allowed for a steady and stable digestion process prior to introducing food scraps into the reactors (Chynoweth & Isaacson, 1987). Since this system consisted of high rate digesters with short HRT (less than 1 day) (Seghezzo et al., 1998), the digester was operated for one week and samples were collected and analyzed over that period of time to show any dynamic change in pH, concentration and biogas production.

Table 2.3.1: Conditions for the mathematic model for the HSAD system

Characteristic	Unit	Solid Food Scraps
TS	g/l	154
VS	g/l	118
Particulate COD (CODp)	gCOD/l	182
Soluble COD (CODs)	gCOD/l	18.8
TOC	gC/l	53.3
IC	mol/l	10.7
TKN	gN/l	5.30
TAN	gN/l	1.30
TP	gP/l	0.46
TOP	gP/l	0.90
VFA	gCOD/l	2.30
pH		5.47

2.3.3.3—Model structure

The reaction kinetics that were incorporated into the ADM1 model were complex with a number of sequential and parallel steps (Batstone et al., 2002). Two main reactions are present within the model, one consisting of biochemical reactions and the other consisting of physicochemical reactions. The ADM1 model included 19 biochemical kinetic processes. All biochemical extracellular steps were assumed to be first order and all intracellular reactions were assumed to exhibit Monod-type kinetics. The biochemical extracellular kinetics including disintegration rate and hydrolysis rate of bioparticles, and decay rate of microorganisms are expressed as:

$$r_j = K_{dis,hyd,dec,j} C_{X,j} \quad 2.3.1$$

where r_j represents the disintegration rate (kgCOD·m^{-3}·d^{-1}), hydrolysis rate and decay rate of bioparticles and microorganisms, respectively. K is the coefficient of the first order reactions (d^{-1}). C is the concentration (kgCOD·m^{-3}) including microorganisms of complex particles, carbohydrates, proteins, lipids, sugars, amino acids, long chain fatty acids (LCFA), C_4, propionate, acetate and hydrogen.

The intracellular kinetics including uptake rate of substrates are expressed as:

$$r_j = K_{m,j} \frac{C_{S,j}}{K_{S,j} + C_{S,j}} C_{X,j} I_i \quad 2.3.2$$

where K_m is the specific Monod maximum uptake rate (kgCOD·m^{-3} _S·kgCOD·m^{-3} _X ·d^{-1}); K_S is the Monod half saturation constant (kgCOD·m^{-3}); and I_i is inhibition function. Inhibitions came from H_2, NH_3, pH and deficit of inorganic N.

Valerate and butyrate are assumed to be consumed by the same microorganism responsible for C_4. Their kinetics differ from the other intracellular reactions and are expressed as:

$$r_{va} = K_{m,c4} \frac{C_{S,va}}{K_{S,c4} + C_{S,va}} C_{X,c4} \frac{1}{1 + C_{S,bu}/C_{S,va}} I_2 \quad 2.3.3$$

$$r_{bu} = K_{m,c4} \frac{C_{S,bu}}{K_{S,c4} + C_{S,bu}} C_{X,c4} \frac{1}{1 + C_{S,va}/C_{S,bu}} I_2 \quad 2.3.4$$

In this study, the ADM1 model was extended to describe a HSAD reactor and an UASB reactor. As described above, the HSAD reactor includes two zones. The upper zone of the HSAD reactor is assumed to be a CSTR where the solid food scraps were mechanically agitated to enhance mass transfer among microorganisms, enzymes, and solid substrates. The temporal change of the concentration is given as the following (Batstone et al., 2002):

$$\frac{dC_{liq,i}}{dt} = \frac{q_{in} C_{in,i} - q_{out} C_{liq,i}}{V_{liq}} + \sum_{j=1-19} r_j v_{i,j} \quad 2.3.5$$

where C is concentration (kgCOD·m^{-3}) including microorganisms and substrates; $\sum_j$=1-19$r_j v_{i,j}$ is the sum of the biochemical rate coefficients ($v_{i,j}$) multiplied by the kinetic rate equations (r_j) for the process; V is the reactor volume (m^3); and q_{in} and q_{out} are the flow rate of influent and effluent, respectively.

The lower zone of the HSAD reactor was assumed to be an ADR, with mechanical agitation in the upper zone not affecting the lower zone of the HSAD reactor. Only liquid leachate and soluble substrates reside in the lower zone, because the solid waste has been pushed back to the upper zone by biogas flotation due to the low SG of food scraps (SG = 1.08). The behavior of substrates transported in the compartment are given as (Reichert, 1998):

$$A\frac{\partial C_{liq,i}}{\partial t} + q\frac{\partial C_{liq,i}}{\partial x} = AD\frac{\partial^2 C_{liq,i}}{\partial x^2} + \sum_{j=1-19} Ar_j v_{i,j} \qquad 2.3.6$$

where A is the cross section area (m^2) of the reactor, and D is the coefficient of dispersion which was set as 20 m^2/day.

Leachate from the lower zone of the HSAD reactor is ultimately sent to the UASB reactor, a high rate methanogenic digester. Most of methanogenic bacteria are immobilized in the granules (Molina et al., 2008), resulting in short HRT, long SRT, and highly active granules with good settling abilities retained in the UASB reactor despite the upflow velocity of the wastewater (Schmidt & Ahring, 1996). To simplify the flow model, the UASB seed reactor is assumed to be an ADR. Methanogenic bacteria including acetic acid and H_2 degrading organisms were assumed to be constant with an average of 15 kg COD/m^3 based on experimental measurement due to a slow growth rate (Liu et al., 2002). The behavior of substrates transported in the UASB reactor are given as (Reichert, 1998):

$$A\frac{\partial C_{liq,i}}{\partial t} + q\frac{\partial C_{liq,i}}{\partial x} = AD\frac{\partial^2 C_{liq,i}}{\partial x^2} + \sum_{j=1-19} Ar_j v_{i,j} \qquad 2.3.7$$

The biogas H_2, CH_4 and CO_2 were calculated from the model using gas liquid transfer kinetic rates.

2.3.3.4—Estimation of model parameters

The model was implemented and solved using AQUASIM 2.0 software tool, a program for the identification and simulation of aquatic systems (Reichert, 1998). The initial parameters used in the ADM1 kinetics were selected from the scientific and technical work reported by the IWA task group (Batstone et al., 2002; Gali et al., 2009; Rosen & Jeppsson, 2006). Kinetic parameters were estimated by minimizing the sum-of-the-squared-difference χ^2 between the measured (y_{exp}) and calculated (y_{cal}) values at the sampling ports over sampling times (N_{time}) and are expressed as follows:

$$\chi^2 = \sum_{i=1}^{N_{time}} \left(\frac{y_{cal,i} - y_{exp,i}}{\sigma_{exp,i}} \right)^2 \qquad 2.3.8$$

where $\sigma_{exp,I}$ is the standard deviation of the measured values.

On the basis of the suggested biochemical parameter values, sensitivity and estimation in the ADM1 report (Batstone et al., 2002), the estimation procedures were applied for the following parameters: kinetic coefficients of K_{dis}, K_{m_ac}, K_{s_ac} and stoichiometric coefficients of f_{ch_xc}, f_{pr_xc}, f_{si_xc}, f_{xi_xc}. Initial and estimated kinetic coefficients for the model are shown in Table 2.3.2.

Table 2.3.2 Model parameters in the HSAD system

Constant	Units	Value
Disintegration and hydrolytic parameters		
K_{dis}	d^{-1}	0.15
K_{hyd_CH}	d^{-1}	10
K_{hyd_PR}	d^{-1}	10
K_{hyd_LI}	d^{-1}	10
Kinetics parameters of acidogenesis		
K_{m_su}	$COD \cdot COD^{-1} \cdot d^{-1}$	30
K_{m_aa}	$COD \cdot COD^{-1} \cdot d^{-1}$	50
K_{s_su}	$kg \cdot m^{-3}$	0.5
K_{s_aa}	$kg \cdot m^{-3}$	0.3
Y_{su}		0.1
Y_{aa}		0.08
K_{dec_su}	d^{-1}	0.02
K_{dec_aa}	d^{-1}	0.02
Kinetics parameters of acetogenesis		
K_{m_fa}	$COD \cdot COD^{-1} \cdot d^{-1}$	6
K_{m_c4}	$COD \cdot COD^{-1} \cdot d^{-1}$	20
K_{m_pr}	$COD \cdot COD^{-1} \cdot d^{-1}$	13
K_{s_fa}	$kg \cdot m^{-3}$	0.4
K_{s_c4}	$kg \cdot m^{-3}$	0.2
K_{s_pr}	$kg \cdot m^{-3}$	0.1
Y_{fa}		0.06
Y_{c4}		0.06
Y_{pr}		0.04
K_{dec_fa}	d^{-1}	0.02
K_{dec_c4}	d^{-1}	0.02
K_{dec_pr}	d^{-1}	0.02
Kinetics parameters of methanogenesis		
K_{m_ac}	$COD \cdot COD^{-1} \cdot d^{-1}$	8
K_{m_h2}	$COD \cdot COD^{-1} \cdot d^{-1}$	35
K_{s_ac}	$kg \cdot m^{-3}$	0.15
K_{s_h2}	$kg \cdot m^{-3}$	7×10^{-6}
Y_{ac}		0.05
Y_{h2}		0.06
K_{dec_ac}	d^{-1}	0.02
K_{dec_h2}	d^{-1}	0.02
Stoichiometric parameters		
f_{ch_xc}		0.50
f_{li_xc}		0.068
f_{pr_xc}		0.28
f_{si_xc}		0.075
f_{xi_xc}		0.05

2.3.4—Results and discussion

2.3.4.1—Sensitivity analysis

A sensitivity analysis was performed on parameters that ADM1 researchers had suggested would be sensitive (Batstone et al., 2002) to understand their impact on the predicted acetic acid and CH_4 production. The absolute-relative sensitivity function (δ) was used to measure the absolute change in acetic acid and CH_4 production for a 100% change in kinetic coefficients of K_{dis}, K_{hyd_CH}, K_{hyd_PR}, K_{m_ac}, K_{s_ac} and stoichiometric coefficients of f_{ch_xc}, f_{pr_xc}, f_{si_xc}, f_{xi_xc} (Reichert, 1998). The behavior of the model was evaluated as a function of variations in input parameters using a one-variable-at-a-time approach, in which only one parameter value was changed each time, while the other parameters were kept constant.

2.3.4.2—Model validation and sensitivity analysis

Figure 2.3.2 compares experimental data to simulation values in the HSAD batch reactor. Overall, the model shows good agreement ($P > 0.05$) with the experimentally determined measurements of pH and biogas production in the pilot-scale HSAD reactor. As shown in Figure 2.3.2 (A), pH in the HSAD reactor dropped sharply on the first day, and then trended slowly downward over time. The effluent of the UASB seed reactor and the feedstock flowed into the HSAD reactor at different ratios. The volume ratios of 5.43, 2.19 and 1.1 corresponded to 5%, 10% and 15% TS in the HSAD reactor, respectively. At the beginning, the pH of the food scraps that was fed in the HSAD reactor was 5.47 while the pH of effluent was 7.9. The subsequent results show that an HRT of less than 1 day can maintain a pH above 6.0 even at the low recirculation ratio of 1.1. This means that the effluent of the UASB seed reactor provided a suitable environment for methanogenic bacteria at a TS concentration of 15% and a HRT of 1 day.

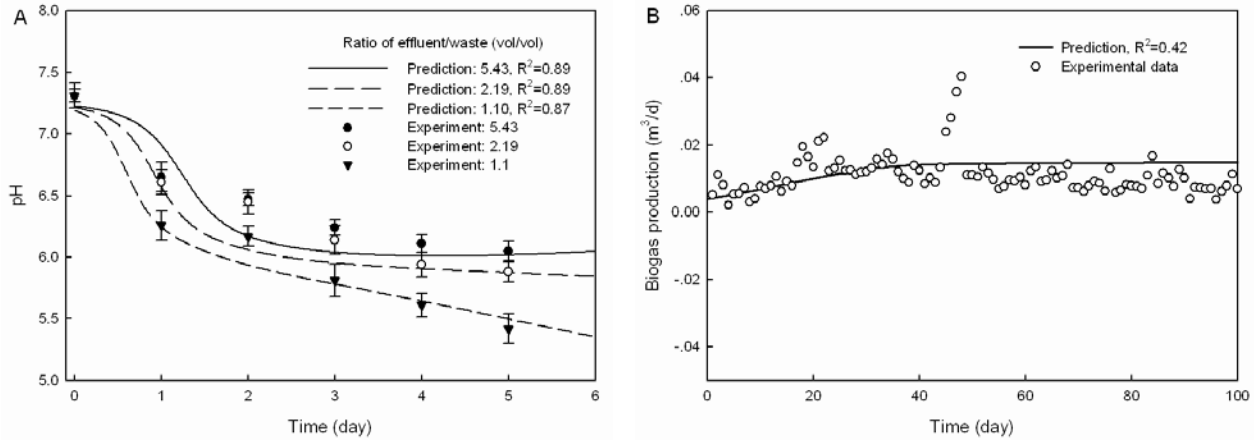

Figure 2.3.2: pH (A) at the different ratio of effluent to waste and biogas production (B) change with time in the HSAD batch reactor without recirculation

Figure 2.3.2 (B) shows the daily biogas production at pH 7.5 and TS of 15% in the HSAD reactor without mechanical mixing or recirculation. An obvious stratification of solid and liquid was observed in the upper and lower zone of the HSAD reactor. The biogas production showed stable operation on a daily and monthly basis. The soluble parts of the solid waste were hydrolyzed into VFA and thereafter the VFA was dissolved in the liquid phase. The insoluble parts of the solid waste stayed in the upper zone of the HSAD reactor. The liquid phase, with its dissolved VFA, flowed into the lower zone. It then flowed out of the HSAD reactor and into the

UASB for CH_4 production. Since VFA was removed from the solid waste, no trend towards acidification occurred.

Figure 2.3.3 compares predicted and experimental daily biogas production, VFA and pH in the UASB seed reactor. The model shows good agreement ($P > 0.05$) with the experimentally determined measurements. The biogas production shown in Figure 2.3.3 (A) was measured when the feed rate of leachate from the HSAD reactor was at 0.038 m^3/week. The highest biogas production was obtained on the first day, when feedstock had the highest VFA (Figure 2.3.3 (B)). Thereafter, an exponential decay of the biogas production was observed. The pH was maintained at the range of 7.5–8.0, indicating stable digester operation.

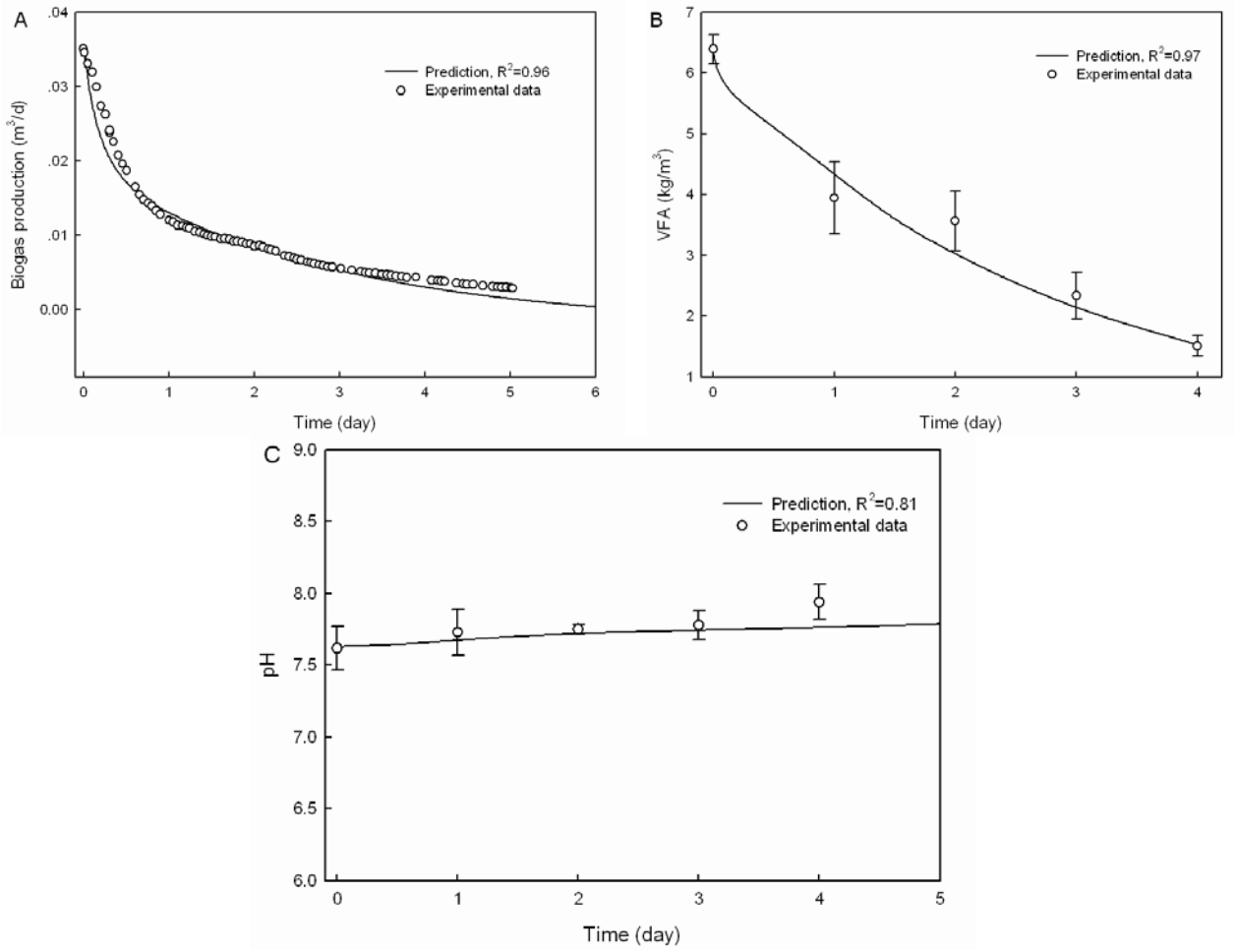

Figure 2.3.3: Biogas production (A), VFA (B) and pH (C) change with time in the UASB seed reactor

Figure 2.3.4 compares predicted and experimental changes in specific VFAs in the UASB seed reactor. The specific VFAs considered included acetic, propionic, butyric and valeric acids. Compared with other VFAs, the consumption rate of propionic acid was relatively slow. The concentration of acetic and propionic acid are critical factors that regulate AD processes since the oxidation of propionic acid to acetic acid is the slowest among the VFA (Dohányos et al., 1985; Inanc et al., 1999; Sonakya et al., 2007). The model shows good agreement ($P > 0.05$) with the experimentally determined measurements of acetic, propionic, and butyric acid in the

pilot-scale UASB seed reactor. However, the calculated results of valeric acid did not fit well with the measurement. This may be due to butyric and valeric acid sharing the same equations in the ADM1 kinetics, as shown in R-2.3 and R-2.4. Therefore, the predicted results for butyric and valeric acid are only different proportionally.

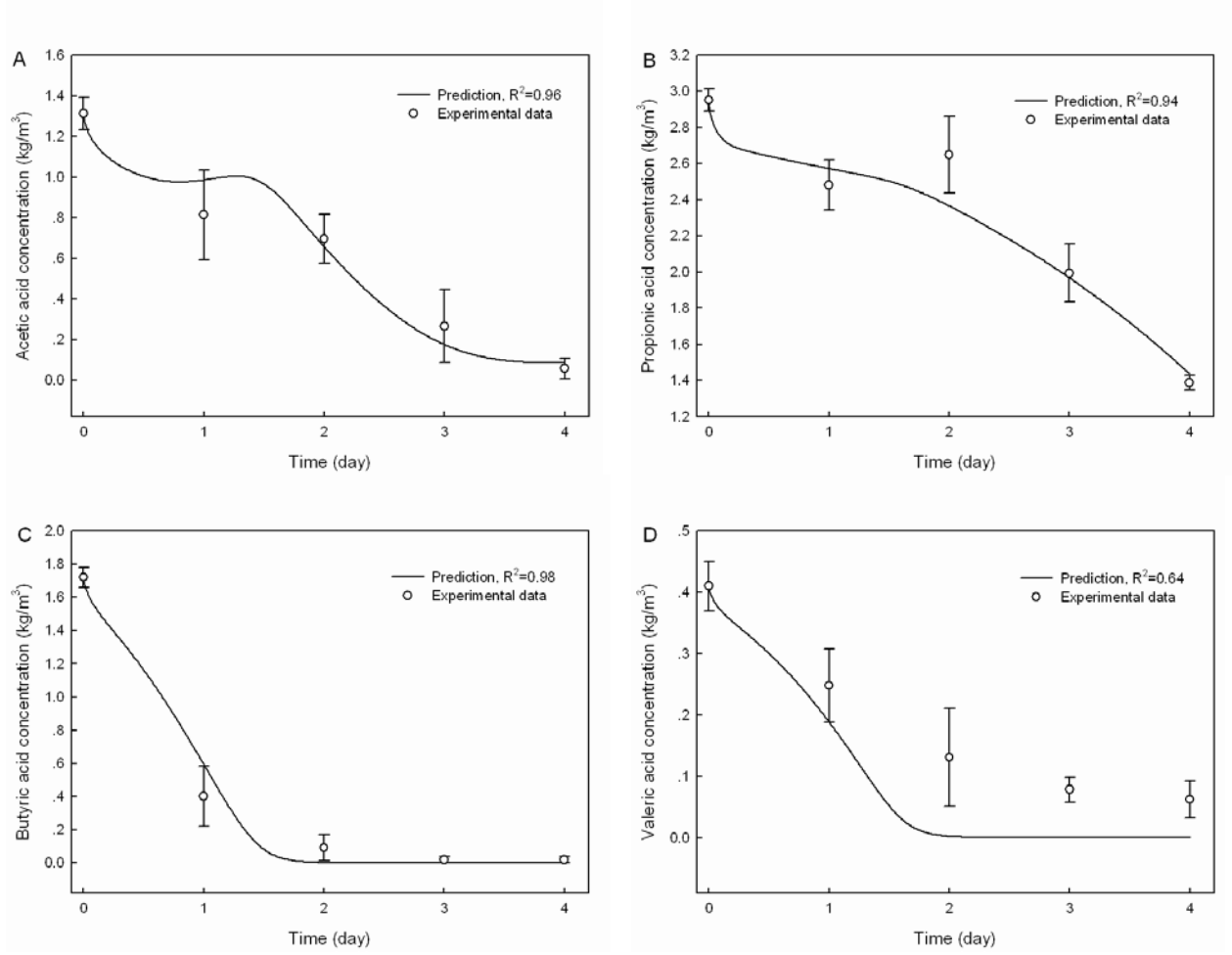

Figure 2.3.4: Change over time in acetic acid (A), propionic acid (B), butyric acid (C) and valeric acid (D) in the UASB seed reactor

The results of the sensitivity analysis are shown in Table 2.3.3. Although there were different sensitivity rankings of acetic acid and CH_4 production between the two reactors, the K_{dis} was the most sensitive parameter as a whole. This suggests that hydrolysis was the rate-limiting step in this HSAD system (Arudchelvam et al., 2010; Zhao et al., 2009). This conclusion is different from that of traditional food scrap AD studies where methanogenesis has been shown to be the rate-limiting step (Velmurugan & Ramanujam, 2011). This suggests that the HSADRS design could enhance the system production rate since sufficient methanogenic bacteria were retained to handle the hydrolytic intermediate products.

Table 2.3.3: Ranking of roots of mean squared sensitivities

1	HSAD upper zone				HSAD lower zone				UASB			
2	Acetic acid		CH_4		Acetic acid		CH_4		Acetic acid		CH_4	
3	Rank	δ^2	Rank	δ^2	Rank	δ^2	Rank	δ^2	Rank	δ^2	Rank	δ^2
	$f_{ch\ xc}$	0.82	$f_{ch\ xc}$	0.45	K_{dis}	0.66	K_{dis}	0.65	$K_{m\ ac}$	0.17	K_{dis}	1.70
	$f_{pr\ xc}$	0.62	K_{dis}	0.21	$f_{ch\ xc}$	0.65	$K_{m\ ac}$	0.63	$K_{s\ ac}$	0.086	$f_{ch\ xc}$	1.24
	K_{dis}	0.53	$f_{pr\ xc}$	0.11	$K_{m\ ac}$	0.63	$f_{ch\ xc}$	0.48	K_{dis}	0.072	$f_{pr\ xc}$	0.69
	$K_{m\ ac}$	0.22	$K_{m\ ac}$	0.034	$f_{pr\ xc}$	0.35	$f_{pr\ xc}$	0.29	$f_{ch\ xc}$	0.067	$f_{si\ xc}$	0.57
	$K_{s\ ac}$	0.095	$f_{si\ xc}$	0.019	$f_{si\ xc}$	0.29	$f_{si\ xc}$	0.16	$f_{pr\ xc}$	0.054	$f_{xi\ xc}$	0.38
	$f_{si\ xc}$	0.066	$f_{xi\ xc}$	0.013	$f_{xi\ xc}$	0.19	$f_{xi\ xc}$	0.11	$f_{si\ xc}$	0.023	$K_{m\ ac}$	0.065
	$f_{xi\ xc}$	0.044	$K_{h\ CH}$	0.006	$K_{s\ ac}$	0.10	$K_{s\ ac}$	0.028	$f_{xi\ xc}$	0.015	$K_{s\ ac}$	0.031
	$K_{h\ CH}$	0.012	$K_{s\ ac}$	0.003	$K_{h\ CH}$	0.011	$K_{h\ CH}$	0.011	$K_{h\ CH}$	0.001	$K_{h\ CH}$	0.024
	$K_{h\ PR}$	0.008	$K_{h\ PR}$	0.002	$K_{h\ PR}$	0.007	$K_{h\ PR}$	0.004	$K_{h\ PR}$	0	$K_{h\ PR}$	0.013

1–Compartments; 2–Outputs; 3–Comparison of sensitivity; δ^2–Roots of mean squared sensitivity

2.3.4.3—Effect of recycled methanogenic seeds on methane concentration in the high solid anaerobic digestion reactor

The established model was used to predict the effect that the recycled methanogenic seeds (from the UASB seed reactor to the HSAD reactor) had on the CH_4 concentration in the HSAD reactor. This is a particularly appropriate issue to explore with modeling, as it is difficult to separate the methanogenic bacteria from the other microorganisms in the experiments, especially in large-scale experiments.

This process can be understood in terms of removing or including the function of methanogenic bacteria in the recycled effluent from the model. The recycling rate of effluent was set at 0.14 m^3/day, while loading rate was set at 15 kg COD/m^3/d. Figure 2.3.5 (A) and (B) shows the change in gas composition over time in the HSAD reactor without methanogenic bacteria. About 65% of hydrogen was produced in the upper zone of the HSAD reactor while the CH_4 content was close to zero due to high loading rate and short HRT. In the lower zone of the HSAD reactor, methanogenic bacteria grew with time in a low TS environment. Therefore, the CH_4 content increased with time. Figure 2.3.5 (C) and (D) show the biogas produced by a system with recycled methanogenic seeds (4.87% acetic acid and hydrogen degrading organisms) in the HSAD reactor. No hydrogen was produced even in the upper zone of the HSAD reactor and the biogas had a high CH_4 content (about 60%) in the HSAD system. This agrees well with experimentally determined measurements (63.9% average).

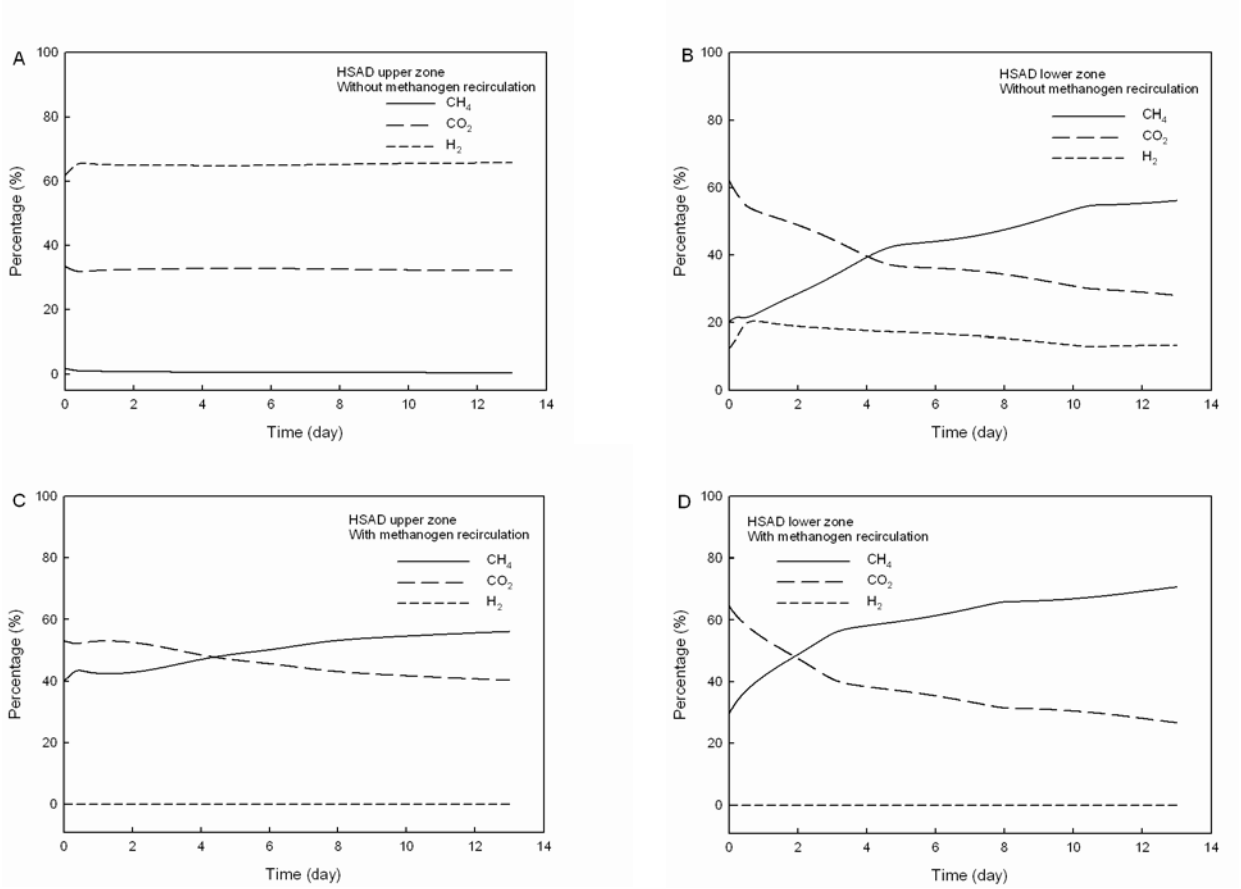

Figure 2.3.5: Effect of recycled methanogenic seeds on CH_4 concentration in the HSAD reactor (A, B) the upper zone and the lower zone without recycled methanogenic bacteria; (C, D) the upper zone and the lower zone with recycled methanogenic bacteria

2.3.4.4—Effect of recycling rate on pH in the high solid anaerobic digestion system

The model was also used to understand the effect of changes in the recycling rate on pH in the HSAD. The results of batch and continuous modes of operation were compared. Batch mode refers to feeding the reactor once with solid waste whereas continuous mode refers to feeding the reactor continuously with solid waste. The loading rate in continuous operation was set at 15 kg COD/m^3/d.

In batch operation, an increase in recycling rate from 0.05 m^3/d to 0.09 m^3/d pushed the HSAD reactor pH back to an optimum range of 7.0–8.0 (Chynoweth & Isaacson, 1987), as shown in Figure 2.3.6 (A) and (B). However, in the continuous mode, the increased recycling rate from 0.14 m^3/d to 0.5 m^3/d caused the pH of the HSAD reactor to deviate from the optimum range as shown in Figure 2.3.6 (C) and (D). Here, the high recycling rate leads to a short retention time for fatty acids to be digested. These results are in accordance with the prediction of grass silage digestion in a 2-stage CSTR digester (Thamsiriroj & Murphy, 2011). In the calculation, it was observed that the acetic acid consumption at a recycling rate of 0.14 m^3/d and loading rate of 15 kg COD/m^3/d was not balanced; although the pH was maintained at the range of 7.0–8.0. This is

because NH_3 was released from solid waste, offsetting the acidification trend caused by acetic acid. In addition, it resulted in a high NH_3 concentration, which inhibited microbial activity.

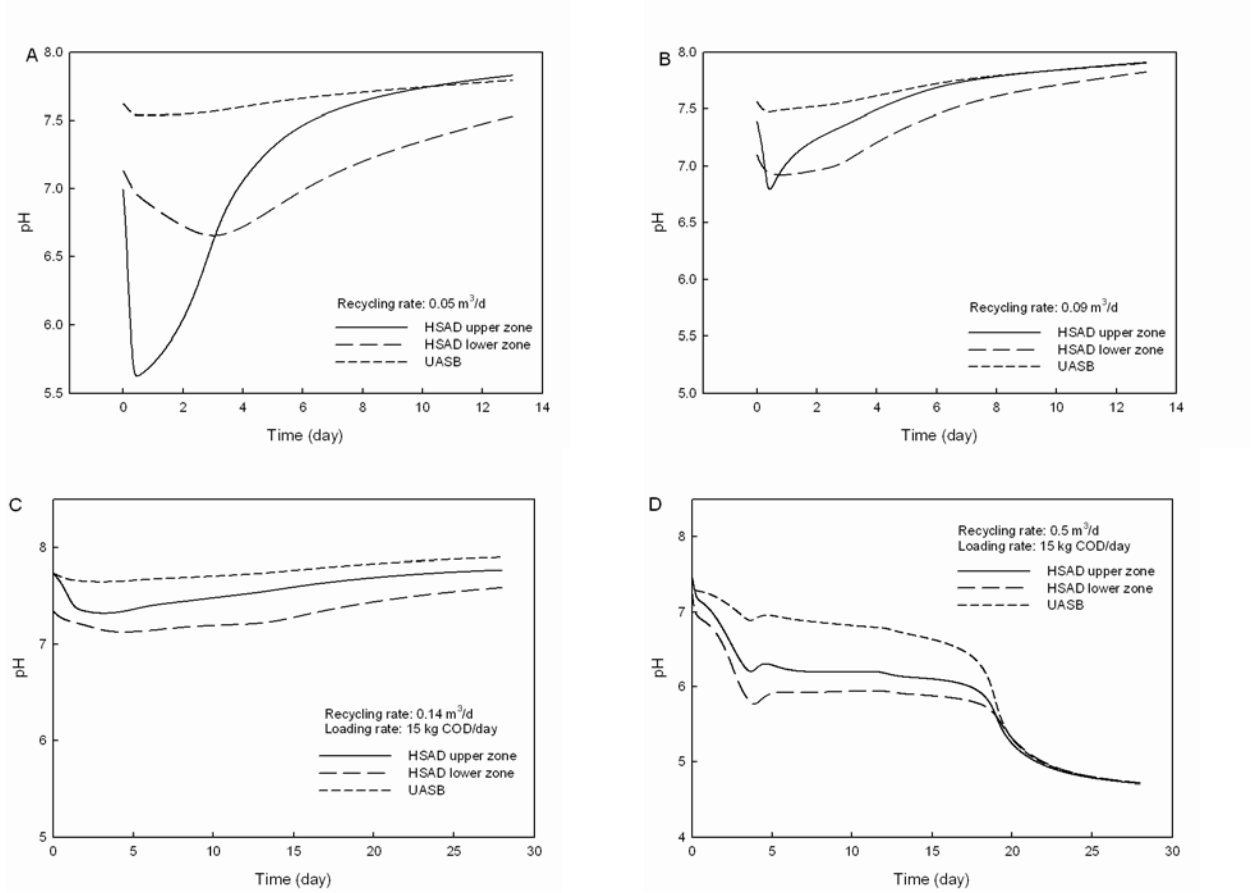

Figure 2.3.6: Effect of recycling rate on pH: (A, B) batch mode at the recycling rate of 0.05 and 0.09 m^3/day; (C, D) continuous mode at the recycling rate of 0.14 and 0.5 m^3/day

2.3.4.5—Comparison of acetic acid in the high solid anaerobic digestion system

Figure 2.3.7 (A), (B), (C), (D) and (E) show the change in acetic acid over time under the conditions of batch mode, continuous mode, increased UASB height, increased UASB cross-sectional area, and increased methanogenic seeding, respectively. The recycling rate of effluent was set at 0.14 m^3/day. In batch mode operation, shown in Figure 2.3.7 (A), the concentration of acetic acid first increased and thereafter decreased slowly in the HSAD reactor while acetic acid was completely consumed in the UASB reactor. Most of the complex particulates were degraded in 8 days, though acetic acid still needed longer time to be completely consumed in the HSAD reactor.

In continuous operation at a loading rate of 5 kg COD/m^3/day (Figure 2.3.7 (B)), the concentration of acetic acid first increased then was maintained stably. If the UASB height was doubled, as shown in Figure 2.3.7 (C), there was little change in acetic acid concentration (compare with Figure 2.3.7 (B)). This indicates the UASB height had minimal impact on the acetic acid concentration over time.

However, altering the UASB cross-sectional area did have an effect on the acetic acid in the HSAD reactor. When the USAB cross-sectional area was doubled (see Figure 2.3.4 (D)), the acetic acid concentration decreased in the HSAD reactor (compare with Figure 2.3.7 (B)). The most dramatic change occurred in the upper zone of the HSAD reactor. This is due to the fact that more acetic acid was produced in the HSAD reactor and transferred to the UASB reactor, allowing for a more complete consumption.

When the recycling rate for methanogenic bacteria was increased 2-fold, as shown in Figure 2.3.7 (E), the acetic acid concentration decreased in the lower zone of the HSAD reactor (compare with Figure 2.3.7 (B)). The concentration of acetic acid in the upper zone of HSAD reactor still remained at a high level due to the high degradable solid concentration.

2.3.4.6—Comparison of methane production in the high solid anaerobic digestion system

Figure 2.3.8 (A), (B), (C), (D) and (E) predict the change in CH_4 production over time under batch mode operation, continuous mode operation, increased UASB height, increased UASB cross-sectional area and increased methanogenic seeds, respectively. Compared to the results for acetic acid production, an opposite tendency was shown in CH_4 production. The highest CH_4 productivity occurred in the UASB reactor while the highest concentration of acetic acid occurred in the HSAD reactor. This indicates that most acetic acid was transported by leachate from the HSAD reactor to the UASB seed reactor, where it was converted into CH_4. In batch mode, shown in Figure 2.3.8 (A), CH_4 productivity first increased with time, reached a peak, and then decreased to zero as acetic acid was depleted.

In continuous operation, at a loading rate of 5 kg COD/m^3/day (see Figure 2.3.8 (B)), the CH_4 production was maintained continuously and steadily in the UASB reactor while there was no CH_4 production in the upper zone of the HSAD reactor. This indicates that the concentration of highly degradable solids inhibited the methanogenic activity. When the UASB height was doubled, as shown in Figure 2.3.8 (C), there was little change in CH_4 production (compare with Figure 2.3.8 (B)). This was in accordance with the acetic acid concentration change shown in Figure 2.3.7 (C). When the UASB cross-sectional area was doubled, as shown in Figure 2.3.8 (D), the CH_4 production increased in the UASB reactor; however, a longer time was needed to reach a peak CH_4 production. The contribution of the increased UASB cross-sectional area for reducing acetic acid might be attributed to lower velocity, i.e. lower mixing intensity. This explanation is supported by other studies, which have shown that vigorous mixing is not suitable in a system where methanogenesis is the rate-limiting step (Padmasiri et al., 2007; Vavilin & Angelidaki, 2005). This is because imperfect (non-vigorous) mixing conditions provides sites where methanogenic bacteria will be protected from rapid acidogenesis. When the recycled methanogenic seeds were increased 2-fold, as shown in Figure 2.3.8 (E), the CH_4 production increased in the lower zone of the HSAD reactor. This confirms other findings that indicate the methanogenic seeds would prefer to be isolated from the concentrated solids.

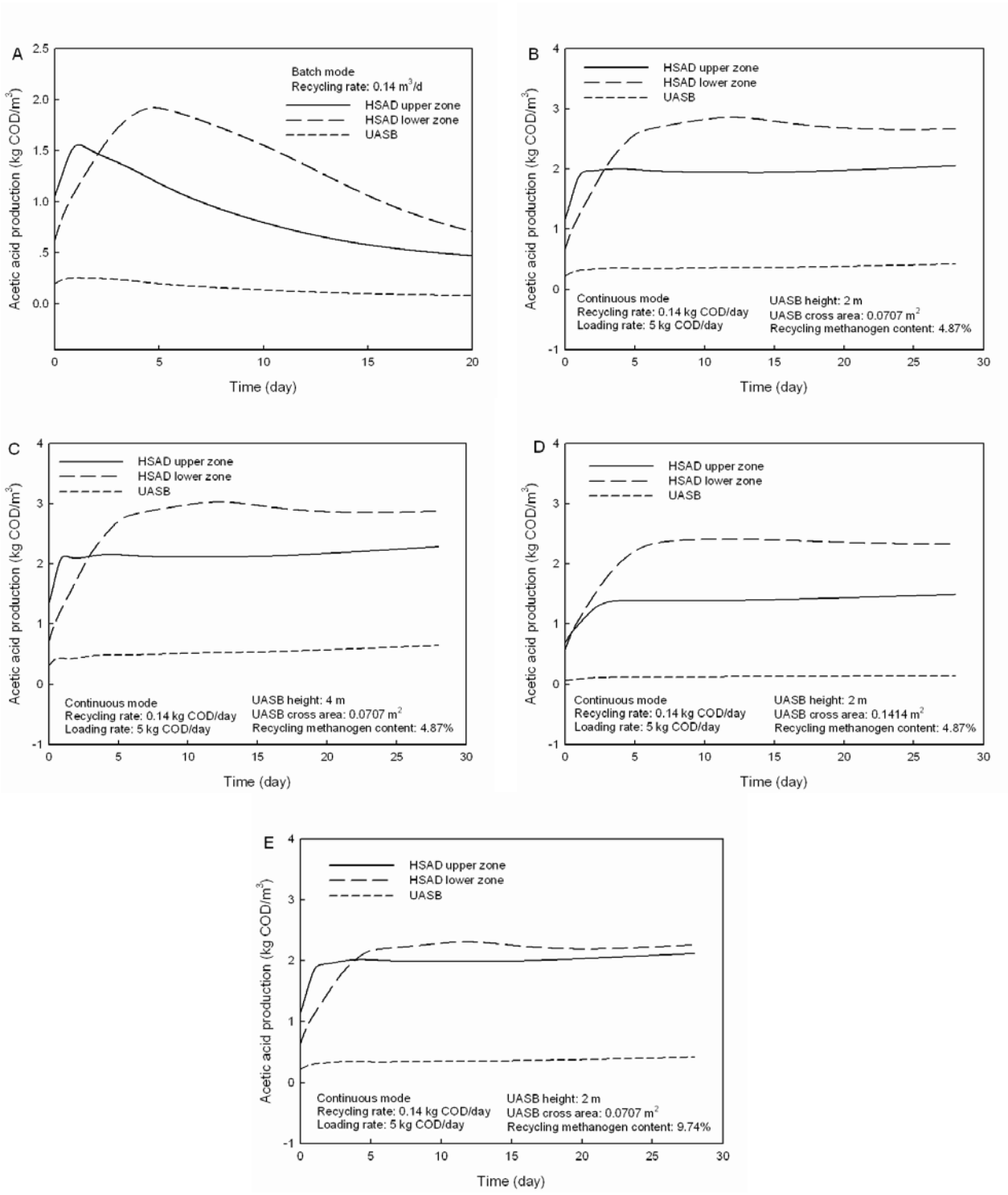

Figure 2.3.7: Comparison of acetic acid production: (A) batch mode; (B) continuous mode; (C) increased UASB height; (D) increased UASB cross-sectional area; (E) increase of recycled methanogenic seeds

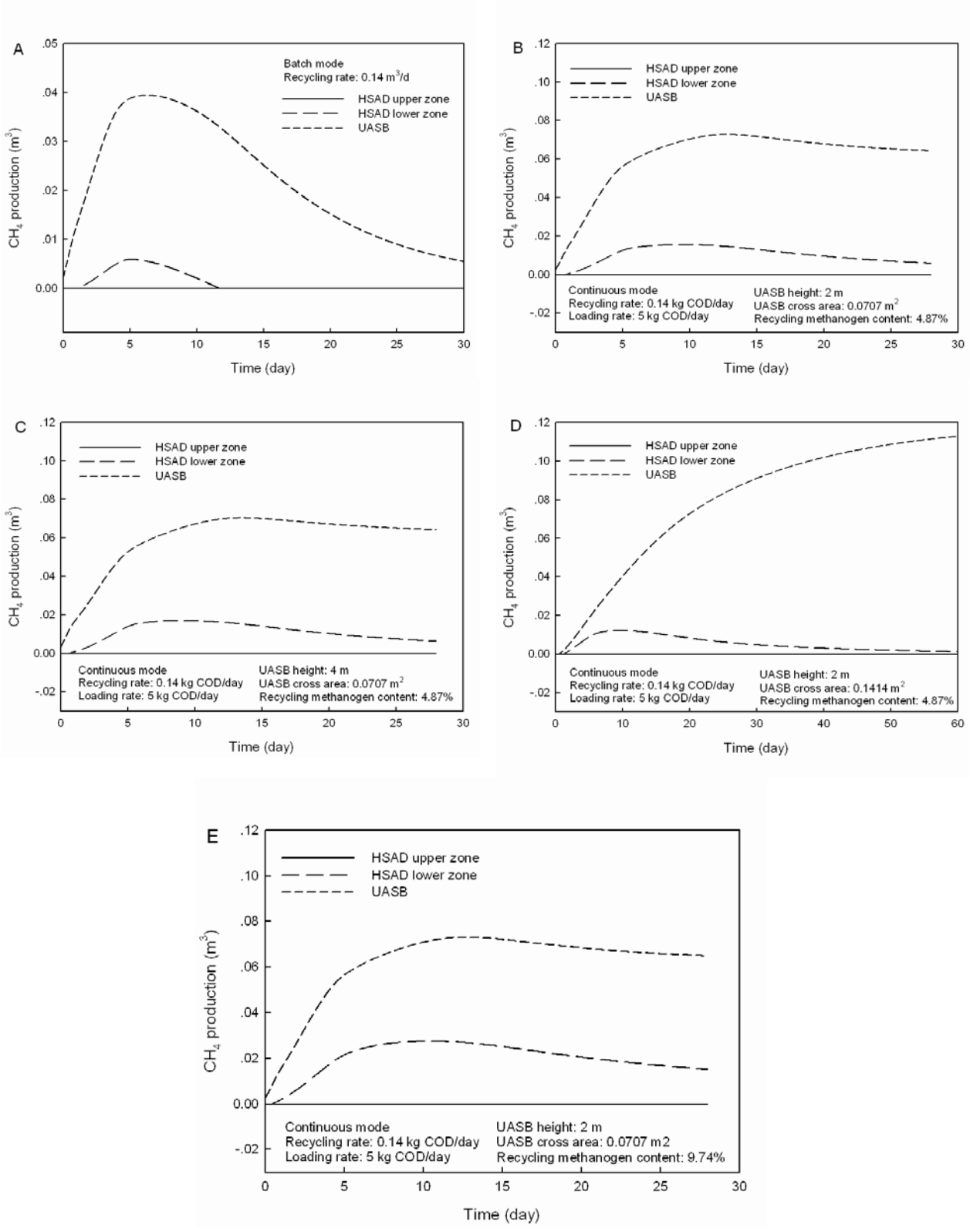

Figure 2.3.8: Comparison of biomethane production: (A) batch mode; (B) continuous mode; (C) increased UASB height; (D) increased UASB cross-sectional area; (E) increase of recycled methanogenic seeds

2.3.4.7—Scale-up effect on methane production

In this study, the modeled two-stage HSAD system was scaled up 100-fold. More specifically, the volume of the CSTR was increased 100-fold while the cross-sectional area and height of ADR were increased 10-fold. Figure 2.3.9 shows the effect the dispersion coefficient had on the CH_4 production. The dispersion coefficient, which represents mixing and mass transfer efficiency, is a useful parameter in traditional reactor design (Li et al., 2013). The dispersion coefficient was set at 20 m^2/day in Figure 2.3.9 (A) and was maintained at the value of the original scale while the dispersion coefficient of 2000 m^2/day in Figure 2.3.9 (B) was increased 100-fold. Figure 2.3.9 (A) shows that the AD process failed because there was not enough mass transfer at the larger scale. Figure 2.3.9 (B) shows the HSAD system operated well when efficient mixing was provided.

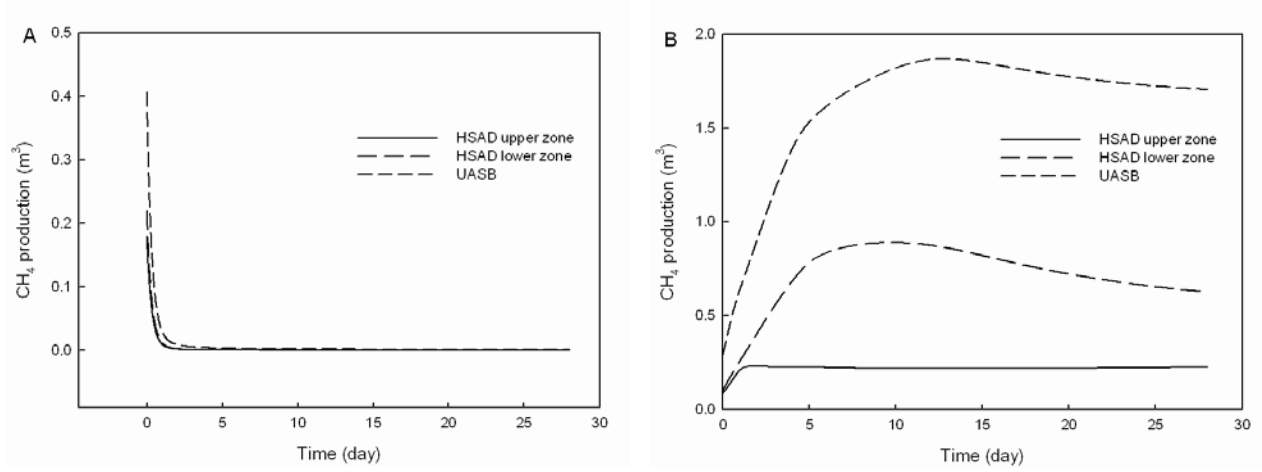

Figure 2.3.9: Effect of dispersion coefficient on the CH_4 production

2.3.5—Conclusions

The introduction ADM1 process model has enhanced the design and construction of new AD technologies for waste treatment by providing an accurate depiction of the AD process, with all of its complexity and interconnectivity between different anaerobic microbes. WSU researchers used ADM1 as a platform for accurately modeling the biochemical and physicochemical reactions taking place in a novel two-stage HSADRS system. The model was developed, and a sensitivity analysis was performed. Good agreement was achieved between modeled and experimental results for a number of different parameters including biogas production, VFA and pH.

Given the good agreement between the experimental data and the model, the model was utilized as a tool to explore alternate design parameters and issues with digester scale-up. The established model of the two-stage HSAD system was used to predict the effect the recycled methanogenic seeds, from the UASB seed reactor to the HSAD reactor, had on the CH_4 concentration in the HSAD reactor. The results showed that recycling the methanogenic bacteria had a significant impact on the CH_4 concentration of the biogas in both the upper and lower zones of the HSAD reactor, with the most impact occurring in the upper zone of the HSAD reactor.

A second study explored the effect the recycling rate had on the pH in both the HSAD (upper and lower) and UASB reactor. As the recycling rate increased in batch operation from 0.05 to

0.09 m^3/day, the pH of both the HSAD and UASB reactor stabilized between 7.5 and 8.0, showing that the digestion process benefited from an increase in the recycling rate. However, if the recycling rate was increased too much, the pH dropped dramatically during continuous operation. Since pH drop has been shown in many studies to be a sign of digester failure it is not advised to increase the recycling rate beyond the threshold determined by the model.

A third study investigated scaling up the reactor by altering the UASB height or cross-sectional area. As the cross-sectional area was increased, CH_4 production increased in the upper zone of the HSAD reactor. However, acetic acid production simultaneously decreased in the lower zone of the HSAD. Therefore, the model clearly showed that there are trade-offs to scaling up the UASB reactor. Having the ability to model this complex process will allow engineers to manipulate the configuration and parameters of digesters to optimize the system without the cost and time of trial and error experimentation.

2.3.6—Disseminate scientific publications developed as a result of this project

The project results have been disseminated through patents, conference presentations, and scientific publications in addition to the project deliverables:

- L. Yu, J. Ma, C. Frear, U. Zaher, S. Chen. 'Anaerobic digester for high solids waste streams'. United States Patent and Trade Office. US Patent: Provisional Patent Application #61563012, Filing Date of November 22, 2011.
- L. Yu, J. Ma, C. Frear, U. Zaher, S. Chen. 'Two-stage anaerobic digestion for solid-liquid phases with recycling effluent'. China Patent: Appl. No: 201210448062.X
- L. Yu, Q. Zhao, J. Ma, C. Frear, S. Chen. Enhance volatile fatty acid (VFA) and biomethane productivity by pretreatment of lawn grass. ASABE International Meeting 2013
- L. Yu, J. Ma, C. Frear, Q. Zhao, B. Zhao, R. Dillon, X. Li, S. Chen. Multiphase modeling of mixing effectiveness in anaerobic sequencing batch reactor (ASBR). Applied Energy (Accepted) 04/24/2013
- L. Yu, Q. Zhao, J. Ma, C. Frear, S. Chen. Experimental and modeling study of a two-stage pilot scale high solid anaerobic digester system. Bioresource Technology 2012, 124(11):8-17.

Pilot-project Pyrolysis and Functionalized Biochars

3.1— Technologies for organic recycling facilities and evolution of these facilities into biorefineries

Manuel Garcia-Perez, Jesus Garcia-Nunez, Brennan Pecha, Nicholas Kennedy, Georgine Yorgey, Craig Frear, Chad Kruger

3.1.1—Abstract

This section represents a review of existing schemes for organic recycling, including a review of the fate of carbon and nutrients in the gas and liquid (leachate) releases. The goal of this review is to determine whether or not emerging technologies (chiefly, pyrolysis and AD) can mitigate these releases from occurring at compost facilities or provide other benefits. Therefore, the review provides background information on composting, and analyzes the most likely scenarios through which AD and pyrolysis could be incorporated into organics recycling facilities, transforming them into biorefineries. It is anticipated that adding AD and pyrolysis technologies can address odor problems plaguing many composting sites throughout the Pacific Northwest, while providing additional revenues to composting facilities via biochar additives to compost, saleable nutrient (N and P) products, and heat and electricity from the pyrolysis unit and digester.

3.1.2—Introduction

Managing residual organic wastes from our cities, including green wastes, food scraps, and recalcitrant materials such as wood scraps and pallets, is one of the major sustainability challenges of the 21st century. Recently, there has been a growing recognition that many “waste” materials that were once disposed of in landfills and WWTPs are in fact valuable raw materials. As such, they can support new local industries, generate renewable energy and yield other sustainable product lines. This document explores the emerging concept of an organic waste biorefinery (Figure 3.1.1). In this integrated waste treatment facility, composting facilities are integrated along with newly emerging technologies: thermal processing, AD, NR and associated technologies that link these bioprocessing facilities together. Existing evidence suggests that this could provide composting facilities with pathways to increase the overall recycling rate of solid organic wastes and generate additional value-added products beyond soil amendments. It would also alleviate some of the existing environmental concerns of composting facilities, and has the potential to improve facility economics. While it is likely that ongoing work will lead to the adaptation of this biorefinery concept before it becomes a reality, this document is meant to summarize the current state of knowledge, and provide a guiding focus for future investments.

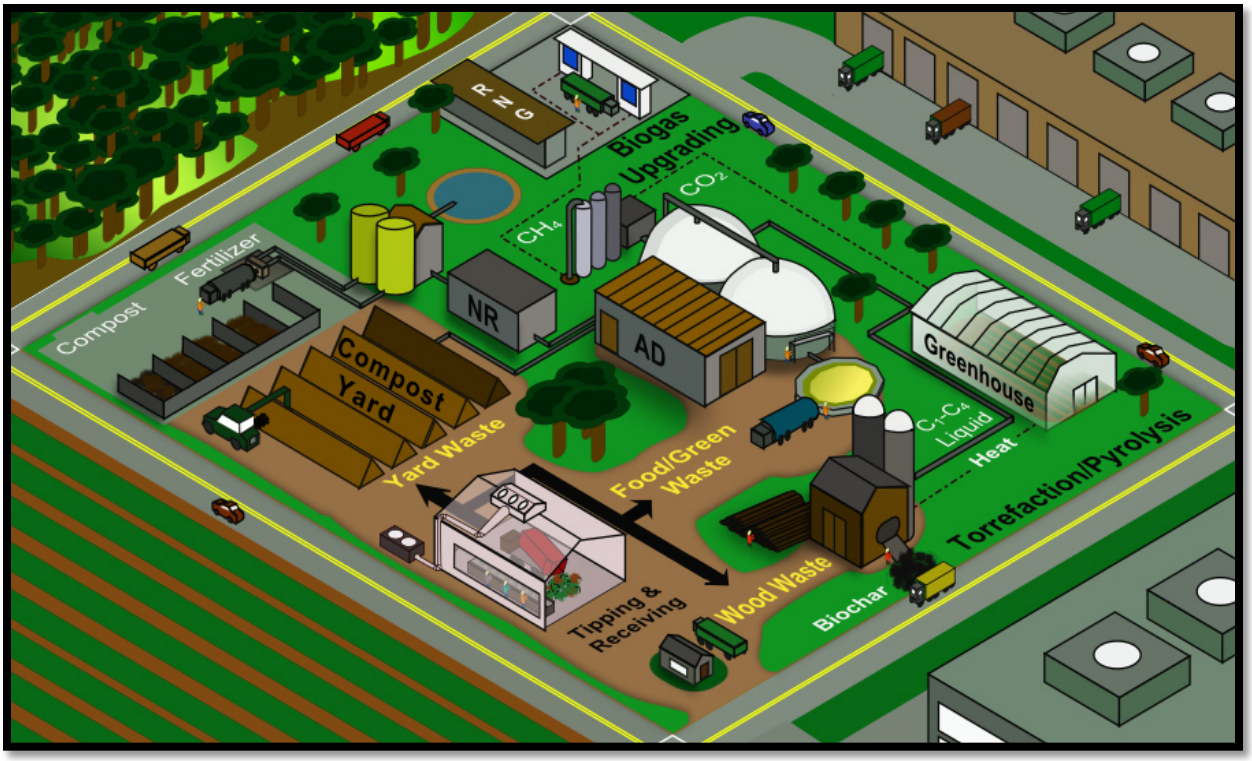

Figure 3.1.1: An organic waste biorefinery that integrates composting, AD, NR and thermal processing

3.1.3—Current strategies for managing municipal solid waste

Municipal solid waste is a heterogeneous waste stream that includes packaging, food scraps, grass clippings, sofas, computers, tires, plastics, glass, refrigerators, and many other items. In 2011, the US generated around 250 million tons of MSW (EPA, 2013a). While this represents a slight decrease from the previous year, waste continues to be one of the top environmental concerns for cities in WA and the nation. The environmental issues associated with discarding MSW in landfills include the generation of CH_4 (a potent GHG), dust, odor, and other gaseous chemicals, as well as the potential release of toxic chemicals and other leachates into water bodies (Ecology, 2011). Landfilling waste also creates costs to taxpayers to build and decommission landfills (Taylor, 1999).

To address these issues, local governments have implemented three general strategies for reducing the amount of MSW entering landfills: source reduction, recycling, and composting (EPA, 2011b). Source reduction has recently begun to successfully transform the waste management landscape. Per person generation of waste in the US peaked in 2000, and is now at 4.4 pounds per person per day, lower than it has been since the 1980s (EPA, 2013). Recycling and composting have also risen rapidly, especially since the 1980s. In 2011, nearly 35% of MSW generated in the US was recycled or composted (Figure 3.1.2) (EPA, 2013a). Items currently recycled at a high rate include auto batteries, newspapers and mechanical papers (e.g. advertising

inserts, direct mail), and steel cans (Figure 3.1.3). Meanwhile, close to 60% of yard trimmings are diverted, predominantly to composting facilities.

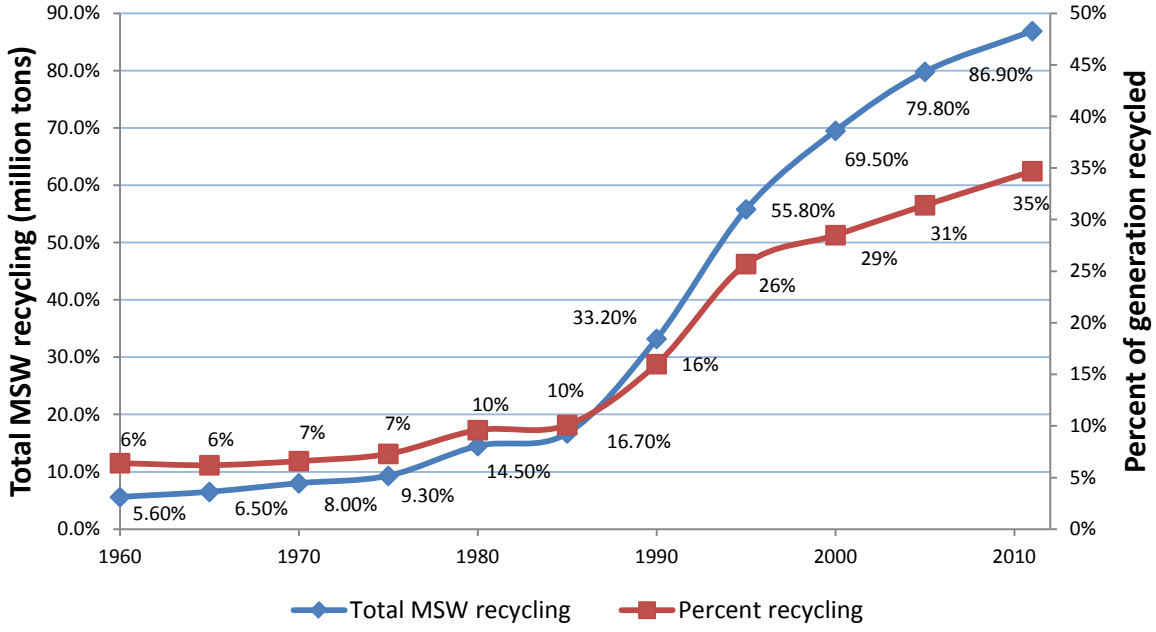

Figure 3.1.2: Combined recycling and composting of MSW from 1960–2011 (EPA, 2013a)

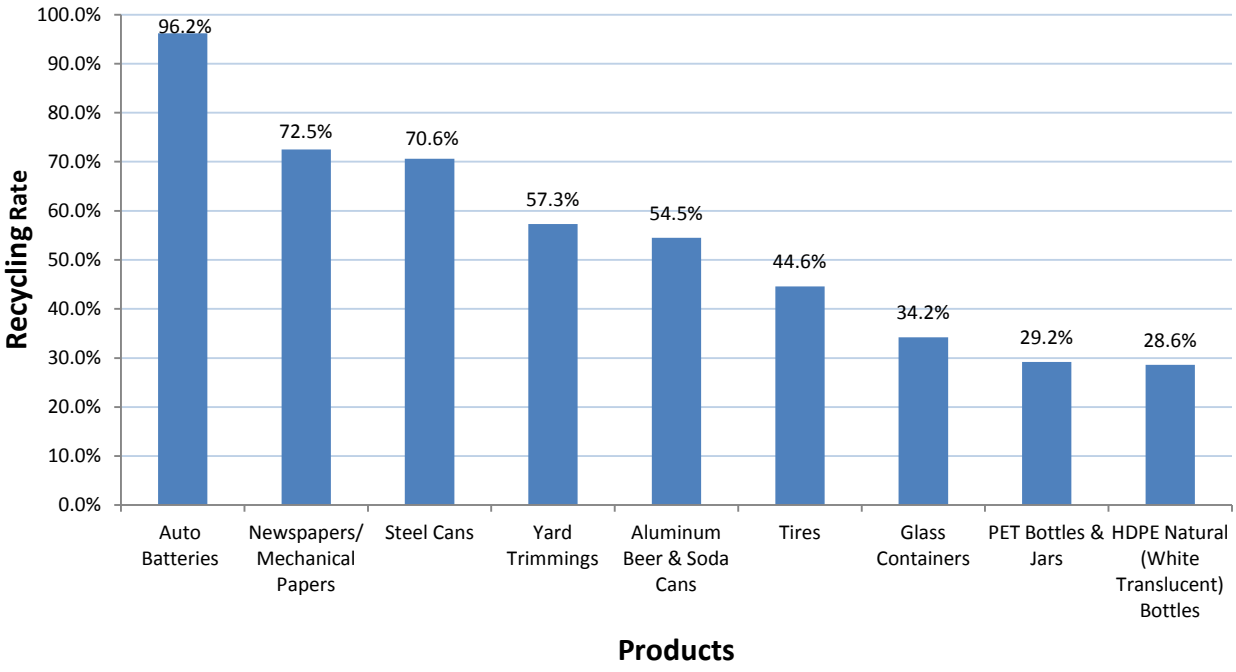

Figure 3.1.3: Recycling rates of selected products in the US in 2011 (EPA, 2013a)

Similar trends in waste management diversion have occurred in WA. Figure 3.1.4 illustrates the total waste generation and waste diversion in Washington since 1999. Total waste generated has decreased since 2005. The amount of waste being sent to landfills has been further reduced by increasing rates of traditional recycling and other waste diversion strategies. In 1999, Ecology began tracking these other waste diversion strategies which includes recycling and reuse of construction and demolition debris, materials burned for energy recovery, and reused materials (Ecology, 2011). The diversion rate has continued to rise over recent years, indicating ongoing success in recycling and composting efforts. However, as in the US, the majority of MSW generated in WA is still being discarded in landfills.

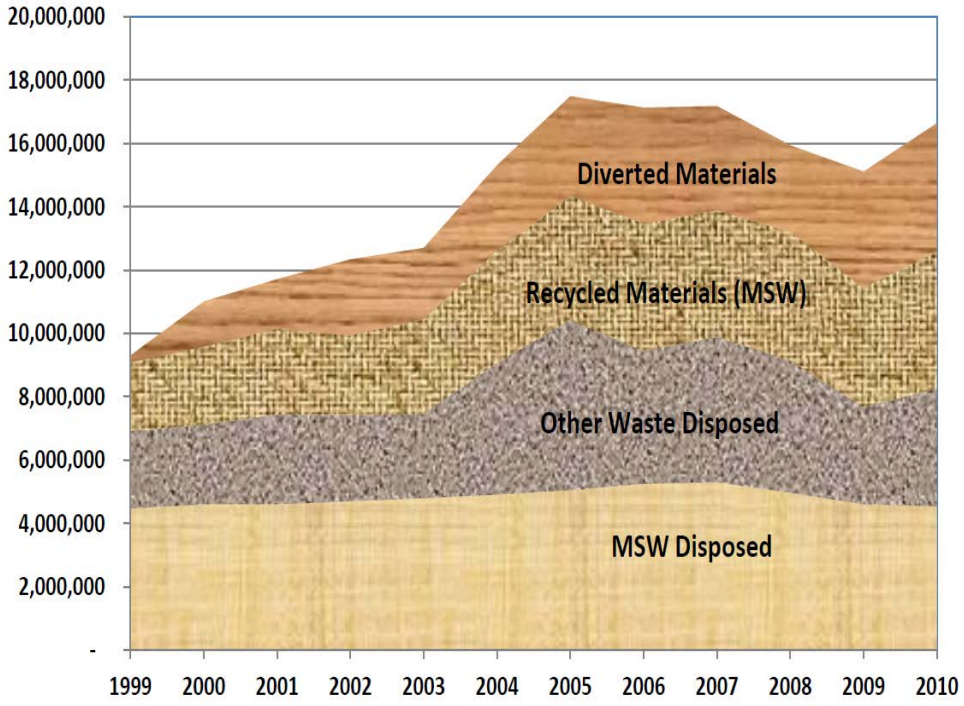

Year	Diversion Rate
1999	28%
2000	37%
2001	41%
2002	45%
2003	46%
2004	49%
2005	48%
2006	50%
2007	47%
2008	47%
2009	55%
2010	54%

Figure 3.1.4: Total solid waste generated in WA (left) and waste diversion rates (right); Diverted materials and diversion rates are for materials that are not traditionally recycled (Ecology, 2011)

Recycling and composting have generated environmental (reduced volume or organics, reduction in CH_4 and odor emissions), economic (lower disposal costs, production of salable final products) and social benefits (food banks) (EPA, 2011b; Lowe & Buckmaster, 1995; Schaub & Leonard, 1996). However, while most organics disposed in the Washington are being recycled at high rates, not all types of organics have seen the same success. Organics in general made up 27.2% of the disposed waste stream in 2009, making it the largest contributor to landfills (Figure 3.1.5). Within that stream, food scraps represented the largest single material disposed of in landfills, 18.3% of the disposed waste stream. Wood debris represented an additional 8.8% of the disposed waste stream (Ecology, 2011).

As ongoing efforts seek to further reduce the amount of wastes landfilled, composting of food scraps is becoming more prevalent. However, continuing efforts to increase this face several challenges. These include the fact that many existing composting facilities to be at or over their

maximum capacities (Ecology, 2011), and many composting facilities accepting food scraps have recently faced challenges due to odor problems (Ma et al., 2013c).\

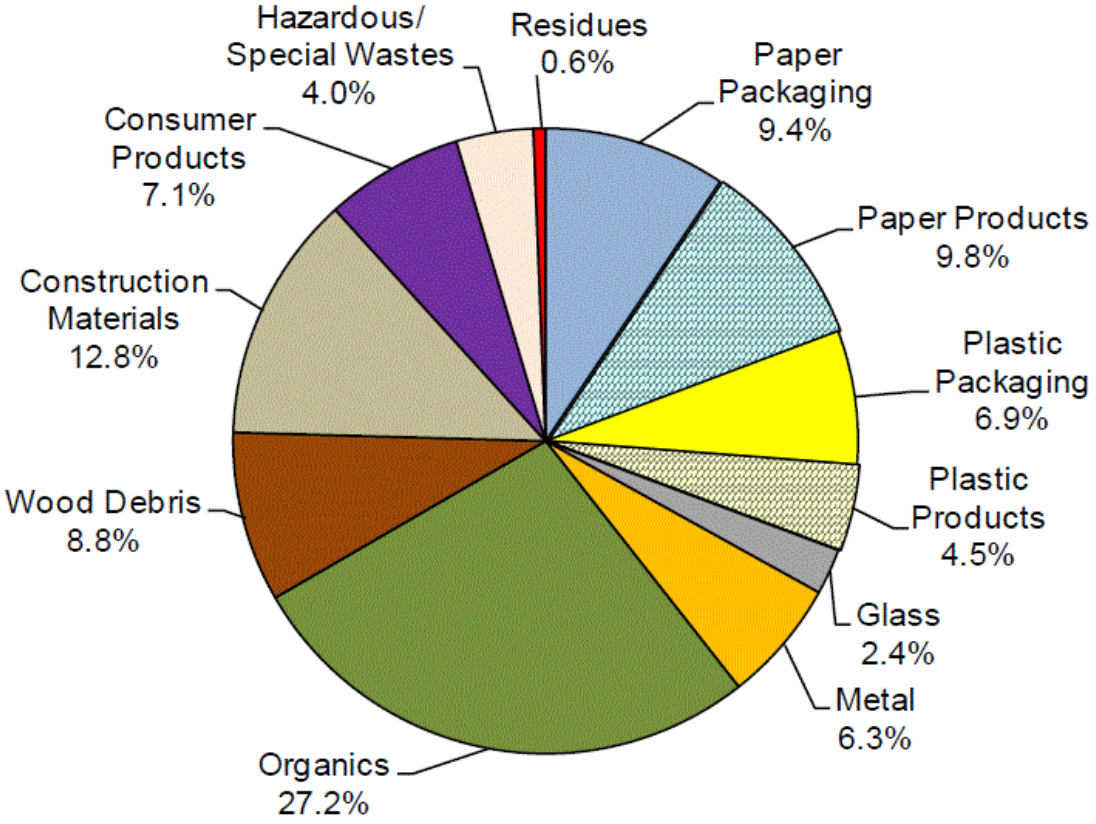

Figure 3.1.5: Composition of disposed waste stream by material class in WA, 2009 (Ecology, 2010)

3.1.4—Composting

Composting, the strategy at the heart of current recovery of organic wastes, is a natural aerobic biochemical process where thermophilic microorganisms transform organic materials into a stable, soil-like product (Schaub & Leonard, 1996). The most common materials composted in US are municipal biosolids, industrial sludge, manure, green waste, septic waste, agricultural waste, food scraps, and other organic portions of MSW (EPA, 2011b). Of these, further detail is merited for two categories:

***Green wastes**:* Green wastes represent the second largest component in the MSW stream, behind paper (EPA, 2013a). In the US, leaves and grass were historically sent to landfills with other refuse. However, in the 1980s many states banned green wastes from municipal landfills. Since then, composting has been used to process most of the diverted green waste (Haug, 1993).

Food scraps: Within the US the number of municipalities with source separated food scrap collection has grown from a total of 24 in 2005 to 183 in 2012, now serving 2.55 million households (Yepsen, 2012). Approximately 60 of these programs are in Washington, roughly

equal to California and many more than other states (Yepsen, 2012). Food scraps have unique properties during composting since they maintain a high concentration of moisture. This can create anaerobic conditions in the compost pile, and may generate odors (Ma et al., 2013c).

During composting, feedstock is placed in a pile, drum, windrow, silo, or other form, depending on the type of process used. Thereafter, decomposition starts to take place. The rate of decomposition depends on a number of physical, chemical and biological factors (EPA, 1994). Finished compost by definition has undergone an initial, rapid stage of decomposition; a longer stage of stabilization; and ultimately an incomplete process of humification (Insam & de Bertoldi, 2007). The specific phases of the process are:

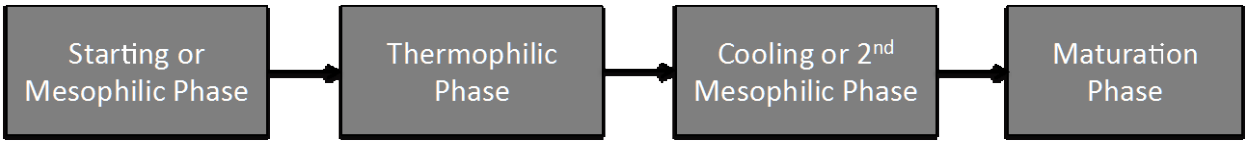

Figure 3.1.6: Composting Steps (Insam & de Bertoldi, 2007)

Composting has been used as a waste management strategy for at least the last 6,000 years. The Sumerians deposited waste in stone-lined pits outside their houses. These wastes naturally degraded over time and were used as a soil (Diaz, 2007). By the thirteenth century, manuscripts written by the Knights Templar indicate the geology, soil biology, art of composting, and the basic elements of agronomy and soil fertility were well understood (Dailliez, 1981). Throughout the 20th century many different approaches to composting have been developed. Some of the more important techniques are described in the following sections.

3.1.4.1—The Indore process

One of the first documented efforts on managing organic residues through composting began in India in the 1930s, when Sir Albert Howard first documented composting and its applications (Diaz, 2007). In collaboration with Jackson, Wad, and other workers, Sir Howard refined a traditional Indian composting system into the "Indore process" (Howard & Wad, 1931). This process involved stacking readily biodegradable material (e.g. human feces, garbage, animal manure, straw, and leaves) to a height of 1.5 m in specially constructed pits 0.6–0.9 m deep. There the waste was allowed to degrade over six months, with two aerations. Due to the infrequent aeration, it is assumed that most of the materials underwent anaerobic biodegradation. Nevertheless, the "Indore process" was widely used and modified throughout the next few decades (Diaz, 2007).

3.1.4.2—Beccari composting system

Mechanical composting processes were first developed in Europe (Diaz, 2007). One widely used early mechanical composting technology was developed by Giovanni Beccari in Florence, Italy, in the 1920s. During the "Beccari" process, feedstock was placed in an enclosed cell, which was designed to control and contain odorous vapors. Wastes first underwent anaerobic fermentation followed an aerobic treatment. At one time, this composting system was used throughout Europe and to a lesser extent in the US. All the systems had issues with odor and leachate and have since been replaced by more efficient modern composting techniques (Gotaas, 1956).

3.1.4.3—VAM composting system

The VAM composting system, another early mechanical composting process that was based on a modification of the Indore process, was developed by a nonprofit utility formed by the Netherlands government. The process, designed to process large quantities of refuse, used mechanical equipment such as trains for delivering feedstock and grappling hooks to remove finished compost from the open compost bins. This was the first documented technique for composting MSW (Fitzpatrick et al., 2005). The refuse was composted from 6 to 8 months, and occasionally underwent mechanical turning. When the cycle was complete a crane was used to dig out the finished compost (Haug, 1993).

3.1.4.4—Rotary drum composting

The first rotary drum system was developed in the 1940s to compost refuse and sludge and was designed by Eric Eweson, in consultation with Sir Albert Howard. Like the Indore system, this rotary drum used an initial anaerobic fermentation step, with the thought that this would accelerate the composting process. After anaerobic fermentation for 3–6 days, windrow composting was used to complete the degradation process (Fitzpatrick et al., 2005). The first full-scale plant based on the Eweson drum went into operation in Sandy, Texas in 1971 and is still in operation today (Fitzpatrick et al., 2005). The technology was licensed to the Bedminster Bioconversion Corp. and they successfully built numerous composting facilities using this technology. This includes a facility in Edmonton, Canada, that is the largest co-composter in North America, with the capacity to process 200,000 MT of residential waste and 25,000 dry MT of biosolids each year (Bedminster, 2013).

Figure 3.1.7: Edmonton Composting Facility using a rotary drum composting technique (Source: www.bedminster.com)

3.1.4.5—Reactor systems

Another type of composting that was developed in the latter half of the 20th century is the reactor system. Agitated bed and silo systems are forms of reactors. In agitated bed systems, composting takes place between walls that form long, narrow channels and a turning device is set on rails at the top of the walls to promote mixing throughout the rows (Fitzpatrick et al., 2005). Silo systems are large vertical reactors that house feedstock for natural degradation. Internal augers turn and mix the feedstock and finished compost is removed from ports in the center (Fitzpatrick et al., 2005).

3.1.4.6—Windrow and static air composting

Among the composting techniques used in modern, commercial scale composting facilities, the two most commonly used systems in WA are windrow and static air composting. Windrow composting is the most common non-reactor, agitated solids bed process. It is employed for composting manures, sewage sludge, leaves, green waste, and food scraps. In this system, waste is piled into long windrows, and aerobic decomposition takes place over a period of time. In many systems, materials are turned with specialized equipment. Ventilation is provided by forced aeration or through a natural chimney (Misra et al., 2003). A roughly trapezoidal cross section is typically observed with sludge-based windrows, though the actual shape is largely a function of the feedstock characteristics and the turning mechanism used (Haug, 1993).

Windrow composting systems are popular because they typically do not require dedicated specialized equipment (Fitzpatrick et al., 2005). This type of composting system is ideal for small to medium scale composting operations but can run into odor problems when even moderately wet feedstocks are mixed into the piles, creating anaerobic conditions (Fitzpatrick et al., 2005). To help with this issue, in the 1970s the US Department of Agriculture Biological Waste Laboratory developed the aerated static pile composting system. In this aeration system, feedstock is placed into rows on top of air distribution systems (see Figure 3.1.8), and air is pumped by fans through perforated pipes to help it maintain an aerobic process. Unlike windrow processing, aerated static piles are not turned.

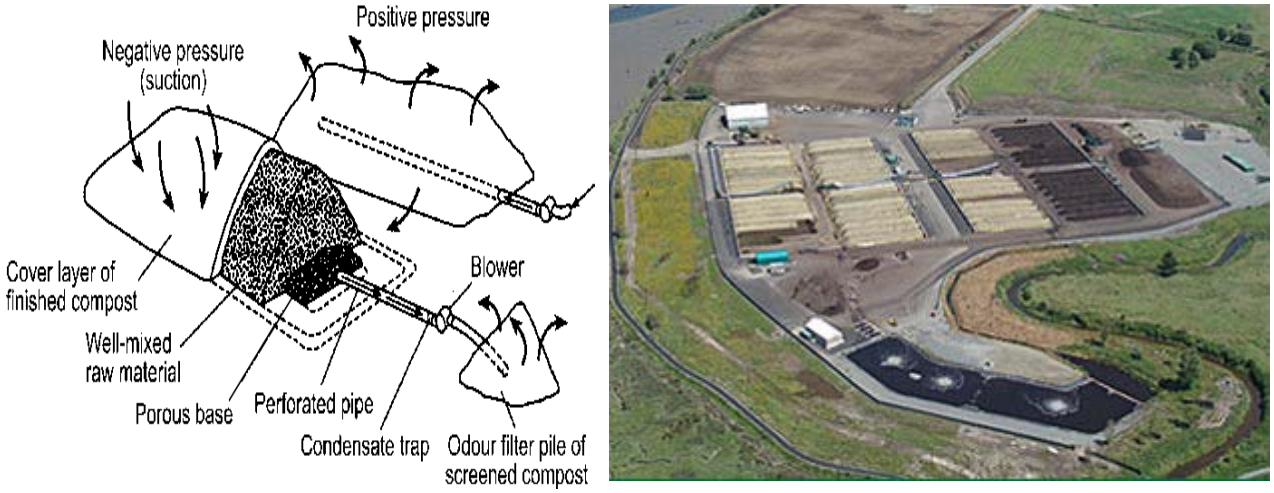

Figure 3.1.8: Window composting with forced aeration design (left) (Dougherty, 1999) composting at Cedar Grove composting facility utilizing windrows in Everett, WA (right) (source www.cedar-grove.com)

Many commercial-scale composting facilities in Washington use windrow or static air composting techniques. Particularly in wetter climatic conditions, an increasing number of composting facilities are using a semi-permeable cover to reduce the impact of moisture and release of odor. Synthetic micro-pore or breathable fabric technology is expensive, but numerous studies show up to 80–90% reduction in total VOC, NH_3, and other odorous compounds compared to non-covered piles (Card & Schmidt, 2008; Card & Schmidt, 2012). Covers can also assist in biofilter odor sequestration, depending upon aeration methodology and biofilter incorporation. However, use of this technology does not completely prevent odor release,

especially during building, preparation, and uncovering of piles (Bary et al., 2012; Winges, 2011).

3.1.5—Acceptance of post-consumer food scraps at composting facilities

Most of the recently established food scrap diversion programs, including the successful programs established in King County and the City of Seattle, send food scraps to existing compost yards. In some cases, this is placing pressure on existing organics processing infrastructure dedicated to aerated compost treatment (Ma et al., 2013c), contributing to issues with odor and leachate release. For example, Cedar Grove Composting received multiple odor violations in 2013 because residents from the nearby town of Maryville, WA complained about odor (Heffter, 2013). Another compost facility, Nature Needs, in North Plains, Oregon, was forced to stop receiving food scraps to their composting facility due to odor. Local residents compared the composting smell to dead animals, rotting flesh and an open sewer (Profita, 2013).

Odors are the result of specific compounds that can be produced before materials arrive at the compost yard, during compost handling and preparation, or during actual composting (Winges, 2011). Compounds primarily responsible for odors include organic sulfides, mercaptans, amines, and VFA (Goldstein, 2002; Miller, 1993). Terpenes, NH_3, alcohols, and H_2S can also contribute to odor (Epstein, 1997). A number of factors control the production of odorants at compost facilities: feedstock, nutrient balance and elemental ratios, oxygen, aeration, time, moisture, bulk density/porosity, temperature, and pH (Buckner, 2002; Coker & Gibson, 2013; Eklind et al., 2007; Ham & Komilis, 2003; Miller, 1993; Sundberg et al., 2011). For more information on how odor is caused and the ways composting facilities are currently trying to improve odor control, refer to a review by researchers at WSU (Ma et al., 2013c).

Another serious concern with composting food scraps is due to leachate release during the compost process. Leachate can arise when high moisture content impacts the compost pile. One field demonstration on food scrap composting showed that fecal coliform and salmonella were present in leachate throughout the bulk of the composting process, potentially creating health issues if not properly managed (TetraTech, 2002). Other environmental concerns associated with low to medium technology composting facilities include phenols above groundwater discharge standards, BOD above normally acceptable levels, and pesticide residues remaining in the finished compost (Williams, 1991). When not properly processed, food scraps can also negatively impact product quality and put stresses on facility economics (Brinton, 2000; IWMB, 2009).

3.1.6—Biorefinery model

There are multiple ways to improve odor issues, leachate, and compost quality when composting food scraps and other wet wastes. Process changes (physical chemical, operational, infrastructural, and biological) are one important class of strategies (Ma et al., 2013c). Meanwhile, the combination of different technologies (composting, thermal processing, AD, and NR) into an organic waste biorefinery has the potential to assist in limiting the production of, and controlling, odorous compounds, while creating a range of environmental and economic benefits.

A biorefinery is a facility that integrates biomass conversion processes and components to produce a multitude of different products including fuels, power, and chemicals from biomass (NREL, 2009). Among existing biorefineries, two types dominate, based on the source of raw materials (Ohara, 2003). Some biorefineries process mainly dedicated crops that are grown solely for this purpose (e.g. corn to ethanol processing in the US). In contrast, Japan and some countries in Europe process wastes in biorefineries, due to the tighter space constraints for landfills and composting, and more limited agricultural production. In these biorefineries, old paper, lumber waste, animal waste and food scraps provide the materials for fermentation and energy production in the form of biogas, heat, and power (Ohara, 2003). These facilities can also produce compost, alcohols, nutrients, or other products. Techniques and technologies can be taken from the large-scale landfill-based biorefineries and integrated at composting facilities.

3.1.7—Converting composting facilities to biorefineries

The new biorefinery vision for existing and new composting facilities includes AD, NR, and thermal conversion unit operations, along with associated technologies to produce high quality byproducts (RNG, fertilizers and greenhouse crops). Innovative integration is used throughout to reduce operating and capital costs. Figure 3.1.1 and Figure 3.1.9 illustrate the biorefinery concept that is built upon a traditional windrow composting facility. Individual units, and the resulting synergies and integration, are described below:

Figure 3.1.9: Organic waste biorefinery

3.1.7.1—Tipping and processing

Waste haulers and the public enter the upgraded organic recycling facility at a single entrance where they pay a tipping fee to dispose of their organic waste. Suitable biomass will be split into three general waste streams at a receiving and processing center:

- green waste
- food scraps, co-mingled and contaminated green waste /food scraps
- wood residues

The receiving and processing center incorporates current infrastructure and technology to remove contaminants, and pre-process wastes efficiently. The center is a large building that allows trucks and loaders to enter for sorting and removal of non-organic materials. Pretreatment takes place within this building, and is particularly important for removing unwanted materials that are present in food scraps and co-mingled waste streams. Separation of cardboard, plastics, metals, etc. can be achieved through a combination of mechanical and human interaction. Mechanical processes such as conveyors, disc screens, shredders, magnets, etc. can be used for the separation and removal of non-organic materials. As appropriate, removed contaminants can

be processed thermally (wood, paper, cardboard, non-recyclable plastics) or sent to a recycling center (recyclable plastics), with landfilling being the last resort.

The receiving and processing center also plays an important role in odor control, as food scraps and green waste (e.g. grass clippings) often enter the compost yard already partially degraded, putrescent and releasing significant odors (Ma et al., 2013c). The facility should therefore incorporate advanced design for this purpose. Negative air pressure contains odors within the building. Adequate size and air handling capacity allows receiving, loading, mixing, and seeding to be carried out under negative air pressure conditions (Goldstein, 2012). Design also allows for 'first in, first out' processing, ensuring that materials do not spend extended periods of time decomposing in the receiving and processing center (Goldstein, 2012). Floor aeration systems can encourage biological processes that control acid chemistry and release of odors, while accentuating airflow to biofilters for sequestration of odorous compounds (Coker, 2012).

Biofiltration can be used to treat air from the facility before it is released to the ambient air. biofiltration uses packed beds of porous media (or biofilters) to capture and biologically treat organic odorous compounds from an air stream (Pagans et al., 2007). Biofiltration can treat a variety of compounds simultaneously and is particularly suitable for the low concentration gas streams produced at compost facilities from the large airflow induced by operations (Pagans et al., 2007). If needed, multiple staged technologies can be used to adequately treat high flow rates (Wu et al., 2011). Figure 3.1.9 shows a negative air pretreatment center with a biofiltration unit. After pretreatment, green waste, green/food scraps, and waste/wood waste is sent to its respective processing facility for conversion to value added products.

3.1.7.2—Traditional composting

Green waste and other typical feedstocks collected at current composting facilities can enter directly to the compost yard where traditional composting techniques (e.g. windrows or aerated static pile) will be used to break down the organic matter into a soil amendment that can be sold off-site or used on-site at a greenhouse (described below).

One of the most important reasons for the biorefinery is that food scraps can be separated from entering into the compost process and diverted to a more contained odor reduction process such as AD (described below) (Ma et al., 2013c). However, if odors persist during composting of green waste, biochar from the thermal processing unit (described below) can be used as a bulking agent. Biochar can help reduce odors because it can hold both air and water, encouraging aerobic bacteria and reducing the number of anaerobic pockets (Conte et al., 2012; Prost et al., 2013; Steiner et al., 2011; Yoshizawa et al., 2005). Because it holds its structure over time, and yet can be included in finished compost, it provides some advantages over other common bulking materials such as straw or wood chips (Ma et al., 2013c). When included in the composting process, it also can improve compost quality by promoting humification and compost maturity, and retaining N and other nutrients and minerals (Chen et al., 2010; Dias et al., 2010; Hua et al., 2009; Jindo et al., 2012; Steiner et al., 2010; Tanaka et al., 2006; Tu et al., 2013). Alternatively, it can be mixed with the finished compost to be sold as a high quality soil amendment due to its high water and nutrient retaining properties (Lehmann et al., 2011).

Biochar has strong affinity and capacity for absorbing organic compounds and thus can reduce leachate from leaving the compost site and storage lagoons (Lehmann, 2009). Biochar also has

the potential to be used to strip nutrients from leachate in the composting operation, and spent materials from this process could be sold as a slow-release fertilizer (Clough et al., 2013; Spokas et al., 2012).

3.1.7.3—Thermal processing – pyrolysis and torrefaction

Wood waste that is problematic for existing composting facilities will be sent to a thermal processing facility where heat will be used to break down this feedstock into heat and/or bio-oil (an energy product) and biochar (a charcoal product that can be used for a variety of purposes). In addition to wood waste, on-recyclable plastics that are removed at the pretreatment processing facility can be pyrolyzed to produce bio-oil.

Torrefaction and pyrolysis are two types of thermal processing that operate at different temperatures. Torrefaction is an anaerobic thermal treatment in the relatively low temperature range of 225–300°C. The process is used mainly to produce biochar and heat. Pyrolysis, on the other hand, is anaerobic thermal treatment process operating at temperatures between 300 and 600°C. It produces biochar, bio-oil, gases and heat. Excess heat as well as thermal heating produced during the char production process can used as valuable BTUs for other processes that would otherwise require off-site energy (e.g. AD, NR, product drying, and greenhouses).

Both near and long-term visions are available for integration of these thermal processes into the biorefinery.

Near term

In the near term, pyrolysis/torrefaction would be used for the production of heat and biochar to control odors and other environmental issues at the biorefinery, primarily as described for the composting operation above. In addition to these internal uses, the biochar could be sold on its own as a charcoal product or stand-alone soil amendment.

In addition to biochar product, excess heat is produced at the pyrolysis/torrefaction facility. Heat that is produced during the pyrolysis/torrefaction process can be piped to the public, or utilized on-site for operation facilities, including the digester, NR operations (described below), or greenhouse.

Long term

The long vision for thermal processing is mainly for the production of bio-oil. Biochar will still be produced, but not to the same extent as in the near term. Under this configuration, larger C_6 compounds will be separated from smaller C_1–C_4 compounds via condensers constructed on-site. The larger C_6 compounds, comprising the bio-oil, will be sent to oil refineries for further refinement into a drop-in transportation fuel. Smaller C_1–C_4 condensates will be sent to the anaerobic digester (described below) for energy production. For more information on the integration of C_1–C_4 compounds in AD, see section 1.3 of this document. Biochar, meanwhile, can be used in a variety of ways on-site or off-site as explained previously.

Figure 3.1.9 depicts the integration of the thermal processing facility within the biorefinery concept. In this scenario, the long term use is depicted with the both biochar and bio-oil being produced. On-site condensers are being used to fractionate the oil. The C_1–C_4 condensate is

being pumped to the high rate digester for biogas production and the heat is being sent throughout the facility as needed.

3.1.7.4—Anaerobic digestion

Food scraps, co-mingled food and green waste, and specifically received organics from industry (e.g. pre-consumer food scraps) will be source separated in the receiving center and sent to ADs on-site. While numerous AD designs exist, they are basically divided into two dominant classes, slurry-based and dry/high solids. Dry/high solid designs have been of keen interest to compost type facilities due to their relative use of less water, which is an important factor when considering a facilities' need to reduce leachate/wastewater production and maintain their present water balance. On the other hand, slurry-based systems generally can achieve higher reaction and biogas production rates but do so while diluting incoming feed and producing more wastewater (Ewing & Frear, 2012).

AD processing will be used to produce biogas, while reducing odors, pathogens, and GHG emissions (Martin, 2004; Martin & Roos, 2007; Martin, 2005; Roos, 2008). Many different pathways exist for utilization of biogas, including production of heat with a boiler, production of electricity with a combined heat and power engine, and production of RNG through removal of CO_2, H_2S, and water vapor. In this particular biorefinery concept, the biogas will be upgraded and piped to a fast filling station located in close proximity to the biorefinery for dedicated fleets such as waste haulers. For simplicity, this is shown on-site in Figure 3.1.1 and 3.1.9. This final use was chosen based on a recent assessment of biogas utilization at a proposed AD unit at a dairy operation in the Columbia Basin (Coppedge et al., 2012), showing that RNG, utilizing a fast fill station, had the highest profit potential compared to other scenarios. Within the biorefinery, a co-benefit of upgrading biogas to RNG is that the stripped out CO_2 can be sent to an on-site greenhouse for the production of organic crops, further reducing the total GHG emissions of the facility.

RNG is also a particularly appropriate end use for the biogas in the biorefinery because RNG can be used directly by the dedicated waste hauling fleet. And, additional cost reductions could be achieved if the empty fleet could coordinate to transport some products (e.g. fiber, compost, soil amendments) off-site to receiving centers.

Besides biogas, the AD process also generates fiber and a nutrient-rich liquid effluent. Within the biorefinery, the fiber will be separated and sent to the compost yard for composting and production of a finished product. Meanwhile, the liquid effluent can be utilized or processed in a variety of ways. In its most simple configuration, the untreated effluent can be applied as saturation water to compost piles in need of additional water and nutrients, with excess flow entering the leachate storage lagoon. A more engineered approach would be to recover the majority of N and P nutrients for sale as soil amendments (as described below). If NR is used, the treated effluent, low in solids and nutrients, is now suitable for use as AD dilution water for the incoming high solids food scraps and green waste. This will reduce overall water use, maintain the present and desired water balance, and permit the use of slurry-based digesters and their more efficient production rates that otherwise would not be feasible (Ewing & Frear, 2012).

3.1.7.5—Nitrogen and phosphorus removal via nutrient recovery

Although the AD process changes the form of N and P in manure, it does not appreciably decrease the total amount of nutrients, most of which are concentrated in the liquid effluent

(Frear et al., 2011). After high rate digestion, the effluent will be sent to a NR system that will strip out N and P, using one of many existing NR technologies to produce a nutrient rich fertilizer (Ma et al., 2013b).The fertilizer can be used either on-site in a greenhouse or sold off-site to nutrient-deficient agricultural operations.

As mentioned above, once nutrients are recovered, the water can be recycled to the digester to dilute high solids feedstocks. It can also be used in the compost operation to add moisture to piles as needed. The process of diverting food scraps from composting and recovering nutrients should also help alleviate the leachate and water imbalance concerns associated with slurry-based AD. For more information on the integration of NR and grass waste/food scraps, please refer to section 1.2.

3.1.7.6—Greenhouses

Many of the outputs produced at the component facilities of the biorefinery, including CO_2, soil amendments, biochar, leachate, and heat, can be utilized in a greenhouse constructed either on-site or nearby. For simplicity, this is shown on-site in Figure 3.1.9. Greenhouses thus become an extremely important component for reducing GHG emissions and preventing leachate from leaving the site. In essence, the greenhouse should be seen as a low-cost sink for pollutants that are being generated at other process facilities. In the absence of the greenhouse, containment and mitigation of these pollutants would come at a higher cost, since infrastructure upgrades would be necessary.

The biorefinery will most likely be located at the urban-rural interfaces due to the costs of urban sites, the public's desire to site biorefineries away from encroaching suburbia to reduce the odor impact, and the need to unload large quantities of compost to agricultural end users. At first glance, this seems like a nuisance to the biorefinery itself, and it raises the transportation costs for wastes, the bulk of which are produced in urban and suburban areas. However, being at the urban-rural interface will allow large enterprises such as Costco and Wal-Mart to co-locate greenhouses in close proximity to the biorefinery. Greenhouses can utilize the CO_2 and waste heat to produce high value products such as cut flowers.

3.1.7.7—Other synergies

While the main process synergies are described above, other potential integrations exist. Further technology development will be needed to investigate these links and the potential they provide to further cut capital and operation costs. For example, the NR technology developed by researchers at WSU has a waste effluent that is high in pH and thus can be used as a replacement absorbent for biogas upgrading, significantly reducing the capital and operation costs of traditional upgrading processes (e.g. water scrubbing, amine scrubbing, pressure swing adsorption). Meanwhile, the effluent coming out of the process will contain higher concentrations of sulfur compounds and carbon, enhancing the nutrient quality of the liquid.

Other interesting possibilities for integration also exist for the biochar beyond those mentioned earlier. Biochar could be used to complete the biogas upgrading process since it has been shown to be an effective adsorbent material for the impurities present in biogas. Biochar could also be used to absorb nutrients from the effluent remaining after NR. This would produce a more nutrient rich soil amendment (if this is its final use). For more information on the nutrient removal properties of biochar, see section 3.3 and 3.4 of the document.

An additional synergy is between the trucking fleet and the fast filling station. By upgrading biogas to RNG standards, a dedicated fleet of natural gas powered trucks can be used to move waste to the facility and switch to an empty back haul and move products off of the facility to receiving centers. Switching to CNG is occurring throughout the US for bus lines, waste trucks, etc. due to the significant reduction in price for CNG compared to diesel and gasoline (Figure 3.1.10)

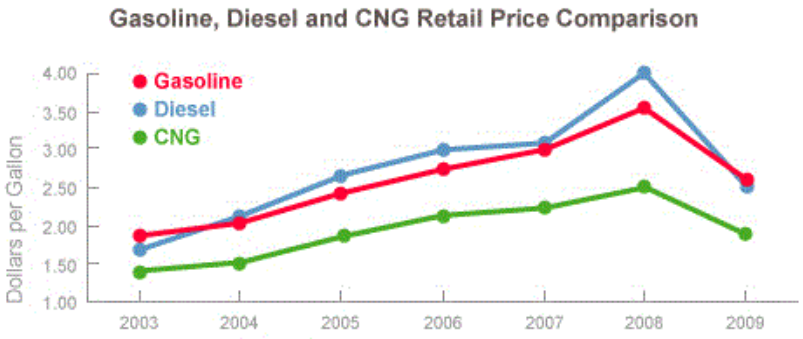

Figure 3.1.10: Price of gasoline, diesel, and CNG from 2003 to 2009 (source: www.socalgas.com)

3.1.8—Environmental and economic benefits

3.1.8.1—Environmental benefits

The biorefinery concept has the potential to provide a number of environmental benefits, including decreasing landfilling of wastes, recycling nutrients, harvesting renewable energy, and decreasing GHG emissions. It also has the potential to lessen the environmental footprint of current composting facilities, by more fully treating leachate and lessening odorous and harmful air emissions.

In addition to these environmental benefits, the biorefinery has sustainable heat and energy balances. Any refinery must maintain an effective heat and water balance throughout to maintain the efficiency of the plant and reduce water consumption and costs. Water is a precious commodity to a refinery because it allows for heat to be transported throughout the refinery and energy to be produced in a usable form (water to steam to electricity). In addition, reducing water use at the refinery will also reduce the water needing treatment and disposal downstream. This is the same case for this organic waste biorefinery and the unique integrations between the unit operations are able to effectively maintain a balance of heat and water. In this biorefinery, processes are consuming energy/water/heat but also creating energy/heat/wastewater to minimize heat and water consumption.

3.1.8.2—Economic benefits

While additional economic analysis needs to be carried out (particularly with regard to added capital, management, and operating costs), several features of the biorefinery model show promise in terms of improving economic performance compared to a stand-alone composting facility. It generates multiple products (e.g. compost, nutrient rich fertilizers, RNG, and biochar) that recycle nutrients, harvest renewable energy, and could improve facility economics. Beyond these products, the environmental benefits described above could in many cases result in credits

or payments such as carbon credits, renewable energy credits, RINs, LCFS, or nutrient trading credits. And lastly, integration provides multiple opportunities for process synergies that cut costs (e.g. heat from one process can be used for another process).

The biorefinery also has the potential to generate economic incentives that will lead to better congruence between achievement of economic and environmental goals. Stand-alone composting facilities rely mostly on tipping fees, with relatively minor contribution from the sale of compost product(Renkow & Rubin, 1998). This can creates adverse incentives that can encourage facilities to accept high quantities of waste, with less emphasis on compost product quality. In contrast, the biorefinery concept towards an emphasis on multiple co-products and revenue streams.

3.1.9—Conclusion

Each component of this biorefinery has been previously developed and used at the commercial scale for other purposes and each has been significantly advanced over the past decade to improve performance and reduce costs. As can be seen elsewhere in this document, researchers at WSU have been testing and refining integration between the core components of this biorefinery (e.g. composting, AD/NR, and pyrolysis/torrefaction) as strategies to reduce environmental impacts (odors, leachate, GHG) and capital and operation costs.

The biorefinery concept is still developing, and is not without its own set of technical and economic challenges. Each processing facility adds major capital and operating costs as well as complexity. However, we have focused on introducing systems that integrate well to reduce overall costs, and produce energy or other revenue-generating products. One major goal of future research should be to generate economic and performance data that can be used to evaluate the economic prospect of each additional facility. Over time, this should result in the development of a compelling business model that could provide current composting facilities with a pathway to enhance their sustainability efforts, increase waste management and decrease odor production.

3.2— Development and validation of a mathematical model for an Auger pyrolysis reactor

Manuel Garcia-Perez, Jesus Alberto Garcia-Nunez, Jeroen de Graaf

3.2.1—Abstract

To allow for the prediction of the distribution of pyrolysis products and the temperature profiles within biomass under different reaction conditions, a pseudo-homogeneous single particle model for pyrolysis was developed and implemented in MS Excel. The model took into account primary and secondary reactions as well as internal and external heat and mass transfer. In a separate study (also described as part of this task), a mathematical model that takes into account the structure of biomass cells was developed and implemented in COMSOL Multiphysics to determine the effective heat and mass transfer of biomass particles; these are the parameters that are needed for the single particle model.

The COMSOL model was validated by comparing the model predictions to reported values for effective mass diffusivity for steam in wood and the effective thermal conductivity of biomass particles. Model results agree well with the experimental data reported in the literature. The simulation results obtained with COMSOL lead to the conclusion that the geometry and structure of biomass cells have a significant influence on the effective heat and mass transfer parameters in woody biomass.

The single particle model was also validated by comparing model results with those reported in an experimental study carried out at Curtin University in Australia. In general the model predicts well the temperature profiles in different internal positions, though it is necessary to take into account some exothermic behavior that occurs during pyrolysis of a wood cylinder in a temperature range of 350 and 400°C. However, due to the fact that there is no information about product yields from the experiments carried out in Australia, it was not possible to validate this aspect of the model. Therefore, a plug flow model describing the behavior of the Auger reactor was developed. Experimental data on the behavior of a 1 kg/h Auger reactor was collected and used to validate the proposed model.

Because of the complexity of this work, this section highlights some of the key outputs from the mathematical models developed. A more in-depth and detailed description of model development, as well as a complete list of all parameters, equations and predictions, is included as Appendix A.

3.2.2—Introduction

The goal of this project was to develop a model that could predict the distribution of pyrolysis products and temperature profiles within woody biomass under different reaction conditions. As described in Section 3.1, models are powerful tools for researchers and engineers due to their ability to quickly and accurately predict outcomes to experiments that would normally take extended periods of time and resources to achieve in the laboratory. For pyrolysis, reliable modeling would open up the possibility for researchers and industry to experiment with the parameters inside the model to provide for a more efficient and higher yielding pyrolysis. Even small improvements, such as a 1% increase in yield, could garner a considerable increase in revenue and thus spur development of the pyrolysis industry as a whole. To achieve this potential, it is imperative that this model accurately portrays data from laboratory testing.

3.2.3—Summary of materials and methods

First, COMSOL Multiphysics, an interactive program for modeling and simulating scientific phenomena, was used to describe heat and mass transfer within a single biomass particle. In this task, models were developed in COMSOL to describe the heat and mass transfer in the different directions inside the particle. Specifically, the models describe heat and mass transfer for pyrolysis with two parameters:

- *Effective thermal conductivity* indicates heat transfer into the particle from the heat source
- *Mass diffusivity* shows mass transfer from the particle to gaseous, liquid and/or solid products.

For pyrolysis, these two parameters enable accurate modeling of the pyrolysis process since all the known parameters that show how a biomass degrades to char, gas, and bio-oil are derived from these phenomena. The models take into account the effect of geometry and moisture

content on the effective thermal conductivity and effective mass diffusivity in the radial and axial direction.

Parameters obtained with the COMSOL model were compared with those from models developed by other authors as well as experimental data reported in literature.

3.2.4—Summary of results and conclusions

As an example of the full results described in Appendix, Figure 3.2.1 shows one of the parameters investigated in the COMSOL model: the effective thermal conductivity. Modeling results were compared to an equation used to describe this phenomena by Hunt et al. (2008) and experimental data conducted by Grønli (1996). Good agreement was found between the COMSOL model and the two other models (Figure 3.2.1).

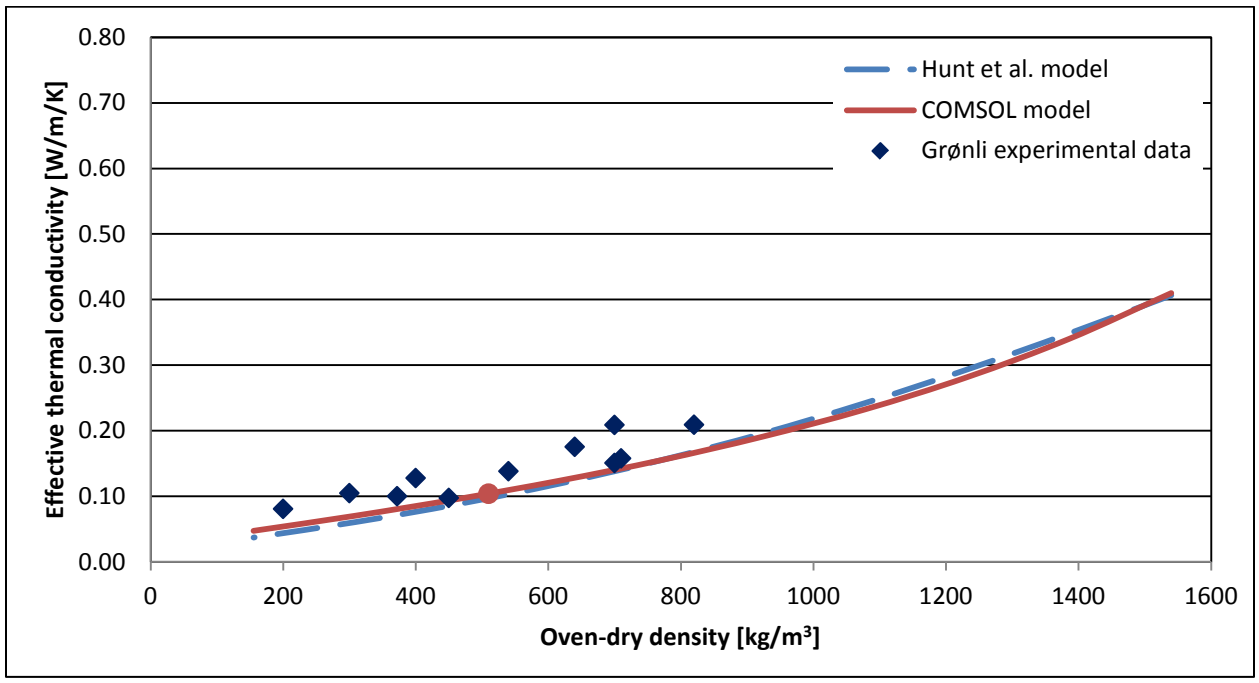

Figure 3.2.1: The effective radial thermal conductivities at 0% moisture content simulated with COMSOL, compared to data calculated from equation developed by Hunt et al. (2008), and measured data from Grønli (1996)

Building on these results, a single particle model was developed that took into account the primary and secondary reactions, heat and mass transfer inside and outside the particle, and the particle moisture content and shrinkage factor (the shrinkage factor depicts the change in size of the particle as it is degraded). The results obtained with this single particle model were compared with experimental results obtained by researchers at Curtin University, Australia. One key output that was compared was the temperature profile. Figure 3.2.2 illustrates the simulated and experimental temperature profiles and shows that the model results agreed well with the temperature profiles at 6 mm and 13 mm from the center of the particle following heating to 400°C.

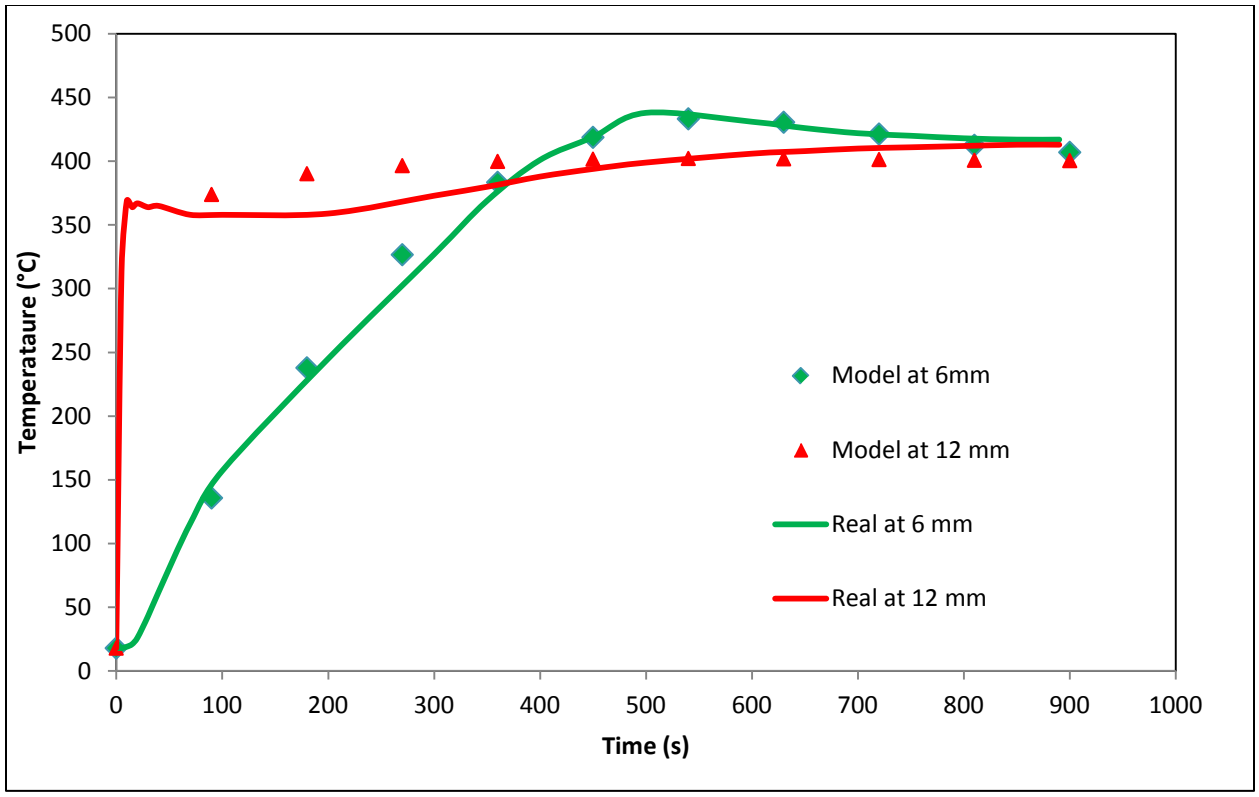

Figure 3.2.2: Experimental and simulated temperature profiles during pyrolysis at 400 °C with 24.4 mm diameter biomass particle and ~1% moisture content

Lastly, a model for the auger pyrolysis reactor was developed and validated using the data obtained in a 1 kg/h auger pyrolysis reactor. It would have been useful to have used information about yields of products from the experiments carried out in Australia, allowing for a more complete model package, but unfortunately no information was available from the experiments. To compensate for this lack of experimental data, data was collected from experiments conducted for model validation purposes on a 1 kg/h Auger reactor developed at WSU.

The values shown in Figure 3.2.3 of the curve wall temperature vs. gas temperature were chosen to adjust the parameters of the model (Liew et al., 2012). The parameters that were adjusted were the heat transfer coefficients, U` U``, and U``` (J/m^2sK). These are heat transfer coefficients between the wall and the gases, between the solid and the gases, and between the wall and the solid phase, respectively. The root mean squared error (RSME) methodology was used to fit the model to the experimental curve, and a good adjustment was obtained as is shown in Figure 3.2.4. These results provide concrete evidence of the power and validity of the model. This work provides a strong base for future model advancement and real-world applications. Additional modeling and applications will contribute to ongoing development of pyrolysis technology.

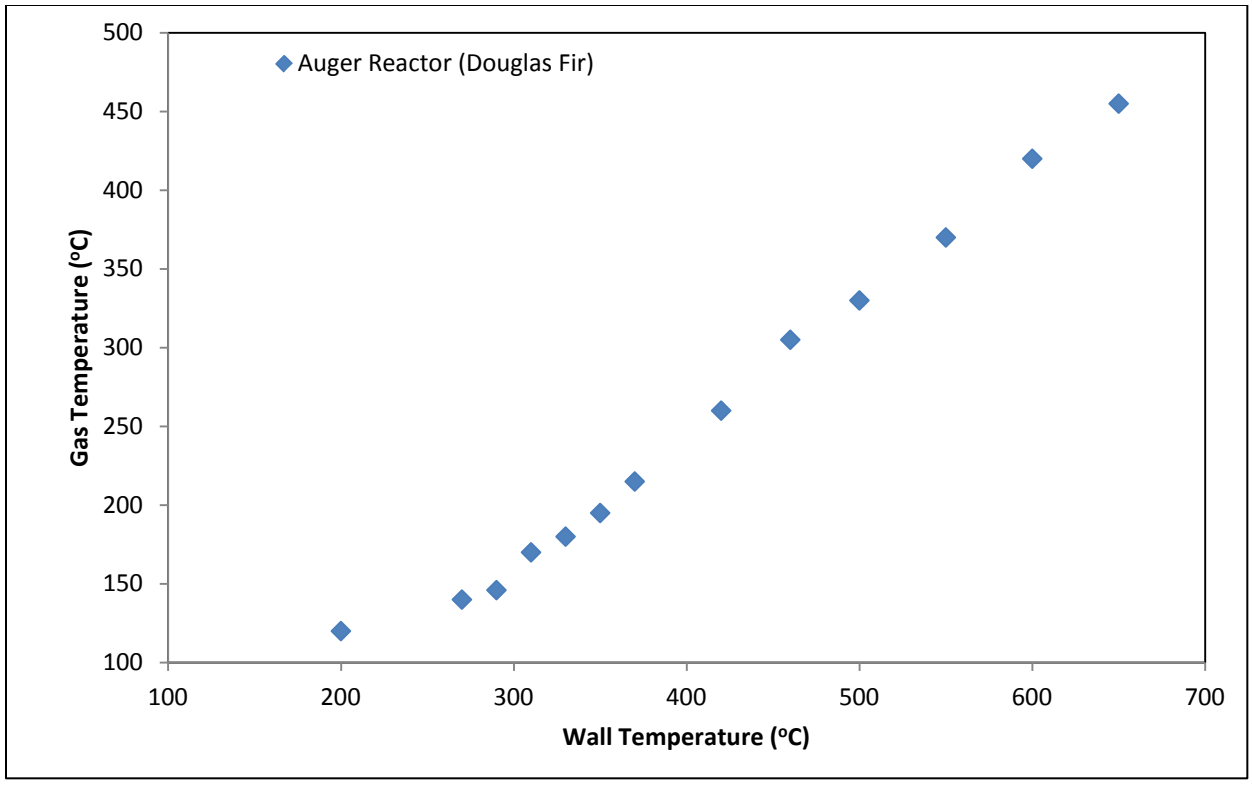

Figure 3.2.3: Auger reactor wall temperature vs. temperature of gases (Liaw et al., 2012)

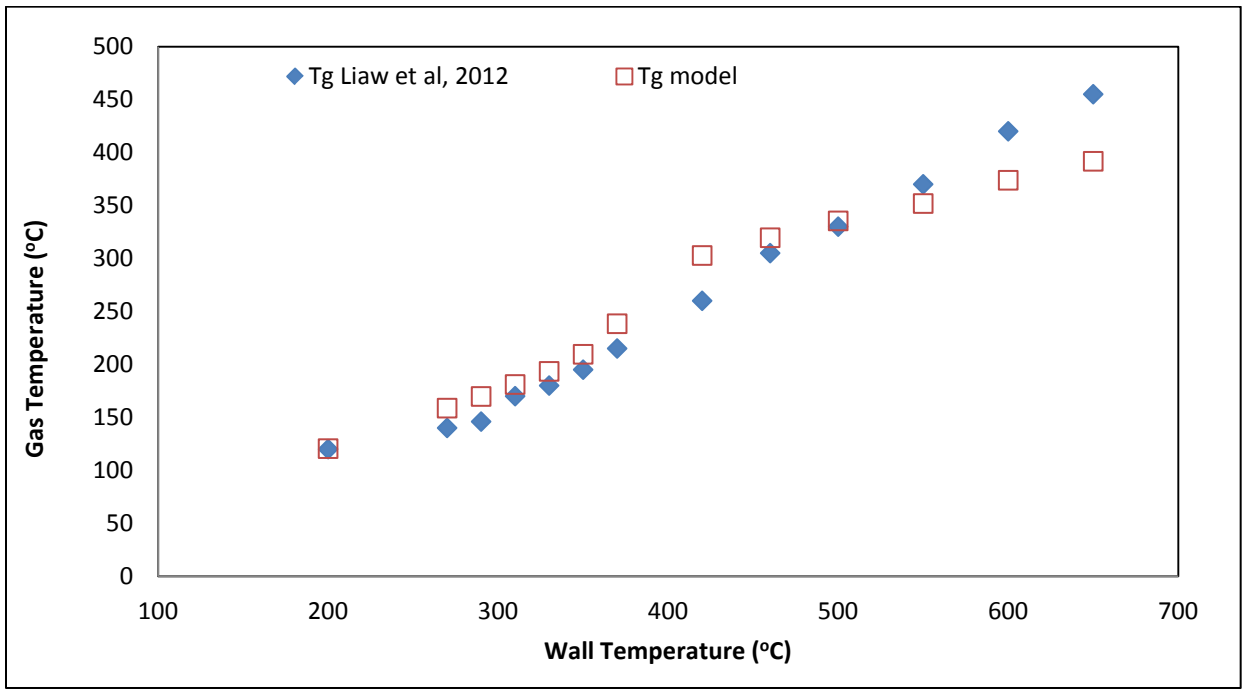

Figure 3.2.4: Wall temperature and gas temperature obtained from Liaw et al., (2012) and the adjusted curve from the model

3.3—Production of engineered biochars with enhanced capabilities to recover nutrients from liquid waste streams

Matt Smith, Waled Suliman, Manuel Garcia-Perez

3.3.1—Abstract

This study investigated techniques to produce engineered biochars from organic fractions currently processed by organics recycling facilities. The goal was to produce biochars that could strip N and P from gaseous, liquid, and solid waste streams. A series of different calcium and iron additions were performed on untreated AD fiber, with pyrolysis at 500°C, in order to enhance phosphate recovery. Untreated char from AD and wood fiber was oxidized under several different conditions to improve the cation exchange capacity (CEC) and ammonium adsorption capacity of the produced chars.

The most promising results for adsorption of phosphates were obtained from pre-pyrolysis precipitation of calcium on the biochar surface. This product achieved 53% removal of phosphate after 12 hrs. An additional investigation of this procedure explored the effect of pH on the deposition of sample calcium groups on the surface through inductively coupled plasma mass spectrometry (ICP-MS) and electron microscopy. Results showed a strong non-linear positive correlation between increasing calcium present in the system and increasing pH. This indicated that elevated pH treatments significantly improved adsorption characteristics. Using biochar modified with calcium at pH 9.35 resulted in a deposit of approximately 1.5 mass% phosphate on the material over the course of 72 hrs. This constituted the removal of approximately 95% of phosphate in the original 25 mg (P)/L solution.

The most promising method for improving the carboxylic acid groups (shown to correlate positively with ammonium absorption) and CEC of AD char was air oxidation for two hrs at 250^{o}C. This treatment increased CEC from a negligible value to more than 40 $cmol_c$/kg, with only a small weight loss due to oxidation. The char was also found to remain relatively stable in solution of moderate pH. The effect of oxidation, however, has been found to be dependent on both the initial feedstock and the pyrolysis conditions. Different effects of pyrolysis temperature on post pyrolysis oxidation were found when pine and hybrid poplar wood chips were used. Hybrid poplar was found to have the highest oxidation rate and was most easily oxidized by air when pyrolyzed at low temperatures. Pine wood, however, did not show a significant effect of temperature on either initial CEC or the effect of air oxidation. The change in carboxylic groups was noted to be the primary factor in determining changes in both CEC and ammonium adsorption and moderate pH.

Results provided concrete evidence that biochar can be an effective adsorption filter for the nutrients contained within dairy manure effluent. Section 3.4 builds upon the work completed in this section by exploring whether a biofilter could be economically deployed on dairy farms to provide them with another tool to mitigate nutrient-related management concerns.

3.3.2—Introduction

Based on prior experimental results, the team visualized, and explored, possible synergies between the production and activation of biochar and existing AD units. The biochar produced from the pyrolysis of digested fibers and woody biomass could be activated (through oxidation and additives) to enhance its capacity to retain N and P from the digester. This concept offers the farmer a way to obtain new products (heat, electricity, a biochar with a high CEC and enriched in nutrients) while reducing the environmental footprint of dairy operations.

Figure 3.3.1 shows a scheme of the proposed integrated system with each stream numbered. Manure is anaerobically digested and the fiber and effluent are separated from one another (11 and 12). Thereafter, the liquid effluent containing relatively high concentrations of N and P enter an activated biochar filtered bed where the adsorption process takes place, cleaning the effluent and producing an enriched biochar (15 and 16). Meanwhile, the fiber that was separated from the effluent after AD is combined with biomass and fed into the pyrolysis reactor to produce electricity (from steam). The resulting liquid vapor blend can be sent as an additive to the AD unit (see Section 1.3). As the pyrolysis process continues, biochar is produced and sent into the activated bed for a closed-loop system (2, 13, and 14).

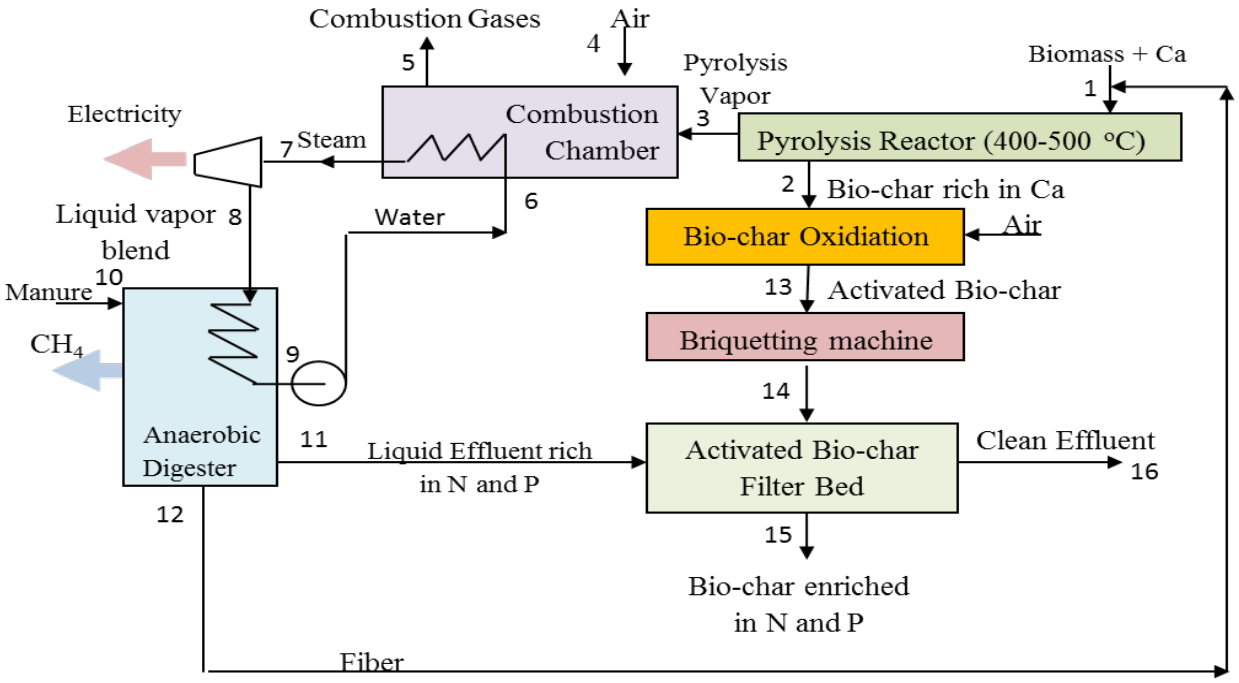

Figure 3.3.1: Integrated pyrolysis-AD system for the production of CH_4, heat, biochar enriched in nutrients and clean water

As can be seen in this schematic, multiple products can be produced through the integration of AD and pyrolysis. This task focused on biochar, which is one of these co-products. Researchers at WSU conducted experiments to test the ability of activated biochar to adsorb N and P. Furthermore, new approaches to produce biochars with high surface area and doped with calcium

oxide, and ferric sulphate/oxide were evaluated as a means to enhance biochar's capacity to remove phosphates.

The development of technologies to remove N and P from waste streams is of particular interest in WA. Currently, more than 1.5 million tons of cow manure is generated within the state each year, containing nearly 19000 tons of P. This P tends to accumulate in lagoons before lagoon water is applied to agricultural lands. The application of lagoon waste to lands typically provides more than 600 kg N $ha^{-1}y^{-1}$ and 160 kg P $ha^{-1}y^{-1}$, significantly more than what is normally required by crops. The over-application of nutrients can result in runoff of excess N and P or leaching of nutrients into groundwater.

Once released to the environment, these excess nutrients pose a risk to environmental quality. Thus, if biochars can effectively and economically strip N and P from dairy effluent, a profitable industry could emerge in the PNW. Furthermore, since biochars are significantly more stable than the fast- and slow-cycling fractions of organic matter in soil, biochar additions to soil could have significant long-term co-benefits in terms of enhanced soil fertility and carbon sequestration (Lehmann, 2007; Lehmann et al., 2006).

While biochar has significant potential as a soil amendment, studies with freshly produced biochars have not been able to reproduce the effectiveness of the centuries old Terra Preta soils of the Amazon Basin (Granatstein et al., 2009). One possible reason is that when the biochar is left in the soil for long periods of time the surface of the char is slowly oxidized. Treatment by ozone at room temperature has been shown to be an effective way of mimicking this process. It rapidly oxidizes the surface of carbonaceous materials (Chiang et al., 2002; Park & Jin, 2005; Valdés et al., 2002), leading to significant increases in the number of acidic surface oxygenated groups including carboxylic acid groups essential for improving nutrient holding capacity (Chiang et al., 2002; Valdés et al., 2002). However, ozone oxidation is unfortunately expensive.

It has been reported that acidic functional groups on the surface of biochar can significantly increase N adsorption capacity. These acidic functional groups can be generated with oxidizing agents such as H_2O (steam) and CO_2 at high temperatures (300–700°C) or with ozone at room temperature (Lehmann et al., 2011). Ozone was selected because functional groups on carbon begin to decompose at temperatures above 350°C (Chiang et al., 2002).

The adsorption of phosphate ions will depend upon the concentration and accessibility of cations found in the ash. Effects of metal ion concentrations in fly ash have been the subject of significant research (Agyei et al., 2002; Lu et al., 2009; Namasivayam & Sangeetha, 2004; Oguz, 2005; Xue et al., 2009). The use of fly ash has been considered for its potential to remove phosphate compounds from wastewater. The application of this information to biochars, for the removal of relatively low concentration phosphates, is of great interest because of the desire to develop an adsorbent capable of removing both N and P compounds from waste streams. The addition of appropriate metal ions to the structure of the biomass should aid in creating additional basic sites on the char surface, which will become positively charged in solution and attract anions to the surface.

Considerable effort has been made towards understanding the primary mechanism of phosphate removal with fly ash. Lu et al. (2009) showed that while the majority of phosphate removal appeared to be due to precipitation reactions, a reasonable level of adsorption can be achieved on the ash itself. Not much attention has been given to the simultaneous removal of ammonium and phosphate, although work by Zhang et al. (2007b) showed significant potential for this research area. The use of aluminum and iron to improve biochar phosphate adsorption is of considerable interest because both ions tend to create mildly acidic groups on the surface rather than the basic groups produced by calcium and sodium.

3.3.3—Materials and methods

3.3.3.1—Improved phosphate adsorption

AD fiber from DeRuyter and Sons Dairy in Outlook, WA, was dried at 105°C for 24 hrs. It was then ground to a 60–200 mesh powder with a mortar and pestle. A portion of sample was ground by hand for 30–60 sec before filtering through a 60 mesh screen; material that did not pass was returned to the mortar and reground for an additional 30–60 sec. This was repeated until approximately 95–98% of the original sample passed through the 60 mesh screen. The material that passed the first screening was then shaken on a 200 mesh screen to remove fine particulates. The retained material was stored at room temperature in sealed polypropylene and glass sample bottles.

100 g of ground sample was acid washed in a 2% nitric acid solution to remove metal impurities. The sample was mixed with 1 L of solution comprising 30 ml of 70% nitric acid and 18 Mohm purified water and stirred for 2 hrs. A series of preliminary calcium and iron additions were carried out following the scheme outlined in Figure 3.3.2.

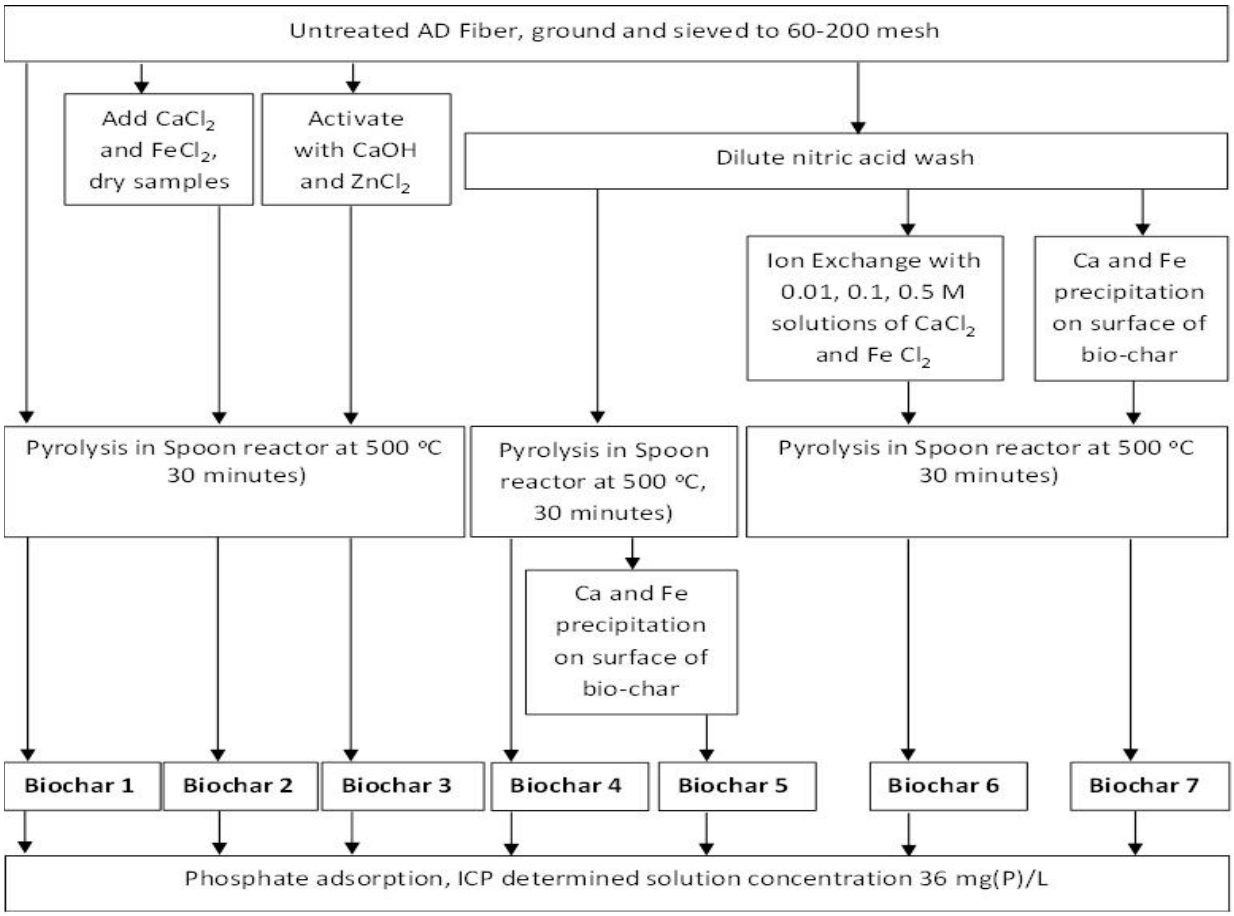

Figure 3.3.2: Diagram of treatments to screen pre- and post- pyrolysis treatment of chars

Ion exchange tests were completed by producing solutions of 0.01, 0.1 and 0.5 M calcium chloride ($CaCl_2$) and iron chloride ($FeCl_2$) solutions. Solutions were mixed at a ratio of 1 g fiber to 10 ml of solution. Precipitation was achieved by following the same method using 0.5 M solutions followed by addition of NaOH until no further precipitation was observed. Samples were then filtered through Whatman #42 filter paper and rinsed with purified water until chloride precipitates could not be detected by silver nitrate ($AgNO_3$). Activation was achieved by wet mixing of calcium hydroxide (CaOH) and zinc chloride ($ZnCl_2$) with fiber at a ratio of 0.5 to 1, with water sufficient to form a slurry. Samples were allowed to sit overnight and then dried at 105°C before pyrolysis.

Controlled precipitation was achieved by mixing fiber with 0.5 M $CaCl_2$ solution at a 1:10 m/v ratio. The solution was then adjusted to pH 6, 8, 9.35, 11, and 12 over a span of 84 hrs by addition of NaOH. The maximum pH measured after addition in each solution was approximately 6, 9, 10, 11.1 and 12.05, respectively. Solution pH was determined by a Mettler-Toledo pH probe. Variation in pH was noted to be less than 0.03 units in each sample between the final 2 measurements taken at a 6 hr interval.

Following treatment, all samples were dried for at least 12 hrs in a 105°C oven and pyrolyzed using a spoon reactor at 500°C for 30 mins under a flow of N_2. Samples were allowed to cool

under N_2 for 20 mins prior to exposure to air and weighing. All pyrolyzed samples were stored at room temperature in sealed glass vials until further analysis.

3.3.3.2—Oxidation for improved cation exchange capacity and ammonium adsorption

Two dairy fiber samples were collected for these experiments. Sample 1 was collected from George DeRuyter and Sons Dairy Digester in Outlook, WA and sample 2 collected from Andgar Corporation in Ferndale, WA. Each sample was ground using a mortar and pestle as described in the previous section to pass a 60 mesh screen and retain on a 200 mesh screen. Samples were charred at 500^{o}C for 30 mins in 0.5 to 1.0 gram batches using a spoon reactor under 2 L/min of N_2 purge.

Three independent oxidation methods were tested using AD fiber sample 1: cold plasma, ozone, and air oxidation at 200–350^{o}C. Cold plasma oxidation was conducted in a custom built reactor at WSU for 20 mins with a voltage of 4.2 kV rms. Ozone oxidation was conducted under an ozone/oxygen gas mixture for 30 mins. The ozone/oxygen gas mixture was produced by a pacific ozone generator at 4% ozone in oxygen gas stream at 2 standard liters per min. Air oxidation was completed variously using the spoon reactor at WSU and a thermogravimetric analyzer (TGA) (Mettler Toledo-SDTA851e). Air oxidation was conducted at temperatures between 200 and 350°C using char from fiber 1. For char from fiber sample 2, air oxidation was conducted for 1–3 hrs in the spoon reactor.

In addition to the fiber, two different woody feedstocks (hybrid Poplar and pine) were air-dried and milled to a particle size of about 590 µm. These feedstocks were pyrolyzed at six different temperature regimes (350, 400, 450, 500, 550 and 600°C) using a lab scale spoon pyrolysis reactor. Charring time was 30 mins, and charring batches consisted of < 1 g of air-dried, ground biomass. N_2 was used at 2 L/min as a purging or sweeping gas to create an oxygen free environment inside the reactor. Half of the produced biochars were then exposed to air at 250°C in order to oxidize them and add oxygenated functional groups on their surfaces. Biochar recovery yield for each pyrolysis temperature was calculated as a percentage of the mass of biochar generated from a dry mass of feedstock according to the following equation (Eq. 3.3.3.1):

$$R_c\ (\text{wt.}\%) = (M_c / M_b)*100 \qquad 3.3.1$$

Where R_c is biochar recovery yield (wt. %), M_c is the biochar mass in grams, and M_b is the oven dry weight in grams.

Woody biochars were oxidized using air oxidation. Based on feedstock type, pyrolysis and post-pyrolysis conditions, wood biochars were classified into four batches (two for each feedstock). For example, the first batch was denoted as HP for the hybrid poplar wood feedstock and HP-350, HP-400, HP-450, HP-500, HP-550, and HP-600 for the resulting biochars created at the six temperatures (350, 400, 450, 500, 550, and 600°C) while the second batch was denoted for air treated samples and abbreviated as HP-350-A, HP-400-A, HP-450-A, HP-500-A, HP-550-A, and HP-600-A. The same abbreviation procedure was applied for pine wood (PW) as well.

3.3.3.3—Analyses

Proximate analyses: A Mettler-Toledo was used to conduct the proximate analysis following ASTM method E1181. All samples were tested using a mass of 5.0±0.5 mg. Pre-pure N_2 (99.999%) was used for analysis while air was used as the oxidizing gas for ash quantification.

Elemental analysis of ash samples: Wet digestion was carried out using a CEM SP-D microwave digestion system. 100 mg of sample (+/− 5 mg) was loaded into a 35 ml quartz digestion vessel. To this vessel, 2 ml of 30% reagent grade hydrogen peroxide was added and allowed to react with the sample for 1 hr. Following, 3 ml of concentrated (69−71%) reagent grade nitric acid was added to each reaction vessel at least 25 mins prior to digestion. A small magnetic stir bar was added before inserting the vessel into the digester. Digestion was carried out following the temperature and pressure program listed in Table 3.3.1. The digested solution resulted typically in a clear liquid with mild granular solids and a small degree of mineral deposits on the wall.

Table 3.3.1: Design parameters

Max Power	300W
Pressure	400 PSI
Temperature	220 C
Ramp time	5 min
Hold time	5 min

Elemental analysis was conducted using an Agelant 7500cx ICP-MS equipped with a collision and reaction cell. Table 3.3.2 provides typical tuned parameters. Multi-element analysis was conducted following EPA method 6020 for the analysis of environmentally important metals. Test solutions were prepared by microwave digestion using a CEM SPD digester.

Digested samples were rinsed into freshly washed 100 ml volumetric flasks and diluted. 1 ml of an internal standard solution containing 10 ppm Li-6, Sc, Ge, Y, In, Tb, and Bi (Accustandard, Environmental Internal Standard Mix) was added to each sample to improve the accuracy of later analysis. Calibration samples were made from a commercially available stock solution (Accustandard Environmental Calibration Standard). Calibration points from 0–100 ppm were used for Na, K, Mg, Ca, and Fe, and 0 to 1000 ppb for all other elements. Linearity was determined to be at least 0.996 for each calibration curve. To improve the accuracy of low and high readings, the calibration curve was broken into 0–5 ppm (0–50 ppb) and 5–100 ppm (50–1000 ppb) segments for data analysis. Linearity for each quantified element was at least 0.999.

Table 3.3.2: ICP-MS settings for multi-element analysis and for phosphorous analysis

Plasma Condition (multi element)			Plasma Condition (phosphorous)		
RF Power	1550 to1600	W	**RF Power**	**1350**	**W**
RF Matching	1.8	V	RF Matching	1.8	V
Smple Depth	8.0 to 8.6	mm	Smple Depth	8.0 to 8.6	mm
Torch-H	0.5 to 1.0	mm	Torch-H	0.5 to 1.0	mm
Torch-V	-0.5 to 0	mm	Torch-V	-0.5 to 0	mm
Carrier Gas	0.87 to 0.9	L/min	Carrier Gas	0.87 to 0.9	L/min
Coptional Gas	0.25 to 0.27	L/min	Coptional Gas	0.25 to 0.27	L/min
Nebulizer Pump	0.1	rps	Nebulizer Pump	0.1	rps
S/C Temp	2	degC	S/C Temp	2	degC
Ion Lenses			Ion Lenses		
Extract 1	3.5 to 6	V	Extract 1	3.5 to 6	V
Extract 2	-160 to -180	V	Extract 2	-160 to -180	V
Omega Bias-ce	-32 to -36	V	Omega Bias-ce	-32 to -36	V
Omega Lens-ce	0	V	Omega Lens-ce	0	V
Cell Entrance	-28 to -32	V	Cell Entrance	-28 to -32	V
QP Focus	0	V	QP Focus	0	V
Cell Exit	-38 to -42	V	Cell Exit	-38 to -42	V
Octople Parameters			Octople Parameters		
OctP RF	158 to 180	V	**OctP RF**	**150-160**	**V**
OctP Bias	-5 to -7.5	V	**OctP Bias**	**-10**	**V**
Q-Pole Parameters			Q-Pole Parameters		
AMU Gain	128		AMU Gain	128	
AMU Offset	124		AMU Offset	124	
Axis Gain	1		Axis Gain	1	
Axis Offset	-0.03		Axis Offset	-0.03	
QP Bias	-3	V	QP Bias	-3	V
Detector Parameters			Detector Parameters		
Discriminator	8	mV	Discriminator	8	mV
Analog HV	1720	V	Analog HV	1720	V
Pulse HV	1130	V	Pulse HV	1130	V
Reaction Gas			Reaction Gas		
He	0	ml/min	**He**	**1.5**	**ml/min**

Scanning electron microscopy (SEM) images were collected using an FEI Quanta 200F microscope. Char samples were found to be sufficiently conducting for use without sputter coating.

Phosphate adsorption capacity was determined in batch by mixing 50 mg of char with 10 ml of phosphate solution ranging from 25–150 mg (P)/L. Samples were shaken at 200 RPM on an orbital shaker for 1–72 hrs and filtered through Whatman #42 filter paper. The filtered solution was stored in sealed polypropylene test tubes until analysis.

Phosphate was determined by ICP-MS using the collision reaction cell with 1.5 ml/min of helium flow. Typical tuning parameters for phosphate are listed in Table 3.3.2; values that differ significantly from the standard tune are listed in bold print. Solutions were prepared for ICP-MS by diluting 5–10 ml of filtered P-containing solution with 0.1 ml of internal standard to 10 ml in a polypropylene test tube. The tube was capped and inverted several times to ensure thorough mixing.

Cation Exchange Capacity: The CEC of the samples were determined according to the method of passive barium exchange with forced magnesium exchange. First, 0.4 g of biochar was washed with 20 ml of 0.1M of hydrogen chloride (HCl) for 1 hr, and then washed with e-pure water three times. Then, 30 ml of 0.1M of barium chloride ($BaCl_2$) was added and agitated for half an hour. The samples were then filtrated and mixed with 0.025 M of $BaCl_2$; pH of the mixtures was adjusted to 5.3. The mixtures were agitated for 24 hrs. After that, the $BaCl_2$ was washed out of the samples with e-pure water and then dried at 105°C. In triplicates, 100 mg of dried samples were re-suspended in 10 ml of 0.01 M magnesium sulfate ($MgSO_4$) solution. After 1 hr of agitation, samples were filtered and the filtrates were analyzed by atomic absorption spectrometer (AAS) (Varian Spectra AA220). The CEC values were calculated and expressed as $cmol_c/kg$ (carboxylic groups, measured in centimols/kg), which numerically is the same as the same CEC values expressed as mequiv /100 g.

Carboxylic acid groups by sodium bicarbonate neutralization: To measure the change in carboxylic functional groups, neutralization of sodium bicarbonate ($NaHCO_3$) by each char sample was tested. Briefly, 60–80mg of oxidized sample was measured into a 15 ml centrifuge tube to which 10 ml of standardized 0.02M $NaHCO_3$ was added. The mixtures were then agitated on an orbital shaker for 48 hrs prior to filtration through Whatman #42 filter paper. After filtration, 1.0 ml of sample was added to 100 ml of deionized water and mixed with 2 ml of 0.02M standardized HCl. This mixture, with an initial pH of approximately 3.5–3.75 was then back titrated to pH 4 using a 0.0080M NaOH solution. A blank solution of 0.02M $NaHCO_3$ solution was used as a zero point reference. Additional samples were also mixed with 0.02M NaOH and agitated to visualize the solubilization of sample at elevated pH.

Total acid groups by pyridine adsorption: To minimize sample usage while determining the effect of air oxidation time, a pyridine adsorption method was used to roughly determine total acidity. Approximately 5 mg of sample was loaded into a 70 uL alumina crucible and heated at 5°C/min to 200°C and held for 30 mins to remove any volatile material. These samples were then removed from the TGA and 50 uL of pyridine was added to each sample and allowed to dry overnight. After drying, the samples were reintroduced to the TGA and run through the same temperature program as before. Differential Thermogravimetric (DTG) curves were produced to determine at what temperature the system deviated from ideal, indicating strongly bound pyridine on the surface requiring higher temperatures to vaporize (normal boiling point of pyridine is 115°C). The average difference between initial and pyridine adsorbed curves at 115–120°C is estimated as the quantity of adsorbed pyridine, with one molecule occupying one acid site.

X-ray photoelectron spectroscopy analysis: The x-ray photoelectron spectroscopy (XPS) measurements were obtained with an AXIS-165 (Kratos Analysis Inc.) using Achromatic X-ray

radiation of 1253.6 eV. A non-linear least squares curve fitting program (XPSPEAK 4.1 software, programmed by R. Kwok, Chinese University of Hong Kong) was used to analyze the XPS spectra. The C1s bending energy was assigned at 285 eV while hydroxyl at 286 eV, carbonyl at 287 eV, and carboxyl groups at 288.6 eV. C1s and O1s spectra were set to the same Full Width Half Maximum (FWHM) and Gaussian-Lorentzian ratios.

BET surface area: The surface area was measured by N_2 sorption analysis at 77K using multipoint Brunauer, Emmet and Teller (BET) analysis on an ASDI RXM catalyst characterization system (Chemisorb2720). Prior to analysis, samples were vacuum degassed at 150°C for 1 hr.

3.3.4—Results and discussion

3.3.4.1—Improved phosphate adsorption

The effect of ion exchange on the mineral content on the fiber was investigated by ICP-MS and demonstrated the increase in calcium and iron with increasing solution concentrations. Results indicate that the bulk of the mineral fraction is water soluble and reached equilibrium with the aqueous solution (Table 3.3.3). Increasing the concentration of calcium and iron was found to have only mild effects on the concentrations of most cations.

Table 3.3.3: Mineral analysis of raw AD char and fiber as well as calcium and iron exchanged fiber

Sample	Na	K	Mg	Ca	Fe	Al	Cu	Zn	Pb
	mg X/ g sample (error ±0.1)						µg X/ g sample (error ±10)		
AD Raw	3.8	12.6	9.7	22.6	4.4	3	84	205	2
ADC Raw	7.2	21.8	19.1	39.1	7.6	8.1	122	364	7
AD Ca 0.01M	0.2	0.7	1.8	6.7	6.1	3.7	564	195	116
AD Ca 0.1M	0.2	0.7	1.4	7.4	5.5	3.5	584	137	110
AD Ca 0.5M	0.2	0.7	1.4	8.4	5.7	3.8	586	92	110
AD Fe 0.01M	0.4	0.8	2.1	3.6	11.3	4.1	589	194	129
AD Fe 0.1M	0.2	0.7	1.6	1.3	16.8	4.1	579	83	125
AD Fe 0.5 M	0.3	0.7	1.4	0.6	19.6	3.7	540	61	117

An important result identified during the mineral analysis of the samples was the increase in copper and lead of all samples. This increase can be attributed to small contaminations of each element in the solution used to wash the material and the strong binding of these minerals to adsorption sites on the raw fiber. This suggests that future work focused on the development of heavy metal filters from either the raw fiber or biochar may be beneficial.

Based on the pre-trial results, it was apparent that calcium precipitates were by far the most effective method for increasing the phosphate retention of biochar. Other methods resulted in either little effect (iron samples) or heavy precipitates when tested without heavy washing ($Ca(OH)_2$ and $ZnCl_2$). Post pyrolysis precipitation of calcium resulted in the best biochar removal rate of 98% when filtered through #42 paper, but this dropped to 35% in unfiltered samples, suggesting that much of the phosphate is bound in small precipitates (< 2.5 µm). The best apparent results for adsorption were obtained from pre-pyrolysis precipitation of calcium on the

biochar surface which reached 53% removal after 12 hrs. The results of these trials are summarized in Table 3.3.4.

Table 3.3.4: Summary of phosphorous removal and mineral leaching from various treated chars

Sample	Fe leached mg/L	Ca leached mg/L	Total leaching mg/L	P-removal After 12 hours
Biochar 1	2.90E-04	4.40E-04	0.028	11%
Biochar 2 Fe Dry	0	0.07	0.09	7%
Biochar 3 $Ca(OH)_2$ activated	Inconclusive, heavy precipitation in solution			
Biochar 3 $ZnCl_2$ activated				
Biochar 4	0	0.0002	0.001	7%
Bio-Char 5 Ca Precipitate	**0**	**0.37**	**0.45**	**98% (filtered) 35% un-filtered**
Bio-char 5 Fe Precipitate	0	0.15	0.15	11%
Biochar 6 Ca 0.5M	0.0001	0.0005	0.011	3%
Biochar 6 Fe 0.5M	1.30E-04	0	0.011	0%
Bio-char 7 Ca Precipitate	**0**	**0.023**	**0.071**	**53%**

Based on these results, the effect of pH on the deposition of sample calcium groups on the surface was investigated by ICP-MS and electron microscopy. The resulting impact on total phosphate adsorption was also studied. Results showed a strong positive non-linear correlation between pH and increasing calcium present in the system (Figure 3.3.3 (A)). Calcium deposition can be seen in the micrographs presented in Figure 3.3.4, where regular mineral deposits can been seen to increase in size and regularity as the pH of the calcium solution was increased. Interestingly, mineral nano fibers were observed on unmodified biochar, but not on any other char structure.

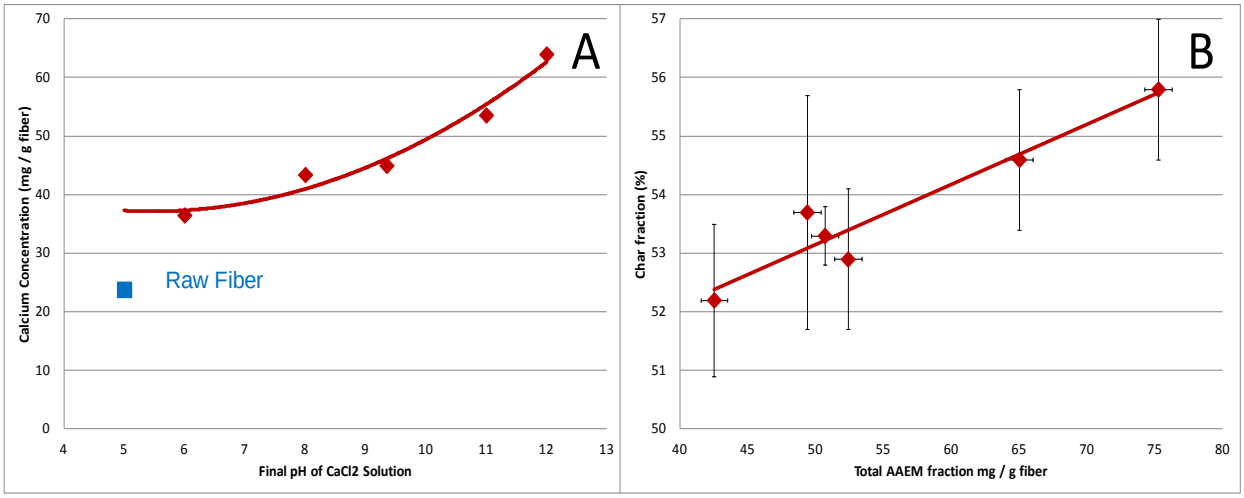

Figure 3.3.3: (A) The effect of pH on the deposition of calcium from a 0.5M $CaCl_2$ solution (B) The effect of increasing alkali and alkaline earth metals (AAEMs) on the char yield from pyrolysis

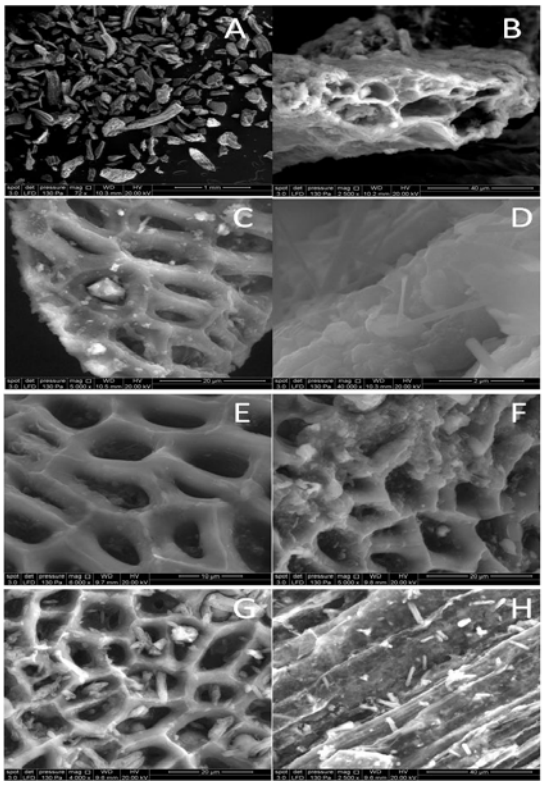

Figure 3.3.4: SEM images of (A) Raw biochar at 72X magnification (B) Raw biochar at 2500X showing internal particle structure (C) Raw biochar at 5000X showing mild mineral deposits on the char (D) Raw biochar at 40000x showing mineral nano filaments (E) pH 6 adjusted char at 6000x showing little mineral deposits (F) pH 8 adjusted char at 5000x showing additional mineral deposits (G) pH 12 adjusted char at 4000x showing significant mineral deposition (H) pH 12 adjusted char at 2500x showing mineral deposition on the outer surface of the char structure

Table 3.3.5: Effect of calcium deposition on the proximate composition of the resulting biochars

Sample	H.V. matter	Volatile	Fixed Carbon	Ash	FC/VM
ADF	8.6	64.0	27.3	25.5	0.43
ADFAW	6.1	60.8	33.1	18.9	0.54
ADCR	8.1	24.0	67.9	40.2	2.83
ADC6	8.4	24.5	67.1	38.4	2.74
ADC8	9.4	26.2	64.3	37.3	2.45
ADC9	9.3	26.4	64.3	39.8	2.43
ADC11	10.4	28.1	61.5	41.3	2.19
ADC12	10.1	28.4	61.5	40.9	2.17

The deposition of calcium was found to mildly increase the formation of ash-free char, though the effect is marginal as can be seen in Figure 3.3.3 (B). The proximate analysis of char, Table

3.3.5, demonstrates that higher concentrations of calcium result in an appreciable increase in volatile matter. The ratio of fixed carbon to volatile matter decreased from 2.83 to 2.17 as the pH of the solution was increased from 6 to 12. This indicates a lower total conversion to highly recalcitrant fixed carbon, and may result in somewhat higher initial char decomposition rates compared to untreated char if applied to soils.

The effect of deposited calcium on phosphate adsorption by the resulting biochars was also evaluated. Elevated pH treatments resulted in significantly improved adsorption characteristics. Equilibrium adsorption from solution and the first order rate constant were found to be linearly correlated to the sum of the concentration of calcium and magnesium in the system (Figure 3.3.5). The first order rate constant for unmodified char was significantly higher than expected; this suggests that the mineral form is considerably different than is found in the calcium adjusted samples, a difference that might be explained by the presence of the nano fibers observed in Figure 3.3.4 (D).

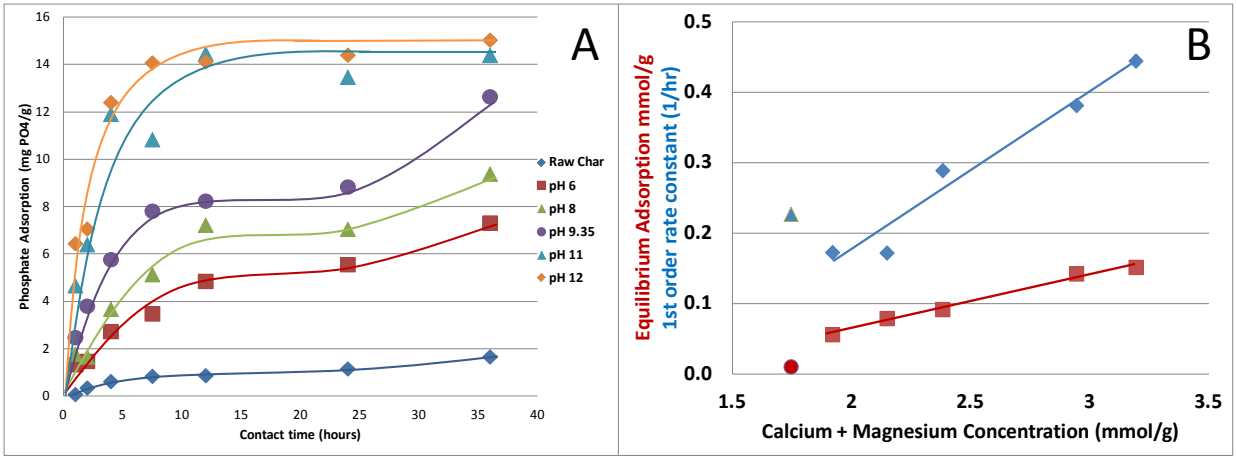

Figure 3.3.5: (A) Phosphate adsorbed per gram of char from a 25 mg (P)/L solution (B) Equilibrium adsorption and 1st order rate constants obtained from kinetic studies compared with the total calcium and magnesium concentration in the char

Biochar modified with calcium at pH 9.35 performed best in terms of removing phosphates, with a deposit of approximately 1.5 mass % phosphate over the course of 72 hrs (Figure 3.3.6). This result constituted the removal of approximately 95% of phosphate in the original 25 mg (P)/L solution. A solution of 150 mg (P)/L was also tested and found to show approximately single layer adsorption behavior during the first 24 hrs of contact with a final maximum adsorption of 1.5–2 mass %.

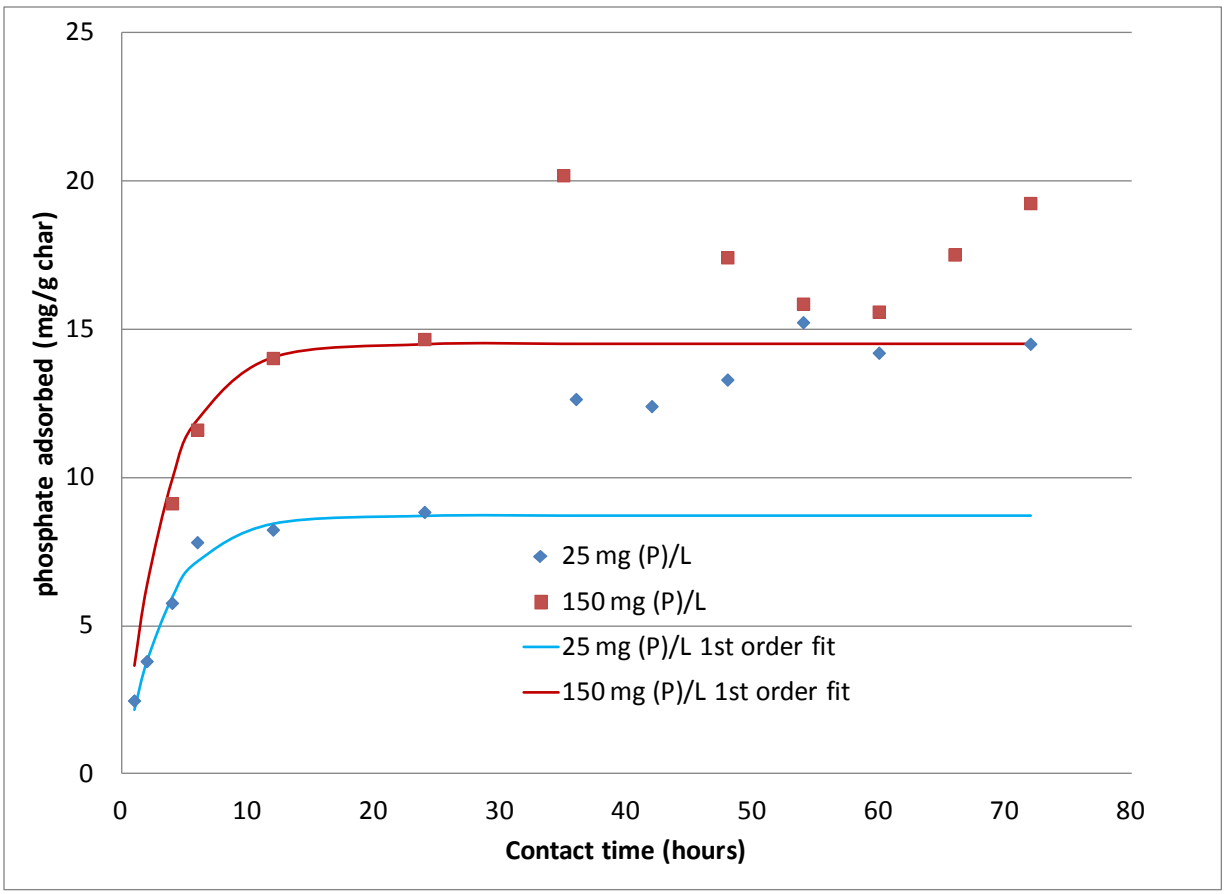

Figure 3.3.6: Phosphate removal over 72 hrs from a 25 mg (P)/L and 150 mg (P)/L phosphate solution. Lines indicate first order fits for the first 24 hours of contacting using k = 0.289 and qmax = to 8.7 and 14.5 mg (PO_4) /L Equation is dq/dt = k*(qmax-q)

The same kinetic constant of 0.289/hr was used with both the 25 and 150 mg/L fit equations and equilibrium adsorption was estimated as the quantity adsorbed at 24 hrs for both solutions. In each case, a very good fit to experimental data was observed over the first 24 hrs. The consistency of these results indicates that the kinetic parameters obtained at low concentration remain applicable at higher concentrations. Results diverged in both cases at high contact times. This divergence suggests that partial multilayer adsorption may be occurring. It also demonstrates the heterogeneity of the samples as the adsorption after 48 hrs should be approximately at the maximum.

3.3.4.2—Oxidation for improved cation exchange capacity and ammonium adsorption

Thermogravimetric analysis of char from AD fiber sample 1 was conducted at temperatures of 200–325°C for up to 4 hrs. Samples were heated to the hold temperature at 50°C/min before initiating the hold time. The results, shown in Figure 3.3.7, indicated very little overall change in mass at temperatures below 250°C while samples above 275°C showed significant and rapid weight loss. In all cases the first derivative of weight loss was nearly stable after 2 hrs, indicating a relatively stable surface had been achieved. Large scale spoon reactor studies were therefore conducted in air over this time frame. Mass loss during trials in the spoon reactor were approximately the same as those obtained in the TGA trials with 6% lost at 250°C and 11 and

21% lost at 275 and 300°C respectively. Conversely, mass loss associated with ozone oxidation and cold plasma treatment was negligible, approximately 2% for each.

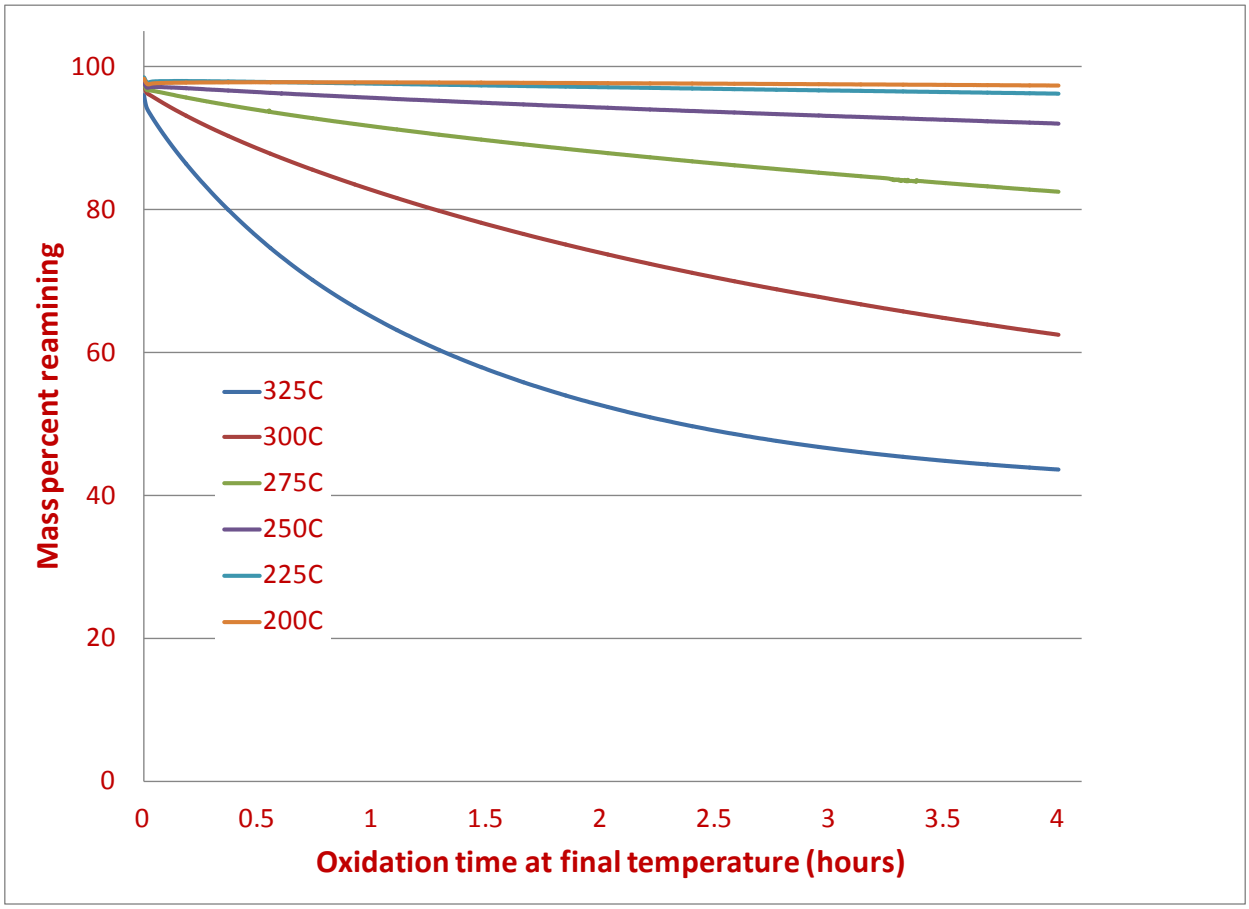

Figure 3.3.7: Mass loss during oxidation of char from AD fiber at various temperatures using a TGA

The effect of each oxidation method on total carboxylic acid groups is given in Figure 3.3.8 (A). These results are somewhat confounded by the mineral content of the char, which can cause mild precipitation of the CO_3^{2-} ions and shift the neutralization readings downward as is seen in the comparison between the untreated char sample and the acid washed char sample without soluble mineral matter. For this reason, the results listed may be up to 5–10 $cmol_c$/kg lower than actual. However, the effectiveness of the oxidation methods are readily apparent by comparison, even if this is true. The results shown in Figure 3.3.8 (A) also indicate that the effect of ozone on the concentration of carboxylic groups is minimal, while a moderate effect is seen from cold plasma oxidation. By comparison, the best results were obtained by air oxidation, with 250°C being the most effective temperature tested. At increasing temperatures, lower acid concentrations are detected due to the poor thermal stability of these groups. At 350°C, these groups are no longer stable on the surface and are no longer detected by titration. The value in determining carboxylic acid groups is that previous results have shown a direct, linear correlation between the quantity of acid groups detected by titration and the removal of ammonium from a single component system as shown in Figure 3.3.8 (B).

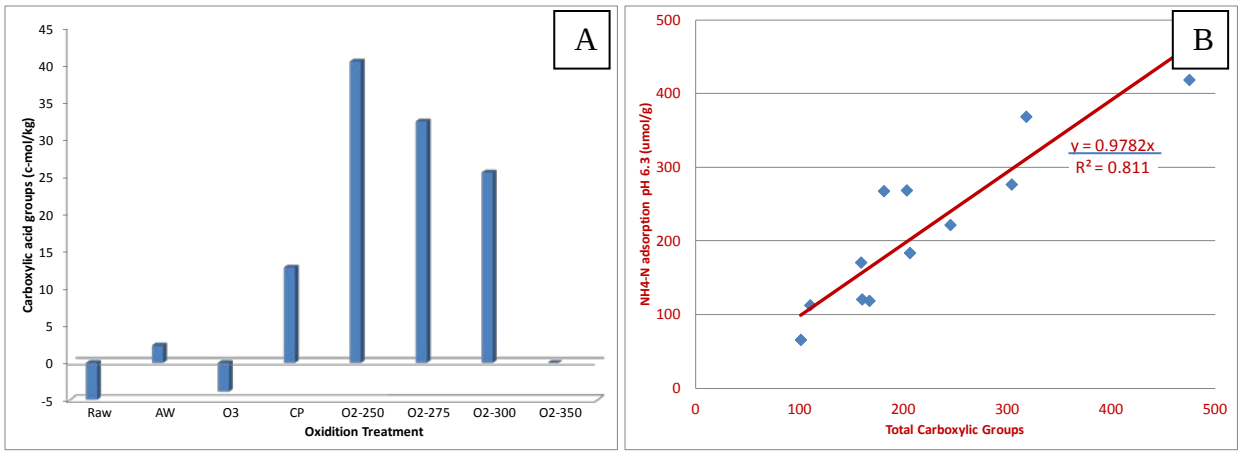

Figure 3.3.8: (A) The carboxylic acid groups detected on the surface of char from AD fiber 1 by oxidation method (B) The effect of carboxylic acid groups on the ammonium adsorption capacity of various biochars oxidized in ozone

For air oxidation, the optimum oxidation time was identified by evaluation of pyridine adsorption curves to determine total acidity of oxidized sample. The mass loss curves generated for the initial and pyridine adsorbed samples for unmodified AD char and AD char oxidized at 250°C for 1 hr (Figure 3.3.9 (A) and (B)) showed a 1.3–3% weight increase at the boiling point of pyridine where DTG curves (Figure 3.3.9 (C) and (D)) diverged from ideal curves approaching zero. Untreated char was found to increase in mass by approximately 1.3%, which translates to approximately 16 $cmol_c$/kg total acid sites, while all of the oxidized samples showed approximately a 3% variation, translating to 38 $cmol_c$/kg acid sites. It is important to note that for all oxidation times between 1 and 3 hrs, each sample was between 35 and 40 $cmol_c$/kg; indicating that no significant variation in the surfaces existed between these samples.

A significant challenge resulting from air oxidation of AD char is the soluble material loss that occurs at elevated pH. Figure 3.3.10 (A) and (B) show images of pH 8–9 and pH 12 solutions contacted with 50 mg of biochar for 48 hrs. As can been seen, at these pH levels, air oxidation resulted in moderate to extreme sample loss to solution. The composition of this material is unknown but represents a significant loss of carbon and acid sites. To reduce this effect, lower oxidation times and more recalcitrant chars were tested, including chars from hybrid poplar pyrolyzed at 350–600°C (Figure 3.3.10, (C) and (D)) and pine wood pyrolyzed at 350–600°C (not shown). As expected, chars from these wood samples proved to be less soluble after 30 mins of oxidation. For chars pyrolyzed at lower temperatures, there were only very mild losses observed in a pH 8–9 solution and mild losses in a pH 12 solution. For chars produced at 600°C, almost no loss was observed.

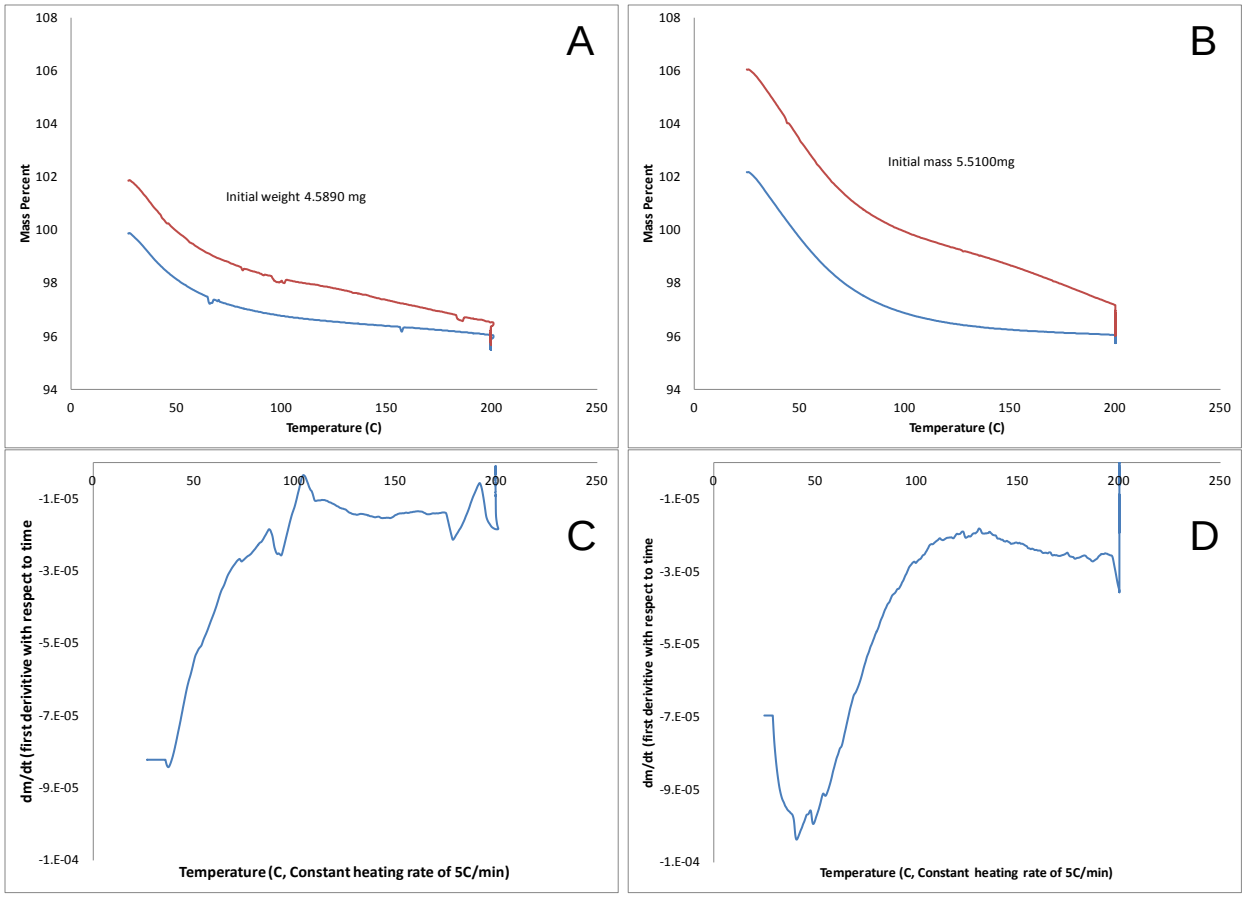

Figure 3.3.9: Adsorption of pyridine by (A) unmodified AD char and (B) AD char oxidized for 2 hrs. DTG curves show (C) only weak pyridine adsorption on the non-oxidized char and (D) stronger adsorption for the oxidized char

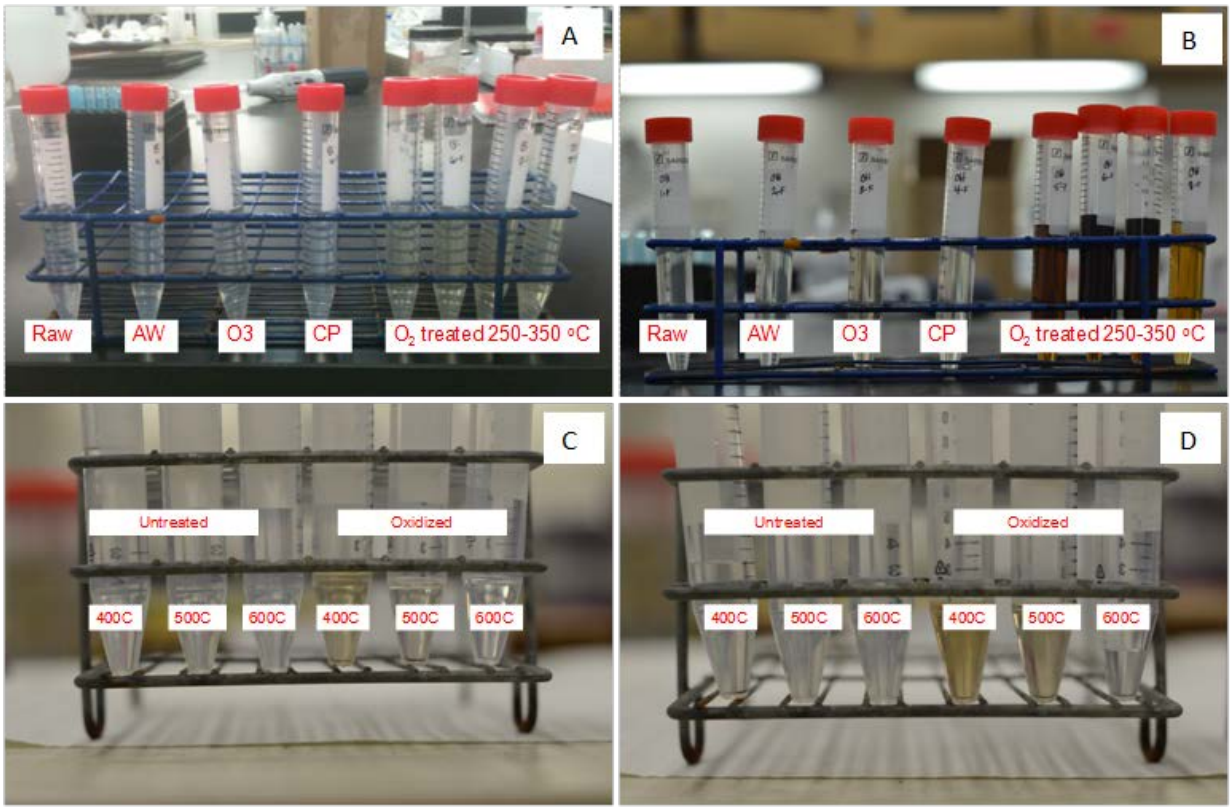

Figure 3.3.10: Soluble material removed over 48 hrs from char produced from AD fiber in (A) pH 8–9 solution (B) pH 12 solution and from hybrid poplar in (C) pH 8–9 solution and (D) pH 12 solution

The yields of biochar for hybrid poplar and pine wood are shown in Figure 3.3.11, parts (A) and (B). The results demonstrate a clear reduction in char yield as the temperature of pyrolysis is increased. At low temperatures between 350 and 450^{o}C char yields from pine wood were considerably more temperature sensitive than yields from hybrid poplar, which showed a linear dependence over the full temperature range. Above 450^{o}C pine wood had a lower char yield than hybrid poplar, while at lower temperatures the inverse was true.

The reactivity of hybrid poplar with oxygen at 250°C decreased as the pyrolysis temperature increased, becoming more or less stable with pyrolysis temperatures between 500–600°C (Figure 3.3.11 (C)). In contrast, pine wood was found to have very poor reactivity throughout the temperature range, showing a nearly constant mass loss of 1–2% regardless of pyrolysis temperature, as shown in Figure 3.3.11 (D). These results suggest that only limited effect of oxidation will be observed on the oxygenated acid groups of pine wood, while a considerable effect should be seen with hybrid poplar char produced at temperatures between 350 and 500°C.

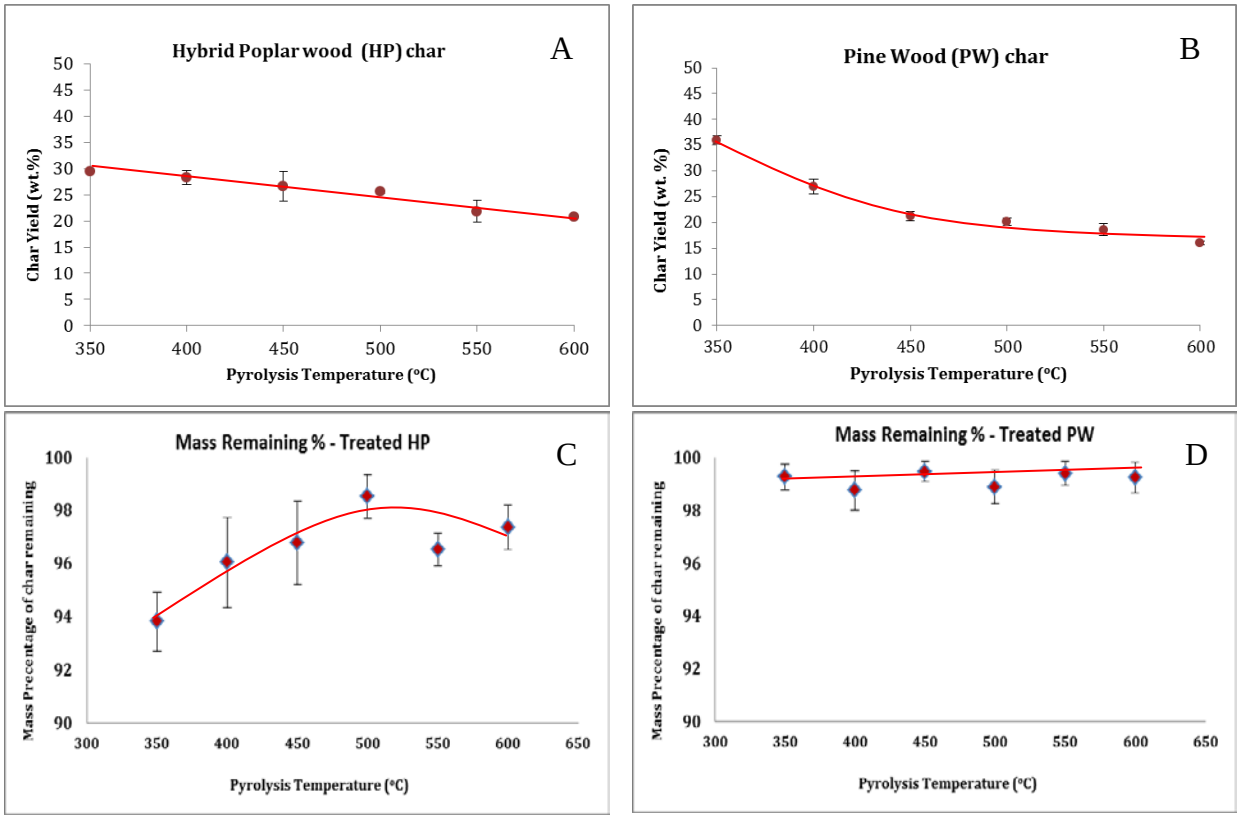

Figure 3.3.11: biochar yield at various pyrolysis temperatures for (A) hybrid poplar wood and (B) pine wood, and mass loss during air oxidation for chars produced at various temperatures for (C) hybrid poplar wood, and (D) pine wood

The results from proximate analysis showed a moderate effect due to oxidation. The ash fraction was not considerably altered, due to the relatively small mass loss associated with the oxidation step. The fixed carbon decreased with oxidization while the volatile content increased by a similar margin. These results were in agreement with previous oxidations studies with ozone that showed similar trends. Increasing the pyrolysis temperature resulted in higher fixed carbon and lower volatile matter, with the fixed carbon to volatile matter (FC:VM) ratio increasing from about 1 at lower temperatures up to between 4 and 5 at 600°C. These higher ratios are indicative of increased thermal and biological stability. Air oxidation by air reduced the FC:VM ratio by approximately 5–30%, with larger changes seen in chars produced at higher temperatures. In comparison, both hybrid poplar wood and pine wood showed similar quantities and trends in terms of fixed carbon and volatile matter as a function of pyrolysis temperature and oxidation (Table 3.3.6).

Table 3.3.6: Proximate analysis of treated and untreated pine wood and hybrid poplar wood

Feedstock	Air treatment	Pyrolysis Temperature (°C)	Ash content (wt.%)	Volatile matter (wt.%)	Fixed carbon (wt.%)	FC/VM ratio
Pine wood	Untreated	350	0.6	49.8	49.6	1.0
		400	0.7	36.1	63.2	1.7
		450	0.8	28.4	70.8	2.5
		500	0.8	23.1	76.1	3.3
		550	1.0	19.2	79.8	4.2
		600	1.1	15.7	83.1	5.3
	Treated	350	0.4	51.2	48.3	0.9
		400	0.6	41.8	57.6	1.4
		450	0.7	35.8	64.4	1.8
		500	0.9	28.8	69.2	2.4
		550	0.8	23.8	77.3	3.2
		600	0.9	20.8	79.3	3.8
Hybrid poplar	Untreated	350	3.5	42.2	54.3	1.3
		400	5.3	30.0	64.7	2.2
		450	6.3	25.6	68.1	2.7
		500	5.3	32.7	62.0	1.9
		550	7.0	20.4	72.6	3.6
		600	6.2	17.8	76.0	4.3
	Treated	350	4.7	46.3	49.0	1.1
		400	3.9	36.6	59.5	1.6
		450	5.2	35.0	59.8	1.7
		500	4.9	30.8	64.4	2.1
		550	5.9	24.4	69.7	2.9
		600	6.0	19.6	74.4	3.8

The CEC for untreated and air treated wood biochars is presented in Figure 3.3.12. As expected from the mass loss data, hybrid poplar char produced at lower pyrolysis temperatures (below 500°C) showed significant increases in total CEC. At temperatures above 500°C, the effects of oxidation were limited, indicative of poor reactivity. Similarly, poor reactivity was observed with pine wood char, which showed only very marginal improvements in total CEC with oxidation. The reactivity of these samples to air during oxidation is likely related to the fixed and volatile carbon fractions as well as the degree of aromatic condensation of the chars, where more condensed aromatic rings are expected to yield lower reactivity (such as with highly condensed structures like graphite and activated carbon). The ash fraction may also play an important role in the oxidation rate as hybrid poplar, with the higher ash fraction, showed considerably better oxidation at low FC:VM ratios than pine wood. At higher FC:VM ratios, the effect of ash may be more limited. Further studies to clarify the roles of these parameters are required.

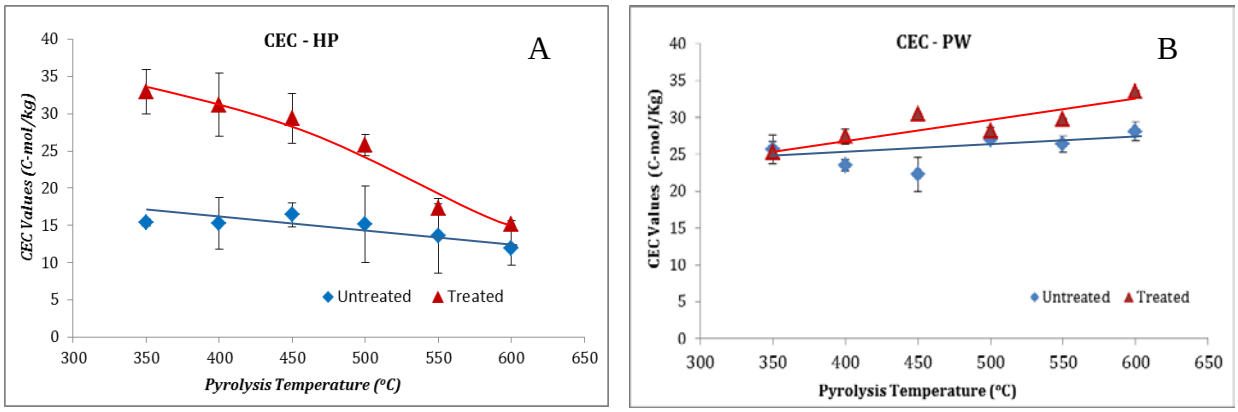

Figure 3.3.12: Cation exchange capacity values for (A) hybrid poplar wood chars and (B) pine wood chars

Total surface area from N adsorption indicates a sharp increase in total surface area when pyrolysis is conducted at temperatures above 500°C (Figure 3.3.13). Total surface area is 3 to 4 times greater when conducted at 600°C as compared to 500°C. In these measurements, the surface area of pine wood was found to increase significantly faster as the temperature of pyrolysis was increased, leading to higher surface area chars at both 550°C and 600°C. The surface area of chars produced at lower temperatures was not evaluated. Surface area measured by N_2 typically reveals surface in micropores as small as 1.5 nm. However, diffusion limitations prevent analysis of smaller channels. Previous work with pine wood has shown through the use of CO_2 at 273K that significant pore structures exist in this size range in chars produced at 500°C, though these structures would be poorly accessible compared to the larger structures determined here.

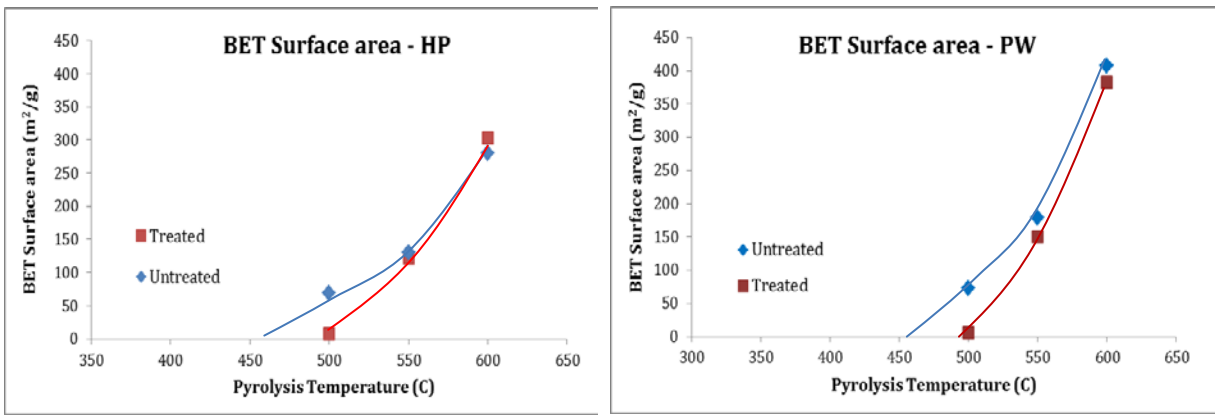

Figure 3.3.13: BET surface area of hybrid poplar wood chars (left, HP) and pine wood chars (right, PW)

The effect of oxidation on the surface concentration of carboxylic groups was determined by XPS (Figure 3.3.14). The results showed that in all samples, oxidation treatment increased the quantity of carboxylic groups on the surface. These results also indicated that in general treatment was more effective on chars generated at lower temperatures. The results did not appear to directly mimic the changes seen in the CEC; however, this is most likely an effect of the increased surface area exposed to analysis in the samples treated at higher temperatures.

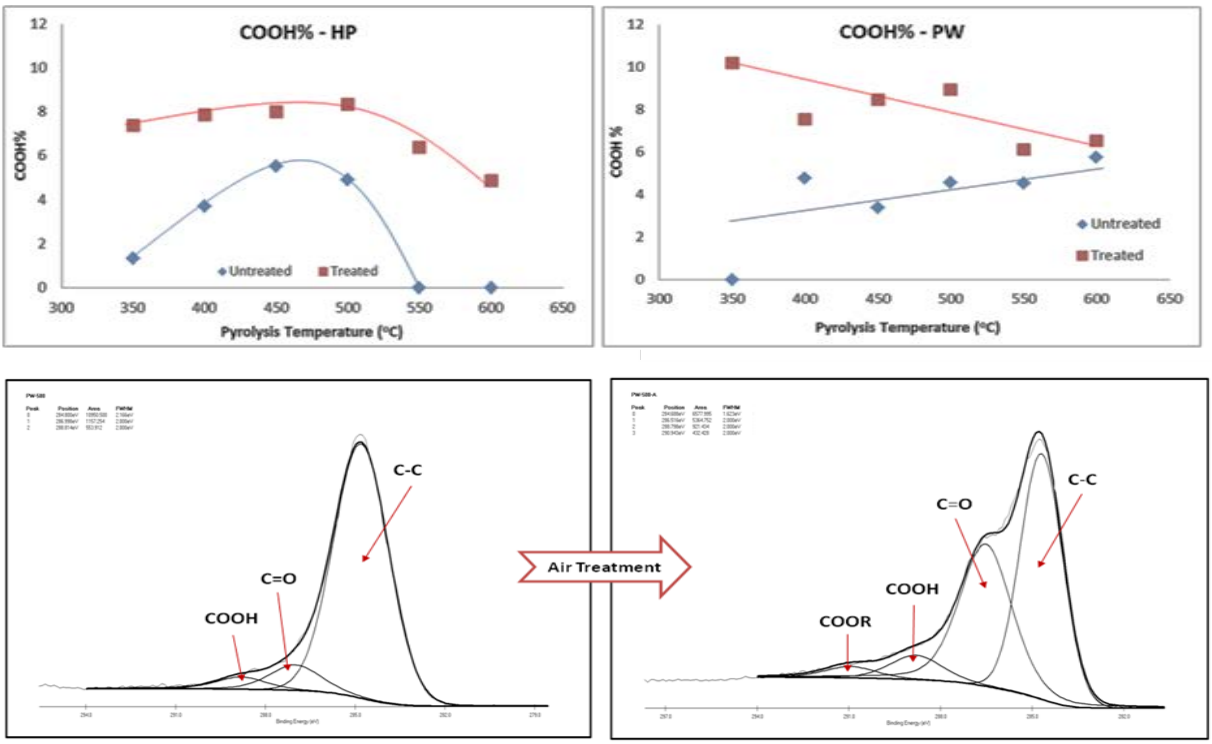

Figure 3.3.14: surface groups identified by XPS for hybrid poplar wood chars (HP) and pine wood chars (PW)

3.3.5—Conclusions

Among the various modifications of biochar tested, results indicated that the highest removal of phosphate resulted from the addition of calcium before pyrolysis. The removal efficiency under these conditions was around 53% after 12 hrs of contact with a sodium phosphate solution. Thereafter, further analysis of calcium addition was investigated to determine whether pH would increase the adsorption of phosphate. Results from these experiments indicated a non-linear positive relationship between pH and removal efficiency. Equilibrium adsorption from solution and the first-order rate constants were found to be linearly correlated to the sum of the concentration of calcium and magnesium in the system. These rate constants will be applied in section 3.4 for scale-up modeling of the system.

Among the modifications of biochar tested for ammonium adsorption, results indicated that for AD fiber, the most carboxylic acid groups were detected on the surface of the char after air oxidation at 250°C, with carboxylic acid groups previously shown to relate directly to improved ammonium adsorption capacity. This method is also likely to be the most practical to implement on a farm or an industrial scale. The effect of oxidation however has been found to be dependent on both the initial feedstock and the pyrolysis conditions. For example, while both AD fiber and hybrid poplar were found to oxidize well under these conditions, pine wood did not. Hybrid poplar chars pyrolyzed at lower temperatures and once oxidized, were found to have significantly higher CEC capacities than those pyrolyzed at higher temperatures, despite much

lower specific surface area as determined by N_2 adsorption. Oxidized char samples were found to have CEC values of up to 35–40 $cmol_c$/kg.

The experiments conducted in this task demonstrate that AD fiber derived biochars can remove P from dairy manure effluent. Section 3.4 builds upon these results, evaluating whether a biofilter could be economically deployed on dairy farms for nutrient management purposes.

3.4—Filtration unit to recover nutrients from waste streams using engineered biochar as filtration media

Matt Smith, Manuel Garcia-Perez

3.4.1—Abstract

The feasibility of using a bed of biochars to retain ammonium and phosphate from dairy manure was assessed in this task. The retention of ammonium on chars is considerably more costly than for phosphate due both to the higher concentration of ammonium typically found in effluents and the lower maximum retention rates that were identified. The maximum possible retention rate based on the results obtained in Section 3.3 is approximately 35 $cmol_c$/kg, or 6.5 kg (NH_4^+)/ton. This rate is higher than could be achieved due to competitive adsorption of other cations. Even assuming 4 kg/ton as feasible, a 1000 cow dairy would require at a minimum 7000 tons of char to filter a 0.5 kg/m^3 waste steam.

Because the requirements for phosphate removal are considerably lower, the feasibility was assessed further, with evaluation of using engineered biochar as a filtration media in a transportable unit for treating stored manure at small dairy farms. Packed bed adsorption characteristics were modeled, and a scenario was developed based on the development of a filter that could be deployed via a tractor trailer to pump and filter lagoon water. Performance was evaluated for a hypothetical 100-cow dairy, producing 12 m^3 of wastewater containing 0.25–1.5 kg/m^3 phosphate. Results indicated that in order to process the waste water, a residence time of 1.4 hrs was required, and a maximum inlet concentration of 0.5 kg (PO_4)/m^3 could be utilized to maintain a target removal of greater than 75%. At this level, the market value of phosphate is insufficient to support the cost of filtration requiring additional economic or regulatory incentives to be considered before the viability of this method can be established.

3.4.2—Introduction

As described more fully in the previous section, the development of technologies to remove N and P from waste streams is of interest to the dairy industry in WA, with the potential to provide economic and environmental benefits. Based on this understanding, the feasibility of using a bed of biochars to retain ammonium and phosphate from dairy manure was assessed in this task.

3.4.3—Nitrogen removal

Assumptions about N removal capabilities were based on the results from experiments described in section 3.3. The results from oxidation of AD char, hybrid polar char and pine wood char showed approximately 35 centimols (NH_4^+)/ kg char to be a reasonable upper estimate of the

potential CEC and retention capacity of chars, given ideal conditions. This translates to approximately 6.5 kg (NH_4^+)/ton of char as the upper retention limit. Table 3.4.1 estimates the amount of modified char required annually to treat dairy effluent at various TAN loadings at a 1000 cow dairy. In these calculations, 1.5 g/L used as the upper limit, with 200–500 mg/L considered as the probable range after NR. The results indicate that 5–40 tons per day of oxidized char would be required to treat the effluent produced. At the lower range this represents a potentially reasonable quantity; however, the upper range would present significant material handling difficulty. A maximum daily production of 115 tons would be required to treat a 1.5 g/L effluent stream assuming 2 kg (NH_4^+)/ton retention.

Table 3.4.1: Annual char required to remove TAN from solution in a 1000 cow dairy assuming single ion retention at various retention rates

	Annual tons of char for 1000 cow AD system		
	Ammonium Retention on Char		
TAN (mg/L)	2 kg/ton	4 kg/ton	6 kg/ton
10	280	140	93
50	1398	699	466
100	2796	1398	932
200	5593	2796	1864
500	13982	6991	4661
1000	27964	13982	9321
1500	41946	20973	13982

However, to fully interpret these results, it is important to understand that an additional concern present for ammonium recovery is competitive inhibition by other cationic species present in the effluent. An example of cation concentrations in a dairy effluent is given in Table 3.4.2. Ammonium absorption has been shown to suffer considerably from competitive inhibition from both Na and K. Both of these are present in significant quantities in dairy effluent. Due to the presence of both Na and K, larger quantities of char will be required to handle ammonium in solution.

Table 3.4.2: Example of metal cation concentrations in digester effluent based on dairy manure

Dairy Digester Effluent			
Species	Conc (g/L)	species	Conc (mg/L)
Na	1.2	Fe	72
Mg	0.4	Al	25
K	10.0	Mn	24
Ca	2.9	Cu	11
		Zn	13
		Ba	2

3.4.4—Phosphate removal

The removal of phosphate by AD fiber is considerably more promising given the lower phosphate concentration and the higher equilibrium adsorption mass. Significant reduction of the ionic phosphate (estimated at 50–100 mg/L) would require only a fifth of the char that would be needed to treat the same waste water for ammonium. Based off of these results and those presented in section 3.3, a transportable filtration system for the removal of phosphate from a dairy lagoon was modeled.

The design criterion for the transportable filtration media was based on the concept of a filter that can be deployed via a tractor-trailer to smaller dairies to pump and filter lagoon water (Figure 3.4.1). To perform successfully in this scenario, the filter should be able to handle at least a month's worth of lagoon water in under 8 hrs (1 day's works) with at least 75% removal of phosphate. Performance was evaluated for a hypothetical 100-cow dairy, producing 12 m^3 of wastewater containing 1.5 kg/m^3 phosphate. Under these conditions, 7.33 tons of char will be required to treat effluent that has accumulated over a one month period; more details can be seen in Table 3.4.3. For the filter model, the minimum char requirement was tripled to ensure adequate removal. The removal efficiency of this filter was modeled assuming ionic phosphate concentrations of 0.025–1.5 kg/m.

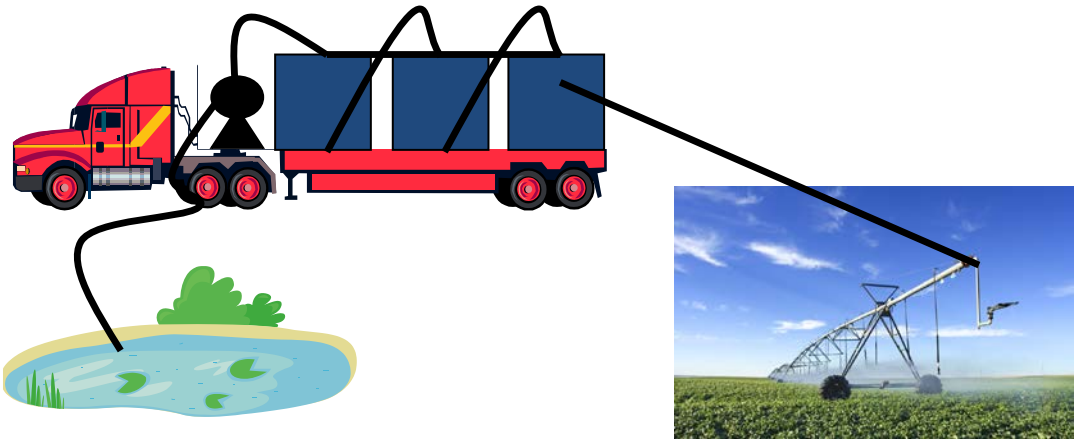

Figure 3.4.1: Scheme where the filter can be deployed on a trailer. The trailer travels to dairy, where P-containing lagoon water is pumped through the biochar and thereafter used for irrigation

Table 3.4.3: List of variables and outputs

Variable	Values
Dairy Parameters	
Cows	100
Water/day (m3)	11.968
Water (m3)/month	359.04
kg (PO4)/m3	.025-1.5
Adsorption Parameters	
ρpb (kg/m3)	300
K (1/hr)	0.45
qm (kg/kg)	0.0245
b (m3/kg)	150
Filter Design	
Tons Char (tons)	21.98
Volume of Char (m3)	73.27
radius of filter (m)	1.25
hight of total filter (m)	14.93
# of filter units	4.00
height of filter units (m)	3.73
v (m/hr)	10.76

Packed bed adsorption characteristics were modeled based upon the kinetic and equilibrium phosphate adsorption data obtained in the previous task. Ammonium adsorption data showed significant variation and was inconclusive for the generation of design parameters. The packed bed column was modeled as a plug flow reactor following first order kinetics as determined previously. The equilibrium between the solid and aqueous phase was determined by a Langmuir isotherm.

3.4.4.1—Continuity equation

The continuity equation is as follows:

$$\frac{\partial C}{\partial t} + \frac{v\partial C}{\partial Z} + \frac{\rho_{pb}\partial q}{\partial t} = 0 \qquad 3.4.1$$

Where:

C = concentration in solution (kg/m^3)

Z = the axial distance along the filter (m)

q = the concentration on the char particle (kg (PO_4^{3-})/kg)

v = the interstitial velocity of the waste water (m/s)

ρ_{pb} = bulk density of the particle (kg/m^3)

The concentration of adsorbate on the char surface was previously found to be well characterized by a first order adsorption model

$$\frac{\rho_{pb}\partial q}{\partial t} = K(qe - q) \qquad 3.4.2$$

Where:
K = the first order rate constant (1/hr)
qe = the equilibrium concentration on the adsorbate at C (kg (PO_4^{3-})/kg)
The variation of the equilibrium concentration was determined by a Langmuir isotherm, where qe is related to C by the following equation:

$$qe = \frac{qm * b * C}{1 + b * C} \quad 3.4.5$$

Where:
qm = the equilibrium constant (kg (PO_4^{3-})/kg)
b = adsorption constant (m^3/kg)

3.4.4.3—Evaluation of filter efficiency

The most promising phosphate adsorption kinetics from Section 3.3.4 were used to determine the scale and efficiency of a hypothetical filter. The system was designed with 8 hrs of feed time and a 1.4 hr residence time. This led to a total operation of 9.4 hrs per day. The 8-hr exit solution concentration profile was generated (Figure 3.4.2). The list of variables and outputs are given in Table 3.4.3. From these results, it is apparent that a 75% reduction of phosphate is not possible at a 1.5 kg/m^3 concentration. At this level, only 36% of the initial phosphate was retained. To achieve total reduction of 75% or more of phosphate, a maximum concentration of approximately 0.5 kg/m^3 is required. With inlet concentrations of 0.5–1.5 kg/m^3, the total mass of phosphate retained during operation would equal 150–200 kg. At this level, the market value of phosphate is insufficient to support the cost of filtration requiring additional economic or regulatory incentives to be considered before the viability of this method can be established.

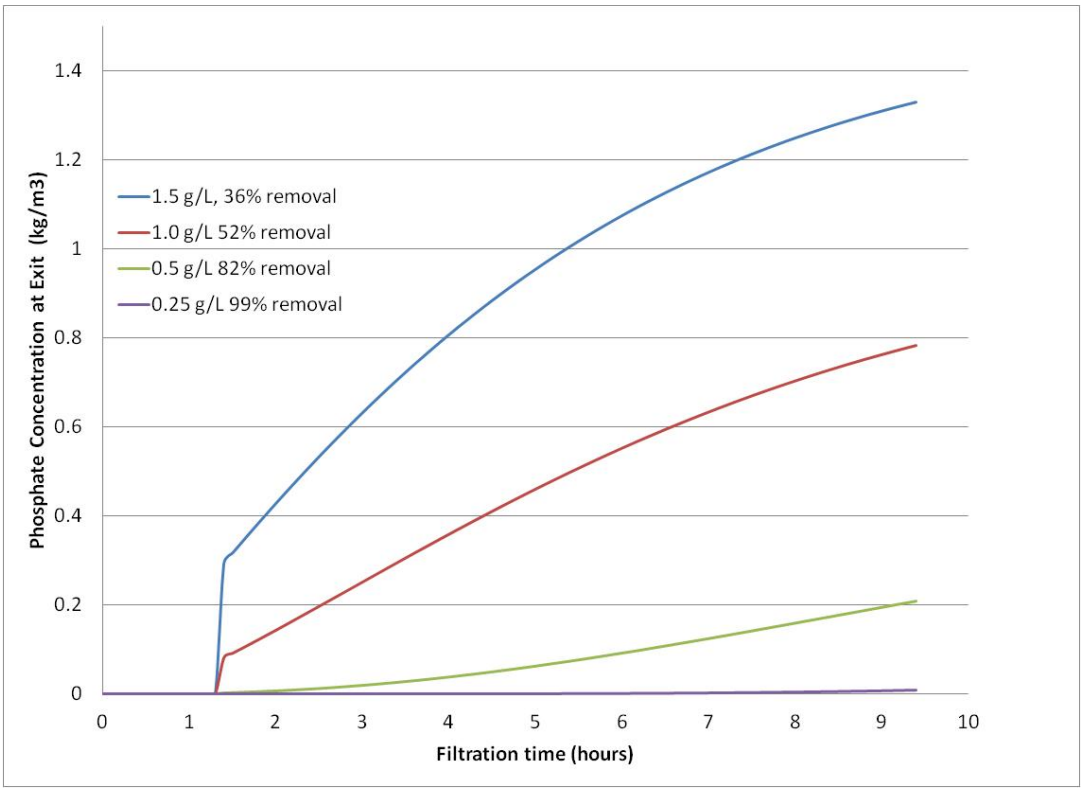

Figure 3.4.2: Concentration profile for adsorption with calcium-infused biochar, simulated ideal plug-flow packed-bed column

3.4.5—Conclusions

A hypothetical packed bed filter, utilizing the most promising phosphate adsorption kinetics from section 3.3.4 and a hypothetical 8 hr feed time with 1.4 hr residence time, was evaluated. Results indicated that at a 1.5 kg/m^3 concentration, only 36% of the initial phosphate was retained. To achieve total reduction of 75% or more of phosphate, a maximum concentration of approximately 0.5 kg/m^3 would be required. With inlet concentrations of 0.5–1.5 kg/m^3, the total mass of phosphate retained during operation would equal 150–200 kg. At this level, the market value of phosphate is insufficient to support the cost of filtration requiring additional economic or regulatory incentives to be considered before the viability of this method can be established.

Appendix A: Development and Validation of a Mathematical Model for an Auger Pyrolysis Reactor

Jesus Alberto Garcia-Nunez[1], Jeroen de Graaf[1,2], Manuel Garcia-Perez[1]

[1]Biological System Engineering Department, WSU
[2]Chemical Engineering Department, University of Twente

1—Introduction

When processing biomass in a pyrolysis reactor different forest and agricultural particles can be used to yield gases, bio-oil and biochar. The yield of these products depends on the outcome of the primary and secondary reactions, which are controlled by the rate of heat and mass transfer inside the particle. All these parameters are dependent on the chemical composition of the feedstock and structure of the biomass processed. Heat and mass transfer rates inside a biomass particle depend on the anatomy dimensions of the biomass particle processed.

Among other factors, the performance of a pyrolysis reactor is a function of the behavior of the single particles, the particle size distribution and the residence time distribution of biomass particles inside the reactor. Unfortunately, experimental testing, to determine the favorable parameters in pyrolysis reactors for the different types of wood particles, is very expensive. Thus, the development of mathematical models to simulate the process and determine the product yield may be a more favorable and economic approach for optimization. The goal of this project is to develop a mathematical model that is able to predict the yield of products obtained during the pyrolysis of forest and agricultural particles in an auger pyrolysis reactor.

The effect of heat on mass transfer in a particle depends on the size, geometry and the moisture content of the particle. The mathematical model to predict the yield of the products will be developed in two model steps.

The first step consists of the description of heat and mass transfer within a single biomass particle. In this task, models will be developed with COMSOL that describe the heat and mass transfer in the different directions inside the particle. COMSOL is a finite element analysis, solver and simulation software package for various physics and engineering applications, especially coupled phenomena. These models will take into account the effect of geometry and moisture content on the effective thermal conductivity and effective mass diffusivity in the radial and axial direction inside biomass particles. The effective thermal conductivity and mass diffusivity obtained with the COMSOL model will be compared with those from models developed by other authors as well as experimental data reported in literature.

The second step consists of a single particle model that will take into account the primary and secondary reactions as well as the heat and mass transfer inside and outside the particle and the moisture content and shrinkage factor. The results obtained with this single particle model will be compared with some experimental results obtained by Li et al at Curtin University, Australia.

Lastly, a model for the auger pyrolysis reactor will be described. The model was validated using the data obtained in a 1 kg/h auger pyrolysis reactor.

In summary, models were developed to describe the phenomena at three levels including (1) the biomass cell wall to estimate the transport properties, (2) the single particle level, and (3) the reactor level.

1.1— Wood structure

The physical model, needed to support the development of a mathematical model to calculate effective heat and mass transfer inside wood particles, depends on the type of transport that needs to be modeled and the direction in which that transport takes place. To determine the effective thermal conductivity and the effective mass diffusivity different physical models are available in literature for the radial and axial direction. All these models take into account the shape of the wood cells. The type of wood (hardwood or softwood) is the first factor for describing how the physical model will take shape (see Figure 1A). Both hard- and softwood generally have tracheids composed of a lumen and a cell wall. The cell wall consists of cellulose, hemicellulose and lignin and these biopolymers are thermally degraded when biomass is heated (Mishnaevsky Jr & Qing, 2008).

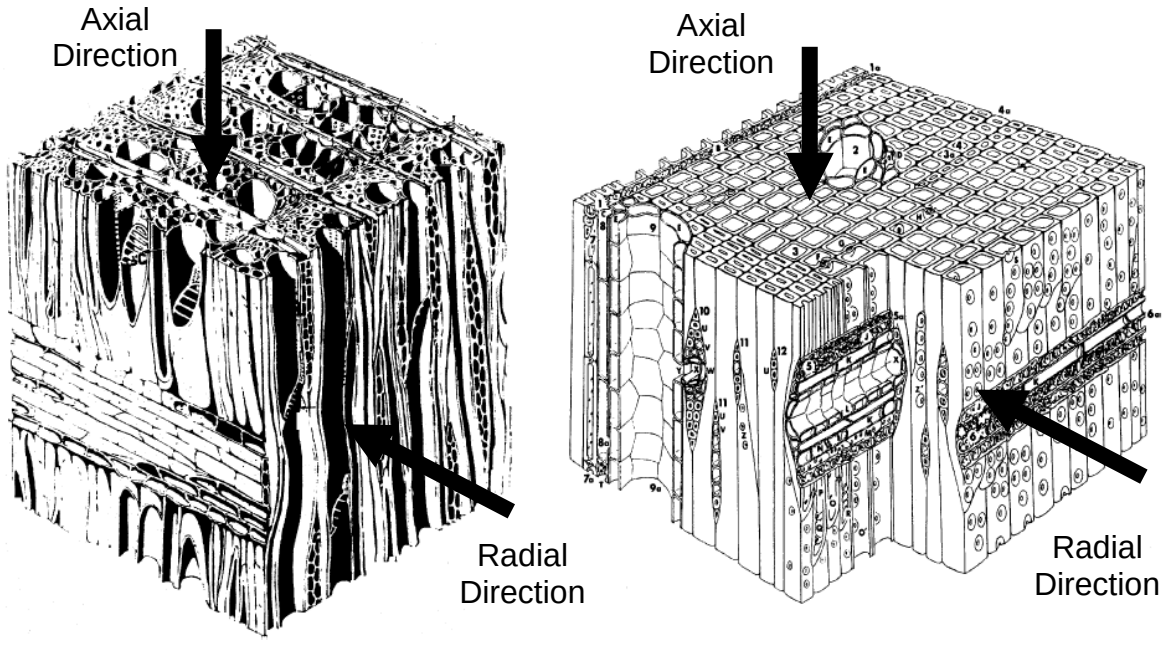

Figure 1A: Fiber structure of hardwood (*left*) and fiber structure of softwood (*left*) (Thunman & Leckner, 2002)

Since wood cells are long and narrow and because of this the effective thermal conductivity and effective mass diffusivity will also differ in each of the directions. The suggested physical models from previous research for the radial and axial orientation of both heat and mass transfer are presented and discussed in the remainder of this section. The single particle model used in this study considers the wood as a nearly homogeneous material and describes heat and mass transfer by the use of effective transport parameters (effective conductivity (k_{eff}) and effective diffusivity (D_{eff})).

1.2—Heat transfer

Several papers and books have been published describing mathematical models to predict the effective thermal conductivity of biomass in the radial and/or axial direction (Eitelberger, 2010; Hunt et al., 2008; Siau, 1984; Thunman & Leckner, 2002).Their research will be used as background information for this project.

1.2.1—Physical model radial heat transfer

For heat transfer in the radial direction, the physical model is described as if looking on top of the lumen (space of a tubular structure) (see Figure 1A). The physical model of one wood cell can be approached by a square cell (see Figure 5A) (Hunt et al., 2008; Siau, 1984; Thunman & Leckner, 2002).

The cell is considered to be formed by four volumes depending on the porosity and moisture content of the wood particle (See Figure 2A). If the particle has no lumen (0% porosity), the cell will only consist of cell wall material. If there is moisture present in the particle, the physical models reported in literature typically consider the presence of bound water inside the cell wall. When the wood cell has a lumen (porosity > 0%), it is initially filled with air. When increasing the moisture content of the wood, cell water will start to fill up the cell as bound water and the lumen is assumed to be filled with saturated air. During this process the bound water is assumed to increase the dimensions of the wood cell. The cell wall can only take up a certain amount of bound water (this will vary per type of wood) and the point at which the cell wall is full of water is called the fiber saturation point. If the moisture content in the wood cell is above the fiber saturation point, a layer of free water will form against the cell wall inside the lumen. It is assumed that this layer is uniform over the entire lumen and that the remainder of the lumen is still filled with saturated air (Hunt et al., 2008).

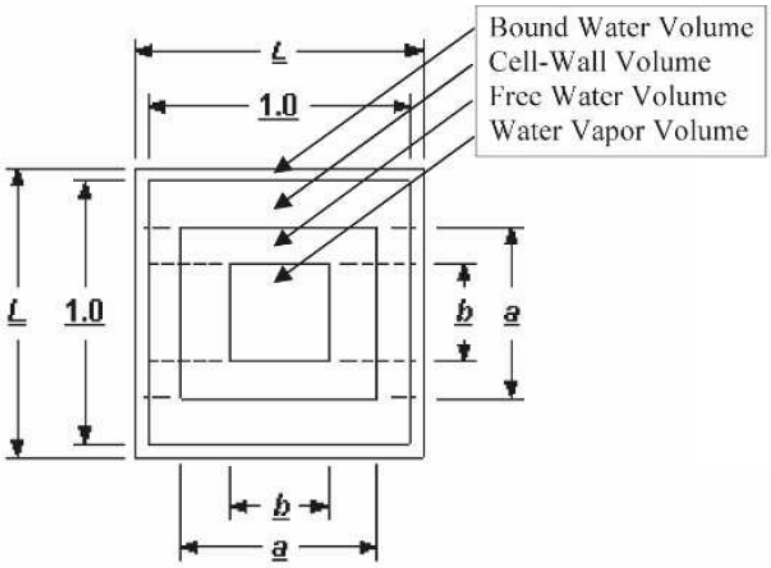

Figure 5A: Representation of the radial physical model of a wood unit cell (Hunt et al., 2008)

Equation (1) was developed based on the physical model shown in Figure 5A to calculate the effective radial thermal conductivity (Hunt et al., 2008). This equation will be used to validate the COMSOL model that is proposed in this study. Equation (1) describes the effect of the geometry on the individual conductivities and combines those into the effective thermal conductivity.

$$\frac{K_{eff,r}}{(L-a)K_f} = \frac{}{(a-L)\left\{\left(\frac{a}{L}-1\right)X_1 + K_f\left[\frac{(a-b)X_2}{(a-L)K_f - aK_{fw}} + \frac{bX_3}{(a-L)K_f + (b-a)K_{fw} - bK_v}\right]\right\}} \quad (1)$$

Where K_{eff}, is the effective thermal conductivity [Watt per meter Kelvin] [W/m/K] of the cell. K_f, K_{fw} and K_v are the thermal conductivities of the fiber (cell wall and bound water), free water and water vapor respectively [W/m/K]. L, b and a represent the dimensionless lengths of the unit cell as described in Figure 5A. X_1, X_2 and X_3 are model parameters for which the values are given in Table 6A in Attachment A.

1.2.2—Physical model axial heat transfer

The physical model in the axial direction is described as a cut through parallel to the lumen while looking from the side of the lumen. The physical model of the wood cell reported in literature consists of multiple rectangles representing the cell wall and its various solid, liquid and gas phases (see

A) (Thunman & Leckner, 2002). Just as with the physical model for radial heat transfer, the physical model for axial heat transfer varies with the porosity and moisture content of the wood. The width of the cell will vary with the porosity, increasing the porosity will increase the width of the gas phase and decrease the width of the solid phases. Increasing the moisture content will first increase the solid phase because the water will first be added as bound water to the cell wall (Hunt et al., 2008). When the fiber saturation point has been reached, an even water layer will form inside the lumen, thus increasing the water volume and decreasing the gas volume (Hunt et al., 2008; Thunman & Leckner, 2002). However, the lumen is not continuous throughout the cell. Tracheids in the tangential direction interrupt the lumen in the axial direction (Eitelberger, 2010; Siau, 1984). This leads to the axial physical model for the wood unit cell as shown in

A.

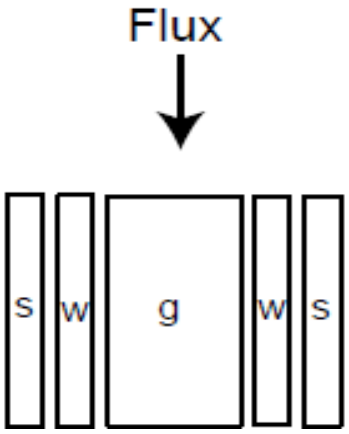

Figure 3A: Representation of the axial physical model of a wood unit cell; solid phase (s), water (w), and gas phase (g) (Thunman & Leckner, 2002)

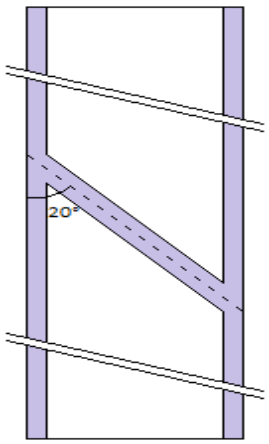

Figure 4A: Representation of the axial physical model of a wood unit cell (tracheid) (Eitelberger, 2010)

Equation (1) was developed based on the physical model shown in

A to calculate the effective axial thermal conductivity (Thunman & Leckner, 2002). This equation will be used to validate the COMSOL model that is proposed in this study. Equation (1) describes the influences of the geometry on the individual conductivities and combines those into the effective thermal conductivity. The assumption is made that the presence of 1 tangential tracheid in the physical model will not have a significant effect on the effective axial heat conductivity and it is therefore assumed that Equation (1) is also applicable to the unit cell as presented in

A.

$$K_{eff,z} = (1 - (1 - \omega_s)^2)K_s + \left((1 - \omega_s)^2 - {\omega_g}^2\right)K_w + {\omega_g}^2\left(K_g + K_{rad}\right) \quad (1)$$

Where K_s, K_w, K_g and K_{rad} are the axial thermal conductivities of the solid phase (cell wall), water phase (free water), gas phase (air or water vapor) and radiation respectively [W/m/K]. ω_s and ω_g represent the dimensionless width of the solid and gas phase respectively.

1.3—Mass transfer

Several papers and books have been published describing mathematical models to predict the effective mass diffusivity for moisture diffusion in the radial and/or axial directions (Eitelberger, 2010; Kang et al., 2008; Siau, 1984). Their research will be used in this project for the development of the proposed mathematical model.

There are numerous pits located in the cell wall, which are small openings in the cell walls between two cells (refer back to Figure A). For the heat transport, the pits in the cell walls are assumed to have no significant influence and are therefore neglected in the physical models for heat transfer. For mass transfer, however, this is not the case. Due to their relatively small diameter and large number, pits have a significant impact on the fluid transport through the wood cell (Kettunen, 2006; Tarmian et al., 2011; USDA, 2010), which means the pits have to be taken into account to effectively describe mass transport. There are different types of pits that can be present in wood cells. They typically consist of a pit chamber, pit aperture and membrane (Grønli, 1996; Kettunen, 2006; Siau, 1984). However, in this project the pits are assumed to be simple openings with a consistent diameter at a specific temperature and moisture content.

1.3.1—Physical model radial mass transfer

Pit diameters in softwoods range in size from 0.02 µm to 4 µm in the axial direction with a logarithmic mean of 0.3 µm (Siau, 1984). The pit aperture contributes over 90% of the resistance of the pits (Siau, 1984) and,, therefore, the assumption is made that the effective pit diameter is equal to the pit aperture diameter.

A physical model for the radial mass transfer is shown in Figure 6A(i). In the radial direction there will be a contribution of both rays and pits to mass transfer, but in this project the effect of the rays will be combined with that of the pits into one effective parameter that influences the porosity of the cell walls (Burr & Stamm, 1947). Figure 6A(ii) shows the physical model for pits.

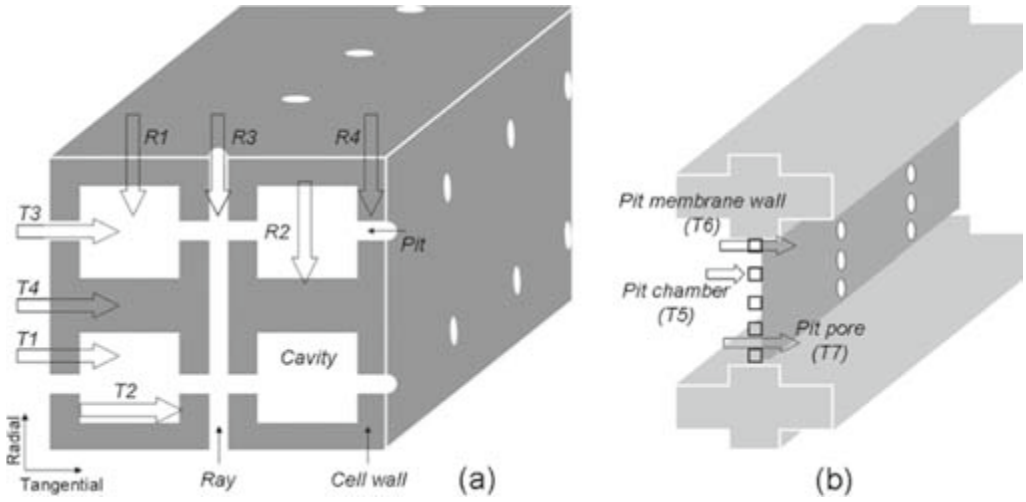

Figure 6A: Representation of the radial physical model for: (i) a wood unit cell, (ii) a pit (Kang et al., 2008); the arrows represent the different resistance paths mass transport can encounter

1.3.2—Physical model axial mass transfer

The physical model for the axial mass transfer is similar to the one used for the axial heat transfer (

A) but it takes into account the presence of pits. For the determination of the effective axial mass diffusivity, the assumption is made that the diffusion through the cell wall is negligible when compared to the diffusion through the lumens. This means that the physical model can be simplified to a physical model of a porous material, which has two different porosities, that of the lumen and that of the wall while taking into account the presence of pits.

1.4—Single particle model

Many authors have researched the pyrolysis of wood particles with the use of models (Chan et al., 1985; Di Blasi, 2000; Di Blasi, 2008; Janse et al., 2000; Kersten et al., 2005; Sadhukhan et al., 2009; Wang et al., 2005). Different authors may focus on different aspects of the pyrolysis process such as the formation of char (Sadhukhan et al., 2009), a study on the effect of using a 1D or 2D single particle models (Kersten et al., 2005), or testing the influence of using different

kinetics or predicting the yield of the different pyrolysis products (Janse et al., 2000; Kersten et al., 2005; Wang et al., 2005)

The developed mathematical models in the literature are validated with experiments conducted by either the author itself or from literature sources. Experimental data is collected under different conditions (temperature, reactor type, wood type, reaction mechanisms) resulting in a diverse availability of developed models. This diverse array of models will be used in this project for the development of the single particle model.

1.5—Auger pyrolysis reactor

The auger pyrolysis reactor is one of the most attractive designs developed today (Garcia-Perez, 2011) because it is able to achieve high yields of oil and a biochar that are free of sand particles. This reactor is fed with biomass at one end through a hopper. An auger (screw) then gradually conveys the wood waste (biomass) through the reactor. Carbonization happens as the particles contact the hot wall (Figure 7A). The gases and vapors are extracted and are carried to a condenser where bio-oils are collected. The resulting biochar falls to the bottom of the reactor. Hot vapors residence time in these reactors can average between 5 and 30 s (Bridgwater, 2012). These reactors can be operated with and without using hot sand, steel or ceramic balls as a heat carrier (Garcia-Perez, 2011). The biochar is discharged through a single tube leading to airtight metal receivers. The lowest level of the main structure consists of a combustion chamber that provides heat to the area in which the carbonization process is continued utilizing either heat furnished from the burning of its own gases or heat from external sources.

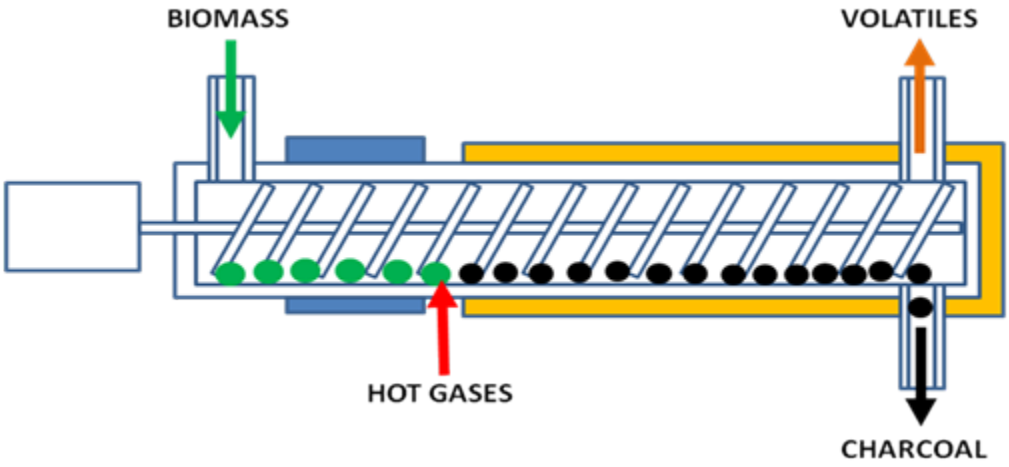

Figure 7A: Schematic representation of an auger pyrolysis reactor (Garcia-Perez, 2011)

Pyrolysis auger reactors can be suited to produce either bio-oil and biochar or biochar and heat. For the bio-oil and biochar production, there currently are companies that are selling this technology. For example, ABRI-Tech has developed heated auger reactors using hot metal beads as a high density heat carrier (Venderbosch & Prins, 2010) and is now selling 1 t/d and 50 t/d units. ABRI-Tech specializes in design of transportable pyrolysis plants. Bioliq Process has developed a system that uses a twin screw mixer reactor with hot sand at temperature between 550 and 660°C., producing bio-oil and charcoal that is converted to syngas in a slagging

pressurized entrained flow reactor (http://www.bioliq.de/english/64.php, date accessed: Nov. 13, 2011). The yields of products are approximately 20% charcoal, 50 to 60% pyrolysis oil, and 20 to 30% gas on a water- and ash-free basis (Dinjus & Dahmen, 2010). Renewable Oil International® LLC (ROI), a company based in Alabama, also targets the development of mobile pyrolysis technologies using auger reactors (Garcia-Perez, 2011). Biogreen® is a French company developing auger pyrolysis reactors for the production of bio-oil, biochar and synthesis gas (Garcia-Perez, 2011).

For the production of biochar and heat, some commercial companies are currently offering technology that achieves these end-products. Agri-Tech Producers (ATP), a company based in Columbia, South Carolina, uses auger reactors for torrefaction and pyrolysis (Garcia-Perez, 2011). Another company commercializing auger pyrolysis units is International Tech Corp. Their thermal recovery unit combusts all the pyrolysis vapors to produce heat. The heat can then be converted into steam. International Tech Corp. develops products from biochar such as activated carbons, soil enrichments and custom carbon products. The system is designed to destroy most forms of solid waste and their system can process 50 t/d of biomass (Garcia-Perez, 2011). eGenesis Industries (based in California) is also developing auger pyrolysis reactors for the production of biochar and heat. Their CR-2 unit is able to operate at 40 kg/h producing an energy output of 64 kW from syngas. The clean syngas can be used as source of heat or be used for power generation. The company is currently designing Model CR-3 for a capacity of 1 t/h (Garcia-Perez, 2011).

The parameters controlling the yields of biochar and bio-oil in auger reactors (heat carrier inlet temperature and mass flow rate, rotational speed of screws in the reactor, and volumetric flow rate of sweep gas) were studied recently by Brown (2012). The optimal conditions for achieving maximum bio-oil yields were at flow rate of sweep gas of 3.5 standard L/min, carrier temperature of ~600°C, high auger speeds of 63 RPM and high heat carrier mass flow rates of 18 kg/h. Figure 8A shows some results using response surfaces methodology for some specific conditions of an auger reactor working with a heat carrier.

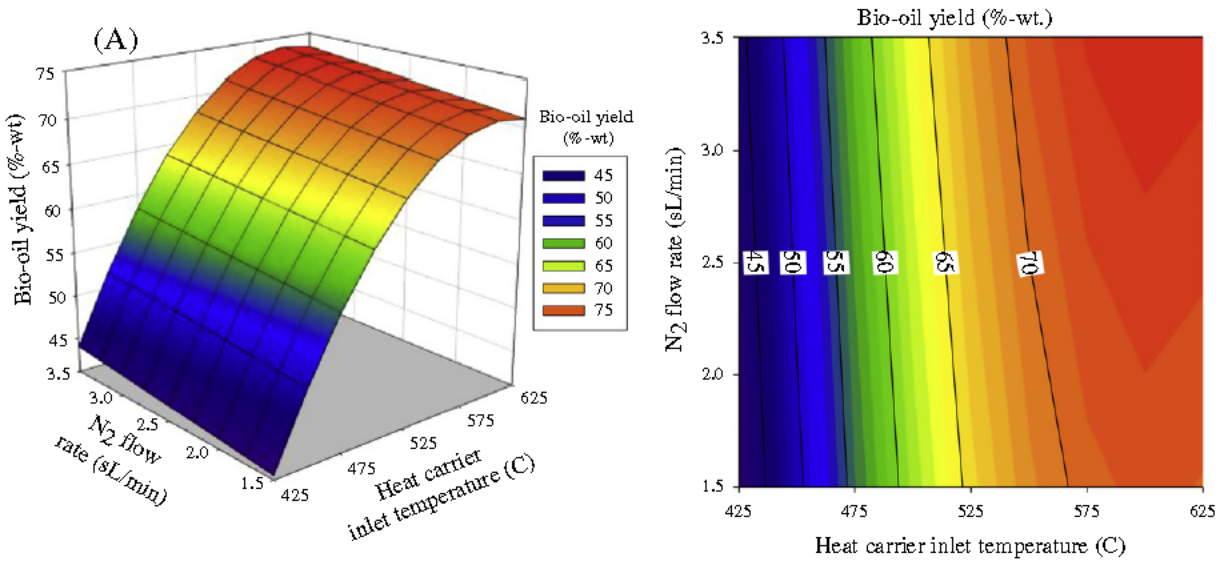

Figure 8A: Response surfaces and contour plots for bio-oil yield as a function of heat carrier inlet temperature and N_2 flow rate (auger speed = 54 RPM, heat carrier mass flow rate = 15 kg/h) (Brown & Brown, 2012)

1.6—Objective

The objective of this project is to develop mathematical models that accurately calculate the effective thermal conductivity and mass diffusivity of wood in the radial and axial direction and that describe the yield of products when a single biomass particle is pyrolyzed in an auger pyrolysis reactor. A mathematical model is constructed for each situation in COMSOL based on the corresponding physical models. Validation of the mathematical model will be done by comparing the results from COMSOL with previous studies from literature. The parameters estimated by COMSOL will then be integrated into a model to describe the behavior of single biomass particles undergoing pyrolysis. This model will then be validated by comparing experimental data and modeling results. The single particle model will be used to simulate temperature profiles of wood cylinders. A model of an auger reactor to describe the temperature profile in the auger pyrolysis reactor was developed and validated with experimental data collected in a 1 kg/h auger pyrolysis reactor.

2—Development of the physical models

2.1—Methodology

In the development of the mathematical model, a general strategy is used, which includes the following 10 steps (Garcia-Perez, 2011):

1. Problem definition
2. Identifying controlling factors
3. Finding a suitable physical model
4. Constructing the mathematical model
5. Preliminary evaluation of the model
6. Solving of the mathematical model
7. Developing an algorithm to solve the problem
8. Computer programming
9. Adjusting the model parameters
10. Validation of the model

This section will contain the development of the physical models, the mathematical model and the method of validation. The actual simulations and results are presented in chapter 3.

2.1.1—Problem definition and controlling factors

For the development of the single particle model, the effective thermal conductivity and mass diffusivity in the axial and radial direction are required. The controlling factors in determining the effective thermal conductivity and mass diffusivity are the geometry of the particle and the moisture content. To obtain a useable single particle model first the physical and mathematical models for the heat and mass transfer will be discussed.

2.2—Heat transfer

To obtain the effective thermal conductivity, the physical model corresponding to the radial or axial physiology was built in COMSOL. The physical models are developed for softwood particles and are shown in FigureA and Figure A.

2.2.1—Physical model radial heat transfer

To determine the effective radial thermal conductivity a unit cell based on the physical model for radial heat transfer (Figure 5A) is used. Literature states that the cell wall dimensions vary from 30 to 50 µm (Basu, 2010; Eitelberger, 2010; Grønli, 1996; Kettunen, 2006; Siau, 1984). These dimensions depend on the wood type and position (heart- or sapwood) and where the wood sample is taken from the wood source. The dimensions of the cell wall for the model are 40 by 40 µm unit cell, of which is transformed into a 10 by 10 cell block Finite Element model. Attached to the right side of this cell block is a 100 µm thick nylon block that is used as a standard of known thermal conductivity to estimate the thermal conductivity of the wood (FigureA).

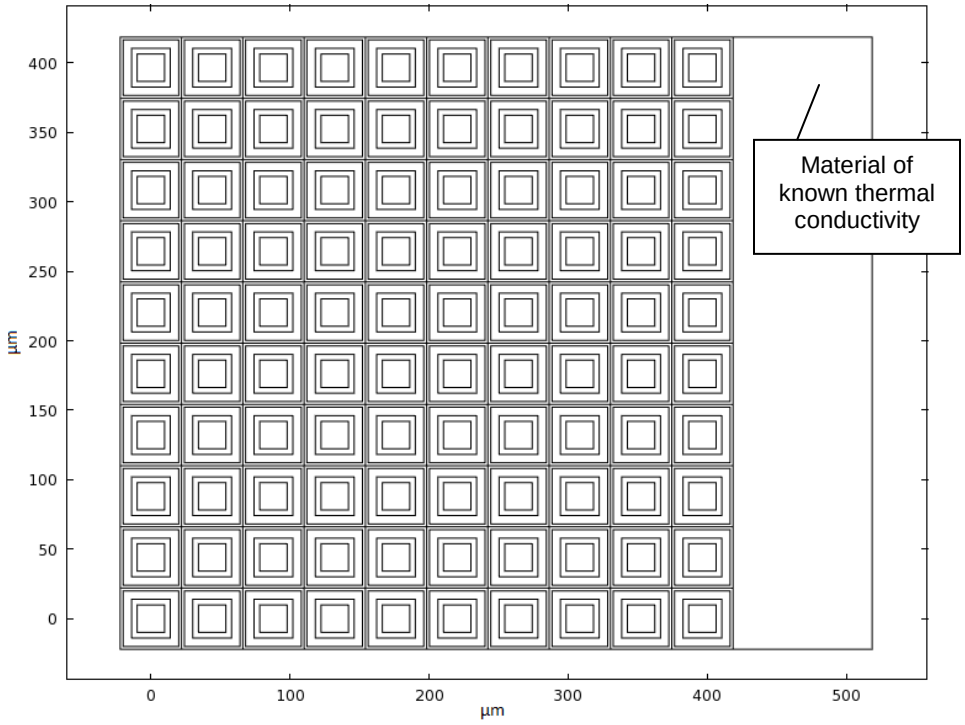

Figure 8A: Example of the COMSOL physical model used in determining the effective radial thermal conductivity. Here the lumen is filled with 50% free water and the wet porosity is 40%

The physical and thermal parameters used for the validation of the effective radial thermal conductivity model are shown in Table A.

Table 1A: Physical and thermal properties used for the effective radial thermal conductivity (at 30°C)

Thermal conductivity [W/m/K]	Density [kg/m^3]	Specific heat [J/kg/K]

Cell wall[a]	0.410	1540	1260
Bound water[a]	0.680	1115	4658
Free water[a]	0.610	1003	4176
Water vapor[a]	0.018	0.734	2278
Air[a]	0.026	1.161	1007
Nylon[b]	0.260	1150	1700

Note:
[a.] *Property values obtained from Hunt(2008).*
[b.] *Property values obtained from COMSOL (version 4.1) material index.*

2.2.2—Physical model axial heat transfer

To determine the effective axial thermal conductivity, the physical model as displayed in

A is used. Literature states that the tracheid length varies from 2000 to 5000 µm (Eitelberger, 2010; Grønli, 1996; Kettunen, 2006; Siau, 1984). The length of the unit cell is taken as 3,000 µm and the width of the unit cell as 50 µm (Figure A) to correspond with the physical model parameters as proposed by Eitelberger (2010). The tangential tracheid is constructed halfway of the unit cell and only consists of cell wall material and bound water (if present). Attached to the bottom of the unit cell is a block that is 1000 µm long in the direction of the lumen and has the properties of nylon.

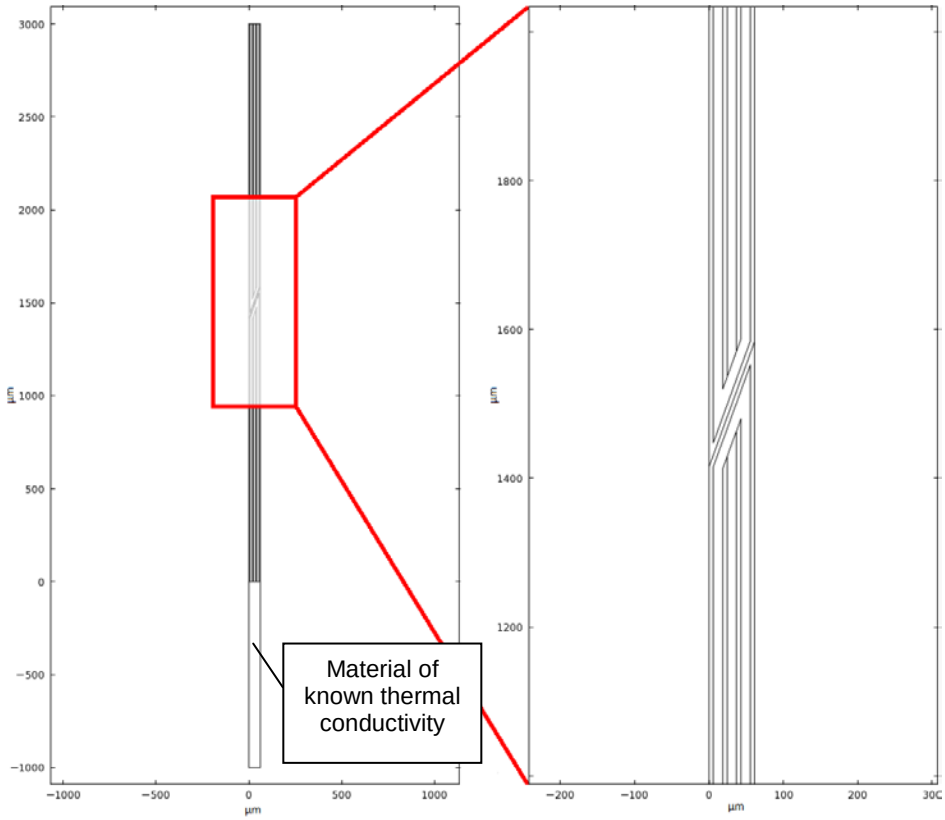

Figure 9A: Example of the COMSOL physical model used in determining the effective axial thermal conductivity; here the lumen is filled with 50% free water and the wet porosity is 40%; left is an overview of the entire model, right is a zoomed section around the tangential tracheid

The physical and thermal parameters used for the validation of the effective axial thermal conductivity model are given in Table A.

Table 2A: Physical and thermal properties used for the effective axial thermal conductivity (at 30°C)

	Thermal conductivity [W/m/K]	Density [kg/m^3]	Specific heat [J/kg/K]
Cell wall	0.73[b]	1480[b]	1260[c]
Bound water	0.611[a]	1000[b]	4180[a]
Free water	0.611[a]	1000[b]	4180[a]
Water vapor[a]	0.019	0.715	2388
Air[a]	0.027	1.149	1006
Nylon[a]	0.260	1150	1700

Note:

[a.] *Property values obtained from COMSOL (version 4.1) material index.*

[b.] *Property values obtained from Thunman and Leckner (2002).*

[c.] *Property values obtained from Hunt et al., (2008).*

2.2.3—Mathematical model heat transfer

For heat transfer of species i in solids COMSOL use the following equation:

$$\rho_i Cp_i \frac{\partial T}{\partial t} - \nabla \cdot \left(K_{eff} \nabla T\right) = Q \quad (2)$$

Where Q is the heat source [J].

For heat transfer in fluids the equation in COMSOL is as follows:

$$\rho_i Cp_i \frac{\partial T}{\partial t} + \rho_i Cp_i \mathbf{u} \cdot \nabla T = \nabla \cdot \left(K_{eff} \nabla T\right) + Q \quad (3)$$

Where **u** is the fluid velocity field [m/s].

When there is no applied velocity field, Equation (3) becomes Equation (2). Under steady-state conditions Equations (2) and (3) can be described by the generalized form known as Fourier's Law:

$$\Phi_h^{"} = -K_{eff} \nabla \mathrm{T} \quad (4)$$

Where $\Phi_h^{"}$ is the heat flux [W/m^2].

2.2.4—Determining the effective thermal conductivity

By applying a temperature gradient over the physical model and then measuring the heat flux, the effective thermal conductivity is calculated by Fourier's Law (Equation (4)).
The theoretical values are determined by using the mathematical model (Equation (1) and Equation (1)) and physical and thermal parameters (Table 1A and Table 2A). Both results are plotted in graphs depicting the effect of the oven-dry density on the effective thermal conductivity for different moisture contents. If the resulting experimental and theoretical graphs correspond with each other, the COMSOL model is assumed to be accurate in predicting the effective thermal conductivity. After this validation, the COMSOL model is ready to be used with the parameters of the desired types of biomass and operating conditions.

2.3—Mass transfer

To obtain the effective mass diffusivity, the physical model corresponding to the radial or axial morphology is built in COMSOL. The physical models are developed for softwood particles and are shown in Figure 10A and Figure 12A.

2.3.1—Physical model radial mass transfer

To determine the effective radial thermal conductivity, a unit cell based on the physical model for radial mass transfer (Figure 6Ai) is used. Literature states that the cell wall dimensions vary from 30 to 50 µm (Basu, 2010; Eitelberger, 2010; Grønli, 1996; Kettunen, 2006; Siau, 1984). These dimensions depend on wood type and position (heart- or sapwood), and where the wood sample is taken from the wood source. The chosen cell wall dimensions for the model is a 40 by 40 µm unit cell of which is transformed into a 10 by 10 cell block Finite Element model. Attached to the right side of this cell block is a 50 µm thick block that is given the properties of air (Figure A).

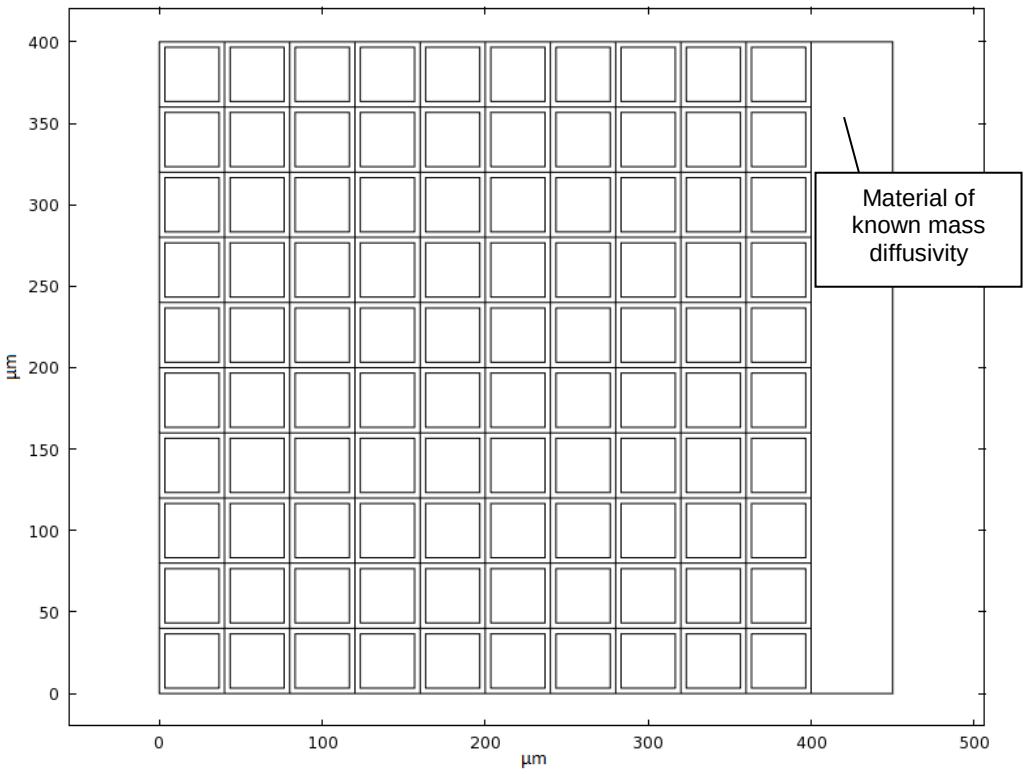

Figure 10A: Example of the COMSOL physical model used in determining the effective radial mass diffusivity

The volume of the lumens will depend on the porosity of the lumen, which can be described as a function of densities and moisture content (Kang et al., 2008):

$$\theta_{lum} = \frac{a^2}{L^2} = 1 - \frac{\rho_{od}}{1 + \frac{\rho_{od}}{\rho_w} MC} \frac{1 + 1{,}53MC}{\rho_{cw}} \tag{5}$$

Where θ_{lum} is the porosity at the lumen, a is the width of the lumen [m], L is the width of the cell [m], ρ_{od} is the oven-dry density [kg/m^3], ρ_w is the density of water (1000 kg/m^3 (Kang et al., 2008)), MC is the moisture content [kg/kg] and ρ_{cw} is the cell wall density (1530 kg/m^3 (Kang et al., 2008)).

The cell walls will have a porosity that depends on the number and size of the pits. The porosity of the cell wall is calculated with the following equation:

$$\theta_{cw} = \frac{n_{pit} {d_{pit}}^2}{n_c L h_c} \tag{6}$$

Where θ_{cw} is the porosity of the cell wall, n_{pit} is the number of pits present on the surface area, d_{pit} is the diameter of one pit [m], n_c is the number of cells in the radial direction and h_c is the height of one cell (tracheid) [m].

The diffusion coefficient of water vapor in air depends on the temperature and pressure and is determined with the following equation (Kang et al., 2008):

$$D_{va} = 2.2 \cdot 10^{-5} \left(\frac{P_a}{P_a + P_v}\right)\left(\frac{T}{273}\right)^{1.75} \quad (7)$$

Where D_{va} is the diffusivity of water vapor in air [m^2/s], P_a is the air pressure (1 atm) [Pa] and P_v is the vapor pressure [Pa].

2.3.2—Physical model axial mass transfer

An adaptation of the axial physical model for mass diffusivity is shown in **Error! Reference source not found.**A, which now includes a visual representation of the pit in the model. As mentioned in the previous chapter, the model can be divided in three sections of which two have the porosity that is equal to the volume ratio of the lumen compared to the cell volume (Equation (5)) and one has the porosity that is equal to the volume ratio of the pit compared to the cell volume (Equation (8)). A schematic of this new model that is used in COMSOL is shown in **Error! Reference source not found.**A. For the validation of the model a length of 3000 µm in the axial direction and a width of 40 µm in both the radial and tangential direction are used for the different wood types. These are in accordance to the averaged parameter values also used for the heat transfer in µm (Eitelberger, 2010; Grønli, 1996; Kettunen, 2006; Siau, 1984). A block of 100 µm long is added at one side in the axial direction with the properties of air.

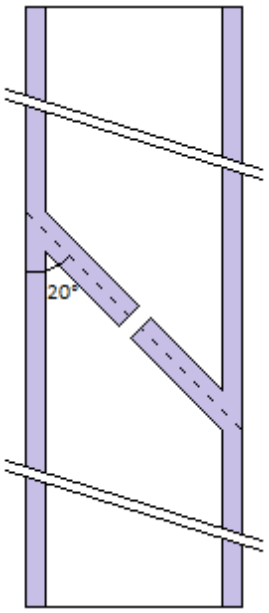

Figure 11A: Representation of the 2D axial physical model of a wood unit cell

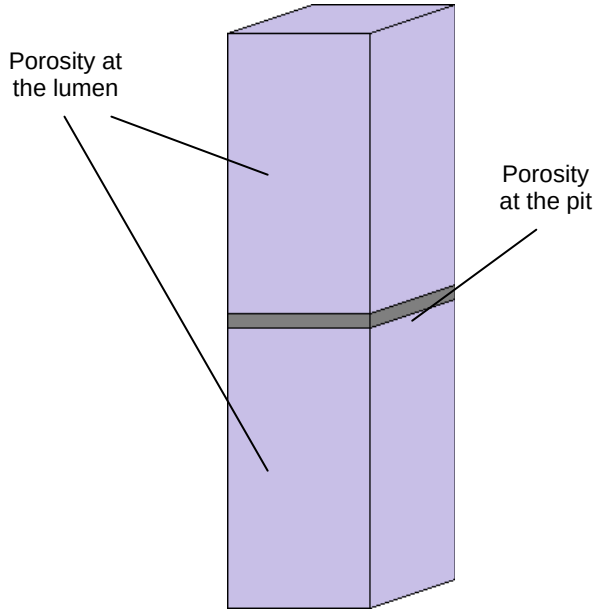

Figure 12A: Representation of the 3D axial physical model of a wood unit cell

The equation for calculating the porosity of the pit section is:

$$\theta_{pit} = \frac{n_{pit} {d_{pit}}^2}{L^2} \quad (8)$$

Where θ_{pit} is the porosity at the pit.

The equation for calculating the porosity of the lumen sections is already given in Equation (5) and uses the same parameters for the density of water and the cell wall (1000 and 1530 kg/m^3 respectively (Kang et al., 2008)).

2.3.3—Mathematical model mass transfer

For mass transfer of a species i through a porous medium, COMSOL uses the following equation:

$$\left(\theta_i + \rho_b \frac{\partial c_{s,i}}{\partial c_i}\right)\frac{\partial c_i}{\partial t} + \left(c_i - \rho_s c_{s,i}\right)\frac{\partial \theta}{\partial t} + \nabla \cdot (c_i \mathbf{u}) = \nabla \cdot \left[-\left(D_{D,i} + D_{eff,i}\right)\nabla c_i\right] \quad (9)$$

Where ρ_b is the bulk (or biomass) density [kg/m^3], c is the concentration [mol/m^3], c_s is the mass of sorbed specie i to solids [mol/kg], ρ_s is the solid phase density [kg/m^3] and D_D is the dispersion tensor [m^2/s].

Since only diffusion is taken into account in this project, Equation (9) can be written as:

$$\theta_i \frac{\partial c_i}{\partial t} = \nabla \cdot \left(-D_{eff,i} \nabla c_i\right) \quad (10)$$

A generalized form of Equation (10) is Fick's Law, which is written as:

$$\Phi_m^{"} = -D_{eff} \nabla c \quad (11)$$

Where $\phi_m^{"}$ is the mass flux.

2.3.4—Determining the effective mass diffusivity

By applying a concentration gradient over the physical model and then measuring the mass flux, the effective mass diffusivity is calculated by using Fick's Law (Equation (11)).

The theoretical values are determined by using the COMSOL mathematical model (Equation (9)) and the physical parameters (Equations (6)–(8)). The results are plotted in graphs depicting the effect of the oven-dry density on the effective mass diffusivity. If the experimental values are within the predicted theoretical range, the COMSOL model is assumed to be able to predict the effective mass diffusivity. After this validation the COMSOL model is ready to be used with the parameters of the desired types of biomass and operating conditions.

2.4—Single particle model

Due to the assumed symmetry of a cylindrical particle only one fourth of the physical model, as shown in Figure 13A, is used as the physical model for the single particle, effectively resulting in a 2D single particle model with length Z and radius R, with the origin in the center of the cylindrical particle.

Through an iterative process, the model will record the temperature change of the particle and the mass change of the different components (wood, char, tars, gas and secondary products) as

the input parameters are changed. For an elaboration on how the single particle model operates, see Attachment E.

Due to symmetry, the center of the particle was chosen as the origin of the cylindrical coordinates of the single particle model.

Through an iterative process the model will record the temperature change of the particle and the mass change of the different components (wood, char, tars, gas, secondary products, moisture, and water vapor) as the input parameters are changed.

The single particle model will be formed by the following equations:

1. Reaction rate equations
2. One mass balance equation per component per phase (one phase because the particle is considered to be pseudo-homogeneous)
3. One energy balance per phase
4. Boundary condition equations (for both heat and mass transfer)

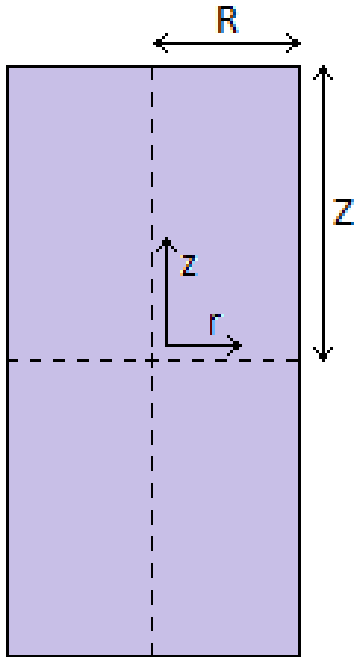

Figure 13A: Physical model single particle

2.4.1—Reaction mechanisms and reaction rate equations

With regard to the kinetics of the single particle model, a simple reaction path model by Shafizadeh and Chin (1977) is used for the primary reactions (Figure 14A) (Di Blasi, 2000; Di Blasi, 2008; Kersten et al., 2005; Shafizadeh & Chin, 1977; Thurner & Mann, 1981; Wagenaar et al., 1993).

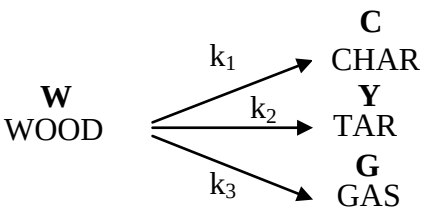

$$k = k_1 + k_2 + k_3$$

Figure 14A: One-component mechanism of primary wood pyrolysis (Di Blasi, 2008; Shafizadeh & Chin, 1977) (where: W: wood, C: char, Y: tars and G: gas)

During pyrolysis, secondary reactions can take place. The secondary reactions that are considered in this project are given in Figure 15A (Di Blasi, 2008). In the remainder of this project the secondary gas, refractory tars and water are considered as one total product (SY) with a kinetic constant k_4.

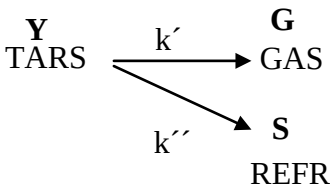

$$k_4 = k' + k''$$

Figure 15A: Secondary reaction mechanism (Antal Jr, 1983; Di Blasi, 2008) (where: Y; tars, G; gas, S: refractory tars)

Moisture content of the biomass has also an effect during pyrolysis; therefore, the moisture is also going to be considered in this model. The water vaporization reaction is given in Figure 16A (Bryden & Hagge, 2003).

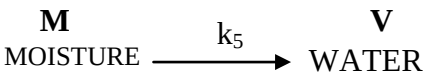

Figure 16A: Vaporization of water (Bryden & Hagge, 2003) (where: M: moisture, V: water)

The reactions in the particle are considered to take place via a first order kinetic scheme (Di Blasi, 2008; Kersten et al., 2005). The reaction rates for the different components in the reaction path are therefore calculated with the following equations, taking into account that these reactions are carried out on the pseudo-solid phase:

$$\frac{\partial W}{\partial t} = -kW = -(k_1 + k_2 + k_3)\, W \tag{12a}$$

$$\frac{\partial C}{\partial t} = k_1 W \tag{12b}$$

$$\frac{\partial Y}{\partial t} = k_2 W \tag{12c}$$

$$\frac{\partial G}{\partial t} = k_3 W \tag{12d}$$

$$\frac{\partial \mathrm{M}}{\partial \mathrm{t}} = -\mathrm{k}_5\,\mathrm{M} \tag{12e}$$

$$\frac{\partial \mathrm{V}}{\partial \mathrm{t}} = \mathrm{k}_5\,\mathrm{M} \tag{12f}$$

Where W, C, Y, G, M and V represent the wood, char, tars, gas, moisture and water vapor components respectively, t is the time [s] and k is the reaction rate constant [s^{-1}].

The reaction rate constant k_i is calculated by the Arrhenius equation:

$$k_{i\,(1,2,3,4,5)} = A_i e^{\left(-E_{a,i}/RT\right)} \tag{13}$$

Where A is the pre-exponential factor [s^{-1}], E_a is the activation energy [J/mol], R is the universal gas constant [J/mol/K] and T is the temperature [K].

The kinetic constants used in Equation (13) are given in Table 3A. Different kinetic values for the primary reactions have been reported in literature (Chan et al., 1985; Di Blasi & Branca, 2001; Thurner & Mann, 1981; Wagenaar et al., 1993). For the validation of the single particle model, the values of Chan et al. (1985) were chosen to comply with the kinetics used in Wang et al. (2005). No parametric study was conducted to evaluate the effect of kinetic parameters on the outcome of the single particle proposed. The secondary reaction scheme as proposed by Antal Jr. (1983) is used and therefore the corresponding kinetic data of the same author is used for the secondary reactions. The water vaporization is taken from Bryden and Hagge (2003).

Table 3A: Kinetic constants for the mechanisms as shown in Figure 12A, Figure 13A and Figure 14A.

	A_i [s^{-1}]	$E_{a,I}$ [kJ/mol]
Char (k_1)[a]	$1.08 \cdot 10^7$	121
Tars (k_2)[a]	$2.00 \cdot 10^8$	133
Gas (k_3) [a]	$1.30 \cdot 10^8$	140
Secondary (k_4) [b]	$3.57 \cdot 10^{11}$	204
Vaporization (k_5)[c]	$5.13 \cdot 10^{10}$	88

Note:
[a.] *Kinetic constants from Chan et.al. as obtained from Di Blasi (2008)*
[b.] *Kinetic constants from Antal as obtained from Di Blasi (2008).*
[c.] *Kinetic constants from Bryden and Hagge (2003)*

2.4.2—Mass balance per component

The mass balances for each of the components in the reaction path are calculated with the following equations including the shrinkage factor:

$$\frac{\partial \rho_W}{\partial t} = \frac{\partial W}{\partial t}\rho_{W_T} - \frac{\rho_W}{\forall}\cdot\frac{\partial \forall}{\partial t} \tag{14a}$$

$$\frac{\partial \rho_C}{\partial t} = \frac{\partial C}{\partial t}\rho_{W_T} - \frac{\rho_c}{\forall}\cdot\frac{\partial \forall}{\partial t} \tag{14b}$$

$$\frac{\partial \rho_Y}{\partial t} = \frac{\partial Y}{\partial t}\rho_{W_T} + D_{eff,Y}\frac{\partial^2 \rho_Y}{\partial z^2} + \frac{\partial(\rho_Y u_z)}{\partial z} - k_4\rho_Y - \frac{\rho_Y}{\forall}\cdot\frac{\partial \forall}{\partial t} \tag{14c}$$

$$\frac{\partial \rho_G}{\partial t} = \frac{\partial G}{\partial t}\rho_{W_T} + D_{eff,G}\frac{\partial^2 \rho_G}{\partial z^2} + \frac{\partial(\rho_G u_z)}{\partial z} + ak_4\rho_Y - \frac{\rho_G}{\forall}\cdot\frac{\partial \forall}{\partial t} \quad (14d)$$

$$\frac{\partial \rho_{SY}}{\partial t} = bk_4\rho_Y + D_{eff,SY}\frac{\partial^2 \rho_{SY}}{\partial z^2} + \frac{\partial(\rho_{SY} u_z)}{\partial z} - \frac{\rho_{SY}}{\forall}\cdot\frac{\partial \forall}{\partial t} \quad (14e)$$

$$\frac{\partial \rho M}{\partial t} = \frac{\partial M}{\partial t}\rho_{W_T} - \frac{\rho_M}{\forall}\cdot\frac{\partial \forall}{\partial t} \quad (14f)$$

$$\frac{\partial \rho_V}{\partial t} = \frac{\partial V}{\partial t}\rho_{W_T} + D_{eff,V}\frac{\partial^2 \rho_V}{\partial z^2} + \frac{\partial(\rho_V u_z)}{\partial z} - \frac{\rho_V}{\forall}\cdot\frac{\partial \forall}{\partial t} \quad (14g)$$

Where ρ is the density [kg/m^3], D_{eff} is the effective mass diffusivity [m^2/s], u_z is the velocity of gas in the interphase, ∀ is the instant volume (shrinkage factor), and z refers to the axial position [m]. The term ρ_{W_T} takes into consideration the sum of the fractions of moisture and dried wood (or biomass).

The mass balances for the biomass, char and moisture (Equations (14a), (14b), and (14f)) depend on both the reaction rate during the process and the shrinkage factor. The scheme used to describe the secondary reactions does not consider the formation of biochar as a result of secondary intra-particle reactions. The tars (both primary and secondary), gas, and water vapor however will diffuse and transport in the particles and will react and therefore a diffusion term and a convective term must be taken into account for the mass balances of tars, gas, and vapor (Equations (14c), (14d), (14e), and (14g)).

The term $\frac{\rho_i}{\forall}\cdot\frac{\partial \forall}{\partial t}$ represents the mass change due to the shrinkage factor. Shrinkage factor is considered by including the instantaneous volume of reaction biomass ∀ on equation (15), where ∀ is given by:

$$\forall = \forall_0 \cdot f_r^2 \cdot f_l \quad (15)$$

Where f_r is the shrinkage factor in radial position and f_l is the shrinkage factor in *z* direction (Sadhukhan et al., 2009). According to Sadhukhan et al. (2009), the experimental value on radial and longitudinal directions is 8% for a cylinder. It assumes that the residual char retains its original structure (Sadhukhan et al., 2009).

2.4.3—One energy balance per phase (pseudo-solid phase)

The overall energy balance for biomass pyrolysis considering velocity of gases and vapors on the radial and axial direction is described by the following equation:

$$\sum_{i=W,C,Y,G,SY,M,V} \rho_i Cp_i \left(\frac{\partial T}{\partial t}\right) + \frac{\partial(\rho_i Cp_i T u_z)}{\partial z} + D_{eff,i}\frac{\partial^2(\rho_i Cp_i T)}{\partial z^2}$$
$$= K_{eff,r}\left[\frac{1}{r}\frac{\partial}{\partial r}\left(r\frac{\partial T}{\partial r}\right)\right] + K_{eff,z}\frac{\partial^2 T}{\partial z^2} + \frac{\partial C}{\partial t}\rho_{W_T}\Delta H_1 + \frac{\partial Y}{\partial t}\rho_{W_T}\Delta H_2$$
$$+ \frac{\partial G}{\partial t}\rho_{W_T}\Delta H_3 + k_4\rho_Y\Delta H_4 + \frac{\partial V}{\partial t}\rho_{W_T}\Delta H_5$$
$$- \sum_{i=W,C,Y,G,SY,M,V} \frac{(\rho_i Cp_i T)}{\forall}\frac{\partial \forall}{\partial t} \quad (16)$$

Where Cp is the specific heat capacity [J/kg/K], H is the enthalpy of reaction [J/kg], M represents the moisture component, Uz is the convection velocity on axial direction, r refers to the radial position [m], and z refers to the axial position [m]. The convection term in radial direction is not considered here due to it is assumed that Ur is negligible.

The convection term in r direction is not considered since the mass in the z direction is greater. On the other hand, in equation (16) the molecular transport is typically much slower than the convective mechanism (Chan et al., 1985), thus:

$$D_{eff,Y}\frac{\partial^2 \rho_i}{\partial z^2} \ll \frac{\partial(\rho_i u_z)}{\partial z}$$

Therefore, the term $D_{eff,i}\frac{\partial^2(\rho_i Cp_i T)}{\partial z^2}$ is not going to be considered in this project.

The velocity u_z can be modeled using Darcy´s law for the flow of fluid through porous medium as:

$$u_z = \frac{K_p}{\eta}\frac{\partial p_T}{\partial z} \quad (17)$$

Where $K_p(m^2)$ is the permeability of wood and char mixture, η is the viscosity of volatiles, and p_T is the total pressure. p_T is expressed as the sum of the partial pressures of the volatiles compounds and it is given by the following expression (Di Blasi, 1996; Sadhukhan et al., 2009)

$$p_T = \sum p_i \quad (18)$$

And

$$p_i = \frac{\rho_i RT}{Mv_i\theta} \quad (19)$$

Where θ, $Mv_i(\frac{kg}{mol})$, $and\ \rho_i$ are the void, mass of each species, and density of each species respectively. The void factor (θ), according to Siau (1984) (cited by Bryden et al., (2002) and Bryden and Hagge (2003)) can be expressed as:

$$\theta = 1 - (\rho_B + \rho_C)/1500 - \rho_M/1000 \quad (20)$$

According to (Bharadwaj et al., 2004), permeability can be expressed as:

$$K_p = XK_{pB} + (1 - X)K_{pC} \quad (21)$$

Where X is the conversion ratio of biomass density, K_{pB} is the permeability of biomass, and K_{pC} is the permeability of char.

$$X = \frac{\rho_B}{\rho_{B0}} \tag{22}$$

For radius equal zero the first part of the right term in Equation (16) can be rewritten as:

$$\left.\begin{aligned} \frac{\partial}{\partial r}\left(r\frac{\partial T}{\partial r}\right) &= \frac{\partial T}{\partial r} + \left(r\frac{\partial^2 T}{\partial r^2}\right) \\ \frac{1}{r}\frac{\partial T}{\partial r} &= \left(\frac{\partial^2 T}{\partial r^2}\right) \end{aligned}\right\}_{r=0} \quad \frac{1}{r}\frac{\partial}{\partial r}\left(r\frac{\partial T}{\partial r}\right) = 2\frac{\partial^2 T}{\partial r^2} \tag{23}$$

Substituting Equation (23) in Equation (16) results in the overall energy balance for biomass pyrolysis at the center of the particle (radius equals zero):

$$\begin{aligned} &\sum_{i=W,C,Y,G,SY,M,V} \rho_i Cp_i\left(\frac{\partial T}{\partial t}\right) + \frac{\partial(\rho_i Cp_i T u_z)}{\partial z} + D_{eff,i}\frac{\partial^2(\rho_i Cp_i T)}{\partial z^2} \\ &= K_{eff,r}\left(2\frac{\partial^2 T}{\partial r^2}\right) + K_{eff,z}\frac{\partial^2 T}{\partial z^2} + \frac{\partial C}{\partial t}\rho_{W_T}\Delta H_1 + \frac{\partial Y}{\partial t}\rho_{W_T}\Delta H_2 \\ &+ \frac{\partial G}{\partial t}\rho_{W_T}\Delta H_3 + k_4\rho_Y\Delta H_4 + \frac{\partial V}{\partial t}\rho_{W_T}\Delta H_5 \\ &+ \sum_{i=W,C,Y,G,SY,M,V} \frac{(\rho_i Cp_i T)}{\forall}\frac{\partial \forall}{\partial t} \end{aligned} \tag{24}$$

Just as with Equation (16) the term $D_{eff,i}\frac{\partial^2(\rho_i Cp_i T)}{\partial z^2}$ in Equation (24) will be neglected.

2.4.4—Boundary conditions

Initial conditions:

$$t = 0, \rho_B = \rho_{B_0}, \rho_M = \rho_{M_0}, \rho_C = \rho_Y = \rho_G = \rho_{SY} = \rho_V = 0,\ T(r,0) = T(z,0) = T_0,\ 0 \le z \le Z,\ 0 \le r \le R \tag{25}$$

Boundary conditions:

$$t > 0, \frac{\partial T}{\partial z}_{z=0} = 0 \tag{26a}$$

$$t > 0, \frac{\partial \rho_i}{\partial z}_{z=0} = 0 \tag{26b}$$

$$t > 0, \frac{\partial T}{\partial r}_{r=0} = 0 \tag{26c}$$

$$t > 0, \frac{\partial \rho_i}{\partial r}_{r=0} = 0 \tag{26d}$$

$$t > 0, -K_{eff,z} \left.\frac{\partial T}{\partial z}\right|_{z=Z} = \alpha(T_S - T_Z) + \varepsilon\sigma(T_S^4 - T_Z^4) \tag{26e}$$

$$t > 0, -K_{eff,r} \left.\frac{\partial T}{\partial r}\right|_{r=R} = \alpha(T_S - T_R) + \varepsilon\sigma(T_S^4 - T_R^4) \tag{26f}$$

Where α is the external heat transfer coefficient [W/m^2/K], β is the external mass transfer coefficient [m/s], ε is the emissivity and σ is the Boltzmann constant ($5.67 \cdot 10^{-8}$ W/m^2/K^4).

2.4.5—Numerical solution of the mathematical model

For the numerical solution of the mathematical model, the finite difference method is used (Garcia-Perez, 2011). In these formulas i represents the radial position, j represents the position in time and k represents the axial position.

$$\left(\frac{\partial T}{\partial t}\right)_{i,j,k} = \frac{1}{\Delta t}\left(T_{i,j,k} - T_{i,j-1,k}\right) \tag{27a}$$

$$\left(\frac{\partial T}{\partial r}\right)_{i,j,k} = \frac{1}{\Delta r}\left(T_{i,j,k} - T_{i-1,j,k}\right) \tag{27b}$$

$$\left(\frac{\partial T}{\partial z}\right)_{i,j,k} = \frac{1}{\Delta z}\left(T_{i,j,k} - T_{i,j,k-1}\right) \tag{27c}$$

$$\left(\frac{\partial^2 T}{\partial r^2}\right)_{i,j,k} = \frac{1}{(\Delta r)^2}\left(T_{i+1,j,k} - 2T_{i,j,k} + T_{i-1,j,k}\right) \tag{27d}$$

$$\left(\frac{\partial^2 T}{\partial z^2}\right)_{i,j,k} = \frac{1}{(\Delta z)^2}\left(T_{i,j,k+1} - 2T_{i,j,k} + T_{i,j,k-1}\right) \tag{27e}$$

Substituting Equations (27a)–(27e) in Equation (16) and (24) results in the following equations, which represents the temperature in the particle at a specific place and time through an implicit numerical equation for the particle (Equation (28)) and for the center of the particle (Equation (29)):

$$T_{i,j,k} = A'T_{i+1,j,k} + B'T_{i-1,j,k} + C'T_{i,j-1,k} + D'T_{i,j,k+1} + E'T_{i,j,k-1} + S' \tag{28}$$

$$T_{i,j,k} = F'T_{i+1,j,k} + F'T_{i-1,j,k} + G'T_{i,j-1,k} + H'T_{i,j,k+1} + I'T_{i,j,k-1} + S'' \tag{29}$$

Where the coefficients of the temperatures are constants that can be found in Attachment B. The same procedure for numerical solutions is applied for the discretization of the mass conservation for the species. The following equations show the finite difference equations using backward substitutions for the change in densities of the species:

$$\left(\frac{\partial \rho_B}{\partial t}\right)_{i,j,k} = \frac{1}{\Delta t}\left(\rho_{B\,i,j,k} - \rho_{B\,i,j-1,k}\right) \tag{30a}$$

$$\left(\frac{\partial \rho_C}{\partial t}\right)_{i,j,k} = \frac{1}{\Delta t}\left(\rho_{C\ i,j,k} - \rho_{C\ i,j-1,k}\right) \quad \text{(30a)b)}$$

$$\left(\frac{\partial \rho_Y}{\partial t}\right)_{i,j,k} = \frac{1}{\Delta t}\left(\rho_{Y\ i,j,k} - \rho_{Y\ i,j-1,k}\right) \quad \text{(30a)c)}$$

$$\left(\frac{\partial \rho_Y}{\partial t}\right)_{i,j,k} = \frac{1}{\Delta t}\left(\rho_{G\ i,j,k} - \rho_{G\ i,j-1,k}\right) \quad \text{(30a)d)}$$

$$\left(\frac{\partial \rho_{SY}}{\partial t}\right)_{i,j,k} = \frac{1}{\Delta t}\left(\rho_{SY\ i,j,k} - \rho_{SY\ i,j-1,k}\right) \quad \text{(30a)e)}$$

$$\left(\frac{\partial \rho_M}{\partial t}\right)_{i,j,k} = \frac{1}{\Delta t}\left(\rho_{M\ i,j,k} - \rho_{M\ i,j-1,k}\right) \quad \text{(30a)f)}$$

$$\left(\frac{\partial \rho_V}{\partial t}\right)_{i,j,k} = \frac{1}{\Delta t}\left(\rho_{V\ i,j,k} - \rho_{V\ i,j-1,k}\right) \quad \text{(30a)g)}$$

Substituting Equations (12a)–(12a) and Equations (30a)–(30a) in Equations (14a)–(14g) results in the following equations, which represents the mass per unit volume in the particle at a specific place and time through an implicit numerical equation for the particle (Equation (31a))) and for the center of the particle (Equation (32a))). For the center of the particle, the mass conservation equations of biomass which have the expression $\frac{\partial(\rho_{Y,\text{or G, or,Sy,or V,}})}{\partial z}$ is going to be zero since this first derivative is going to be a maximum or a minimum.

$$\rho_{B\ i,j,k} = \frac{\rho_{B\ i,j-1,k} - (k_1 + k_2 + k_3)B_{i,j-1,k}\rho_{T_0}\Delta t}{2 - \frac{\forall_{i,j-2,k}}{\forall_{i,j-1,k}}} \quad \text{(31a)}$$

$$\rho_{C\ i,j,k} = \frac{\rho_{C\ i,j-1,k} + (k_1)B_{i,j-1,k}\rho_{T_0}\Delta t}{2 - \frac{\forall_{i,j-2,k}}{\forall_{i,j-1,k}}} \quad \text{(31b)}$$

$$\rho_{Y\ i,j,k} = \frac{\rho_{Y\ i,j-1,k} - \rho_{Y\ i,j,k-1}\frac{u_{z\ i,j-1,k}\Delta t}{\Delta z} + (k_2)B_{i,j,k}\rho_{T_0}\Delta t}{2 - \frac{u_{z\ i,j-1,k}\Delta t}{\Delta z} + k_4\Delta t - \frac{\forall_{i,j-2,k}}{\forall_{i,j-1,k}}} \quad \text{(31c)}$$

$$\rho_{G\ i,j,k} = \frac{\rho_{G\ i,j-1,k} - \rho_{G\ i,j,k-1}\frac{u_{z\ i,j-1,k}\Delta t}{\Delta z} + (k_3)B_{i,j-1,k}\rho_{T_0}\Delta t}{2 - \frac{u_{z\ i,j-1,k}\Delta t}{\Delta z} - ak_4\Delta t - \frac{\forall_{i,j-2,k}}{\forall_{i,j-1,k}}} \quad \text{(31d)}$$

(31e)

$$\rho_{SY\ i,j,k} = \frac{\rho_{SY\ i,j-1,k} - \rho_{SY\ i,j,k-1}\frac{u_{z\ i,j,k-1}\Delta t}{\Delta z} + \ b(k_4)\rho_{Y\ i,j,k}\Delta t}{2 - \frac{u_{z\ i,j,k}\Delta t}{\Delta z} - \frac{\forall_{i,j-2,k}}{\forall_{i,j-1,k}}}$$

$$\rho_{M\ i,j,k} = \frac{\rho_{M\ i,j-1,k} - (k_5)M_{i,j-1,k}\rho_{T_0}\Delta t}{2 - \frac{\forall_{i,j-2,k}}{\forall_{i,j-1,k}}} \tag{31f}$$

$$\rho_{V\ i,j,k} = \frac{\rho_{V\ i,j-1,k} - \rho_{V\ i,j,k-1}\frac{u_{z\ i,j,k-1}\Delta t}{\Delta z} + \ (k_5)M_{i,j-1,k}\rho_{T_0}\Delta t}{2 - \frac{u_{z\ i,j,k-1}\Delta t}{\Delta z} - \frac{\forall_{i,j-2,k}}{\forall_{i,j-1,k}}} \tag{31g}$$

For the center of the particle the corresponding equations are the following:

$$\rho_{B\ i,j,k} = \frac{\rho_{B\ i,j-1,k} - (k_1 + k_2 + k_3\ )B_{i,j-1,k}\rho_{T_0}\Delta t}{2 - \frac{\forall_{i,j-2,k}}{\forall_{i,j-1,k}}} \tag{32a}$$

$$\rho_{C\ i,j,k} = \frac{\rho_{C\ i,j-1,k} + (k_1)B_{i,j-1,k}\rho_{T_0}\Delta t}{2 - \frac{\forall_{i,j-2,k}}{\forall_{i,j-1,k}}} \tag{32b}$$

$$\rho_{Y\ i,j,k} = \frac{\rho_{Y\ i,j-1,k} - \rho_{Y\ i,j,k-1}\frac{u_{z\ i,j-1,k}\Delta t}{\Delta z} + \ (k_2)B_{i,j,k}\rho_{T_0}\Delta t}{2 - \frac{u_{z\ i,j-1,k}\Delta t}{\Delta z} + \ k_4\Delta t - \frac{\forall_{i,j-2,k}}{\forall_{i,j-1,k}}} \tag{32c}$$

(32d)

$$\rho_{G\ i,j,k} = \frac{\rho_{G\ i,j-1,k} - \rho_{G\ i,j,k-1}\frac{u_{z\ i,j-1,k}\Delta t}{\Delta z} + \ (k_3)B_{i,j-1,k}\rho_{T_0}\Delta t}{2 - \frac{u_{z\ i,j-1,k}\Delta t}{\Delta z} - \ ak_4\Delta t - \frac{\forall_{i,j-2,k}}{\forall_{i,j-1,k}}}$$

2.5—Auger pyrolysis reactor model

Figure 17A shows the auger pyrolysis reactor that was used for this modeling work.

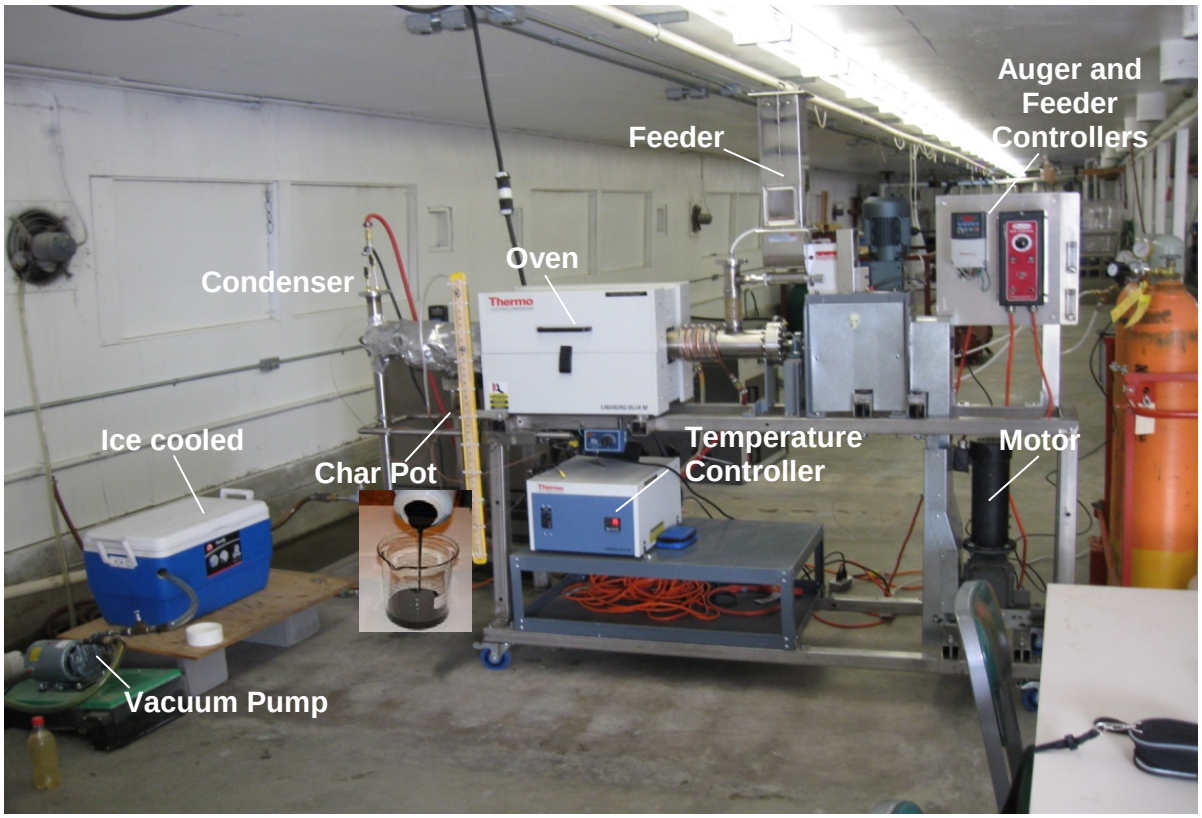

Figure 17A: Auger pyrolysis reactor at WSU

The reactor subjected to modeling is an auger reactor with external heating. The inert atmosphere is supplied with N_2. The controlling factors (independent variables) are (1) temperature of the wall (T_{wall}), (2) initial temperature of the gas (T_{G0}), and (3) speed of the auger. RPM of the auger reactor controls the residence time (RT) of the material inside the reactor. This speed also defines the bed height (a) and the angle of the segment (ɵ) occupied for the biomass inside the reactor. Figure 18A shows a frontal and lateral representation of the auger reactor with some parameters that are going to be used in the proposed model.

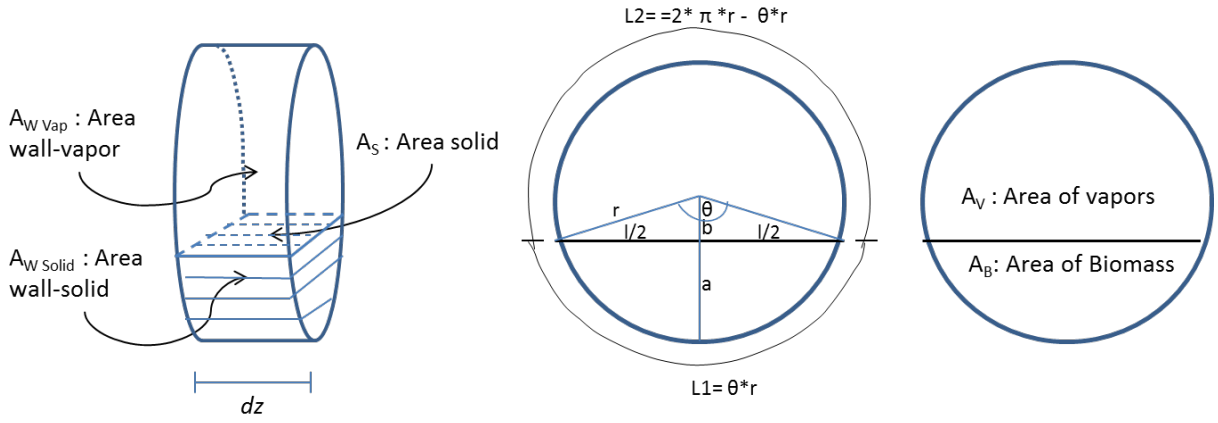

Figure 18A: Schematic representation of a frontal and lateral view of the auger reactor where; r = radius, A_A = area of gases normal to the flux, A_B = area of biomass normal to the flux, $A_{W\ Vap}$ = area of heat transfer from the wall to the volume of vapor, $A_{W\ Solid}$ = area of heat transfer from the wall to the volume of solid, A_S = area of heat transfer between the volume of solid and the volume of the vapors, a = height bed, l = width bed, θ= sector angle in radians, L1 = length arc for A_B, L2 = length arc for A_V (Area of vapors)

The following equations are going to be used during modeling using diameter (d) instead of radius (r):

$$A_B = \frac{d^2}{8}(\theta - \sin(\theta)) \tag{33}$$

$$A_V = \frac{d^2}{4}(\pi - \frac{1}{2}(\theta - \sin(\theta)) \tag{34}$$

$$L1 = d\frac{\theta}{2} \tag{35}$$

$$L2 = d\left(\pi - \frac{\theta}{2}\right) \tag{36}$$

$$A_{W\ Vap} = d\left(\pi - \frac{\theta}{2}\right)dz \tag{37}$$

$$A_{W\ Solid} = d\frac{\theta}{2}dz \tag{38}$$

$$A_S = d\sin\left(\frac{\theta}{2}\right)dz \tag{39}$$

$$b = \frac{d}{2}\cos\left(\frac{\theta}{2}\right) \tag{40}$$

$$a = \frac{d}{2}\left(1 - \cos\left(\frac{\theta}{2}\right)\right) \quad (41)$$

$$\frac{2A_B}{r^2} = \left(\theta - \sin(\theta)\right) \quad (42)$$

Where the terms are defined in Figure 18A above.

The main geometrical characteristics of the auger reactor are: d = 10", length (heating zone) = 4". Table 4A shows the main geometrical characteristic of the auger pyrolysis reactor as a function of the speed of the auger.

Table 4A: Main characteristics of the auger at different velocities (rpm) that implies different residence time

Velocity of Auger	Residence Time (s)		Tot. mass	Total Vol	ratio	Area	A_B=A_C	A_A=A_D	A
(rpm)	Measured	Calculated	(kg)	(m^3)	V biomass/ V react	(%)	(m^2)	(m^2)	(m^2)
5	72	75.3	1.9E-02	3.1E-05	8.5E-03	0.85	6.9E-05	8.0E-03	3.0E-03
7	54	52.0	1.3E-02	2.2E-05	5.8E-03	0.58	4.7E-05	8.1E-03	2.3E-03
10	36	35.1	8.8E-03	1.5E-05	3.9E-03	0.39	3.2E-05	8.1E-03	1.8E-03
13	27	26.3	6.6E-03	1.1E-05	3.0E-03	0.30	2.4E-05	8.1E-03	1.5E-03
15	22.5	22.5	5.6E-03	9.4E-06	2.5E-03	0.25	2.1E-05	8.1E-03	1.3E-03
18	18	18.4	4.6E-03	7.7E-06	2.1E-03	0.21	1.7E-05	8.1E-03	1.2E-03
20	16.2	16.4	4.1E-03	6.8E-06	1.8E-03	0.18	1.5E-05	8.1E-03	1.1E-03

Where: A_A = area of gases normal to the flux, A_B = area of biomass normal to the flux, (see Figure 18A)

2.5.1—Physical model

A plug flow model (PFM) is going to be used to simulate the auger reactor (Figure 17A). There is going to be two phases, a solid phase with the biomass (B) and char (Ch), and a gas phase with the carrier gas (A) and the volatile compounds (D) (Figure 19A).

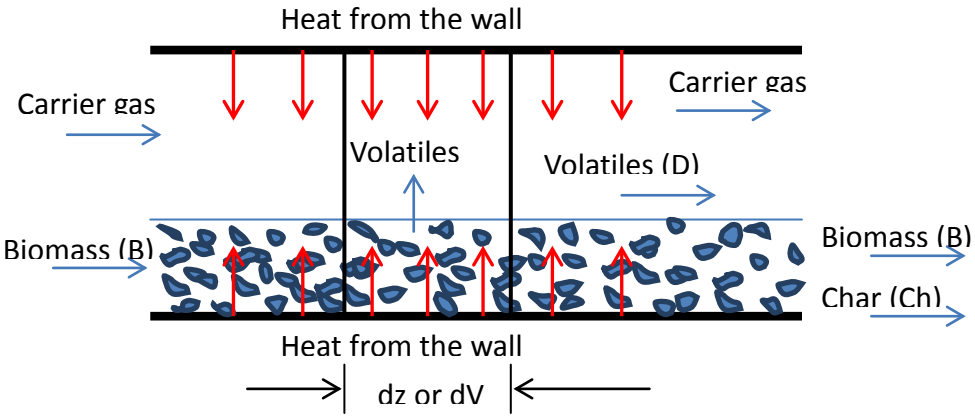

Figure 19A: Control volume to be considered during the modeling of the auger reactor

2.5.2—Mathematical model

A simple model for pyrolysis thermal conversion of biomass into volatiles and char are going to be used as follows:

$$Biomass\ (B) \overset{k_1}{\rightarrow} a \cdot Volatiles\ (D) + b \cdot Charcoal\ (Ch) \tag{43}$$

The reaction in this conversion is considered to take place via a first order kinetic scheme. The reaction rate constant, k_1, is calculated through an Arrhenius equation (Equation (13)).

A conversion factor of biomass (α) is defined as (Varhegyi et al., 1997):

$$\alpha = \frac{(\dot{m}_{B0} - \dot{m}_B)}{(\dot{m}_{B0} - \dot{m}_{Bf})} \tag{44}$$

Where $\dot{m}_{B0}$ is the initial mass flux of biomass (kg/s), $\dot{m}_{Bf}$ is the final mass flux assuming total conversion, and $\dot{m}_B$ is the mass flux at any moment and space inside the control volume.

The reaction rate of α (R_α) is defined as a first order kinetic scheme as follows (Varhegyi et al., 1997):

$$R\alpha = \frac{d\alpha}{dt} = k_1(1-\alpha) = A_1 e^{\left(-E_1/RT\right)}(1-\alpha) \tag{45}$$

dt can be expressed in terms of dz using the velocity of the biomass flux (V_{Bz}) in z direction as follows:

$$V_{Bz} = \frac{dz}{dt} \tag{46}$$

Therefore, eq. (45) can be expressed as:

$$\frac{d\alpha}{dz} = \frac{A_1}{V_{Bz}} e^{\left(-E_1/RT\right)}(1-\alpha) \tag{47}$$

2.5.3—General mass balances

Expressing the mass balance for each material (A, B, Ch, D) in the control volume (i) in terms of the conversion factor we have:

$$\dot{m}_{A\,i} = \dot{m}_{A\,0} \tag{48}$$

$$\dot{m}_{B\,i} = \dot{m}_{B\,0} - m_{B0} \cdot \alpha_i \quad (49)$$

$$\dot{m}_{Ch\,i} = \dot{m}_{Ch0} + b \cdot m_{B0} \cdot \alpha_i \quad (50)$$

$$\dot{m}_{D\,i} = \dot{m}_{D\,0} + a \cdot m_{B0} \cdot \alpha_i \quad (51)$$

$$\dot{m}_{Vap\,i} = \dot{m}_{A\,0} + \dot{m}_{Di} \quad (52)$$

Where $\dot{m}_{Vap\,i}$ (mass flux of vapors) is the sum of the mass flux of inert gas (N) and the volatiles (D) produced during the biomass conversion.

The total flow of vapors (Q_{Vapi}) is the sum of the flow of the carrier gas ($Q_{A\,0}$) and the flow of the volatiles compounds from the biomass thermal conversion (Q_{Di}).

$$Q_{Vap\,i} = Q_{A0} + Q_{D\,i} \quad (53)$$

Using the universal gas law (PV=nRT) it is possible to obtain Q_{A0} and Q_{Di} by the following equations:

$$Q_A = \frac{\dot{m}_{A\,0}}{M_A}\frac{RT_i}{P} \quad (54)$$

$$Q_{D\,i} = \frac{\dot{m}_{D\,i}}{M_D}\frac{RT_i}{P} \quad (55)$$

Where M_A and M_D are the molecular weight of the carrier gas and the volatiles in kg/kmol and P is the pressure in N/m^2.

Therefore, the velocity of the vapors (V_{Vapi}) is defined as:

$$V_{Vap\,i} = \frac{Q_{Vap\,i}}{A_v} \quad (56)$$

The conservation law can be expressed as:

$$\dot{m}_{B\,i} = \dot{m}_{B0} - \dot{m}_{D\,i} - \dot{m}_{Ch\,i} \quad (57)$$

2.5.4—Overall energy balance

The general energy balance is given by the following equation:

$$\rho C_P \left(\frac{\partial T}{\partial t} + Vz\frac{\partial T}{\partial z}\right) = S_R + E_T + R \quad (58)$$

Where:

$\rho C_P \frac{\partial T}{\partial t}$: Rate of energy acumulation, which is zero in steady state

$\rho C_P Vz \frac{\partial T}{\partial z}$: Energy transport by convection

S_R: Heat associated with chemical reactions. It is zero in the gas phase

E_T : Heat transport through the interface

R : Heat due to radiation

2.5.5—Gas phase energy balance

Equation (58) can be expressed in terms of mass flux as follows:

$$\frac{\dot{m}_A}{A_V}C_{PA}\frac{dT_G}{dz}+\frac{\dot{m}_D}{A_V}C_{PD}\frac{dT_G}{dz}=\frac{C_{PD}}{A_V}(T_S-T_G)\frac{d\dot{m}_D}{dz}+U'\frac{dA_{Wvap}}{A_V dz}(T_W-T_G)+U''\frac{dA_S}{A_V dz}(T_S-T_G) \quad (59)$$

Where C_{PA} and $C_{PD}$are the specific heat capacity (J/kg K) of the carrier gas and volatiles respectively; T_S , T_G, and T_W (K) the temperatures of the solid phase, gas phase and wall respectively; $U'$and $U''$are the heat transfer coefficients (kJ/m^{2}s K) between the wall and the gases and between the solid and the gases respectively. The values of C_P are going to be considered constant in this first approach.

2.5.6—Energy balance for solid phase

The energy balance for the solid phase is given by the following equation:

$$\frac{\dot{m}_B}{A_B}C_{PB}\frac{dT_S}{dz}+\frac{\dot{m}_{Ch}}{A_B}C_{PCh}\frac{dT_S}{dz} = \frac{d\dot{m}_B}{dz}\frac{\Delta H}{A_B}+U'''\frac{dA_{W\,solid}}{A_B dz}(T_W-T_S)-U''\frac{dA_S}{A_B dz}(T_S-T_G)+\varepsilon\sigma\frac{dA_S}{A_B dz}(T_W^4-T_s^4) \quad (60)$$

Where C_{PB} and C_{PCh} are the specific heat capacity (J/kg K) of the biomass and volatiles char; H is the enthalpy of reaction (J/kg); $U'''$is the heat transfer coefficients (kJ/m^2 s K) between the wall and the solid phase; ε is the emissivity and σ is the Boltzmann constant (5.67·10 $^{-8}$ W/m^2 K^4).

2.5.7—Boundary conditions

Initial conditions: for z= 0, $\alpha_0 = 0$, $(1-\alpha)_0$

2.5.8—Mathematical model numerical solution

For the numerical solution of the mathematical model the finite difference method is used. In these formulas i represents the position in z direction.

$$\left(\frac{dT_G}{dz}\right)_i=\frac{1}{\Delta z}(T_{G\,i+1}-T_{G\,i}) \quad (61)$$

$$\left(\frac{dT_s}{dz}\right)_i=\frac{1}{\Delta z}(T_{S\,i+1}+1-T_{S\,i}) \quad (62)$$

From equation to calculate conversion and taking finite differences we obtain the following expression:

$$\alpha_i=\alpha_{i-1}+\frac{A_1}{V_{Bz}}e^{\left(-E_1/RT_{s\,i-1}\right)}(1-\alpha_{i-1})\Delta z \quad (63)$$

The temperatures of the gases and solid phases can be obtained from the following numerical solutions:

$$T_{Gi}=T_{Gi-1}+\frac{C_{PD}(T_{Si-1}-T_{Gi-1})\Delta\dot{\boldsymbol{m}}_{\boldsymbol{Di-1}}+U'\Delta A_{Wvap}(T_W-T_{Gi-1})-U''\Delta A_S(T_{Gi-1}-T_{Si-1})}{\dot{m}_A C_{PA}+\dot{m}_{Di-1}C_{PD}} \quad (64)$$

$$T_{Si}=T_{Si-1}+\frac{\Delta\dot{\boldsymbol{m}}_{\boldsymbol{Bi-1}}\Delta H+U'''\Delta A_{W\,solid}(T_W-T_{Si-1})+U''\Delta A_S(T_{Gi-1}-T_{Si-1})+\varepsilon\sigma\Delta A_S\left(T_W^4-T_{si-1}^4\right)}{\dot{m}_{Bi-1}C_{PB}+\dot{m}_{Chi-1}C_{PCh}} \quad (65)$$

3—Modeling and simulations

3.1—Effective radial thermal conductivity

An initial temperature of 25°C (298 K) is used for the cell block and nylon block. A constant temperature of 85°C (358 K) is applied to the entire left boundary of the cell block while the right side of the nylon block is kept at 25°C. The simulation is run for 100 s to approach steady state conditions. The temperature at the border of the cell block and the nylon block are measured at 10 s intervals. Using Fourier's Law (Equation (4)) and the data on nylon from COMSOL, the heat flux through the nylon block at steady state is calculated. Using Fourier's Law (under steady state conditions) again gives the effective radial thermal conductivity by putting in the heat flux determined with the nylon block. The results are compared with literature values obtained from Equation (1) using data from Table 1A. An example of a COMSOL simulation is given in Figure 20A.

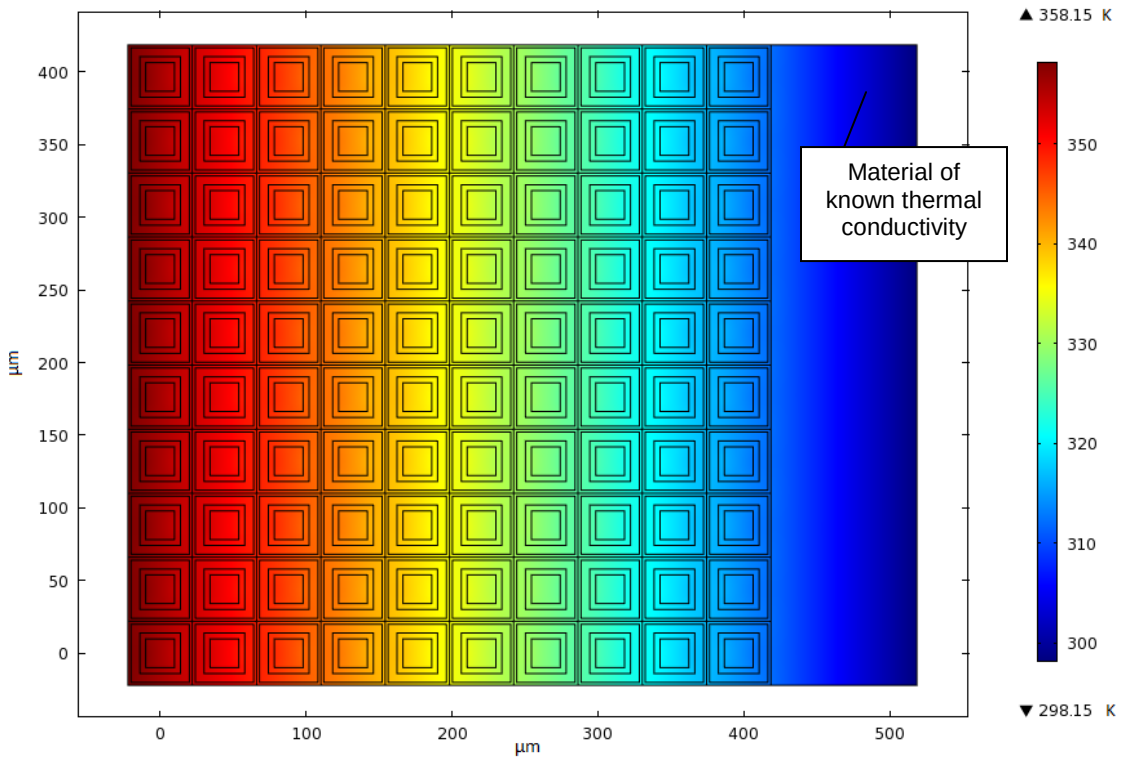

Figure 20A: Example of the COMSOL simulation used in determining the effective radial thermal conductivity; here the lumen is filled with 50% free water and the wet porosity is 40%

3.2—Effective axial thermal conductivity

The unit cell and the nylon block both have an initial temperature of 25°C. At the top of the unit cell a temperature of 85°C is applied and to the bottom of the nylon block the temperature is kept constant at 25°C. The simulation is run for 1000 s to approach steady state conditions and the temperature at the border of the unit cell and the nylon block are measured with at 100 s intervals. Using Fourier's Law (Equation (4)) and the data on nylon from COMSOL, the heat flux through the nylon block at steady state is calculated. Using Fourier's Law the effective axial

thermal conductivity is calculated by using the heat flux determined with the nylon block. The results are validated with the literature values obtained from Equation (1) using data from Table 2A. An example of a COMSOL simulation is given in Figure 21A.

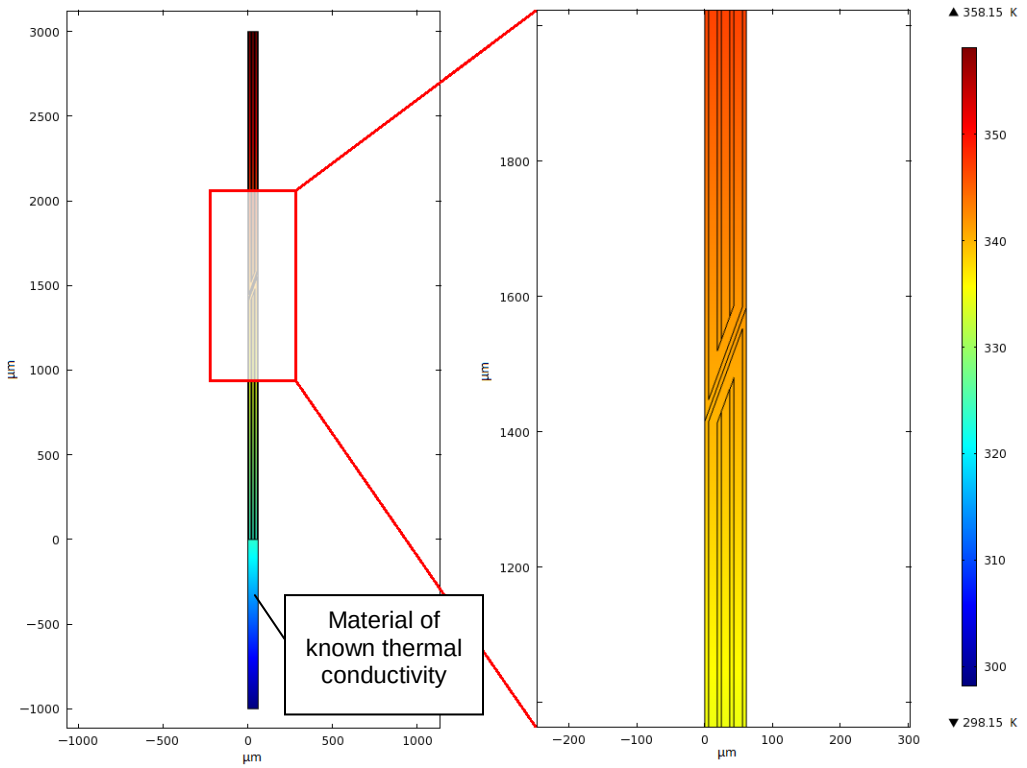

Figure 21A: Example of the COMSOL simulation used in determining the effective axial thermal conductivity; here the lumen is filled with 50% free water and the wet porosity is 40%; left is an overview of the entire model, right is a zoomed section around the tangential tracheid

3.3—Effective radial mass diffusivity

An initial concentration of 0 mol/m^3 is used for the cell block and air block. A constant concentration, calculated through an adaption of the ideal gas law (Equation (66b)), is applied to the entire left boundary of the cell block while the right side of the air block is kept at 0 mol/m^3. The simulation is run for 106 s to approach steady state conditions. The concentration at the border of the cell block and the air block are measured at 105 s intervals. Using Fick's Law (Equation (11)) and the diffusivity obtained from Equation (7), the mass flux through the air block at steady state is calculated. Using Fick's Law again gives the effective radial mass diffusivity by putting in the mass flux determined with the air block. The results for different porosities (Equation (6)) are compared with experimental literature values (Avramidis and Siau, 1987). An example of a COMSOL simulation is given in Figure 22A.

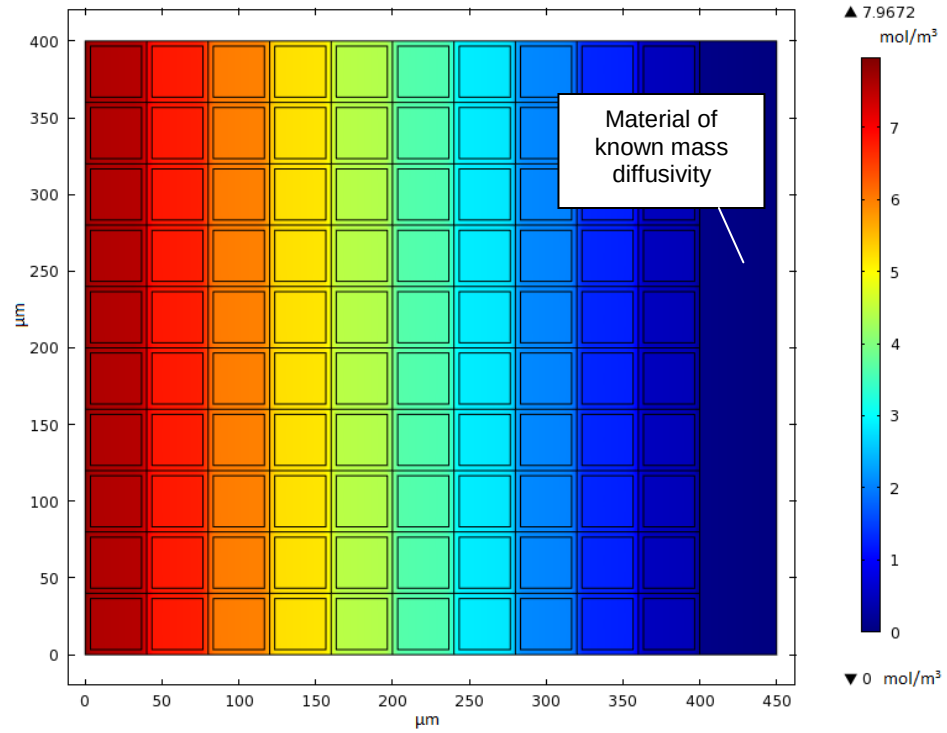

Figure 22A: Example of the COMSOL simulation used in determining the effective radial mass diffusivity

The equation for the ideal gas law (66a) was adapted to calculate the concentration (66b):

$$PV = n_{mol}RT \tag{66a}$$

$$c = \frac{n_{mol}}{V} = \frac{P}{RT} \tag{66b}$$

Where V is the volume [m^3] and n_{mol} is the amount of moles.

3.4—Effective axial mass diffusivity

An initial concentration of 0 mol/m^3 is used for the unit cell and air block. A constant concentration, calculated through an adaption of the ideal gas law (Equation (66b)), is applied to the upper boundary of the unit cell while the bottom side of the air block is kept at 0 mol/m^3. The simulation is run for 10^5 s to approach steady state conditions. The concentration at the border of the unit cell and the air block are measured at 10^4 s intervals. Using Fick's Law (Equation (11)) and the diffusivity obtained from Equation (7), the mass flux through the air block at steady state is calculated. Using Fick's Law again gives the effective axial mass diffusivity by putting in the mass flux determined with the air block. The results for different porosities (Equations (5) and (8)) are compared with experimental literature values (Çolakoglu, 2009). An example of a COMSOL simulation is given in Figure 23A.

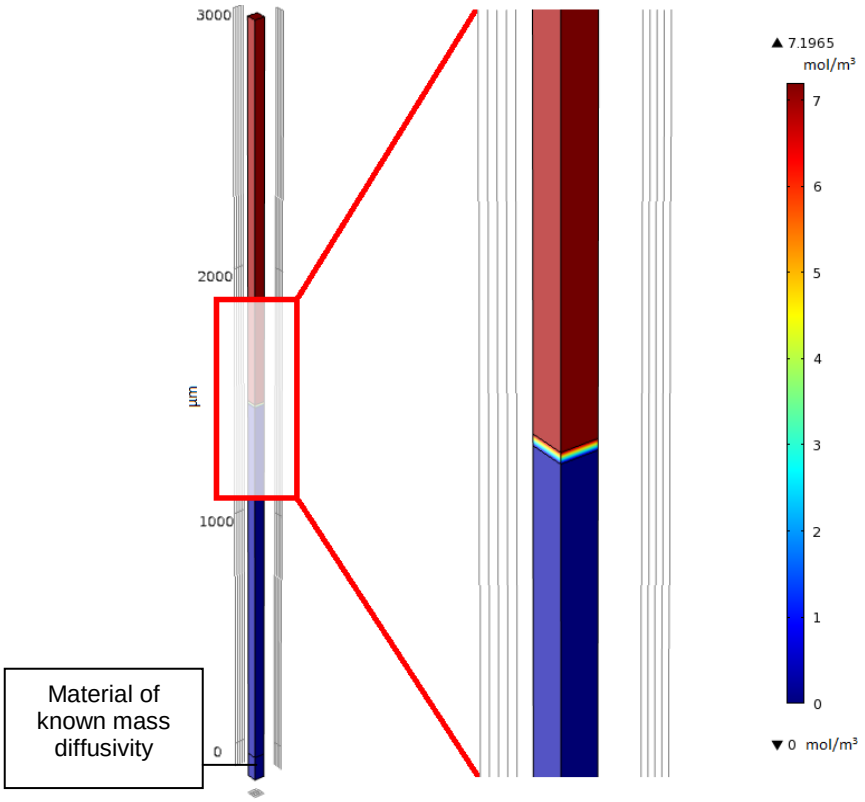

Figure 23A: Example of the COMSOL simulation used in determining the effective axial mass diffusivity; right is a zoomed section around the pit area

3.5—Single particle model

The parameter inputs used for all single particle model simulations are given in Table 5A.

Table 5A: Parameters used for model simulations

Parameter	Range	Value	References
Specific heat capacity, Cp [J/kgK]			
Wood (biomass), W or B	1670–2300	1670	Pyle and Zaror (1984); Di Blasi (1993)
Moisture, M	4180	4180	Incropera and DeWitt (2007)
Char, C	1000–1000	1000	Pyle and Zaror (1984); Di Blasi (1993)
Tar, T	2400	2400	Bryden et al., (2002)
Gas, G	1100	1100	Di Blasi (1993)
Secondary Tars, SY	2400	2400	Assumed to be the same as Tar
Water Vapor, V	2060	2060	Incropera and DeWitt (2007)
Density of biomass, ρb [kg/m³]	510–650	600	Di Blasi (1993)
Molecular weight of tar, Mv [kg/mol]	110	110	Bryden and Hagge (2003)
Molecular weight of gas, Mg [kg/mol]	26	26	Bryden and Hagge (2003)
Molecular weight of SY, Msy [kg/mol]	110	110	Bryden and Hagge (2003)
Molecular weight of V, Mv [kg/mol]	18	18	Bryden and Hagge (2003)
Shrinkage factor, f0 [%]	8	8	Bryden et al., (2002); Sadhukhan et al., (2009)
Emissivity, ε	0.9–1.0	0.9	Incropera and DeWitt (2007)
External mass transfer coefficient, β (m/s)	1.5E−03	1.5E−03	Westerhout, (1997) (average value)
External heat transfer coefficient, α [W/m^2/K]	400	400	Kersten, (2005)
Viscosity of volatiles, η [Pa s]	1.00E−05	1.00E−05	Chan et al., (1985)
Boltzman constant, σ [W/m²/K^4]	5.67E−08	5.67E−08	Incropera and DeWitt (2007)
Universal gas constant R [J/mol/K]	8.314	8.314	Incropera and DeWitt (2007)
Heat of reaction Moisture-Vapor, ΔH5 [J/kg]	−2440000	−2440000	Bryden et al., (2002)
Pyrolysis and vapor kinetics		See Table 3A	

The parameters used for adjusting the model are given in Table 6A.**Error! Reference source not found.** The particle size, moisture content, time step, initial and final temperature are fixed according with the experimental conditions that were simulated.

Table 6A: Parameters that were adjusted for model simulation

Parameter	Range	References
Radial thermal conductivity, Keff r [W/mK]	0.104–0.190	Incropera and DeWitt (2007) and generated with COMSOL model in this report
Axial thermal conductivity, Keff z [W/mK]	0.055–0.271	Incropera and DeWitt (2007) and generated with COMSOL model in this report
Heat of reaction Biomass-Char, ΔH1 [J/kg]	−420000	Bryden et al., (2002); Di Blasi (1993)
Heat of reaction Biomass-Tar, ΔH2 [J/kg]	−420000	Bryden et al., (2002); Di Blasi (1993)
Heat of reaction Biomass-Gas. ΔH3 [J/kg]	−420000	Bryden et al., (2002); Di Blasi (1993)
Heat of reaction Tar-Gas + char, Tar-Gas + SY, ΔH4 [J/kg]	−220500–40000	Bryden et al., (2002) ; Sadhukhan et al., (2009)
Permeability of biomass, Kpb [m^2]	10^{-14}–10^{-5}	Sadhukhan et al., (2009), Bharadwaj, (2004); Chan et al., (1985); Bryden et al., (2002)
Permeability of char, Kpc [m^2]	10^{-11}–0.2	Sadhukhan et al., (2009), Bharadwaj, (2004); Chan et al., (1985); Bryden et al., (2002)

3.5.1—Effect of temperature

The temperatures curves obtained from this model are compared with the temperature curves obtained by Professor Chun-Zhu Li's group at Curtin University in Australia. The experimental setup was as follows.

A quartz reactor with product collection and temperature measurement system was designed to pyrolyze a single mallee (Eucalyptus) particle. Electric furnace of capacity 6 KW was used to heat up the reactor. A schematic diagram of the experimental setup is shown in Figure 24A. Argon was used as the fluidizing gas that was introduced from the bottom of the reactor at a flow rate of 4 L/min. Fluidizing gas was preheated in the reactor line before entering into the sand bed. 200 g silica sand with 250–350 μm particle size was used as the fluidized bed material. The unfluidized sand bed height was 73 mm, which was enough to cover the whole mallee trunk.

Type-K (chromel-alumel) thermocouples were used to measure the temperature in sand bed or in the biomass sample. Three thermocouples were set into different vertical positions of the sand bed during heating of the reactor to ensure temperature is uniform throughout the bed. Once the reactor was stable, at the desired pyrolysis temperature, the thermocouple bundle was taken out from the reactor and the biomass sample was put into the reactor immediately. More thermocouples were inserted into the biomass at different radial positions as well as outside the biomass in different axial or radial positions of the sand bed to monitor the temperature profiles. The biomass sample was fixed into the sand bed with the help of the inserted thermocouples. After pushing the sample into the sand bed, the height was determined to be 100 mm under reaction conditions. Thermocouples measuring temperature at different position were connected

with a digital multi-channel data logger that can record the data with a maximum sampling rate of 5 times/s and show trends on a LCD monitor. For type-K thermocouples, the logger can read from −2000°C to 13700°C with ±10°C accuracy.

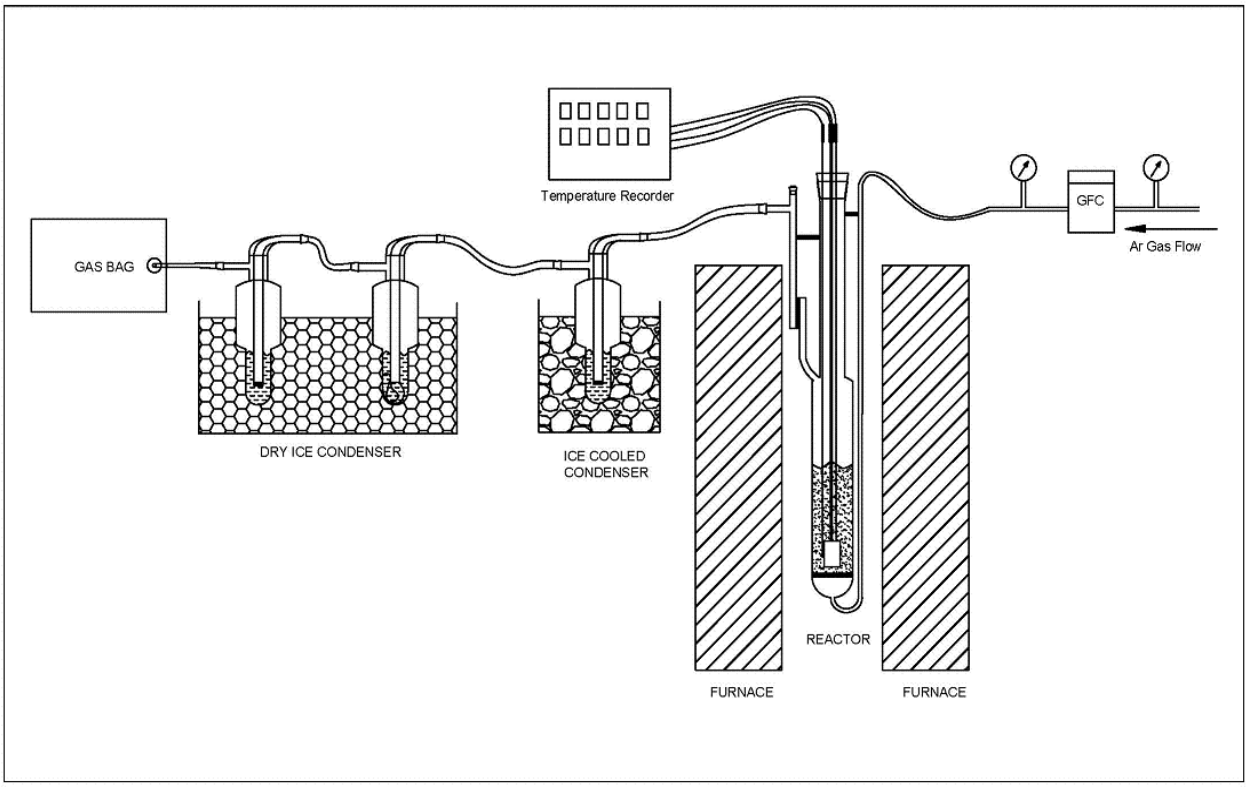

Figure 24A: Schematic diagram of single wood pyrolysis experimental setup (Courtesy of Prof. Chun-Zhu Li, Curtin University)

To study the temperature profile in a sample, it is necessary to make sure that the measuring thermocouples are always kept inside the biomass sample during the pyrolysis. Most of the pyrolysis studies are done using large particles (Bilbao et al., 1993; Chan et al., 1985; Di Blasi & Branca, 2003; Wang et al., 2005) and high temperature or high heat intensity, which results in the breakage of char after a certain time. The thermocouples measuring the temperature seldom reached more than the set pyrolysis temperature. Therefore, it was decided to study the pyrolysis at lower temperatures (300–400°C) in which case a whole piece of char will be found ensuring the thermocouples are kept inside the char during the reaction.

Figure 25A and Figure 26A show two sets of temperature profiles obtained in this setup. Thermocouple 1 (named T/C1 12 mm) is located in the center of the cylinder, whereas thermocouple 5 (named T/C 5) is located outside. The others thermocouples are located between these two in the biomass cylinder.

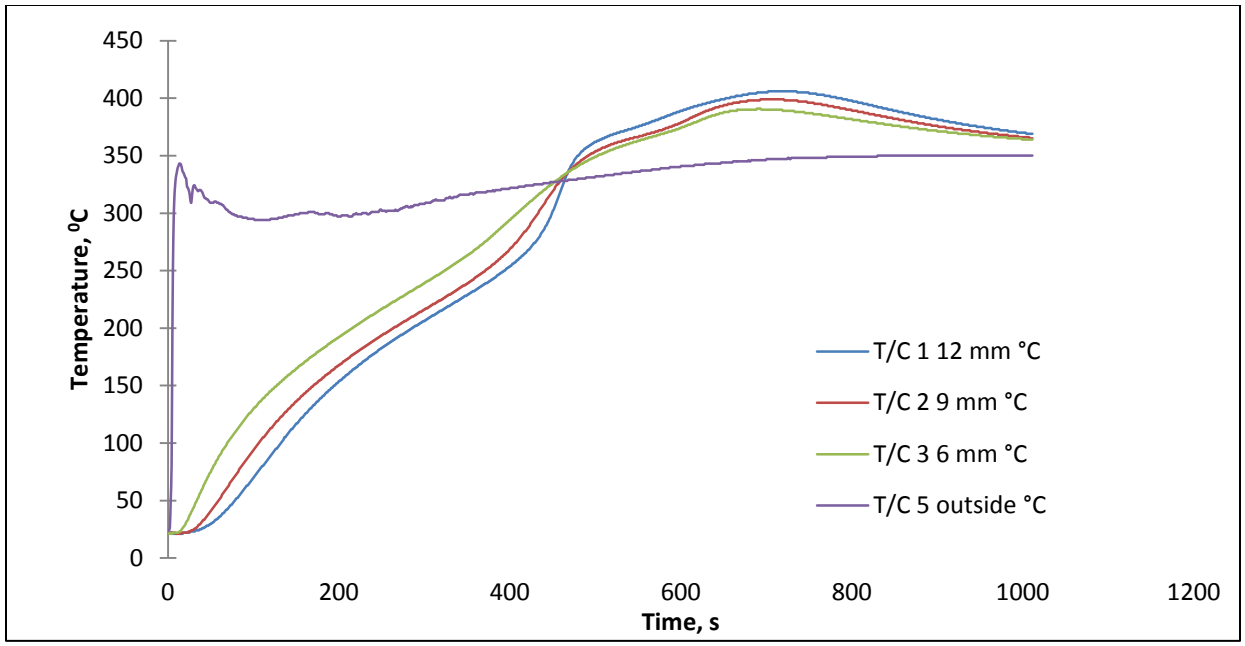

Figure 25A: Pyrolysis at 350°C with 25.35 mm diameter sample, 3–thermocouples inside, ~1% moisture content (Courtesy of Prof. Chun-Zhu Li, Curtin University)

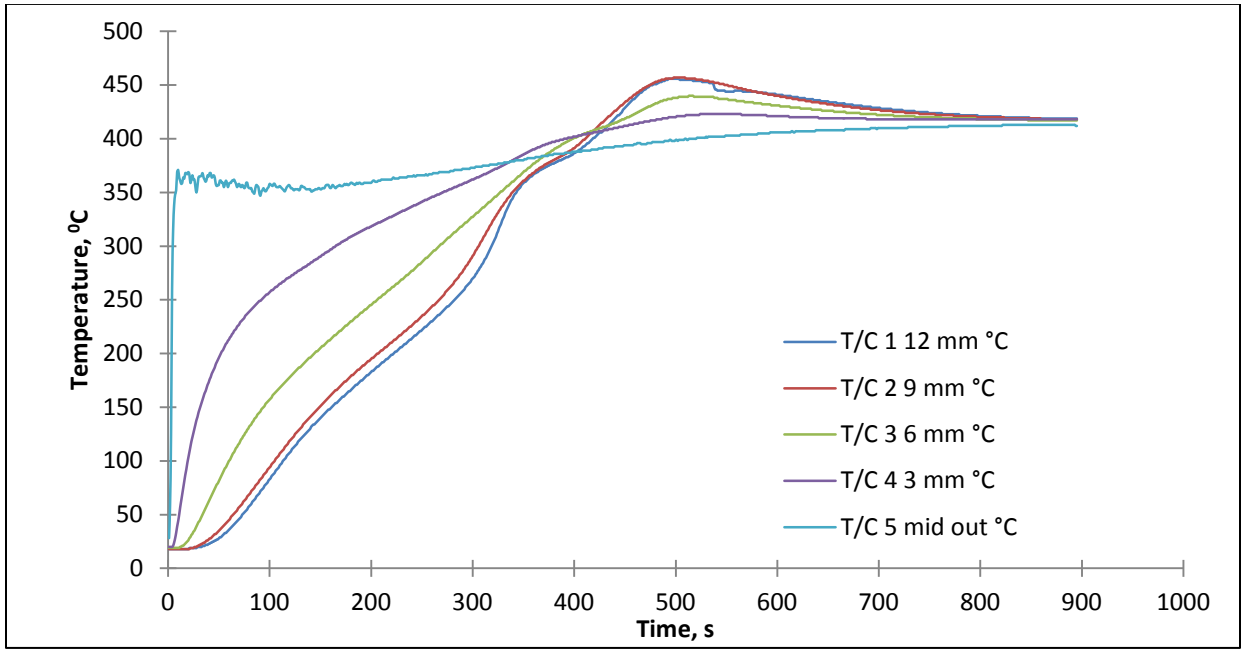

Figure 26A: Pyrolysis at 400°C with 24.4mm diameter sample, 4–thermocouples inside, ~1% moisture content (Courtesy of Prof. Chun-Zhu Li, Curtin University)

3.6—Auger pyrolysis reactor model

The parameter inputs used for all the auger reactor model simulations are given in Table 7A.

Table 7A: Values of parameters used in the numerical solution of the model

Parameter	Unit	Value
$\boldsymbol{R}$, universal gas constant	J/mol/K	8.31145
$\boldsymbol{M_A}$, molecular weight of carrier gas (N_2)	kg/kmol	28
$\boldsymbol{M_D}$, molecular weight of volatiles (Assuming for TAR)	kg/kmol	110[a]
$\boldsymbol{\alpha_0}$, Initial conversion factor		0
P, pressure	Nw/m^2	101325
$\boldsymbol{C_{PA}}$, specific heat capacity of the carrier gas (N_2)	J/kg/K	1040
$\boldsymbol{C_{PB}}$, specific heat capacity of the biomass (wood)	J/kg/K	1067[b]
$\boldsymbol{C_{PD}}$, specific heat capacity of the volatiles (assuming steam vapor)	J/kg/K	2080
$\boldsymbol{C_{PCh}}$, specific heat capacity of the char	J/kg/K	1000[b]
$\boldsymbol{\varepsilon}$, emissivity of the solid		0.95[b]
$\boldsymbol{\sigma}$, Boltzmann constant	$W/m^2/K^4$	$5.67x10^{-8}$
$\boldsymbol{H}$, enthalpy of reaction	J/kg	1.5E+05

[a:]Bryden & Hagge, (2003); [b:]Pyle & Zaror (1984)

The conversion factors of biomass into volatiles and biochar, the initial mass flux of biomass and the carrier gas, the velocity of the biomass flux, and the wall temperature are fixed according to the results modeled.

3.6.1—Effect of wall temperatures on products yields

The product yields versus the wall temperatures obtained from this model are compared with those obtained by the group of Professor Garcia-Perez (Liaw et al., 2012) at WSU. The experimental setup, as described by Liaw et al., (2012), is presented as follows.

3.6.2—Biomass collection and characterization

The Douglas fir wood used as feedstock was grown in Port Angeles, Washington and was donated by Herman Brothers Logging & Construction, Incorporated (Port Angeles, WA). The samples were stored in a refrigerator at 4°C. A pioneer mill (Model number 400 HD, serial number 2404, Bliss Industries, Inc.) was used to grind the received samples to a 2 mm fraction or less. The contents of ash, extractives, cellulose, lignin, and hemicelluloses in the Douglas fir wood were measured following ASTM methods.

3.6.3—Pyrolysis

Between 500 and 600 g of biomass sample with a reduced content of AAEM was dried and pyrolyzed using the auger pyrolysis reactor as shown in Figure 18A. The dried biomass was introduced into the hopper of a volumetric feeder (Barbender Technologies) and fed into the auger reactor at a feeding rate of 10–12 g/min. N_2 at 20 L/min was used as the carrier gas. The estimated residence time of the vapors inside the pyrolysis reactor was about 8 s. The biomass was pushed through the hot zone of the reactor with an auger screw driven by a 1 hp variable speed motor. All the tests were conducted at auger speeds of 13 rpm which corresponds to a biomass residence time inside the reactor of 1 min. A stainless-steel tube with a length of 58.5 cm and diameter of 10 cm was heated by a Lindberg/Blue M (model HTF55322A) furnace to be the hot zone.

The temperature on the external wall of the reactor was recorded and maintained at set temperatures. Because of the relatively low heat transfer coefficient between the wall and the biomass moving bed, a significant temperature gradient was established between the biomass bed and the wall of the reactor. The temperature of the solid residue produced was also quantified. Figure 27A shows the relationship between temperature at the wall of the reactor and the temperature of the gases and vapors leaving the auger reactor.

The charred particles were collected, left to cool for 2 h and weighed in a char pot. The pyrolysis vapors were condensed in three condensation units. The first unit was a vertical tube with cooling water coils where pyrolysis vapors were cooled to approximately 24°C. The second condensation unit consisted of four traps in series immersed in ice. The third unit, a bubbling trap with water cooled by ice, was used to precipitate the aerosols not collected in the two previous condensers. The pressure inside the reactor was kept close to atmospheric pressure (under a very slight vacuum −2 mm H_2O) by applying suction at the final condenser. A vacuum pump with a valve to regulate the suction had a dual purpose which included (1) helping to suck the pyrolysis vapors from the pyrolysis reactor, and (2) the centrifugal force of the pump impeller helped to remove the aerosols that did not condense.

The yield of liquid was determined by weighing the traps, the vacuum pump and the liquid collected in the first condenser. The liquid condensed in the first condenser was collected in a bottle of known weight. The liquid left on the wall of the condenser was recovered by washing it with acetone. The weight of the residues left on the wall of the first condenser was quantified after acetone removal at the rotary evaporator. The non-condensable gases were calculated by the difference.

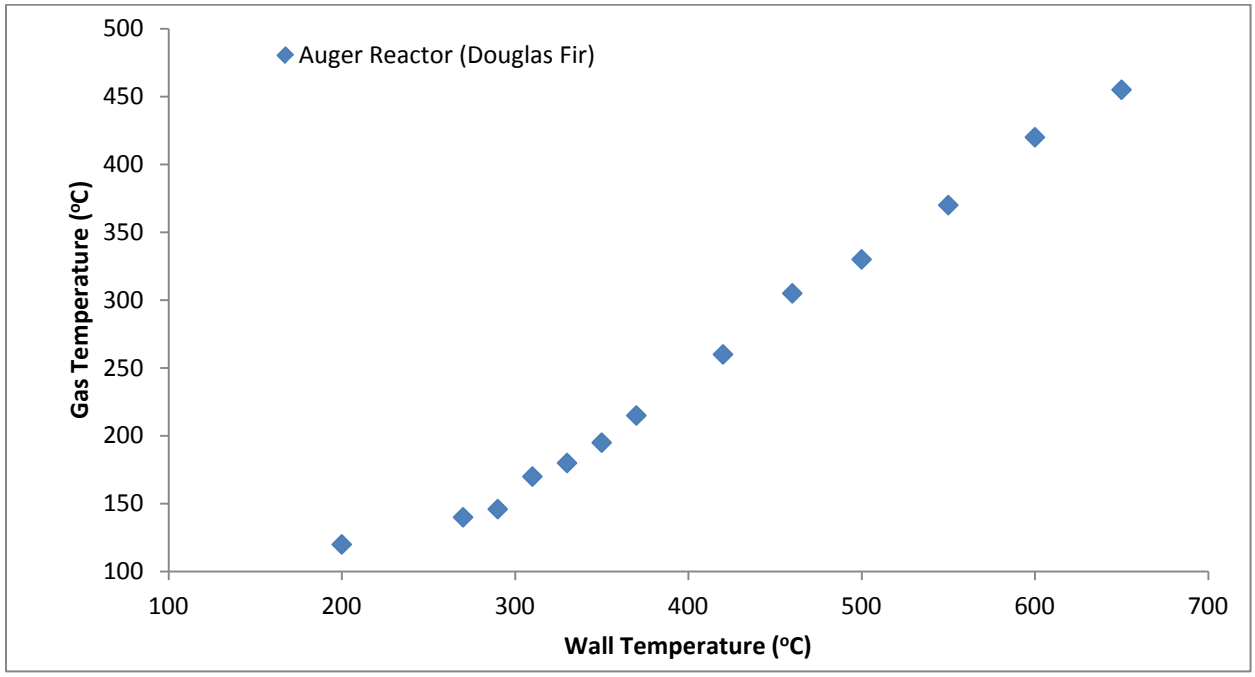

Figure 27A: Auger reactor wall temperature vs. temperature of gases (Liaw et al., (2012))

Figure 28A shows the yield of liquids, biomass and gas obtained from Liaw et al., (2012). In order to compare these curves with the auger pyrolysis reactor model, it is necessary to add up the liquid and gas to obtain the fraction of "vapors" that is going to be simulated. Similarly, the curve named "biomass" in Figure 28A is going to be compared with the sum of the biomass and biochar content reproduced by the model.

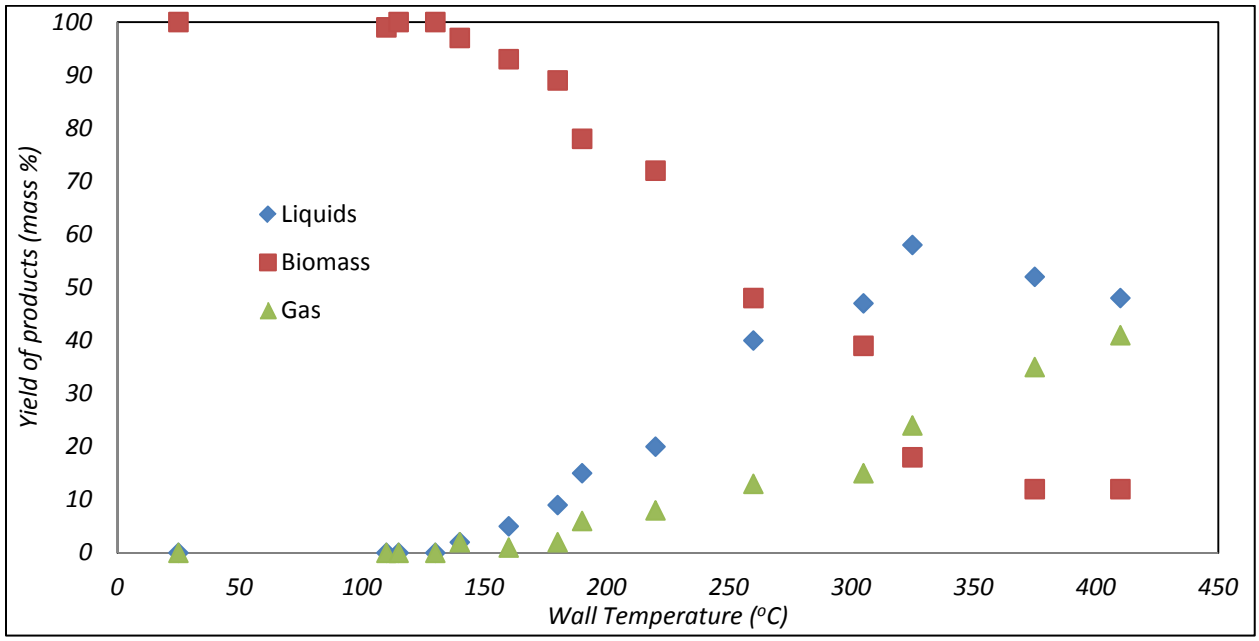

Figure 28A: Products yield obtained from the pyrolysis of Douglas fir at different temperatures in an auger reactor (Liaw et al., 2012).

4—Results

4.1—Effective thermal conductivity

The results of the validation of the COMSOL model for the effective thermal conductivity are displayed in Figure 29A and Figure 30A. Figure 29A shows the effective radial thermal conductivity according to Equation (1) (Hunt et al., 2008), the COMSOL model and experimental data from Grønli (1996). Figure 30A shows the effective axial thermal conductivity according to Equation (1) (Thunman & Leckner (2002) model), the COMSOL model for both 0 and 1 tangential tracheids in the unit cell and experimental data from Grønli (1996). Both figures show the results for the 0% moisture content condition, the results for other moisture conditions can be found in Attachment D.

The results show that with regard to the effective thermal conductivity, the COMSOL model follows the expected trends for radial as well as axial direction with little deviation for the variable oven-dry densities at different moisture conditions when compared to the theoretical models as well as the experimental data.

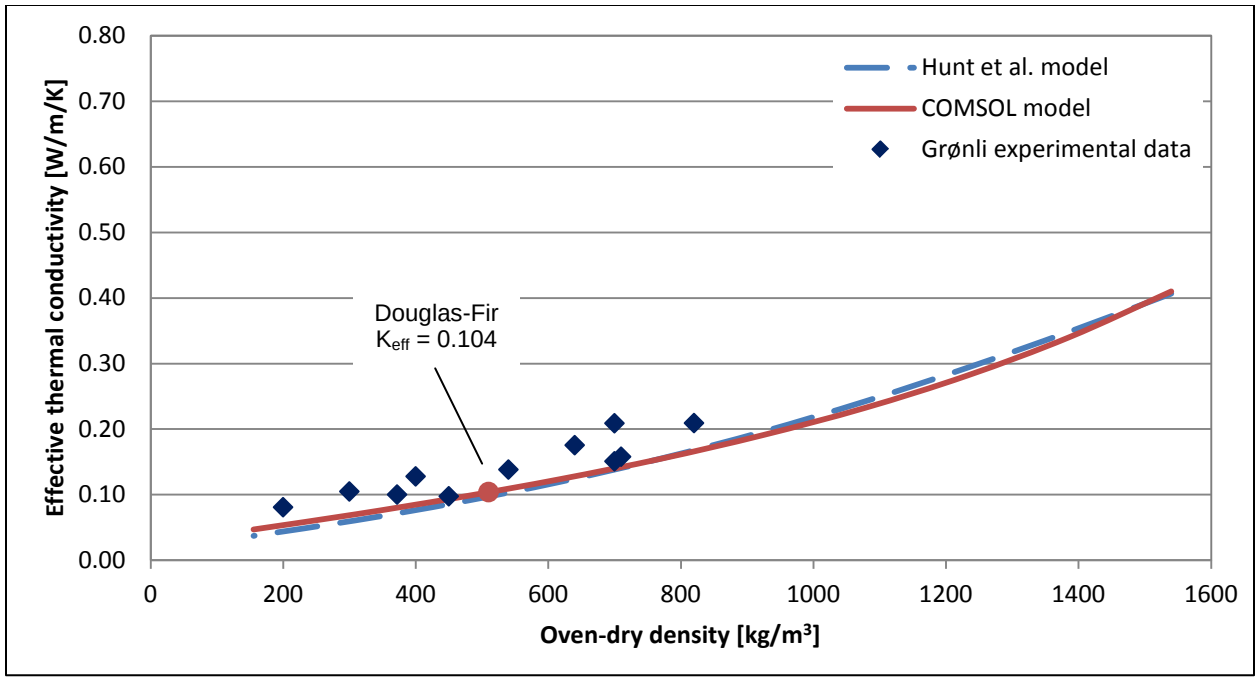

Figure 29A: The effective radial thermal conductivities at 0% moisture content calculated with Equation (1) (Hunt et al., 2008), measured data from Grønli (1996) and determined with the COMSOL model

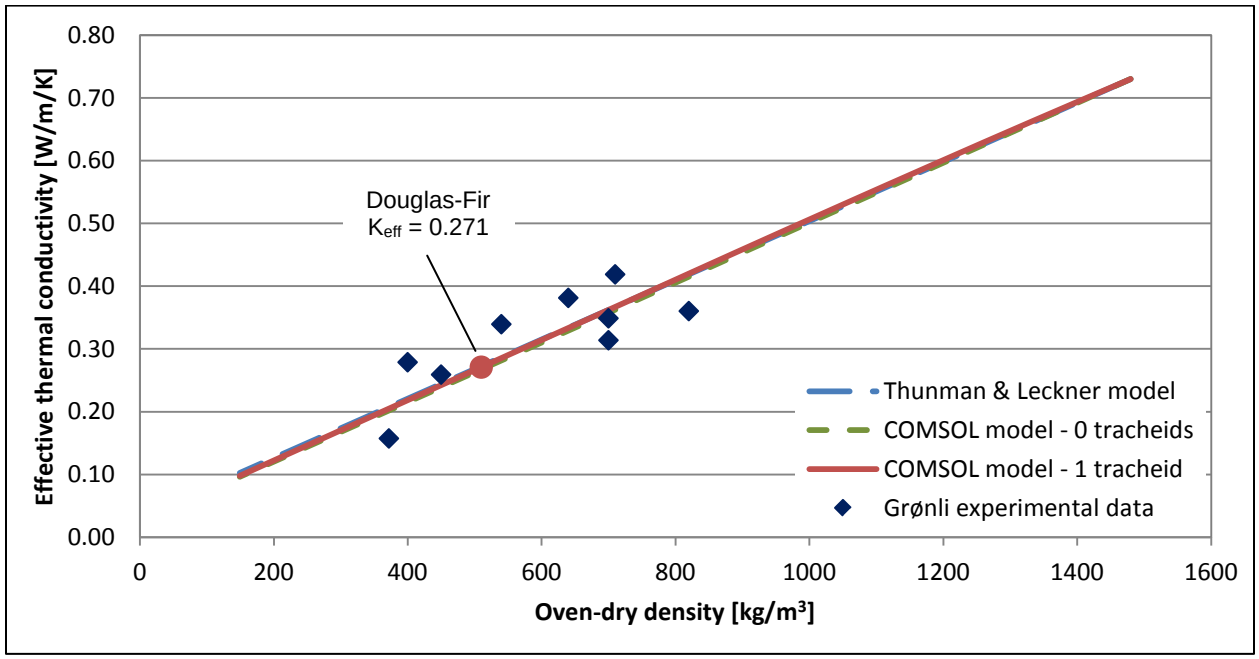

Figure 30A: The effective axial thermal conductivities at 0% moisture content calculated with Equation (1), measured data from Grønli (1996)and determined with the COMSOL model

4.2—Effective mass diffusivity

The results of the validation of the COMSOL model for the effective mass diffusivity are displayed in Figure 31A, Figure 32A and Figure 33A. In the validation of the COMSOL model, the values of effective pit openings and number of pits present were unknown. Literature reports that the values for the pit aperture openings are between 0.02 µm and 4 µm with a logarithmic mean of approximately 0.3 µm (Siau, 1984). The number of pits in radial/tangential direction for typical softwoods is within the range of 50 to 300 pits per tracheid wall (Burr & Stamm, 1947; Siau, 1984) with a logarithmic average of approximately 122 pits. These values are used to determine the minimum, maximum and average porosities with Equation (6) (radial direction) and Equations (5) and (8) (axial direction).

Figure 31A and Figure 32A shows the effective radial mass diffusivities determined with COMSOL and according to the experimental data from Avramidis and Siau (1987) for Western white pine wood at 30 and 70°C, respectively. Figure 33A shows the effective axial mass diffusivities determined with COMSOL and according the experimental data from Çolakoğlu (2009) for different wood types.

From the following figures it can be concluded that the experimental values are within the expected range for the effective mass diffusivities that were determined with the COMSOL model. All experimental values are below the average value and for the effective axial mass diffusivity, some experimental values are close to the minimum expected value. This is assumed to be caused by other resistances that are present in the pit membrane (USDA, 2010) and due to factors such as pit aspiration (Fotsing & Tchagang, 2005). Furthermore, it shows that the effective mass diffusivities determined with COMSOL are larger in the axial direction than in the radial direction, which is in accordance with literature (Burr & Stamm, 1947; Fotsing & Tchagang, 2005; Haas et al., 2009; Siau, 1984).

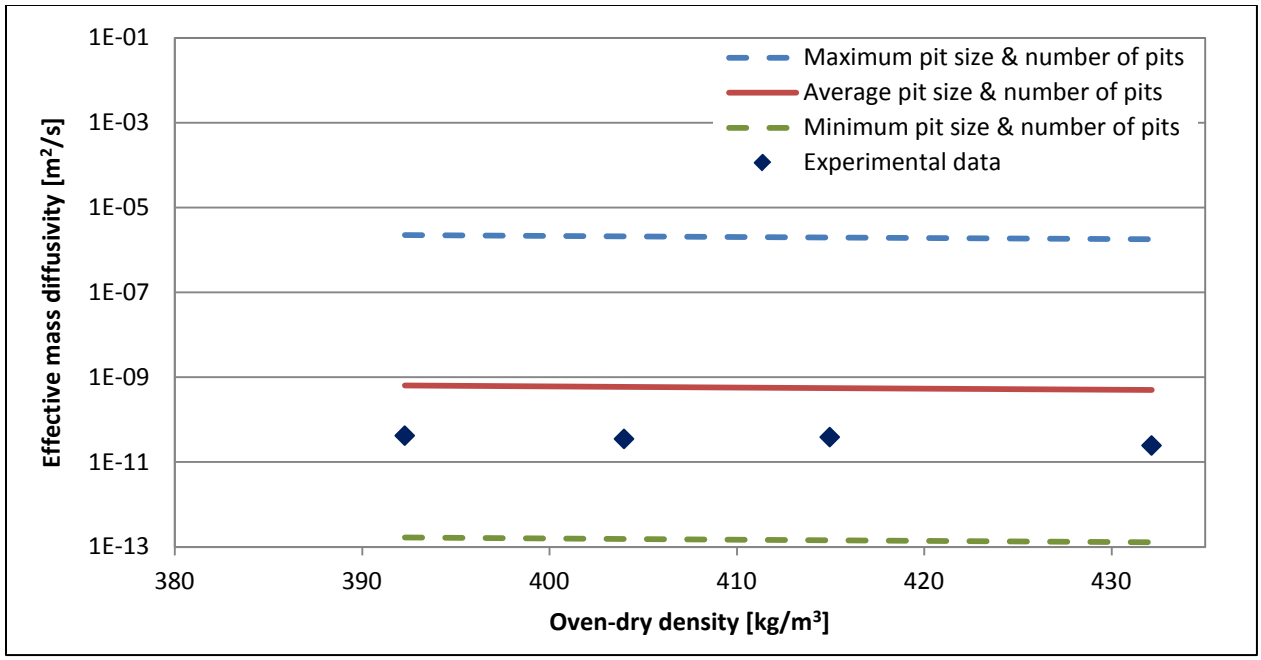

Figure 31A: Effective radial mass diffusivity at 30°C for Western white pine wood according to the experimental data from Avramidis & Siau (1987) and determined with the COMSOL model for minimum, maximum and logarithmic average pit aperture sizes and number of pits

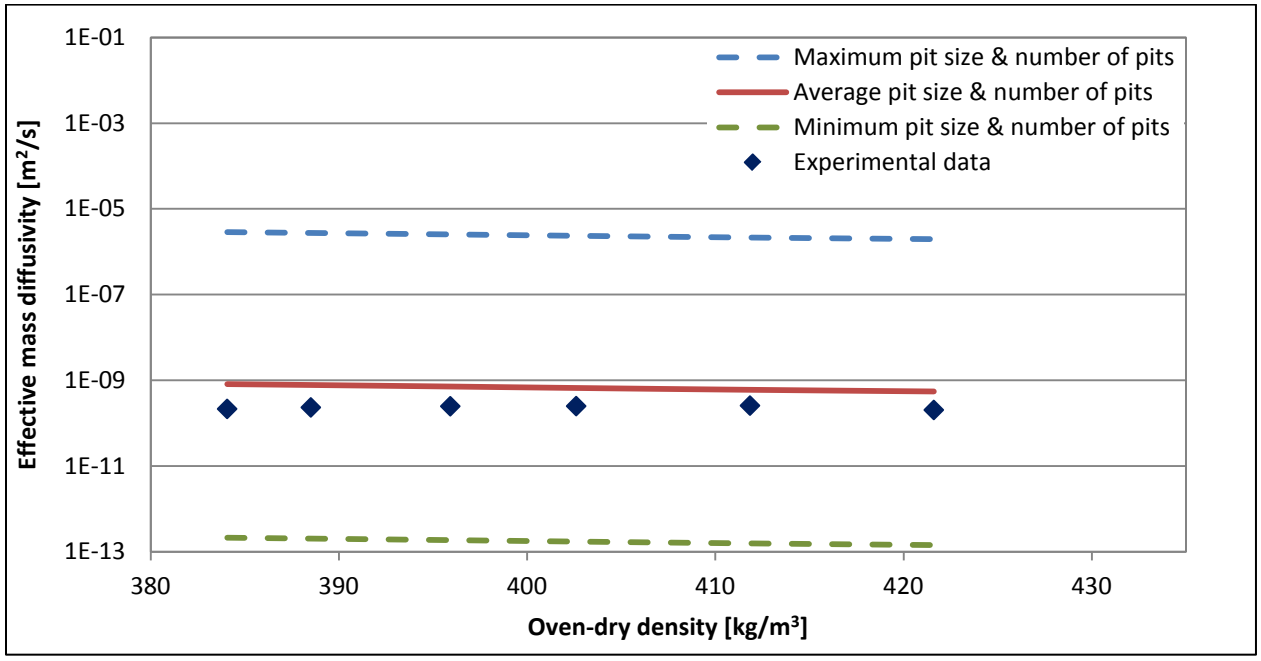

Figure 32A: Effective radial mass diffusivity at 70°C for Western white pine wood according to the experimental data from Avramidis & Siau (1987) and determined with the COMSOL model for minimum, maximum and logarithmic average pit aperture sizes and number of pits

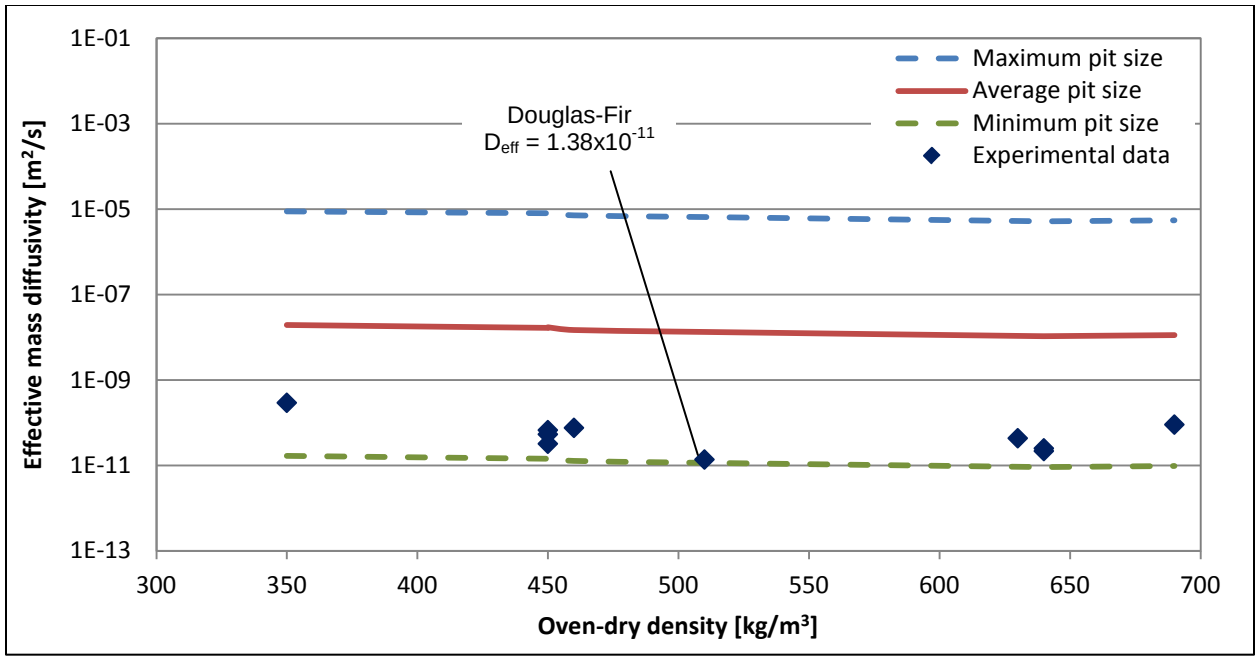

Figure 33A: The effective axial mass diffusivity according to experimental data from Çolakoğlu (2009) and determined with the COMSOL model for maximum, minimum and logarithmic average pit aperture sizes

4.3—Single particle model

To validate the single particle model, the results of the previously described simulations are collected and compared to experimental and simulated data from literature.

4.3.1—Model adjustment

To adjust the parameters of the model mentioned in Table 6A, the internal temperature profile at the center of the particle at 400°C was selected. After using root mean square error (RMSE) methodology to fit the model to the experimental curve, a very good adjustment is achieved as it can be seen in Figure 34A. The parameters obtained are shown in Table 8A.

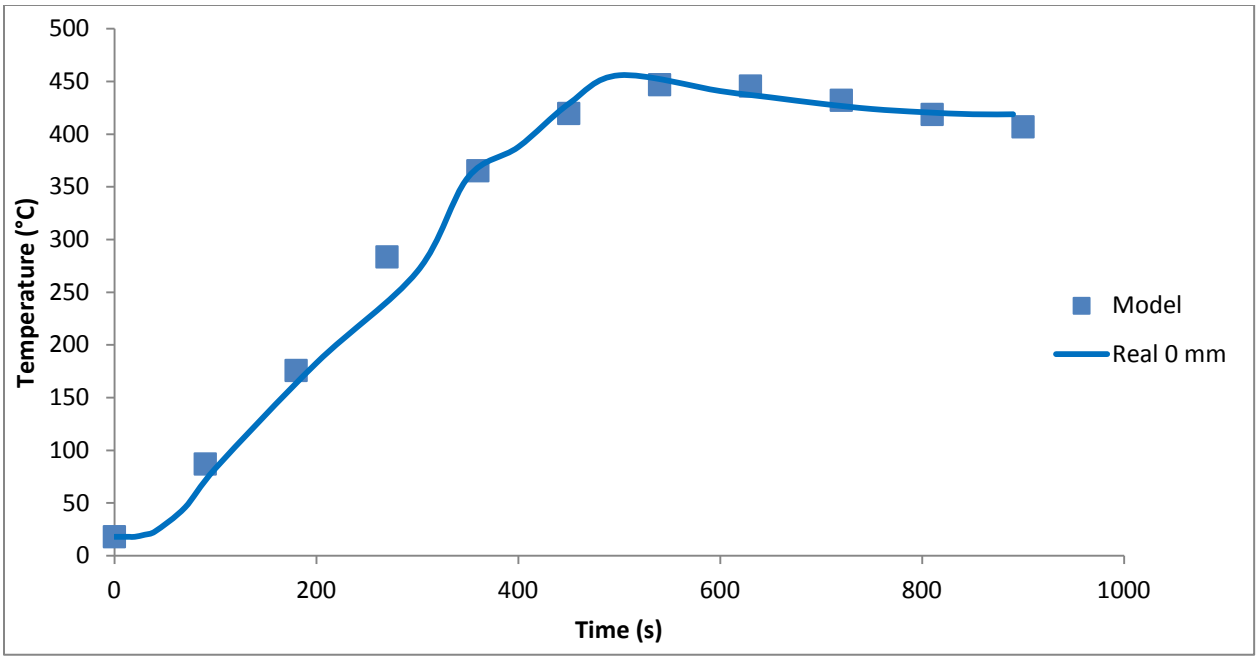

Figure 34A: Temperature profile in the center of a 24.4 D biomass sample heated a 400^{o}C and the adjusted temperature profile using the single particle model

Table 8A: Adjusted parameters for model simulation

Parameter	Value
Radial thermal conductivity, Keff r [W/mK]	0.190
Axial thermal conductivity, Keff z [W/mK]	0.4
Heat of reaction Biomass-Char, ΔH_1 [J/kg]	420000
Heat of reaction Biomass-Tar, ΔH_2 [J/kg]	−34797
Heat of reaction Biomass-Gas. ΔH_3 [J/kg]	−90907
Heat of reaction Tar-Gas + char, Tar-Gas + SY, ΔH4 [J/kg]	40000
Permeability of biomass, Kpb [m^2]	10^{-16}
Permeability of char, Kpc [m^2]	10^{-16}

4.3.2—Model validation

Figure 35A shows that the model results agreed well with the temperature profiles at 6 mm and 13 mm from the center of the particle following heating to 400°C. Figure 36A also shows that the particle model can follow very well with the trend of the temperature profiles at different distances from the center of the particle when it is heated at 300°C.

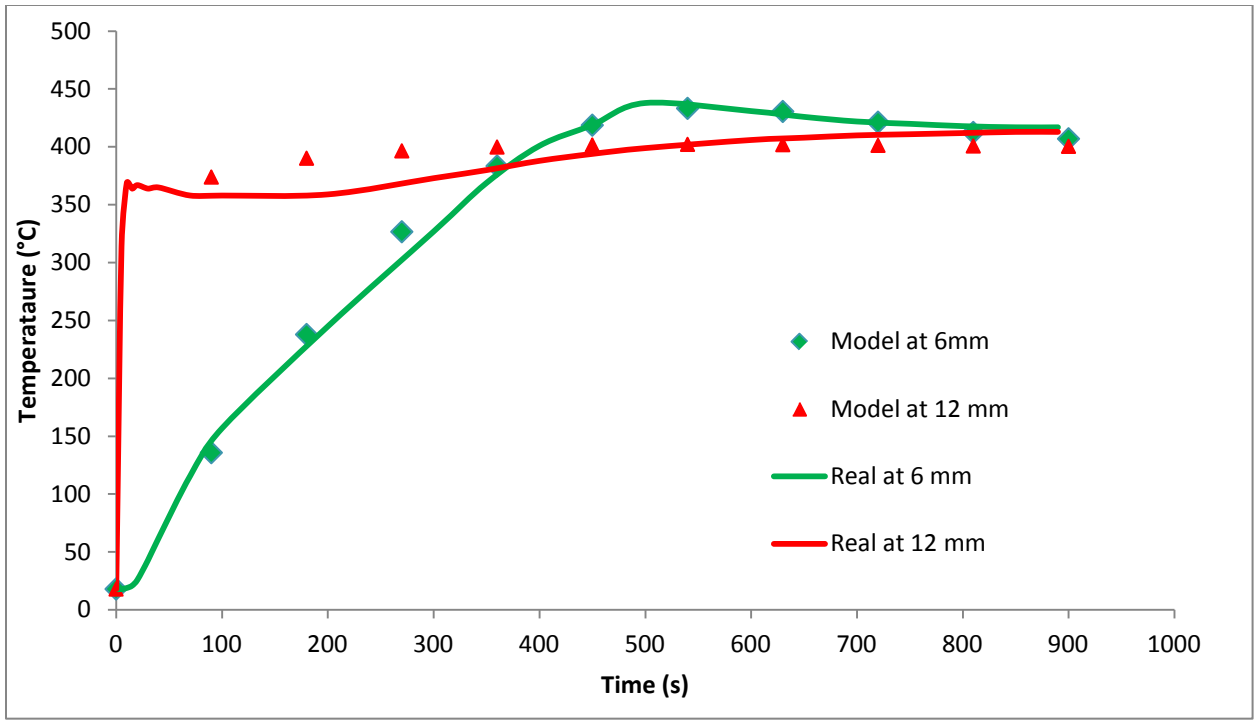

Figure 35A: Measured (real) and simulated temperature profiles during pyrolysis at 400 ^{o}C with 24.4 mm diameter biomass particle and ~1% moisture content

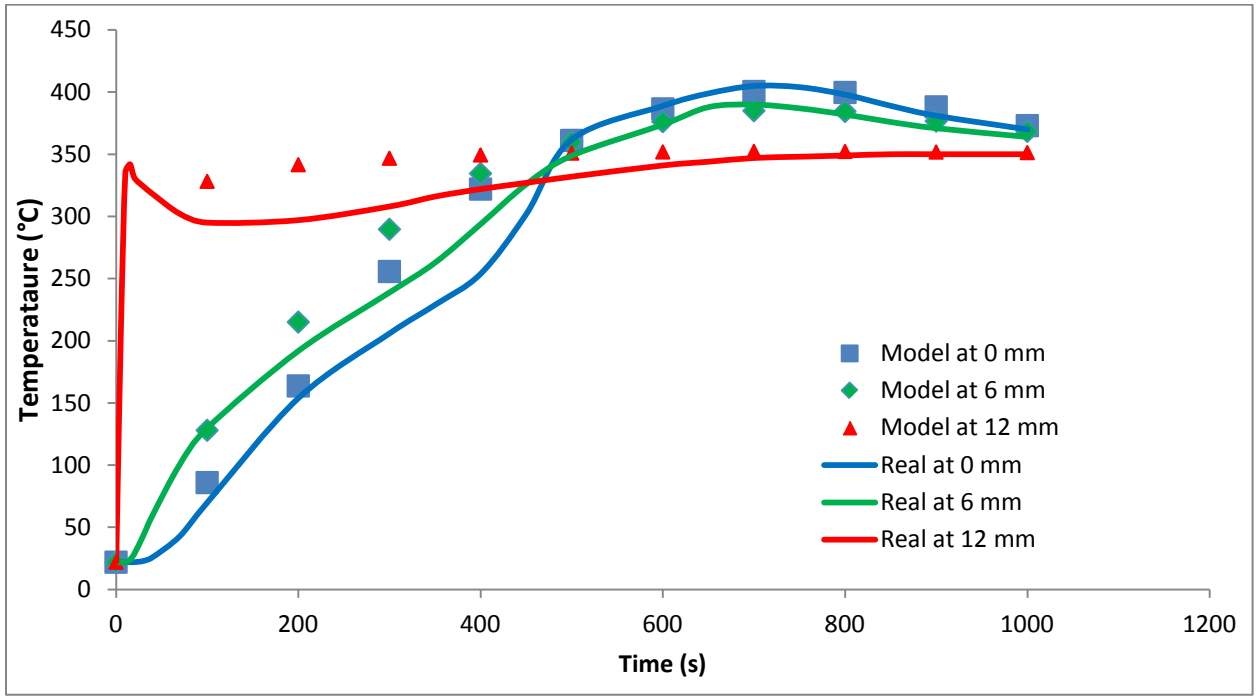

Figure 36A: Measured (real) and simulated temperature profiles during pyrolysis at 350^{o}C with 25.13 D biomass sample and ~1% moisture content

The concave nature of the temperature profiles for the inner thermocouples might be due to the combined action of heat transfer and the endothermic reaction. The temperature of the inner thermocouples started to rise a bit after the experiment started because of the heat transfer resistance along the radial direction of the wood sample. However, as soon as it started to rise, the temperature profile (Temperature vs. time) was concave. The temperature profile for situations in which a particle is heated without the existence of chemical reactions is typically a straight line. The effect of the two endothermic reactions is obviously less important than the heat transferred towards the center of the sample, which results in steady increase in temperature.

Heat produced during the exothermic reactions exceeded the heat absorbed by the endothermic reactions, which caused the overall local temperature to rise. This sharp increase in temperature could not be seen in the outer most thermocouple that reached a similar final temperature well before the inner thermocouples. Therefore, heat produced during the exothermic reaction in the outer layer might be directed inward to supply the heat needed for the endothermic reactions in the inner layers of the particle.

In pyrolysis tests at 350 and 400°C (Figure 36A and Figure 35A, respectively), a sudden change in temperature profile around 350°C could be observed. The heating rate decreased significantly (almost a flat region in 350°C pyrolysis) and proved to be the dominating period of endothermic cellulose depolymerization over exothermic polycondensation reactions. This phenomenon matches the highest mass loss rate observed around 360°C (Figure 37A and Figure 38A) during cellulose pyrolysis reported in literature (Shen & Gu, 2009; Yang et al., 2006) This decrease follows another increase in temperature profile that might be because of exothermic degradation of lignin and levoglucosan. Specifically, at 400°C pyrolysis (Figure 34A and Figure 35A), the increase in temperature is sharp around 375°C; one possible reason behind this drastic increase might be due to high rate of polycondensation reactions at around 370°C (Yang et al., 2006).An important issue in this situation is that the endothermic cellulose degradation is continuing during the highest exothermic polycondensation reactions. This is one of the reasons behind why the center temperature dropped after reaching a peak value during pyrolysis.

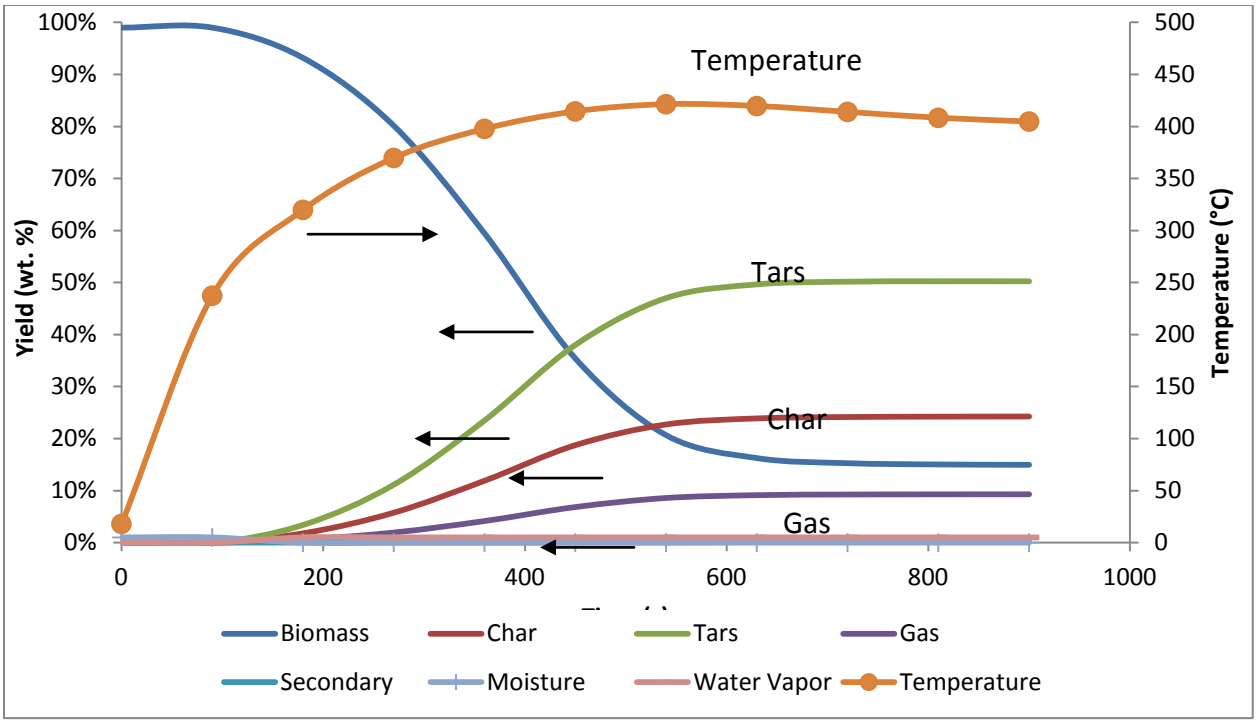

Figure 37A: Simulated particle average temperatures and product distributions during pyrolysis at 400°C with 24.4 D biomass sample and ~1% moisture content (The arrow indicates which Y axis should be used to read the data)

The adjusted heat of reaction values of the model presented in Table 9A showed that both exothermic and endothermic reactions are needed to reproduce the concave behavior of the temperature profiles. However, lack of experimental data on the yield of products in the Curtin University study did not allow us to validate the model with respect to the product distribution (the results obtained with the model are shown in Figure 37A and Figure 38A).

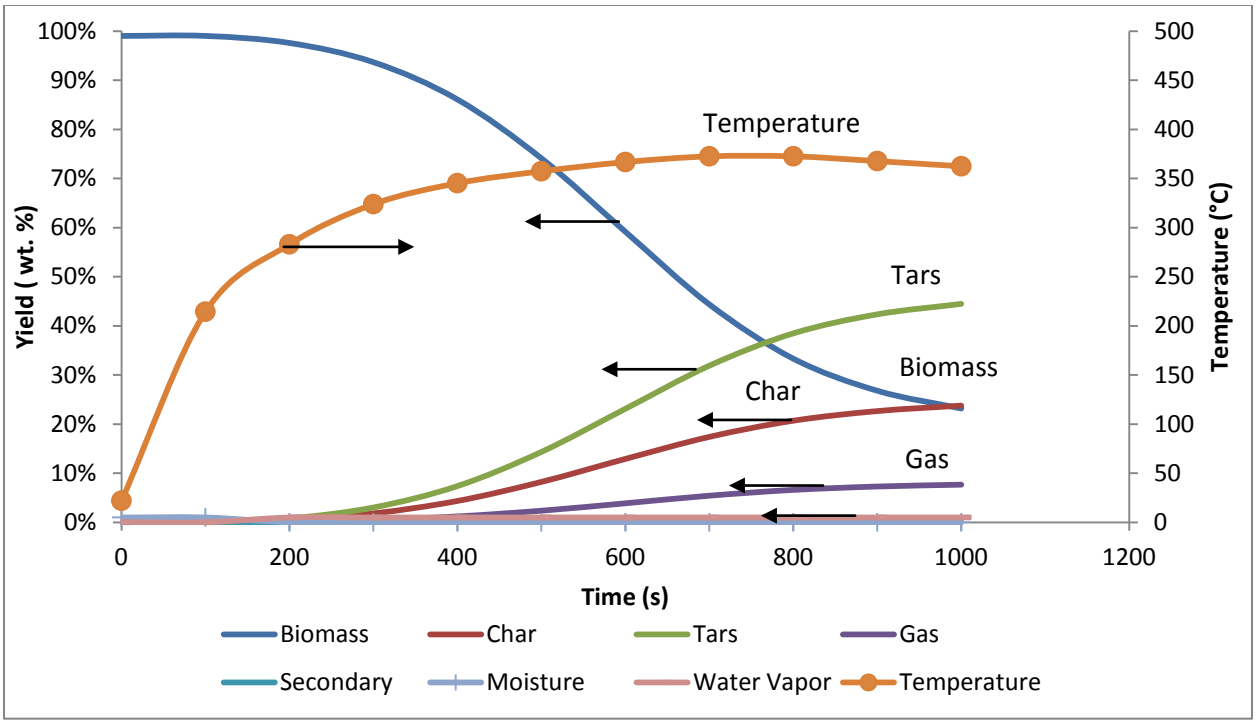

Figure 38A: Simulated particle average temperatures and products distributions during pyrolysis at 350°C with 25.13D biomass sample and ~1% moisture content

4.4—Auger pyrolysis reactor model

To adjust and validate the auger pyrolysis reactor model, the results of the previously described simulations were compared with the work carried out by Liaw et al., (2012).

4.4.1—Model adjustment

Some of the parameters of the model develop for the Auger reactor (for example, the heat transfer coefficients) cannot be estimated by theoretical or empirical correlations. To adjust the parameters of the model, the values shown in the curve wall temperature vs. gas temperature were chosen (Figure 27A) (Liaw et al., 2012). The parameters that were adjusted were the heat transfer coefficients, U` U``, and U``` (J/m^2sK) between the wall and the gases, between the solid and the gases, and between the wall and the solid phase respectively. After using the RSME methodology to fit the model to the experimental curve, a good adjustment was obtained as is shown in Figure 39A.

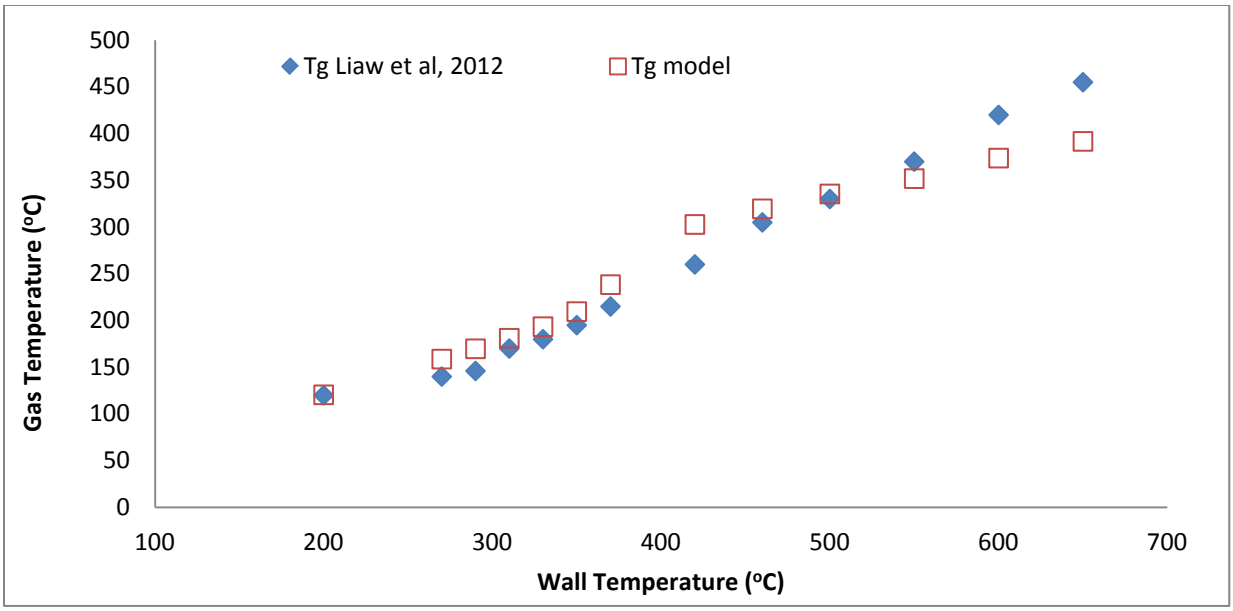

Figure 39A: Wall temperature and gas temperature obtained from Liaw et al., (2012) and the adjusted curve from the model

And additional adjustment was carried out for the Arrhenius constants (Activation Energy (E_1) and Pre-exponential factor (A_1)) using the solid component as it was described in section 3.6.1 of Appendix A. The curves obtained after this adjustment are shown in Figure 40A.

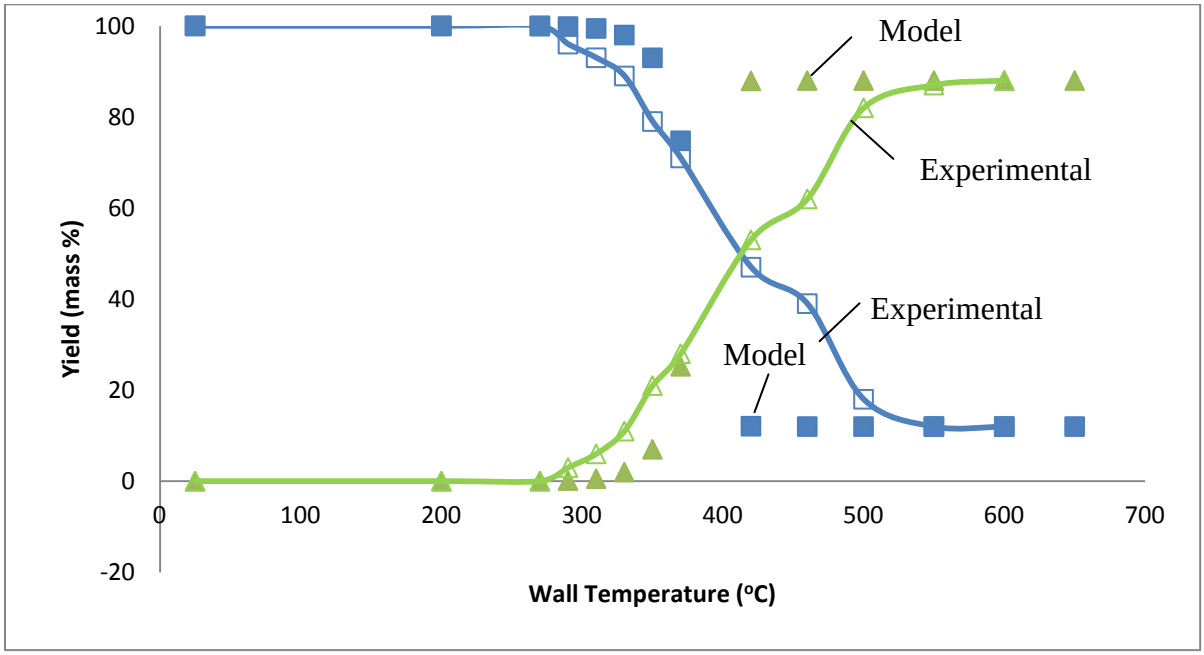

Figure 40A: Wall temperature and inner temperature obtained from Liaw et al., (2012) and the adjusted curve from the model

The parameters obtained are shown in Table 9A. These parameters can then be used for the design and scale up of pyrolysis reactors.

Table 9A: Values of parameters adjusted and fixed in the numerical solution of the model

Parameter	Unit	Value
$\boldsymbol{E_1}$, activation energy in Arrhenius equation	J/mol	183795
$\boldsymbol{A_1}$, pre-exponential factor in Arrhenius equation	s^{-1}	1.60E+14
$\boldsymbol{U'}$, heat transfer coefficients between the wall and the gases	J/m^2sK	9.87
$\boldsymbol{U''}$, heat transfer coefficients between the solids and the gases	J/m^2sK	9.87
$\boldsymbol{U'''}$, heat transfer coefficients between the wall and the solid	J/m^2sK	500.00
b, Final fraction of biochar	mass/mass	0.12

5—Conclusions

Mathematical models at three levels (cells, particle and the reactor) were developed to describe the behavior of an Auger pyrolysis reactor. Each of the models contributes to describe phenomena critical for the performance of this reactor.

To obtain accurate heat and mass transfer parameters, models that predict the effective thermal conductivity and mass diffusivity were developed in COMSOL. The developed COMSOL models are able to estimate these parameters as a function of the geometry and moisture content of the particle. The COMSOL simulation results were compared with the corresponding literature to validate the models.

The mass transfer inside a particle depends heavily on the structure of the wood cells. Small changes in the effective area of pits can cause large changes in the effective diffusivity. The effective mass diffusivity in the axial direction is much higher than in the radial direction, consequently radial mass transport can be neglected when compared to axial mass transport. This result is important because this model allows to estimate the effective transport properties (which are very difficult to measure experimentally) for other biomasses if the morphology of the biomass particle is known.

A 2D single particle model (SP) was developed to describe the pyrolysis of a single wood particle. This model took into account primary and secondary reactions as well as internal and external heat and mass transfer. The model was validated by comparing the results obtained with the model with those reported in a study carried out at Curtin University in Australia. In general the SP model predicts well the temperature profiles in different internal positions within the particle. Therefore, this model can be used to calculate the time a biomass particle needs to be inside a reactor to be completely converted to end-products. In addition, this model is critical for describing the behavior of reactors using large biomass particles with important temperature gradients.

A mathematical model describing the behavior of an auger pyrolysis reactor was developed and the experimental data needed to validate the model was collected in a 1 kg/h auger pyrolysis reactor at WSU. The model developed and the parameters adjusted (heat transfer coefficients)

can be used to simulate the operation of auger pyrolysis reactors or can be used to scale up and design larger reactors.

6—Recommendations

The results of the three models developed are in good agreement with the literature and with the experimental data collected. However, there are several factors that need to be taken into account before using the models that were developed in this study.

The COMSOL model that was developed for the determination of the effective mass transfer parameters requires several geometrical parameters of the wood particle that is used, such as effective pit size and the amount of pits present in the particle. These values should be determined experimentally in SEM studies of the materials studied.

The kinetic data of primary and secondary reactions reported in literature are not consistent and will result in different predictions of the product yields depending on the biomass used. It is recommended to conduct kinetic studies for the biomass samples studied at heating rates comparable with those obtained experimentally and to use the kinetic parameters obtained for the validation of the single particle model developed.

The effect of different moisture content was not validated in the single particle model. This is an ongoing issue that the authors in this study are going to work on very soon since the model is currently being enhanced to be able to work with varying moisture contents. Similarly, data on the yield of products is needed to validate the product distributions during pyrolysis.

The plug flow model developed to describe the behavior of the Auger reactor is robust however, it considers ideal flow patterns. This assumption may not be valid for large systems. Residence time studies are needed to confirm the flow pattern on the reactors simulated with this model. Furthermore, the model developed for the auger pyrolysis reactor has to be validated with additional experimental data. And more precise experimental information of biomass-char temperature is needed to improve the predictability of the model developed.

Attachments to Appendix A

A. Nomenclature

Table 10A: List of used symbols and their descriptions for the single particle model

Symbol	Description	Unit (if applicable)
2D	Two dimensional	
3D	Three dimensional	
A	Pre-exponential factor	$[s^{-1}]$
a	Lumen dimension	[m]
b	Vapor dimension inside the lumen	[m]
C	Char	
c	Concentration	$[mol/m^3]$
Cp	Specific heat capacity	[J/kg/K]
D	Mass diffusivity	$[m^2/s]$
D_D	Dispersion tensor	$[m^2/s]$
d	Diameter	[m]
E_a	Activation energy	[J/mol]
G	Gas	
H	Enthalpy of reaction	[J/kg]
h	Height	[m]
L	Full width and height of the cell	[m]
L/d	Length/diameter	
K	Thermal conductivity	[W/m/K]
k	Reaction rate constant	$[s^{-1}]$
MC	Moisture content	[kg/kg]
n	Number/amount of	
P	Pressure	[Pa]

Symbol	Description	Unit (if applicable)
Q	Heat source	[J]
R	Universal gas constant	[J/mol/K]
r	Radial (position)	[m]
SY	Secondary products from tar	
T	Temperature	[K]
t	Time	[s]
u	Velocity field	[m/s]
V	Volume	[m^3]
W	Wood	
Y	Tars	
z	Axial (position)	[m]
Greek letters		
α	Heat transfer coefficient from surrounding to particle	[$W/m^2/K$]
ε	Emissivity	
θ	Porosity	
μ	Moisture	
ρ	Density	[kg/m^3]
σ	Stefan Boltzmann constant ($5{,}67 \cdot 10^{-8}$)	[$W/m^2/K^4$]
$\Phi_h^{"}$	Heat flux	[W/m^2]
$\Phi_m^{"}$	Mass flux	[$mol/m^2/s$] or [$kg/m^2/s$]
ω	Dimensionless width	
Subscript		
a	Air	
b	Bulk	
C	Char	
c	Cell(s)	

Symbol	Description	Unit (if applicable)
Subscript		
cw	Cell wall	
eff	Effective	
f	Fiber (or cell wall with bound water)	
fw	Free water	
G or g	Gas	
h	Heat	
lum	Lumen	
m	Mass	
mol	Mole(s)	
od	Oven-dry	
pit	Pit(s)	
r	Radial	
rad	Radiation	
S	Surroundings	
s	Solid	
SY	Refractory tars and H_2O	
v	Water vapor	
va	Water vapor in air	
W	Wood	
w	Water	
Y	Tars	
z	Axial	

B. Equations

Constants used in Equation (28):

$$A' = \frac{\frac{K_{eff,r}}{(\Delta r)^2}}{\frac{\sum_{i=W,C,Y,G,SY,M,V}\ \rho_{i\ i,j-1,k}Cp_i}{\Delta t} + \frac{u_{z\ i,j-1,k}\sum_{i=Y,G,SY,V}\ \rho_{i\ i,j-1,k}Cp_i}{\Delta z} - \frac{K_{eff,r}}{i\Delta r} + 2\frac{K_{eff,r}}{(\Delta r)^2} + 2\frac{K_{eff,z}}{(\Delta z)^2} + \frac{\sum(\rho_{i\ i,j-1,k}Cp_i)}{\forall}\ \frac{\forall_{i,j-1,k} - \forall_{i,j-2,k}}{\Delta t}} \quad (28a)$$

$$B' = \frac{\frac{K_{eff,r}}{(\Delta r)^2} - \frac{K_{eff,r}}{r\Delta r}}{\frac{\sum_{i=W,C,Y,G,SY,M,V}\ \rho_{i\ i,j-1,k}Cp_i}{\Delta t} + \frac{u_{z\ i,j-1,k}\sum_{i=Y,G,SY,V}\ \rho_{i\ i,j-1,k}Cp_i}{\Delta z} - \frac{K_{eff,r}}{i\Delta r} + 2\frac{K_{eff,r}}{(\Delta r)^2} + 2\frac{K_{eff,z}}{(\Delta z)^2} + \frac{\sum(\rho_{i\ i,j-1,k}Cp_i)}{\forall}\ \frac{\forall_{i,j-1,k} - \forall_{i,j-2,k}}{\Delta t}} \quad (28b)$$

$$C' = \frac{\frac{\sum_{i=B,C,Y,G,SY,M,V}\ \rho_i Cp_i}{\Delta t}}{\frac{\sum_{i=W,C,Y,G,SY,M,V}\ \rho_{i\ i,j-1,k}Cp_i}{\Delta t} + \frac{u_{z\ i,j-1,k}\sum_{i=Y,G,SY,V}\ \rho_{i\ i,j-1,k}Cp_i}{\Delta z} - \frac{K_{eff,r}}{i\Delta r} + 2\frac{K_{eff,r}}{(\Delta r)^2} + 2\frac{K_{eff,z}}{(\Delta z)^2} + \frac{\sum(\rho_{i\ i,j-1,k}Cp_i)}{\forall}\ \frac{\forall_{i,j-1,k} - \forall_{i,j-2,k}}{\Delta t}} \quad (28c)$$

$$D' = \frac{\frac{K_{eff,z}}{(\Delta z)^2}}{\frac{\sum_{i=W,C,Y,G,SY,M,V}\ \rho_{i\ i,j-1,k}Cp_i}{\Delta t} + \frac{u_{z\ i,j-1,k}\sum_{i=Y,G,SY,V}\ \rho_{i\ i,j-1,k}Cp_i}{\Delta z} - \frac{K_{eff,r}}{i\Delta r} + 2\frac{K_{eff,r}}{(\Delta r)^2} + 2\frac{K_{eff,z}}{(\Delta z)^2} + \frac{\sum(\rho_{i\ i,j-1,k}Cp_i)}{\forall}\ \frac{\forall_{i,j-1,k} - \forall_{i,j-2,k}}{\Delta t}} \quad (28d)$$

$$E' = \frac{\frac{u_z\sum_{i=Y,G,SY,V}\ \rho_i Cp_i}{\Delta z} + \frac{K_{eff,z}}{(\Delta z)^2}}{\frac{\sum_{i=W,C,Y,G,SY,M,V}\ \rho_{i\ i,j-1,k}Cp_i}{\Delta t} + \frac{u_{z\ i,j-1,k}\sum_{i=Y,G,SY,V}\ \rho_{i\ i,j-1,k}Cp_i}{\Delta z} - \frac{K_{eff,r}}{i\Delta r} + 2\frac{K_{eff,r}}{(\Delta r)^2} + 2\frac{K_{eff,z}}{(\Delta z)^2} + \frac{\sum(\rho_{i\ i,j-1,k}Cp_i)}{\forall}\ \frac{\forall_{i,j-1,k} - \forall_{i,j-2,k}}{\Delta t}} \quad (28e)$$

$$S' = \frac{k_1 B_{i,j-1,k}\rho_{B_0}\Delta H_1 + k_2 B_{i,j-1,k}\rho_{B_0}\Delta H_2 + k_3\, B_{i,j-1,k}\rho_{B_0}\Delta H_3 + k_4\rho_Y\Delta H_4 + k_5\, M_{i,j-1,k}\rho_{M_0}\Delta H_5}{\frac{\sum_{i=W,C,Y,G,SY,M,V}\ \rho_{i\ i,j-1,k}Cp_i}{\Delta t} + \frac{u_{z\ i,j-1,k}\sum_{i=Y,G,SY,V}\ \rho_{i\ i,j-1,k}Cp_i}{\Delta z} - \frac{K_{eff,r}}{i\Delta r} + 2\frac{K_{eff,r}}{(\Delta r)^2} + 2\frac{K_{eff,z}}{(\Delta z)^2} + \frac{\sum(\rho_{i\ i,j-1,k}Cp_i)}{\forall}\ \frac{\forall_{i,j-1,k} - \forall_{i,j-2,k}}{\Delta t}} \quad (28f)$$

Constants used in Equation (29):

$$A'' = \frac{\frac{2K_{eff,r}}{(\Delta r)^2}}{\frac{\sum_{i=W,C,Y,G,SY,M,V}\ \rho_{i\,i,j-1,k}Cp_i}{\Delta t} + \frac{u_{z\,i,j-1,k}\sum_{i=Y,G,SY,V}\ \rho_{i\,i,j-1,k}Cp_i}{\Delta z} + 4\frac{K_{eff,r}}{(\Delta r)^2} + 2\frac{K_{eff,z}}{(\Delta z)^2} + \frac{\sum(\rho_i Cp_i)}{\forall}\ \frac{\forall_{i,j-1,k} - \forall_{i,j-2,k}}{\Delta t}} \quad (29a)$$

$$B'' \frac{\frac{2K_{eff,r}}{(\Delta r)^2}}{\frac{\sum_{i=W,C,Y,G,SY,M,V}\ \rho_{i\,i,j-1,k}Cp_i}{\Delta t} + \frac{u_{z\,i,j-1,k}\sum_{i=Y,G,SY,V}\ \rho_{i\,i,j-1,k}Cp_i}{\Delta z} + 4\frac{K_{eff,r}}{(\Delta r)^2} + 2\frac{K_{eff,z}}{(\Delta z)^2} + \frac{\sum(\rho_i Cp_i)}{\forall}\ \frac{\forall_{i,j-1,k} - \forall_{i,j-2,k}}{\Delta t}} \quad (29b)$$

$$C'' = \frac{\frac{\sum_{i=W,C,Y,G,SY,M,V}\ \rho_i Cp_i}{\Delta t}}{\frac{\sum_{i=W,C,Y,G,SY,M,V}\ \rho_{i\,i,j-1,k}Cp_i}{\Delta t} + \frac{u_{z\,i,j-1,k}\sum_{i=Y,G,SY,V}\ \rho_{i\,i,j-1,k}Cp_i}{\Delta z} + 4\frac{K_{eff,r}}{(\Delta r)^2} + 2\frac{K_{eff,z}}{(\Delta z)^2} + \frac{\sum(\rho_i Cp_i)}{\forall}\ \frac{\forall_{i,j-1,k} - \forall_{i,j-2,k}}{\Delta t}} \quad (29c)$$

$$D'' = \frac{\frac{K_{eff,z}}{(\Delta z)^2}}{\frac{\sum_{i=W,C,Y,G,SY,M,V}\ \rho_{i\,i,j-1,k}Cp_i}{\Delta t} + \frac{u_{z\,i,j-1,k}\sum_{i=Y,G,SY,V}\ \rho_{i\,i,j-1,k}Cp_i}{\Delta z} + 4\frac{K_{eff,r}}{(\Delta r)^2} + 2\frac{K_{eff,z}}{(\Delta z)^2} + \frac{\sum(\rho_i Cp_i)}{\forall}\ \frac{\forall_{i,j-1,k} - \forall_{i,j-2,k}}{\Delta t}} \quad (29d)$$

$$E'' = \frac{\frac{u_z\sum_{i=Y,G,SY,V}\ \rho_i Cp_i}{\Delta z} + \frac{K_{eff,z}}{(\Delta z)^2}}{\frac{\sum_{i=W,C,Y,G,SY,M,V}\ \rho_{i\,i,j-1,k}Cp_i}{\Delta t} + \frac{u_{z\,i,j-1,k}\sum_{i=Y,G,SY,V}\ \rho_{i\,i,j-1,k}Cp_i}{\Delta z} + 4\frac{K_{eff,r}}{(\Delta r)^2} + 2\frac{K_{eff,z}}{(\Delta z)^2} + \frac{\sum(\rho_i Cp_i)}{\forall}\ \frac{\forall_{i,j-1,k} - \forall_{i,j-2,k}}{\Delta t}} \quad (29d)$$

$$S'' = \frac{k_1 B_{i,j-1,k}\rho_{B_0}\Delta H_1 + k_2 B_{i,j-1,k}\rho_{B_0}\Delta H_2 + k_3\, B_{i,j-1,k}\rho_{B_0}\Delta H_3 + k_4\boldsymbol{\rho_Y}\Delta H_4 + k_5\, M_{i,j-1,k}\rho_{M_0}\Delta H_5}{\frac{\sum_{i=W,C,Y,G,SY,M,V}\ \rho_{i\,i,j-1,k}Cp_i}{\Delta t} + \frac{u_{z\,i,j-1,k}\sum_{i=Y,G,SY,V}\ \rho_{i\,i,j-1,k}Cp_i}{\Delta z} + 4\frac{K_{eff,r}}{(\Delta r)^2} + 2\frac{K_{eff,z}}{(\Delta z)^2} + \frac{\sum(\rho_i Cp_i)}{\forall}\ \frac{\forall_{i,j-1,k} - \forall_{i,j-2,k}}{\Delta t}} \quad (29d)$$

C. Tables

Table 11A. Parameter estimates for Equation (1)

Parameter	Estimated value	Standard Error
X_1	1,00825	0,00663
X_2	0,9938	0,00792
X_3	1,07389	0,00911

D. Figures

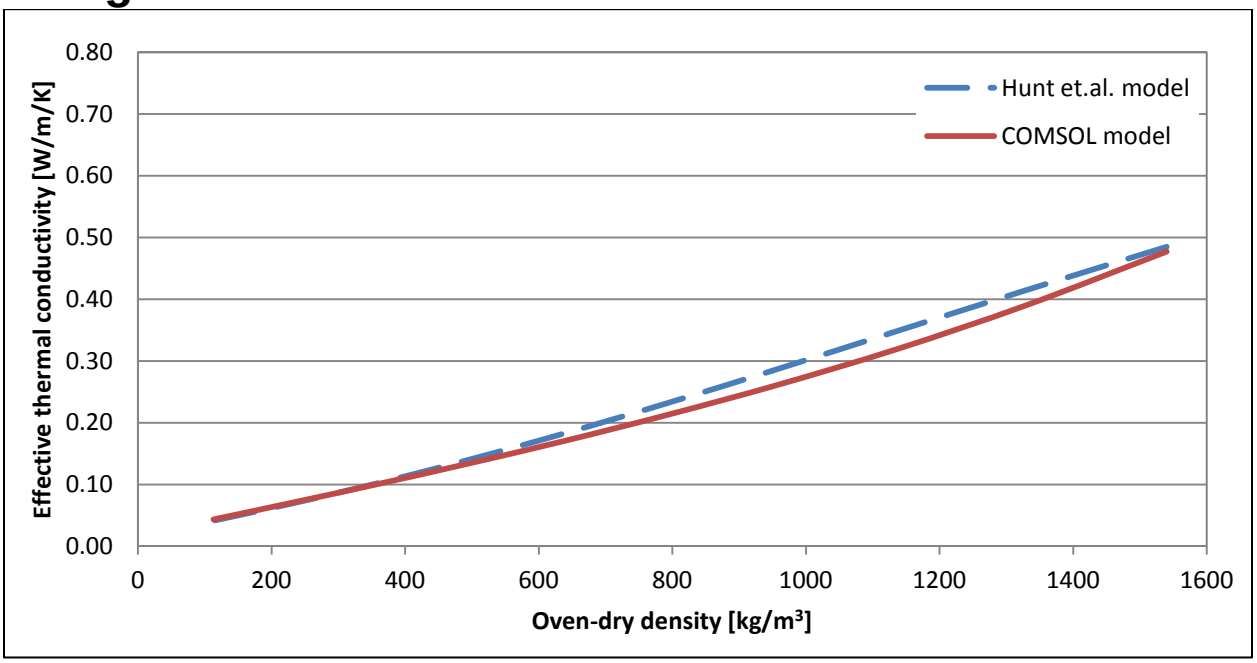

Figure 41A: The effective radial thermal conductivities calculated with Equation (1) and determined with the COMSOL model at fiber saturation point

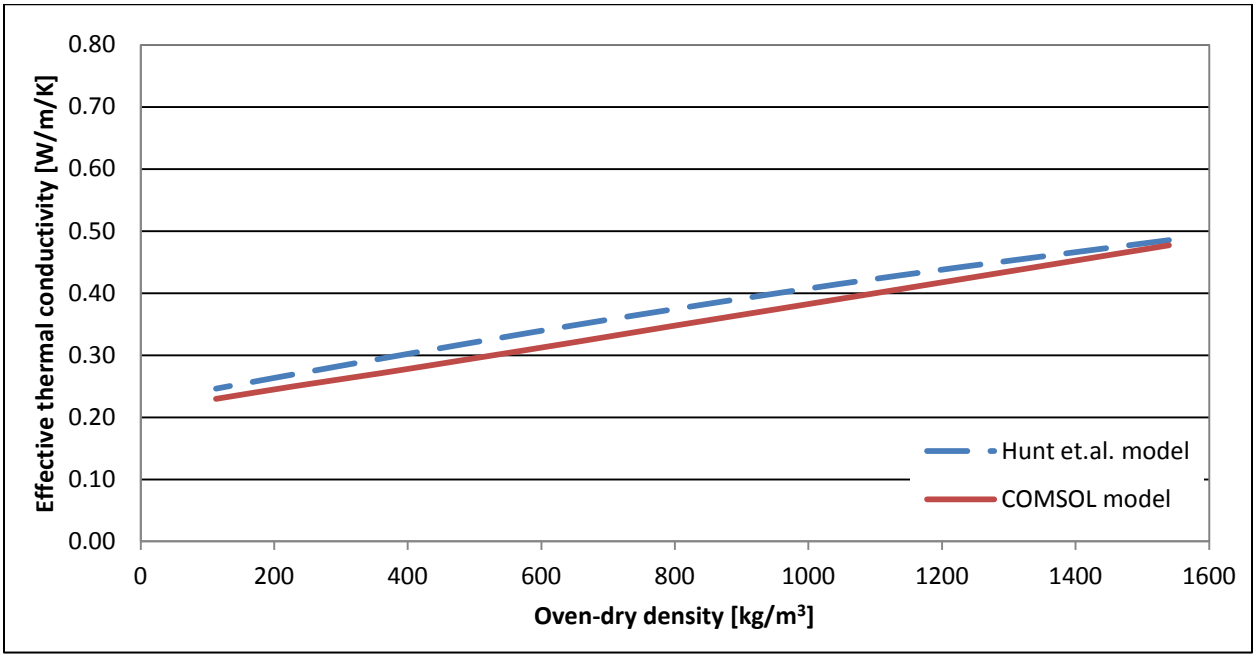

Figure 42A: The effective radial thermal conductivities calculated with Equation (1) and determined with the COMSOL model at 50% free water in the lumen

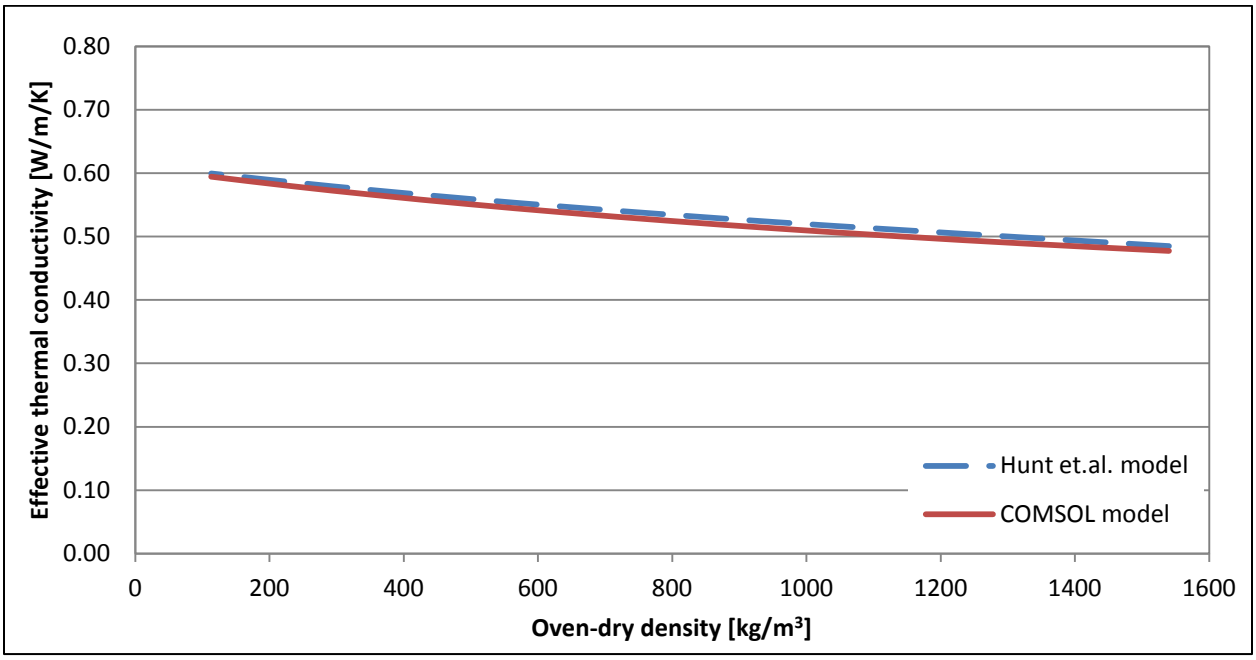

Figure 43A: The effective radial thermal conductivities calculated with Equation (1) and determined with the COMSOL model at a fully saturated lumen

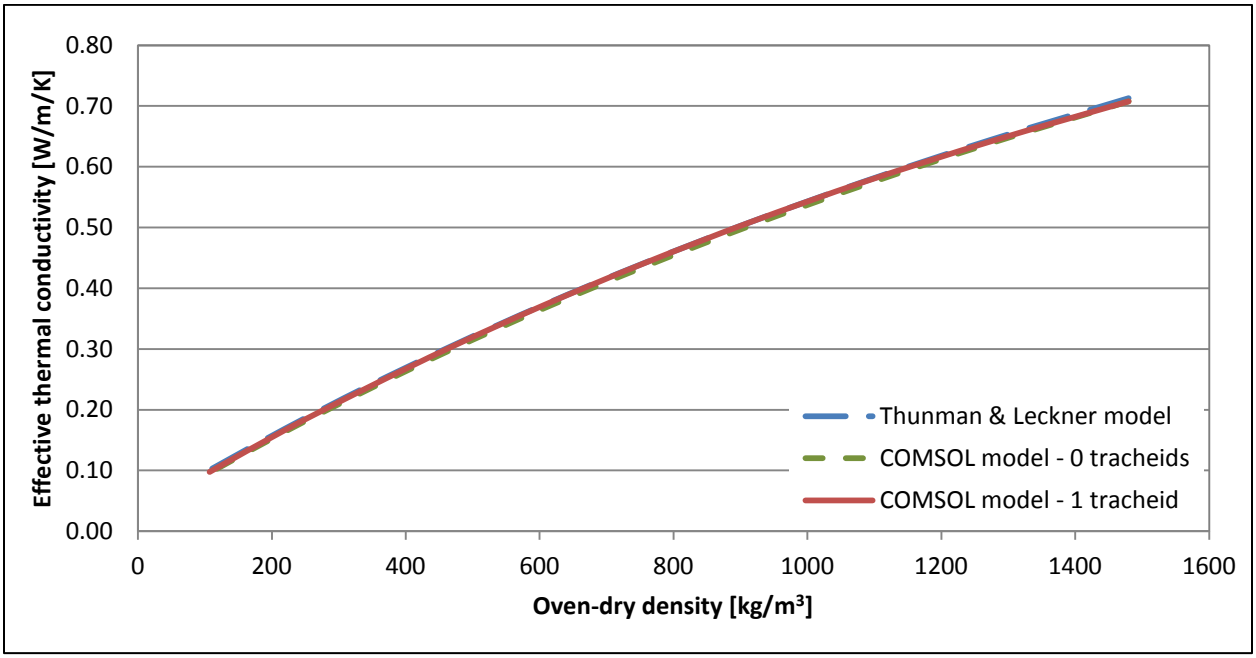

Figure 44A: The effective axial thermal conductivities calculated with Equation (1) and determined with the COMSOL model at fiber saturation point

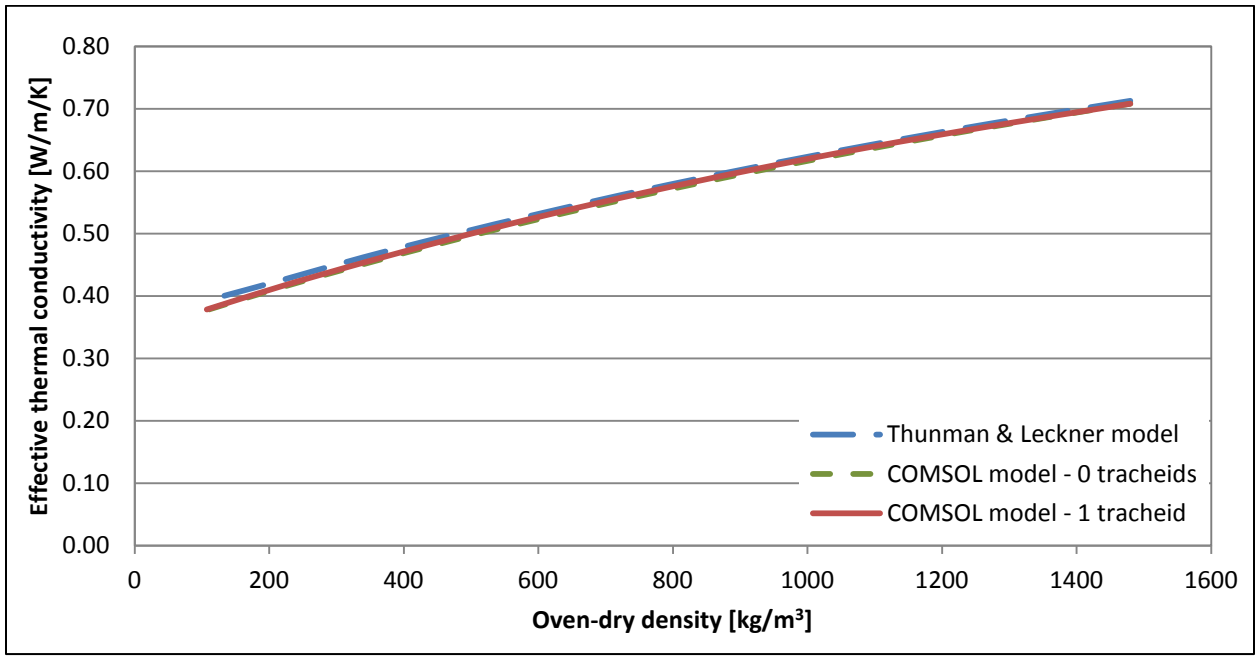

Figure 45A: The effective axial thermal conductivities calculated with Equation (1) and determined with the COMSOL model at 50% free water in the lumen

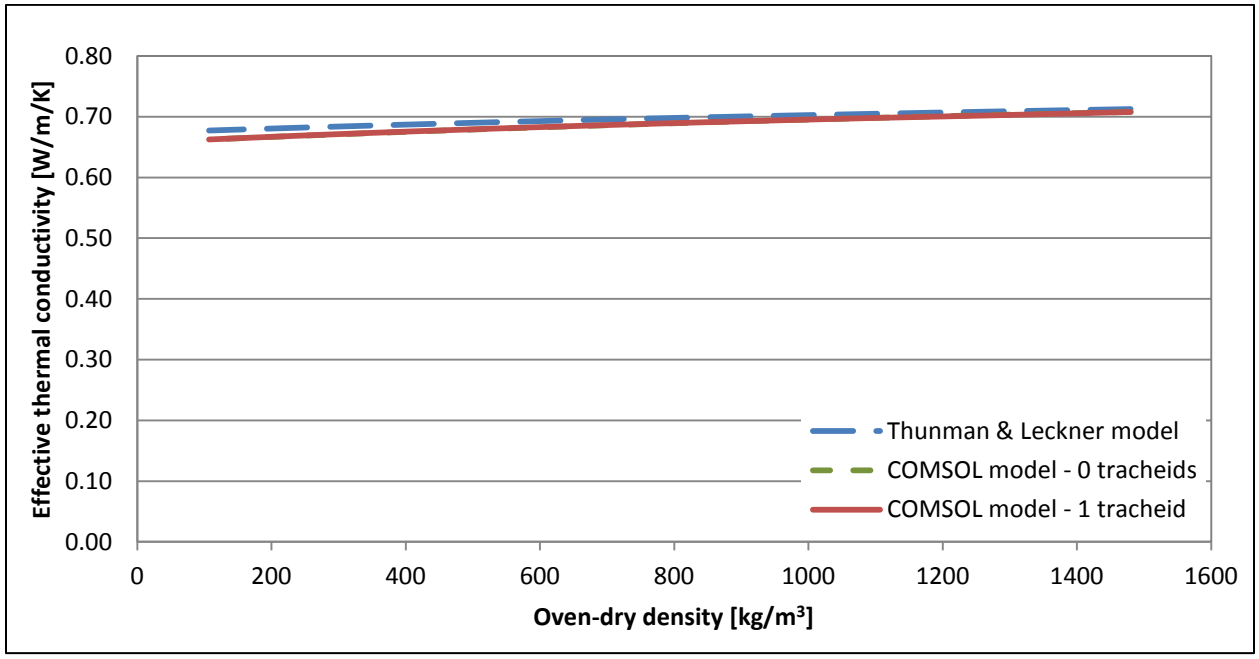

Figure 46A: The effective axial thermal conductivities calculated with Equation (1) and determined with the COMSOL model at a fully saturated lumen

E. Single particle model details

This attachment elaborates on how the single particle model operates. The single particle model is developed with Microsoft Office Excel software.
The single particle model consists of multiple tables representing the progression of temperature and mass distribution inside the particle as a function of reaction time. Each table shows one fourth of the actual particle that is being simulated with the origin of the particle located in the top left corner of each table.

The changes in the temperature and mass distribution in the axial and radial direction are given for one specific time through an iterative process. The model produces these distributions for the initial situation (t = 0) and for 10 subsequent positions in time with a time step that is an input parameter. The recordings are collected in a table and graph once the iteration is complete.

The temperature at a specific place at a specific time is calculated with Equations (28) and (29) by referring to temperatures in a previous time and previous and subsequent places. The mass at a specific place at a specific time is calculated with Equations (14a) through (14e) by referring to the mass at a previous time, the diffusivity data and the kinetic data.

For the borders of the particle there are boundary conditions (Equations (26c) through (26e)). The boundary condition for the external mass transfer (Equation (26e)) is solved using the same numerical technique used in for the temperature in Equations (27a) through (27e). The boundary conditions for the external heat transfer is a quartic equation (4^{th} degree polynomial) and first had to be reduced.

The model does not take into account changes in the specific heat capacity or diffusivity and thermal conductivity as temperature and density of the particle change. Also the particle is considered to be dry, which means there is no moisture present.

The single particle model requires inputs for the following parameters:

- *Density of the wood [kg/m^3]*
- *Initial temperature of the wood particle [K]*
- *Temperature of the reactor/surroundings [K]*
- *Radius of the particle [mm]*
- *Length of the particle [mm]*
- *Time step [s]*
- *Specific heat capacity of the wood [J/kg/K]*
- *Effective radial thermal conductivity of the wood [W/m/K]*
- *Effective axial thermal conductivity of the wood [W/m/K]*
- *Effective diffusivity of tars [m^2/s]*

- *Effective diffusivity of gas [m^2/s]*

References

Achkari-Begdouri, A., Goodrich, P. 1992. Rheological properties of Moroccan dairy cattle manure. *Bioresource Technology*, **40**, 149-156.

Agbor, V.B., Cicek, N., Sparling, R., Berlin, A., Levin, D.B. 2011. Biomass pretreatment: Fundamentals toward application. *Biotechnology Advances*, **29**(6), 675-685.

Agler, M.T., Wrenn, B.A., Zinder, S.H., Angenent, L.T. 2011. Waste to bioproduct conversion with undefined mixed cultures: the carboxylate platform. *Trends in Biotechnology*, **29**(2), 70-78.

Agyei, N.M., Strydom, C., Potgieter, J. 2002. The removal of phosphate ions from aqueous solution by fly ash, slag, ordinary Portland cement and related blends. *Cement and Concrete Research*, **32**(12), 1889-1897.

Ahring, B.K., Sandberg, M., Angelidaki, I. 1995. Volatile fatty-acids as indicators of process imbalance in anaerobic digesters. *Applied Microbiology and Biotechnology*, **43**(3), 559-565.

Alatriste-Mondragón, F., Samar, P., Cox, H.H., Ahring, B.K., Iranpour, R. 2006. Anaerobic codigestion of municipal, farm, and industrial organic wastes:a survey of recent literature. *Water Environment Research*, **78**(6), 607-36.

Andrews, J.F. 1968. Dynamic model of the anaerobic digestion process *Proceedings of the 23rd Industrial Waste Conference* Engineering Technical Reports Collection, Purdue University. pp. 285-310

Angelidaki, I., Ellegaard, L., Ahring, B.K. 1999. A comprehensive model of anaerobic bioconversion of complex substrates to biogas. *Biotechnology and Bioengineering*, **63**(3), 363-372.

Antal Jr, M.J. 1983. Effects of reactor severity on the gas-phase pyrolysis of cellulose-and kraft lignin-derived volatile matter. *Industrial & Engineering Chemistry Product Research and Development*, **22**(2), 366-375.

Appels, L., Baeyens, J., Degreve, J., Dewil, R. 2008. Principles and potential of the anaerobic digestion of waste-activated sludge. *Progress in Energy and Combustion Science*, **34**(6), 755-781.

Arudchelvam, Y., Perinpanayagam, M., Nirmalakhandan, N. 2010. Predicting VFA formation by dark fermentation of particulate substrates. *Bioresource Technology*, **101**(19), 7492-7499.

Bary, A., Carpenter-Boggs, L., Cogger, C., Frear, C., Jobson, T., Kruger, C., Pressley, S. 2012. Meeting immediate organic management needs while building the foundation for future organics industry development Phase 1: Odor Sampling Study. Center for Sustaining Agriculture and Natural Resources, Washington State University.

Basu, P. 2010. *Biomass gasification and pyrolysis: practical design and theory*. Academic press.

Batstone, D., Keller, J., Angelidaki, I., Kalyuzhnyi, S., Pavlostathis, S.G., Rozzi, A., Sanders, W.T.M., Siegrist, H., Vavilin, V.A. 2002. *Anaerobic digestion model No.1 (ADM1)*. IWA Publishing, London, UK.

Batstone, D.J., Keller, J., Steyer, J.P. 2006a. A review of ADM1 extensions, applications, and analysis: 2002-2005. *Water Science & Technology*, **54**(4), 1-10.

Batstone, D.J., Keller, J., Steyer, J.P. 2006b. A review of ADM1 extensions, applications, and analysis: 2002-2005. *Water Science and Technology*, **54**(4), 1-10.

Bedminster. 2013. Edmonton Composting Facility. Dublin, Ireland. http://www.bedminster.com/downloads/Edmonton%20Composting%20Facility.pdf.
Ben-Ghedalia, D., Miron, J. 1981. The effect of combined chemical and enzyme treatments on the saccharification and in vitro digestion rate of wheat straw. *Biotechnology Bioengineering*, **23**(4), 823-831.
Bharadwaj, A., Baxter, L.L., Robinson, A.L. 2004. Effects of intraparticle heat and mass transfer on biomass devolatilization: experimental results and model predictions. *Energy & Fuels*, **18**(4), 1021-1031.
Bilbao, R., Millera, A., Murillo, M.B. 1993. Temperature profiles and weight loss in the thermal decomposition of large spherical wood particles. *Industrial & Engineering Chemistry Research*, **32**(9), 1811-1817.
Binder, A., Pelloni, L., Fiechter, A. 1980. Delignification of straw with ozone to enhance biodegradability. *Applied Microbiology and Biotechnology*, **11**(1), 1-5.
Bloom, J. 2010. *American wasteland:how America throws away nearly half of its food (and what we can do about it)*. De Capo Press, Cambridge, MA.
Blumensaat, F., Keller, J. 2005. Modelling of two-stage anaerobic digestion using the IWA Anaerobic Digestion Model No. 1 (ADM1). *Water Research*, **39**(1), 171-183.
Bougrier, C., Albasi, C., Delgenes, J., Carrere, H. 2006. Effect of ultrasonic, thermal and ozone pre-treatments on waste activated sludge solubilisation and anaerobic biodegradability. *Chemical Engineering and Processing: Process Intensification*, **45**(8), 711-718.
Bridgwater, A.V. 2012. Review of fast pyrolysis of biomass and product upgrading. *Biomass and Bioenergy*, **38**, 68-94.
Brinton, W.F. 2000. Compost quality standards and guidelines: an international view. New York State Association of Recyclers.
Brown, J., Brown, R. 2012. Process optimization of an auger pyrolyzer with heat carrier using response surface methodology. *Bioresource Technology*, **103**(1), 405-414.
Bryden, K.M., Hagge, M.J. 2003. Modeling the combined impact of moisture and char shrinkage on the pyrolysis of a biomass particle. *Fuel*, **82**(13), 1633-1644.
Bryden, K.M., Ragland, K.W., Rutland, C.J. 2002. Modeling thermally thick pyrolysis of wood. *Biomass and Bioenergy*, **22**(1), 41-53.
Buckner, S.C. 2002. Controlling odors during grass composting. *Biocycle*, **43**(9), 42-47.
Bule, M.V., Gao, A.H., Hiscox, B., Chen, S. 2013. Structural modification of lignin and characterization of pretreated wheat straw by ozonation. *Journal of Agricultural and Food Chemistry*, DOI: 10.1021/jf4001988.
Burr, H.K., Stamm, A.J. 1947. Diffusion in wood. *The Journal of Physical Chemistry*, **51**(1), 240-261.
Bush, R.A., Hall, K.M. 2006. Process for the production of ethanol from algae, Google Patents.
Card, T.R., Schmidt, C.E. 2008. Organic material composting and drying focusing on greenwaste compost air emissions data review. Air Pollution Control District, San Joaquin Valley.
Card, T.R., Schmidt, C.E. 2012. Controlling air emissions from composting facilities. Portland OR.
Carlsson, M., Lagerkvist, A., Morgan-Sagastume, F. 2012. The effects of substrate pre-treatment on anaerobic digestion systems: A review. *Waste Management*, **32**(9), 1634-1650.
Carucci, G., Carrasco, F., Trifoni, K., Majone, M., Beccari, M. 2005. Anaerobic digestion of food industry wastes: effect of codigestion on methane yield. *Journal of Environmental Engineering*, **131**(7), 1037-1045.

Chan, W.-C.R., Kelbon, M., Krieger, B.B. 1985. Modelling and experimental verification of physical and chemical processes during pyrolysis of a large biomass particle. *Fuel*, **64**(11), 1505-1513.

Chandra, R., Takeuchi, H., Hasegawa, T. 2012. Hydrothermal pretreatment of rice straw biomass: A potential and promising method for enhanced methane production. *Applied Energy*, **94**, 129-140.

Chang, V.S., Burr, B., Holtzapple, M.T. 1997. Lime pretreatment of switchgrass. *Applied Biochemistry and Biotechnology*, **63-5**, 3-19.

Chen, Y.-X., Huang, X.-D., Han, Z.-Y., Huang, X., Hu, B., Shi, D.-Z., Wu, W.-X. 2010. Effects of bamboo charcoal and bamboo vinegar on nitrogen conservation and heavy metals immobility during pig manure composting. *Chemosphere*, **78**(9), 1177-1181.

Chen, Z.B., Hu, D.X., Zhang, Z.P., Ren, N.Q., Zhu, H.B. 2009. Modeling of two-phase anaerobic process treating traditional Chinese medicine wastewater with the IWA Anaerobic Digestion Model No. 1. *Bioresource Technology*, **100**(20), 4623-4631.

Chiang, H.-L., Chiang, P., Huang, C. 2002. Ozonation of activated carbon and its effects on the adsorption of VOCs exemplified by methylethylketone and benzene. *Chemosphere*, **47**(3), 267-275.

Chidthaisong, A., Conrad, R. 2000. Specificity of chloroform, 2-bromoethanesulfonate and fluoroacetate to inhibit methanogenesis and other anaerobic processes in anoxic rice field soil. *Soil Biology & Biochemistry*, **32**(7), 977-988.

Chisti, Y. 2007. Biodiesel from microalgae. *Biotechnology Advances*, **25**(3), 294-306.

Christiansen, E. 2009. Best management practices for incorporation of food residuals into existing yard waste composting operations. U.S. Composting Council. Ronkonkama, NY.

Chudacek, M.W. 2002. Impeller power numbers and impeller flow numbers in profiled bottom tanks. *Industrial & Engineering Chemistry Process Design and Development*, **24**(3), 858–867.

Chynoweth, D.P., Isaacson, R. 1987. *Anaerobic Digestion of Biomass*. Elsevier Applied Science, London and New York.

Clough, T.J., Condron, L.M., Kammann, C., Müller, C. 2013. A review of bochar and soil nitrogen dynamics. *Agronomy*, **3**(2), 275-293.

Coker, C. 2012 Going on offense against odors III *Biocycle*, **53**(6), 25.

Coker, C., Gibson, T. 2013. Design considerations in aerated static pile composting. *Biocycle*, **54**(1), 30.

Çolakoglu, M.H. 2009. Determination of change in moisture ratios of some woods during air-rrying by finite element analysis. *Journal of Applied Sciences*, **9**(22), 4091-4094.

Cole, J., Chai, B., Farris, R., Wang, Q., Kulam, S., McGarrell, D., Garrity, G., Tiedje, J. 2005. The ribosomal database project (RDP-II): sequences and tools for high-throughput rRNA analysis. *Nucleic Acids Research*, **33**(suppl 1), D294-D296.

Conte, P., Marsala, V., De Pasquale, C., Bubici, S., Valagussa, M., Pozzi, A., Alonzo, G. 2012. Nature of water-biochar interface interactions. *GCB Bioenergy*.

Coppedge, B., Coppedge, G., Evans, D., Jensen, J., Kanoa, E., Scanlan, K., Scanlan, B., Weisberg, P., Frear, C. 2012. Renewable natural gas and nutrient recovery feasibility for deruyter: an anaerobic digester case study for alternative offtake markters and remediation of nutrient loading concerns within the region. Washington State Department of Commerce. Olympia, WA.

Dailliez, L. 1981. *Les templiers et l'agriculture ou Les composts templiers*. Alpes Méditerranée-Edition Impres' Sud.
de Hullu, J., Massen, J.I.W., van Meel, P.A., Shazad, S., Vaessen, J.M.P. 2008. Comparing different biogas upgrading techniques. Eindhoven University of Technology.
De Schamphelaire, L., Verstraete, W. 2009. Revival of the biological sunlight-to-biogas energy conversion system. *Biotechnology and Bioengineering*, **103**(2), 296-304.
DeBusk, J.A. 2007. Conservation of nitrogen via nitrification and nhemical phosphorus removal for liquid dairy Manure. in: *Biological Systems Engineering*, Virginia Polytechnic Institute and State University. Blacksburg.
Di Blasi, C. 1993. Analysis of convection and secondary reaction effects within porous solid fuels undergoing pyrolysis. *Combustion Science and Technology*, **90**(5-6), 315-340.
Di Blasi, C. 1996. Heat, momentum and mass transport through a shrinking biomass particle exposed to thermal radiation. *Chemical Engineering Science*, **51**(7), 1121-1132.
Di Blasi, C. 2000. The state of the art of transport models for charring solid degradation. *Polymer International*, **49**(10), 1133-1146.
Di Blasi, C. 2008. Modeling chemical and physical processes of wood and biomass pyrolysis. *Progress in Energy and Combustion Science*, **34**(1), 47-90.
Di Blasi, C., Branca, C. 2001. Kinetics of primary product formation from wood pyrolysis. *Industrial & Engineering Chemistry Research*, **40**(23), 5547-5556.
Di Blasi, C., Branca, C. 2003. Temperatures of wood particles in a hot sand bed fluidized by nitrogen. *Energy & fuels*, **17**(1), 247-254.
Dias, B.O., Silva, C.A., Higashikawa, F.S., Roig, A., Sánchez-Monedero, M.A. 2010. Use of biochar as bulking agent for the composting of poultry manure: Effect on organic matter degradation and humification. *Bioresource Technology*, **101**(4), 1239-1246.
Diaz, L.F. 2007. Compost science and technology. Elsevier. Amsterdam; Boston, 9780080545981 008054598X. http://public.eblib.com/EBLPublic/PublicView.do?ptiID=299421.
Dinjus, E., Dahmen, P.D.N. 2010. The bioliq process. *MTZ worldwide*, **71**(12), 4-8.
Dishisha, T., Alvarez, M.T., Hatti-Kaul, R. 2012. Batch- and continuous propionic acid production from glycerol using free and immobilized cells of Propionibacterium acidipropionici. *Bioresource Technology*, **118**, 553-562.
Dohányos, M., Kosová, B., Zábranská, J., Grau, P. 1985. Production and utilization of volatile fatty acids in various types of anaerobic reactors. *Water Science & Technology*, **17**(1), 191–205.
Dong, F., Zhao, Q.B., Li, W.W., Sheng, G.P., Zhao, J.B., Tang, Y., Yu, H.Q., Kubota, K., Li, Y.Y., Harada, H. 2011. Novel online monitoring and alert system for anaerobic digestion reactors. *Environmental Science & Technology*, **45**(20), 9093-9100.
Dougherty, M. 1999. *Field guide to on-farm composting*. Natural Resource, Agriculture, and Engineering Service, Cooperative Extension, Ithaca, N.Y.
Eaton, A.D., Franson, M.A.H., American Public Health, A., American Water Works, A., Water Environment, F. 2005. *Standard methods for the examination of water & wastewater*. American Public Health Association.
Ecology. 2010. Solid waste in washington state. Washington State Department of Ecology: http://www.ecy.wa.gov/biblio/1007031.html. March, 8. 2011.
Ecology, W.S.D.o. 2011. Solid waste in washington state: 20th annual status report. Washington State Department of Ecology. Olympia, WA.

ECOregon. 2009. Dairy manure anaerobic digester feasibility study report. ECOregon. Eugene.
Eitelberger, J. 2010. *Modelling of transport processes in wood: development and validation of a multiscale homogenization model for transport properties of softwood*. Saarbrücken: VDM Verlag Dr. Müller Aktiengesellschaft & Co.
Eklind, Y., Sundberg, C., Smårs, S., Steger, K., Sundh, I., Kirchmann, H., Jönsson, H. 2007. Carbon turnover and ammonia emissions during composting of biowaste at different temperatures. *Journal of Environmental Quality*, **36**(5), 1512-1520.
El-Mashad, H.M., van Loon, W.K.P., Zeeman, G., Bot, G.P.A. 2005. Rheological properties of dairy cattle manure. *Bioresource Technology*, **96**(5), 531-535.
EPA. 1994. Composting of yard trimmings and municipal solid waste. U.S. Environmental Protection Agency, Office of Solid Waste and Emergency Response. [Washington, D.C.].
EPA. 2008. Municipal solid waste in the united states: 2007 facts and figures. Office of Solid Waste and Emergency Response, Washington DC.
EPA. 2010. Municipal solid waste generation, recycling, and disposal in the united states: facts and figures for 2010. Washington, DC.
EPA. 2011a. Reducing greenhouse gas emissions through recycling and composting: A report by the Materials Management Workgroup of the West Coast Climate and Materials Management Forum. US EPA. Seattle, WA.
EPA. 2011b. Wastes - non-hazardous waste - municipal solid waste. http://www.epa.gov/wastes/nonhaz/municipal/.
EPA. 2013a. Municipal solid waste generation, recycling, and disposal in the United States: Facts and figures for 2011. http://www.epa.gov/osw/nonhaz/municipal/pubs/MSWcharacterization_508_053113_fs.pdf.
EPA. 2013b. Relation between nitrate in water wells and potential sources in the lower yakima valley, washington. EPA. Yakima, WA.
Epstein, E. 1997. *The Science of Composting*. Technomic Publishing Company, Lancaster, Pennsylvania, USA.
Ewing, T., Frear, C. 2012. Developing and commercializing high solids anaerobic digesters for converting municipal wastes to fuel and fertilizer. Report to Washington State Department of Ecology. Olympia Washington.
Fitzpatrick, G., Worden, E., Wagner, V. 2005. Historical development of composting technology during the 20th century.
Fotsing, J., Tchagang, C. 2005. Experimental determination of the diffusion coefficients of wood in isothermal conditions. *Heat Mass Transfer Heat and Mass Transfer*, **41**(11), 977-980.
Frear, C. 2009. Anaerobic digestion strategies for dairy manures. in: *Biological Systems Engineering*, Vol. Doctor of Philosophy Washington State University. Pullman, pp. 143.
Frear, C., Dvorak, S. 2010. Commercial demonstration of nutrient recovery of ammonium sulfate and phosphorus rich fines from AD effluent Washington State University. Pullman.
Frear, C., Ewing, T., Chen, S., Liao, W. 2011. Evaluation of Co-Digestion at a Commercial Dairy Anaerobic Digester. *Clean Soil Air Water Clean - Soil, Air, Water*, **39**(7), 697-704.
Frear, C., Shulin, C., Dvorak, S., Loo, B.V. 2010. An integrated nutrient recovery, class-A fiber production process, and H_2S scrubbing system that works in series with dairy manure anaerobic digesters - farm-scale demonstration at two washington state dairies with digesters. Washington State University. Pullman, WA.

Frigon, J.C., Mehta, P., Guiot, S.R. 2012. Impact of mechanical, chemical and enzymatic pre-treatments on the methane yield from the anaerobic digestion of switchgrass. *Biomass & Bioenergy*, **36**, 1-11.
Fu, Z., Holtzapple, M.T. 2010a. Anaerobic mixed-culture fermentation of aqueous ammonia-treated sugarcane bagasse in consolidated bioprocessing. *Biotechnology Bioengineering*, 216-227.
Fu, Z., Holtzapple, M.T. 2010b. Consolidated bioprocessing of sugarcane bagasse and chicken manure to ammonium carboxylates by a mixed culture of marine microorganisms. *Bioresource Technology*, **101**(8), 2825-2836.
Fu, Z., Holtzapple, M.T. 2011. Anaerobic thermophilic fermentation for carboxylic acid production from in-storage air-lime-treated sugarcane bagasse. *Applied Microbiology and Biotechnology*, 1669-1679.
Gali, A., Benabdallah, T., Astals, S., Mata-Alvarez, J. 2009. Modified version of ADM1 model for agro-waste application. *Bioresource Technology*, **100**(11), 2783-2790.
Gao, A.H., Bule, M.V., Laskar, D.D., Chen, S.L. 2012. Structural and thermal characterization of wheat straw pretreated with aqueous ammonia soaking. *Journal of Agricultural and Food Chemistry*, **60**(35), 8632-8639.
Garcia-Cubero, M.A., Gonzalez-Benito, G., Indacoechea, I., Coca, M., Bolado, S. 2009. Effect of ozonolysis pretreatment on enzymatic digestibility of wheat and rye straw. *Bioresource Technology*, **100**(4), 1608-13.
Garcia-Perez, M. 2011. *Process modeling and simulation, in Lectures*. Washington State University, Pullman, WA.
Ghirardi, M.L., Zhang, L., Lee, J.W., Flynn, T., Seibert, M., Greenbaum, E., Melis, A. 2000. Microalgae: a green source of renewable H_2. *Trends in Biotechnology*, **18**(12), 506-511.
Goldstein, N. 2002. Getting to know the odor compounds. *Biocycle*, **43**(7), 42-44.
Goldstein, N. 2012. Building solutions for somposting, anaerobic digestion. *Biocycle*, **53**(6), 30.
Gotaas, H.B. 1956. *Composting. sanitary Disposal and Reclamation of Organic Wastes*. World Health Organization, Geneva.
Gouleke, W., Oswald, J., Gotaas, H.B. 1954. Anaerobic digestion of algae. *Applied Microbiology*, **5**, 47-55.
Granatstein, D., Kruger, C., Collins, H., Galinato, S., Garcia-Perez, M., Yoder, J. 2009. Use of biochar from the pyrolysis of waste organic material as a soil amendment. Final project report. *Center for Sustaining Agriculture and Natural Resources, Washington State University, Wenatchee, WA*.
Grønli, M.G. 1996. A theoretical and experimental study of the thermal degradation of biomass, Norwegian University of Science and Technology.
Haas, T.J., Nimlos, M.R., Donohoe, B.S. 2009. Real-time and post-reaction microscopic structural analysis of biomass undergoing pyrolysis. *Energy & fuels*, **23**(7), 3810-3817.
Ham, R.K., Komilis, D. 2003. A Laboratory Study to Investigate Gaseous Emissions and Solids Decomposition During Composting of Municipal Solid Wastes. US Environmental Protection Agency, National Risk Management Research Laboratory.
Harun, R., Singh, M., Forde, G.M., Danquah, M.K. 2010. Bioprocess engineering of microalgae to produce a variety of consumer products. *Renewable and Sustainable Energy Reviews*, **14**(3), 1037-1047.
Haug, R.T. 1993. *The practical handbook of compost engineering*. Lewis Publishers, Boca Raton.

He, Y.F., Pang, Y.Z., Li, X.J., Liu, Y.P., Li, R.P., Zheng, M.X. 2009. Investigation on the changes of main compositions and extractives of rice straw pretreated with sodium hydroxide for biogas production. *Energy & Fuels*, **23**, 2220-2224.

Heffter, E. 2013. Cedar grove composting faces two new suits over 'sickening odor'. in: *The Seattle Times*. Seattle, WA.

Hess, M., Sczyrba, A., Egan, R., Kim, T.W., Chokhawala, H., Schroth, G., Luo, S., Clark, D.S., Chen, F., Zhang, T. 2011. Metagenomic discovery of biomass-degrading genes and genomes from cow rumen. *Science*, **331**(6016), 463.

Hobson, P.N. 1987. A model of some aspects of microbial-degradation of particulate substrates. *Journal of Fermentation Technology*, **65**(4), 431-439.

Hoffmann, R.A., Garcia, M.L., Veskivar, M., Karim, K., Al-Dahhan, M.H., Angenent, L.T. 2008. Effect of shear on performance and microbial ecology of continuously stirred anaerobic digesters treating animal manure. *Biotechnology and Bioengineering*, **100**(1), 38-48.

Holtzapple, M.T., Davison, R.R., Ross, M.K., Aldrett-Lee, S., Nagwani, M., Lee, C.M., Lee, C., Adelson, S., Kaar, W., Gaskin, D. 1999. Biomass conversion to mixed alcohol fuels using the MixAlco process. *Applied Biochemistry and Biotechnology*, **79**(1), 609-631.

Holtzapple, M.T., Granda, C.B. 2009. Carboxylate platform: the MixAlco process part 1: comparison of three biomass conversion platforms. *Applied Biochemical Biotechnology*, **156**(1-3), 95-106.

Howard, A., Wad, Y.D. 1931. The waste products of agriculture : their utilization as humus. *Journal of Royal Society of Arts*.

Hua, L., Wu, W., Liu, Y., McBride, M.B., Chen, Y. 2009. Reduction of nitrogen loss and Cu and Zn mobility during sludge composting with bamboo charcoal amendment. *Environmental Science and Pollution Research*, **16**(1), 1-9.

Hunt, J.F., Gu, H., Lebow, P.K. 2008. Theoretical thermal conductivity equation for uniform density wood cells. *Wood and Fiber Science*, **40**(2), 167-180.

Inanc, B., Matsui, S., Ide, S. 1999. Propionic acid accumulation in anaerobic digestion of carbohydrates: An investigation on the role of hydrogen gas. *Water Science and Technology*, **40**(1), 93-100.

Incropera, F.P., Dewitt, D.P. 2007. *Fundamentals of heat and mass transfer*. Wiley: Asia.

Insam, H., de Bertoldi, M. 2007. Chapter 3: Microbiology of the composting process. in: *Waste Management Series*, (Eds.) L.F. Diaz, M.d. Bertoldi, W. Bidlingmaier, E. Stentiford, Elsevier, pp. 25-48.

IWMB. 2009. Food waste composting regulations white paper. California Integrated Waste Management Board. Sacramento, CA.

Janse, A.M.C., Westerhout, R.W.J., Prins, W. 2000. Modelling of flash pyrolysis of a single wood particle. *Chemical Engineering and Processing*, **39**(3), 239-252.

Jiang, A., Zhang, T., Frear, C., Chen, S. 2011. Combined nutrient recovery and biogas scrubbing system integrated in series with animal manure anaerobic digester, Vol. 7909995, Washington State University Research Foundation. USA.

Jindo, K., Suto, K., Matsumoto, K., García, C., Sonoki, T., Sanchez-Monedero, M.A. 2012. Chemical and biochemical characterisation of biochar-blended composts prepared from poultry manure. *Bioresource Technology*, **110**, 396-404.

Johnson, L.A., Soltis, D.E. 1994. matK DNA sequences and phylogenetic reconstruction in Saxifragaceae s. str. *Systematic Botany*, 143-156.

Kang, W., Kang, C.-W., Chung, W., Eom, C.-D., Yeo, H. 2008. The effect of openings on combined bound water and water vapor diffusion in wood. *Journal of Wood Science*, **54**(5), 343-348.

Karama, A.B., Onyejekwe, O.O., Brouckaert, C.J., Buckley, C.A. 1999. The use of Computational Fluid Dynamics (CFD). Technique for evaluating the efficiency of an activated sludge reactor. *Water Science and Technology*, **39**(10-11), 329-332.

Katehis, D., Diyamandoglu, V., Fillos, J. 1998. Stripping and recovery of ammonia from centrate of anaerobically digested biosolids at elevated temperatures. *Water Environment Research*, **70**(2), 231-240.

Kennedy, N. 2012. Biogas Purification: A Novel Technique Using Pretreated Digester Effluent. in: *Biological Systems Engineering*, Vol. Master of Science, Washington State University. Pullman.

Kent, A.D., Smith, D.J., Benson, B.J., Triplett, E.W. 2003. Web-based phylogenetic assignment tool for analysis of terminal restriction fragment length polymorphism profiles of microbial communities. *Applied and Environmental Microbiology*, **69**(11), 6768-6776.

Kersten, S.R.A., Wang, X., Prins, W., van Swaaij, W.P.M. 2005. Biomass pyrolysis in a fluidized bed reactor. part 1: literature review and model smulations. *Industrial & Engineering Chemistry Research*, **44**(23), 8773-8785.

Kettunen, P.O. 2006. *Wood structure and properties*. Trans Tech Publications Ltd., Uetikon-Zuerich; Enfield, N.H.

Koutrouli, E.C., Kalfas, H., Gavala, H.N., Skiadas, I.V., Stamatelatou, K., Lyberatos, G. 2009. Hydrogen and methane production through two-stage mesophilic anaerobic digestion of olive pulp. *Bioresource Technology*, **100**(15), 3718-3723.

Krich, K., Augenstein, D., Batmale, J., Benemann, J., Rutledge, B., Salour, D. 2005. Biomethane from dairy waste: a sourcebook for the production and use of renewable natural gas in california

Kumar, S. 2011. Composting of municipal solid waste. *Critical Reviews in Biotechnology*, **31**(2), 112-136.

Labatut, R.A., Gooch, C.A. 2012. Monitoring anaerobic digestion process to optimize performance and minimize system failure. Cornell University. Ithaca, NY.

Lakaniemi, A.M., Hulatt, C.J., Thomas, D.N., Tuovinen, O.H., Puhakka, J.A. 2011. Biogenic hydrogen and methane production from Chlorella vulgaris and Dunaliella tertiolecta biomass. *Biotechnology Biofuels*, **4**(1), 34.

Landry, H., Lague, C., Roberge, M. 2004. Physical and rheological properties of manure products. *Applied Engineering in Agriculture*, **20**(3), 277-288.

Lehmann, J. 2007. Bio-energy in the black. *Frontiers in Ecology and the Environment*, **5**(7), 381-387.

Lehmann, J., Gaunt, J., Rondon, M. 2006. Bio-char sequestration in terrestrial ecosystems–a review. *Mitigation and adaptation strategies for global change*, **11**(2), 395-419.

Lehmann, J., Rillig, M.C., Thies, J., Masiello, C.A., Hockaday, W.C., Crowley, D. 2011. Biochar effects on soil biota–a review. *Soil Biology and Biochemistry*, **43**(9), 1812-1836.

Lehmann, J.J.S. 2009. Biochar for environmental management science and technology. Earthscan. London; Sterling, VA, 9781849770552 1849770557. http://public.eblib.com/EBLPublic/PublicView.do?ptiID=476570.

Li, J., Ge, W., Wang, W., Yang, N., Liu, X., Wang, L., He, X., Wang, X., Wang, J., Kwauk, M. 2013. Academic applications of EMMS drag. in: *From Multiscale Modeling to Meso-Science*, Springer Berlin Heidelberg, pp. 359-375.

Liaw, S.-S., Wang, Z., Ndegwa, P., Frear, C., Ha, S., Li, C.-Z., Garcia-Perez, M. 2012. Effect of pyrolysis temperature on the yield and properties of bio-oils obtained from the auger pyrolysis of Douglas Fir wood. *Journal of Analytical and Applied Pyrolysis*, **93**, 52-62.

Lidholm, O., Ossiansson, E. 2008. Modeling anaerobic digestion - validation and calibration of the siegrist model with uncertainty and sensitivity analysis. in: *Water and Environmental Engineering, Department of Chemical Engineering*, Vol. Master, Lunds University. Lund, Sweden, pp. 116.

Liu, Y., Xu, H.-L., Show, K.-Y., Tay, J.-H. 2002. Anaerobic granulation technology for wastewater treatment. *World Journal of Microbiology and Biotechnology*, **18**(2), 99-113.

Lowe, E.D., Buckmaster, D.R. 1995. Dewatering makes a big difference in compost strategies. snack food facility in pennsylvania shows how to make a policy of "reduce, recycle and reuse" economically sound by composting dewatered residuals. *BioCycle*, **36**(1), 78.

Lu, S., Bai, S., Zhu, L., Shan, H. 2009. Removal mechanism of phosphate from aqueous solution by fly ash. *Journal of Hazardous Materials*, **161**(1), 95-101.

Lubken, M., Gehring, T., Wichern, M. 2010. Microbiological fermentation of lignocellulosic biomass: current state and prospects of mathematical modeling. *Applied Microbiology and Biotechnology*, **85**(6), 1643-1652.

Luo, J.Y., Issa, R.I., Gosman, A.D. 1994. Prediction of impeller-induced flows in mixing vessels using multiple frames of reference. in: *Institution of Chemical Engineers Symposium Series*, Vol. 136, pp. 549-556.

Ma, J., Frear, C., Wang, Z.-w., Yu, L., Zhao, Q., Li, X., Chen, S. 2013a. A simple methodology for rate-limiting step determination for anaerobic digestion of complex substrates and effect of microbial community ratio. *Bioresource Technology*, **134**(0), 391-395.

Ma, J., Kennedy, N., Zhao, Q., Yorgey, G., Frear, C. 2013b. Review of emerging nutrient recovery technologies for farm-based anaerobic digesters and other renewable energy systems Washington State University. Pullman, WA.

Ma, J., Wilson, K., Zhao, Q., Yorgey, G., Frear, C. 2013c. Odor in compost: Literature review and critical analysis. Washington State Department of Ecology. Olympia, WA, 13-07-066.

Mairet, F., Bernard, O., Cameron, E., Ras, M., Lardon, L., Steyer, J.P., Chachuat, B. 2011a. Three-reaction model for the anaerobic digestion of microalgae. *Biotechnology Bioengineering*.

Mairet, F., Bernard, O., Ras, M., Lardon, L., Steyer, J.P. 2011b. Modeling anaerobic digestion of microalgae using ADM1. *Bioresource Technology*, **102**(13), 6823-9.

Marchaim, U., Krause, C. 1993. Propionic to acetic acid ratios in overloaded anaerobic digestion. *Bioresource Technology*, **43**(3), 195-203.

Martin, J. 2004. A comparision of dairy cattle manure management with and without anaerobic digestion and biogas utilization. Eastern Research Group, Inc. Boston, MA.

Martin, J., Roos, K. 2007. Comparison of the performance of a conventional and a modified plug-flow digester for scraped dairy manure. *International Symposium on Air Quality and Waste Management for Agriculture. CD-Rom Proceedings of the 16-19 September 2007 Conference (Broomfield, Colorado), ASABE Publication*.

Martin, J.H. 2005. An evaluation of a Mesophilic, modified plug flow anaerobic digester for dairy cattle manure. *Eastern Research Group, Inc. EPA Contract No. GS 10F-0036K Work Assignment/Task Order*(9).

McGinn, P.J., Dickinson, K.E., Bhatti, S., Frigon, J.C., Guiot, S.R., O'Leary, S.J. 2011. Integration of microalgae cultivation with industrial waste remediation for biofuel and bioenergy production: opportunities and limitations. *Photosynthesis Research*, **109**(1-3), 231-47.

Melis, A., Happe, T. 2001. Hydrogen production. Green algae as a source of energy. *Plant physiology*, **127**(3), 740-748.

Metzner, A.B., Otto, R.E. 1957. Agitation of non-newtonian fluids. *AIChE Journal*, **3**(1), 3-10.

Metzner, A.B., Reed, J.C. 1955. Flow of non-Newtonian fluids-correlation of laminar, transition and turbulent-flow regions. *AIChE Journal*, **1**, 434–440.

Miller, F.C. 1993. Minimizing odor generation. in: *Science and Engineering of Composting*, (Eds.) H.A.J. Hoitink, H.M. Keener, Ohio State University. OH.

Mishnaevsky Jr, L., Qing, H. 2008. Micromechanical modelling of mechanical behaviour and strength of wood: State-of-the-art review. *Computational Materials Science*, **44**(2), 363-370.

Misra, R.V., Roy, R.N., Hiraoka, H. 2003. On farm composting methods. rome: food and agruculture organization of the united nations.

Molina, F., Garcia, C., Roca, E., Lema, J.M. 2008. Characterization of anaerobic granular sludge developed in UASB reactors that treat ethanol, carbohydrates and hydrolyzed protein based wastewaters. *Water Science and Technology*, **57**(6), 837-842.

Montiel-Escobar, J.L., Alcaraz-Gonzalez, V., Mendez-Acosta, H.O., Gonzalez-Alvarez, V. 2012. ADM1-based robust interval observer for anaerobic digestion processes. *Clean-Soil Air Water*, **40**(9), 933-940.

Morales-Barrera, L., Cristiani-Urbina, E. 2006. Removal of hexavalent chromium by Trichoderma viride in an airlift bioreactor. *Enzyme and Microbial Technology*, **40**(1), 107-113.

Mussgnug, J.H., Klassen, V., Schlüter, A., Kruse, O. 2010. Microalgae as substrates for fermentative biogas production in a combined biorefinery concept. *Journal of Biotechnology*, **150**(1), 51-56.

NA. 2006. Fluent 6.3 User's Guide, Fluent, Inc. . Lebanon, NH.

Namasivayam, C., Sangeetha, D. 2004. Equilibrium and kinetic studies of adsorption of phosphate onto $ZnCl_2$ activated coir pith carbon. *Journal of Colloid and Interface Science*, **280**(2), 359-365.

Noike, T., Endo, G., Chang, J.E., Yaguchi, J.I., Matsumoto, J.I. 1985. Characteristics of carbohydrate degradation and the rate-limiting step in anaerobic digestion. *Biotechnology and Bioengineering*, **27**(10), 1482-1489.

NREL. 2009. What is a Biorefinery?, http://www.nrel.gov/biomass/biorefinery.html. Sept 20. 2013.

O'Fallon, J., Busboom, J., Nelson, M., Gaskins, C. 2007. A direct method for fatty acid methyl ester (FAME) synthesis: Application to wet meat tissues, oils and feedstuffs. *Journal of Animal Science*, jas. 2006-491v1.

Oguz, E. 2005. Sorption of phosphate from solid/liquid interface by fly ash. *Colloids and Surfaces A: Physicochemical and Engineering Aspects*, **262**(1), 113-117.

Ohara, H. 2003. Biorefinery. *Applied Microbiology & Biotechnology*, **62**(5/6), 474-477.

Oswald, W.J., Golueke, C.G. 1960. Biological transformation of solar energy. *Advances in Applied Microbiology*, **2**, 223-262.
Padmasiri, S.I., Zhang, J.Z., Fitch, M., Norddahl, B., Morgenroth, E., Raskin, L. 2007. Methanogenic population dynamics and performance of an anaerobic membrane bioreactor (AnMBR) treating swine manure under high shear conditions. *Water Research*, **41**(1), 134-144.
Pagans, E., Font, X., Sanchez, A. 2007. Coupling composting and biofiltration for ammonia and volatile organic compound removal. *Biosystems Engineering*, **97**(4), 491-500.
Park, S.-J., Jin, S.-Y. 2005. Effect of ozone treatment on ammonia removal of activated carbons. *Journal of Colloid and Interface Science*, **286**(1), 417-419.
Parkin, G.F., Owen, W.F. 1986. Fundamental of anaerobic-digestion of wastewater sludge. *Journal of Environmental Engineering*(112), 867-920.
Patwardhan, A.W. 2001. Prediction of flow characteristics and energy balance for a variety of downflow impellers. *Industrial & Engineering Chemistry Research*, **40**(17), 3806-3816.
Paul, E.L., Atiemo-Obeng, V.A., Kresta, S.M. 2004. Handbook of industrial mixing, John Wiley & Sons. New Jersey.
Pavlostathis, S.G., Giraldogomez, E. 1991. Kinetics of anaerobic treatment - A critical-review. *Critical Reviews in Environmental Control*, **21**(5-6), 411-490.
Pella, E. 1990. Elemental organic analysis. Part 2. State of the art. *Am. Lab*, **22**(12), 28-32.
Pougatch, K., Salcudean, M., Gartshore, I., Pagoria, P. 2007. Computational modelling of large aerated lagoon hydraulics. *Water Research*, **41**(10), 2109-2116.
Profita, C. 2013. Washington county cuts food waste at compost facility. in: *Oregon Public Broadcasting*. Oregon.
Prost, K., Borchard, N., Siemens, J., Kautz, T., Séquaris, J.-M., Möller, A., Amelung, W. 2013. Biochar affected by composting with farmyard manure. *Journal of Environmental Quality*, **42**(1), 164-172.
Pyle, D., Zaror, C. 1984. Heat transfer and kinetics in the low temperature pyrolysis of solids. *Chemical Engineering Science*, **39**(1), 147-158.
Reeves, T.G. 1972. Nitrogen Removal: A Literature Review. *Water Pollution Control Federation*, **44**(10), 1895-1908.
Reichert, P. 1998. *AQUASIM 2.0: computer program for the identification and simulation of aquatic systems*. Swiss Federal Institute for Environmental Science and Technology (EAWAG), Switzerland.
Renkow, M., Rubin, A.R. 1998. Does municipal solid waste composting make economic sense? *Journal of Environmental Management*, **53**(4), 339-47.
Riebesell, U., Wolf-Gladrow, D., Smetacek, V. 1993. Carbon dioxide limitation of marine phytoplankton growth rates.
Ripley, L.E., Boyle, W.C., Converse, J.C. 1986. Improved Alkalimetric Monitoring for Anaerobic Digestion of High-Strength Wastes. *Water Pollution Control Federation*, **58**(5), 406-411.
Roos, K. 2008. An evaluation of a covered anaerobic lagoon for flushed dairy cattle manure stabilization and biogas production, EPA.
Rosen, C., Jeppsson, U. 2006. Aspects on ADM1 Implementation within the BSM2 framework,Technical Report. Department of Industrial Electrical Engineering and Automation, Lund University. Lund, Sweden.

Rughoonundun, H., Granda, C., Mohee, R., Holtzapple, M.T. 2010. Effect of thermochemical pretreatment on sewage sludge and its impact on carboxylic acids production. *Waste Management*, **30**(8-9), 1614-21.
Rumburg, B., Neger, M., H. Mount, G., Yonge, D., Filipy, J., Swain, J., Kincaid, R., Johnson, K. 2004. Liquid and atmospheric ammonia concentrations from a dairy lagoon during an aeration experiment. *Atmospheric Environment*, **38**(10), 1523-1533.
Ryckebosch, E., Drouillon, M., Vervaeren, H. 2011. Techniques for transformation of biogas to biomethane. *Biomass and Bioenergy*, **35**(5), 1633-1645.
Sadhukhan, A.K., Gupta, P., Saha, R.K. 2009. Modelling of pyrolysis of large wood particles. *Bioresource Technology*, **100**(12), 3134-3139.
Samson, R., Leduyt, A. 1982. Biogas production from anaerobic digestion of Spirulina maxima algal biomass. *Biotechnology Bioengineering*, **24**(8), 1919-24.
Samson, R., LeDuyt, A. 1986. Detailed study of anaerobic digestion of Spirulina maxima algal biomass. *Biotechnology Bioengineering*, **28**(7), 1014-23.
Saravanan, V., Sreekrishnan, T.R. 2006. Modelling anaerobic biofilm reactors - A review. *Journal of Environmental Management*, **81**(1), 1-18.
Schaub, S.M., Leonard, J.J. 1996. Composting: An alternative waste management option for food processing industries. *Trends in Food Science & Technology*, **7**(8), 263-268.
Schmidt, J.E., Ahring, B.K. 1996. Granular sludge formation in upflow anaerobic sledge blanket (UASB) reactors. *Biotechnology and Bioengineering*, **49**(3), 229-246.
Scott, S.A., Davey, M.P., Dennis, J.S., Horst, I., Howe, C.J., Lea-Smith, D.J., Smith, A.G. 2010. Biodiesel from algae: challenges and prospects. *Current Opinion in Biotechnology*, **21**(3), 277-286.
Seghezzo, L., Zeeman, G., van Lier, J.B., Hamelers, H.V.M., Lettinga, G. 1998. A review: The anaerobic treatment of sewage in UASB and EGSB reactors. *Bioresource Technology*, **65**(3), 175-190.
Shafizadeh, F., Chin, P.P. 1977. Thermal deterioration of wood. *ACS Symposium Series*. ACS Publications. pp. 57-81.
Sheehan, J.T., Dunahay, J., Benemann, J.R., Roessler, P.G. 1998. *A look back at the US Department of Energy's Aquatic Species Program: Biodiesel from algae*. National Renewable Energy Laboratory Golden, CO.
Shen, D., Gu, S. 2009. The mechanism for thermal decomposition of cellulose and its main products. *Bioresource Technology*, **100**(24), 6496-6504.
Shilton, A., Kreegher, S., Grigg, N. 2008. Comparison of computation fluid dynamics simulation against tracer data from a scale model and full-sized waste stabilization pond. *Journal of Environmental Engineering-Asce*, **134**(10), 845-850.
Shyu, C., Soule, T., Bent, S.J., Foster, J.A., Forney, L.J. 2007. MiCA: a web-based tool for the analysis of microbial communities based on terminal-restriction fragment length polymorphisms of 16S and 18S rRNA genes. *Microbial Ecology*, **53**(4), 562-570.
Sialve, B., Bernet, N., Bernard, O. 2009. Anaerobic digestion of microalgae as a necessary step to make microalgal biodiesel sustainable. *Biotechnology Advances*, **27**(4), 409-416.
Siau, J. 1987. An investigation of the external and internal resistance to moisture diffusion in wood. *Wood Science and Technology*, **21**(3), 249-256.
Siau, J.F. 1984. Transport processes in wood. *Transport Processes in wood.*

Sluiter, A., Hames, B., Ruiz, R., Scarlata, C., Sluiter, J., Templeton, D., Crocker, D. 2008. Determination of structural carbohydrates and lignin in biomass. Nartional Renewable Energy Laboratory.

Sluiter, A., Ruiz, R., Scarlata, C., Sluiter, J., Templeton, D. 2005. Determination of extractives in biomass. Nartional Renewable Energy Laboratory.

Sonakya, V., Raizada, N., Hausner, M., Wilderer, P.A. 2007. Microbial populations associated with fixed- and floating-bed reactors during a two-stage anaerobic process. *International Microbiology*, **10**(4), 245-251.

Spokas, K.A., Novak, J.M., Venterea, R.T. 2012. Biochar's role as an alternative N-fertilizer: ammonia capture. *Plant and soil*, **350**(1-2), 35-42.

Steiner, C., Das, K., Melear, N., Lakly, D. 2010. Reducing nitrogen loss during poultry litter composting using biochar. *Journal of Environmental Quality*, **39**(4), 1236-1242.

Steiner, C., Melear, N., Harris, K., Das, K. 2011. Biochar as bulking agent for poultry litter composting. *Carbon Management*, **2**(3), 227-230.

Sun, Y., Cheng, J. 2002. Hydrolysis of lignocellulosic materials for ethanol production: a review. *Bioresource technology*, **83**(1), 1-11.

Sundberg, C., Franke-Whittle, I.H., Kauppi, S., Yu, D., Romantschuk, M., Insam, H., Jönsson, H. 2011. Characterisation of source-separated household waste intended for composting. *Bioresource Technology*, **102**(3), 2859-2867.

Sundberg, C.S.S.J.H. 2004. Low pH as an inhibiting factor in the transition from mesophilic to thermophilic phase in composting. *Bioresource Technology*, **95**(2).

Tanaka, S., Yoshizawa, S., Ohata, M., Mineki, S., Goto, S., Fujioka, K., Kokubun, T. 2006. Morphological change of microbial community structure during composting rice bran with charcoal. *Transactions-Materials Research Society of Japan*, **31**(4), 981.

Tarmian, A., Azadfallah, M., Gholamiyan, H., Shahverdi, M. 2011. Inter-tracheid and cross-field pitting in compression wood and opposite wood of norway spruce (picea abies l.). *Notulae Scientia Biologicae*, **3**(2).

Taylor, D. 1999. Talking trash: the economic and environmental issues of landfills. *Environmental Health Perspectives*, **107**(8), 404-9.

Terashima, M., Goel, R., Komatsu, K., Yasui, H., Takahashi, H., Li, Y.Y., Noike, T. 2009. CFD simulation of mixing in anaerobic digesters. *Bioresource Technology*, **100**(7), 2228-2233.

TetraTech. 2002. Commercial food waste composting study project report. Oregon Department of Environmental Quality Land Quality Division, Solid Waste Program. Seattle, WA.

Thamsiriroj, T., Murphy, J.D. 2011. Modelling mono-digestion of grass silage in a 2-stage CSTR anaerobic digester using ADM1. *Bioresource Technology*, **102**(2), 948-959.

Thunman, H., Leckner, B. 2002. Thermal conductivity of wood—models for different stages of combustion. *Biomass and Bioenergy*, **23**(1), 47-54.

Thurner, F., Mann, U. 1981. Kinetic investigation of wood pyrolysis. *Industrial & Engineering Chemistry Process Design and Development*, **20**(3), 482-488.

Tomei, M.C., Braguglia, C.M., Cento, G., Mininni, G. 2009. Modeling of anaerobic digestion of sludge. *Critical Reviews in Environmental Science and Technology*, **39**(12), 1003-1051.

Tu, Q., Wu, W., Lu, H., Wang, C., Chen, Y. 2013. The effect of biochar and bacterium agent on humification during swine manure composting. in: *Functions of Natural Organic Matter in Changing Environment*, Springer, pp. 1021-1025.

Ueda, R., Hirayama, S., Sugata, K., Nakayama, H. 1996. Process for the production of ethanol from microalgae, Google Patents.

Uellendahl, H., Ahring, B.K. 2010. Anaerobic digestion as final step of a cellulosic ethanol biorefinery: Biogas production from fermentation effluent in a UASB reactor-pilot-scale results. *Biotechnology and Bioengineering*, **107**(1), 59-64.
USCC. 2012. USCC Position Statement: Keeping Organics Out of Landfills US Composting Council Ronkonkoma.
USDA. 2010. *Wood Handbook: Wood as an Engineering Material*. U.S. Department of Agriculture, Forest Service, Forest Products Laboratory, Madison, WI
Washington, D.C.
Valdés, H., Sánchez-Polo, M., Rivera-Utrilla, J., Zaror, C. 2002. Effect of ozone treatment on surface properties of activated carbon. *Langmuir*, **18**(6), 2111-2116.
Varhegyi, G., Antal Jr, M.J., Jakab, E., Szabó, P. 1997. Kinetic modeling of biomass pyrolysis. *Journal of Analytical and Applied Pyrolysis*, **42**(1), 73-87.
Vavilin, V.A., Angelidaki, I. 2005. Anaerobic degradation of solid material: Importance of initiation centers for methanogenesis, mixing intensity, and 2D distributed model. *Biotechnology and Bioengineering*, **89**(1), 113-122.
Velmurugan, B., Ramanujam, R.A. 2011. Anaerobic digestion of vegetable wastes for biogas production in a fed-batch reactor. *International Journal of Emerging Sciences*, **1**(3), 478-486.
Venderbosch, R.H., Prins, W. 2010. Fast pyrolysis technology development. *Biofuels, Bioproducts and Biorefining*, **4**(2), 178-208.
Vitousek, P.M., Aber, J.D., Howarth, R.W., Likens, G.E., Matson, P.A., Schindler, D.W., Schlesinger, W.H., Tilman, D.G. 1997. Human alteration of the global nitrogen cycle sources and consequences. *Ecological Applications Ecological Applications*, **7**(3), 737-750.
Wagenaar, B., Prins, W., Van Swaaij, W. 1993. Flash pyrolysis kinetics of pine wood. *Fuel Processing Technology*, **36**(1), 291-298.
Wang, X., Kersten, S.R., Prins, W., van Swaaij, W.P. 2005. Biomass pyrolysis in a fluidized bed reactor. Part 2: Experimental validation of model results. *Industrial & Engineering Chemistry Research*, **44**(23), 8786-8795.
Weimer, P.J., Russell, J.B., Muck, R.E. 2009. Lessons from the cow: What the ruminant animal can teach us about consolidated bioprocessing of cellulosic biomass. *Bioresource Technology*, **100**(21), 5323-5331.
Wen, Z., Frear, C., Chen, S. 2007. Anaerobic digestion of liquid dairy manure using a sequential continuous-stirred tank reactor system. *Journal of Chemical Technology & Biotechnology*, **82**(8), 758-766.
Westerhout, R., Waanders, J., Kuipers, J., Van Swaaij, W. 1997. Kinetics of the low-temperature pyrolysis of polyethene, polypropene, and polystyrene modeling, experimental determination, and comparison with literature models and data. *Industrial & Engineering Chemistry Research*, **36**(6), 1955-1964.
Wijffels, R.H., Barbosa, M.J. 2010. An outlook on microalgal biofuels. *Science*, **329**(5993), 796.
Williams, D. 1991. Environmental implications of composting. University of Illinois at Urbana-Champaign. http://web.aces.uiuc.edu/vista/pdf_pubs/COMPOST.PDF.
Winges, K. 2011. An air quality modeling investigation of potential odors from a composting facility. Cedar Grove Composting Facility. Everett, Washington

Wood, M.G., Greenfield, P.F., Howes, T., Johns, M.R., Keller, J. 1995. Computational fluid dynamic modeling of waste-water ponds to improve design. *Water Science and Technology*, **31**(12), 111-118.

Wu, B.X., Chen, S.L. 2008. CFD simulation of non-Newtonian fluid flow in anaerobic digesters. *Biotechnology and Bioengineering*, **99**(3), 700-711.

Wu, C.F., Wang, Q.H., Sun, X.H., Xue, N.T., Liu, S., Xie, W.M. 2011. Effect of aeration modes on the characteristics of composting emissions and the NH_3 removal efficiency by using biotrickling filter. *Waste Management*, **31**(8), 1702-1710.

Wu, J., Pullum, L. 2000. Performance analysis of axial-flow mixing impellers. *AIChE Journal*, **46**(3), 489-498.

Xie, S., Frost, J.P., Lawlor, P.G., Wu, G., Zhan, X. 2011. Effects of thermo-chemical pre-treatment of grass silage on methane production by anaerobic digestion. *Bioresource Technology*, **102**(19), 8748-8755.

Xue, Y., Hou, H., Zhu, S. 2009. Characteristics and mechanisms of phosphate adsorption onto basic oxygen furnace slag. *Journal of Hazardous Materials*, **162**(2), 973-980.

Yang, H., Yan, R., Chen, H., Zheng, C., Lee, D.H., Liang, D.T. 2006. In-depth investigation of biomass pyrolysis based on three major components: hemicellulose, cellulose and lignin. *Energy & fuels*, **20**(1), 388-393.

Yen, H., Brune, D. 2007. Anaerobic co-digestion of algal sludge and waste paper to produce methane. *Bioresource Technology*, **98**(1), 130-134.

Yepsen, R. 2012. Residential food waste collection in the united states. *Biocycle*.

Yilmaz, P., Kottmann, R., Field, D., Knight, R., Cole, J.R., Amaral-Zettler, L., Gilbert, J.A., Karsch-Mizrachi, I., Johnston, A., Cochrane, G. 2011. Minimum information about a marker gene sequence (MIMARKS) and minimum information about any (x) sequence (MIxS) specifications. *Nature Biotechnology*, **29**(5), 415-420.

Yoshizawa, S., Tanaka, S., Ohata, M., Mineki, S., Goto, S., Fujioka, K., Kokubun, T. 2005. Composting of food garbage and livestock waste containing biomass charcoal. *Proceedings of the International Conference and Natural Resources and Environmental Management*. pp. 2011.

Yu, L. 2012. Simulation of flow, mass transfer and bio-chemical reactions in anaerobic digestion. in: *Department of Biological Systems Engineering*, Vol. PhD, Washington State University. Pullman, pp. 193.

Yu, L., Ma, J.W., Chen, S.L. 2011. Numerical simulation of mechanical mixing in high solid anaerobic digester. *Bioresource Technology*, **102**(2), 1012-1018.

Zamalloa, C., De Vrieze, J., Boon, N., Verstraete, W. 2011. Anaerobic digestibility of marine microalgae Phaeodactylum tricornutum in a lab-scale anaerobic membrane bioreactor. *Applied Microbiology Biotechnology*.

Zhang, R., El-Mashad, H.M., Hartman, K., Wang, F., Liu, G., Choate, C., Gamble, P. 2007a. Characterization of food waste as feedstock for anaerobic digestion. *Bioresource Technology*, **98**(4), 929-935.

Zhang, X., Ye, J., Jensen, O.N., Roepstorff, P. 2007b. Highly efficient phosphopeptide enrichment by calcium phosphate precipitation combined with subsequent IMAC enrichment. *Molecular & Cellular Proteomics*, **6**(11), 2032-2042.

Zhao, B.-H., Yue, Z.-B., Ni, B.-J., Mu, Y., Yu, H.-Q., Harada, H. 2009. Modeling anaerobic digestion of aquatic plants by rumen cultures: Cattail as an example. *Water Research*, **43**(7), 2047-2055.

Zhao, B., Wang, H., Li, R., Mao, X. 2010. Thalassospira xianhensis sp. nov., a polycyclic aromatic hydrocarbon-degrading marine bacterium. *International Journal of Systematic and Evolutionary Microbiology*, **60**(5), 1125.

Zhao, Q., Dvorak, S.W., Chen, S., Frear, C., VanLoo, B.J. 2012. Nutrient recovery systems and methods, Vol. US 2012/0118035 A1. USA.

Zhou, S., Wang, Z., Liaw, S.-s., Li, C.-Z., Garcia-Perez, M. 2013. Effect of sulfuric acid on the pyrolysis of douglas fir and hybrid poplar wood: Py-GC/MS and TG studies. *Journal of Analytical and Applied Pyrolysis*, **104**, 117-130.